

Electronic Thesis and Dissertation Repository

3-27-2020 1:45 PM

Light downshifting zinc oxide-ethylene vinyl acetate nanocomposite greenhouse films

David V. Hiscott, *The University of Western Ontario*

Supervisor: Charpentier, Paul A., *The University of Western Ontario*

A thesis submitted in partial fulfillment of the requirements for the Doctor of Philosophy degree in Chemical and Biochemical Engineering

© David V. Hiscott 2020

Follow this and additional works at: <https://ir.lib.uwo.ca/etd>

 Part of the [Polymer Science Commons](#)

Recommended Citation

Hiscott, David V., "Light downshifting zinc oxide-ethylene vinyl acetate nanocomposite greenhouse films" (2020). *Electronic Thesis and Dissertation Repository*. 6981.
<https://ir.lib.uwo.ca/etd/6981>

This Dissertation/Thesis is brought to you for free and open access by Scholarship@Western. It has been accepted for inclusion in Electronic Thesis and Dissertation Repository by an authorized administrator of Scholarship@Western. For more information, please contact wlsadmin@uwo.ca.

Abstract

One method to increase the productivity of greenhouse agriculture is to increase the amount of photosynthetically available light within. This was accomplished using nanocomposite greenhouse film comprised of light downshifting zinc oxide quantum dots and ethylene vinyl acetate copolymer. As this material will be used on a commodity scale, two different approaches – a large batch process and continuous plug flow reactor – were designed for mass production of zinc oxide. A design of experiment was performed to determine which synthesis parameters contribute more strongly to the quantum dot's growth. This was done for a small-scale batch synthesis and a continuous plug flow reactor. In both cases, temperature was determined to be the most important factor, with total reagent concentration being the second most important factor. The growth parameters for the plug flow reactor were tested for their effect on the quantum yield of the nanomaterial; in this case, the ratio between the hydroxide base and zinc ions was the most important factor. Furthermore, the effects of capping agents on the growth was also analyzed and it was determined that siloxane and polymer capping agents were found to give the most luminescent quantum dots. Different siloxane agents, with differing functional group side chains, were successfully attached to zinc oxide nanomaterial and these were melt-mixed into nanocomposites with ethylene vinyl acetate copolymer to ascertain their effects on the composite's material properties. It was found that vinyltrimethoxysiloxane was the capping agent which gave the greatest increase in material properties at a loading of 1 %. This composite was also found to be resistant to UV induced weathering and possessed a greater thermal stability. The composite was also shown to increase the hydrophobicity and decrease the thermicity for greenhouse films. Lastly, the light downshifting ability was measured and shown to increase the growth rate of photosynthetic green algae by 4.7 %. This material shows excellent promise for use as a greenhouse film – it has a higher tensile strength, resistance to degradation, more hydrophobic, insulates better, and increases available light.

Keywords

Zinc oxide, Nanocomposite, Greenhouse films, Light downshifting, Quantum dots, Solar films, UV blocking, Ethylene vinyl acetate copolymer, ZnO synthesis

Summary for Lay Audience

The objective of this research project was to produce transparent film nanocomposites for greenhouses that contain tiny zinc oxide crystals within. These crystals absorb UV light and reemit it as blue light, thus increasing the quantity of light available within the greenhouse for the plants to use to grow. The optimal methods to produce the zinc oxide was studied and two methods for large-scale production were devised – a large batch process and a continuous reactor. Lastly modifications were made to the zinc oxide crystals to enhance several properties of the composites including strength, stability, insulation and wettability. These novel films should increase the productivity of greenhouses they are installed in.

Co-Authorship Statement

Title: Determining the significant parameters for the growth of zinc oxide quantum dots in batch and continuous reactor systems and optimizing the quantum yield for quantum dots grown in a continuous reactor

Authors: Hiscott, DV, Zhou, Z, Machin, D & Charpentier, PA

This work was conducted by David Hiscott who performed the syntheses under the supervision of Prof. Paul A. Charpentier. Ze Zhou performed the PFR growth study, while Devin Machin obtained the quantum yields for the PFR samples. Further experiments are being planned then this work will be prepared for publication.

Title: Large scale synthesis and purification of silane-capped ZnO quantum dots

Authors: Hiscott, DV, Xu, Z, Machin, D, Esbroeck, J & Charpentier, PA

The experiment was conducted by David Hiscott who designed its approach, under the supervision of Prof. Paul A. Charpentier. Dr. Zhiming Xu aided with performing the NMR analysis and interpretation of the results. Devin Machin aided with the XRD analysis of the samples. The synthesis of the large batch was performed at Sunwash Technologies with the aid of Jeremy Esbroeck. Parts of this work are being prepared for a communication.

Title: The effect of different siloxane capping agents on the mechanical properties of transparent zinc oxide-ethylene vinyl acetate copolymer nanocomposites

Authors: Hiscott, DV, Wu, W, Leidl, J, Machin, D & Charpentier, PA

This experiment was conducted by David Hiscott who synthesized the capped quantum dots and performed most of the analyses under the supervision of Prof. Paul A. Charpentier. Dr. Wei Wu aided in the mechanical testing, helping prepare the samples for DMA analysis and provided training on the instrument. Jamie Leidl aided in melt-mixing the nanocomposites and pressing the films. Devin Machin aided in with the TGA analysis of the quantum dots. This manuscript is under preparation for publication.

Title: Light downshifting silane capped zinc oxide-ethylene vinyl acetate copolymer nanocomposite greenhouse films

Authors: Hiscott, DV, Cvetkovska, M, Mumin, MA, Tran, M & Charpentier, PA

This experiment was conducted by David Hiscott who developed the nanoparticles used, their capping, and designing the algal growth experiment under the supervision of Prof. Paul A. Charpentier. The testing of the light downshifting and algae growth experiments were performed at the University of Ottawa in the laboratory of Prof. Marina Cvetkovska, who advised on algae growth and measurement techniques. Dr. Md Abdul Mumin aided with the thermicity measurements, performing the tests and analyzing the data. Michelle Tran sampled the algae tubes daily and plotted the curves. This manuscript is under preparation for publication.

Acknowledgments

I would like to thank Prof Paul A. Charpentier for his support and guidance during the course of my PhD project. He always allowed the research to proceed in a manner which I saw fit but was always available if I needed ideas or advice.

Special thanks to the postdocs in our lab – Dr. Wei Wu and Dr. William Z. Xu – for their training and help with the instrumentation. I would also like to thank my colleagues in the lab who aided in many ways.

I would like to thank Prof. Marina Cvetkovska and Prof. Norman A. Hüner for helping me with the algae growth experiments, which were critical as the proof-of-concept that our nanocomposite films had a positive impact on the growth rate of photosynthetic organisms. I was not familiar with biological systems and testing, but they helped me design the experiment.

I would like to thank my family and friends for support and encouragement during the years of my program.

Finally, I would like to mention that this work has been carried out with financial support from Natural Science and Engineering Research Council of Canada (NSERC), Ontario Ministry of Agriculture, Food and Rural Affairs (OMAFRA), Ontario Greenhouse Vegetable Growers (OGVG) and ReMAP network. Collaborations with Sunwash Technologies and DuPont also helped with running experiments and providing material.

Table of Contents

Abstract.....	ii
Summary for Lay Audience.....	iii
Co-Authorship Statement.....	iv
Acknowledgments.....	vi
Table of Contents.....	vii
List of Tables.....	xi
List of Figures.....	xiii
List of Appendices.....	xviii
List of Equations.....	xix
List of Abbreviations.....	xx
Chapter 1 : Introduction.....	1
1.1 Motivation.....	2
1.2 Literature review.....	2
1.2.1 Quantum dots.....	2
1.2.2 Zinc oxide quantum dot overview.....	3
1.2.3 Zinc oxide photoluminescence.....	4
1.2.4 Synthesis of ZnO quantum dots.....	6
1.2.5 Capping of zinc oxide quantum dots.....	9
1.2.6 Nanocomposites.....	11
1.2.7 Greenhouse film overview.....	13
1.2.8 Properties of greenhouse films that can be improved with nanotechnology.....	15
1.3 Objective.....	24
Chapter 2 :.....	26

2	Determining the significant parameters for the growth of zinc oxide quantum dots in batch and continuous reactor systems and optimizing the quantum yield for quantum dots grown in a continuous reactor	26
2.1	Introduction.....	28
2.2	Experimental.....	31
2.2.1	Materials	31
2.2.2	Batch synthesis of ZnO growth rate design of experiment.....	31
2.2.3	Plug flow reactor synthesis of ZnO growth rate design of experiment	34
2.2.4	Effect of reaction parameters on QY of ZnO synthesized in PFR.....	36
2.2.5	Effect of capping agents on quantum yield of ZnO synthesized in PFR..	38
2.3	Results and Discussion	39
2.3.1	Batch synthesis of ZnO growth rate design of experiment.....	39
2.3.2	Plug flow reactor synthesis of ZnO growth rate design of experiment	45
2.3.3	Effect of reaction parameters on QY of ZnO synthesized in PFR.....	47
2.3.4	Effect of capping agents on quantum yield of ZnO synthesized in PFR..	48
2.4	Conclusion	51
	Chapter 3.....	52
3	Large scale synthesis and purification of silane-capped ZnO quantum dots	52
3.1	Introduction.....	54
3.2	Experimental.....	55
3.2.1	Materials	55
3.2.2	ZnO quantum dot synthesis	55
3.2.3	Characterization of quantum dots	57
3.2.4	Scaled up purification	57
3.3	Results and Discussion	58
3.3.1	Reaction yield of ZnO synthesis	58
3.3.2	Photoluminescence of ZnO quantum dots	60

3.3.3	XPS analysis of uncapped and silane-capped ZnO quantum dots	61
3.3.4	EDX analysis of small- and large-scale VTS-ZnO synthesis batches	67
3.3.5	XRD analysis of small- and large-scale VTS-ZnO synthesis batches	69
3.3.6	Scaled-up purification of VTS-ZnO quantum dots via centrifugation	72
3.4	Conclusion	73
Chapter 4	75
4	The effect of different siloxane capping agents on the mechanical properties of transparent zinc oxide-ethylene vinyl acetate copolymer nanocomposites	75
4.1	Introduction.....	77
4.2	Experimental.....	79
4.2.1	Materials	79
4.2.2	ZnO quantum dot synthesis	79
4.2.3	Characterization of ZnO quantum dots.....	81
4.2.4	Nanocomposite production	82
4.2.5	Determination of nanocomposite material properties.....	82
4.2.6	Optical measurements for UV-VIS transmission and dispersion	83
4.3	Results and discussion	83
4.3.1	ZnO quantum dot size estimates	83
4.3.2	Confirmation of ligand attachment	84
4.3.3	Dynamic mechanical analysis of nanocomposites.....	85
4.3.4	Tensile testing on nanocomposites	91
4.3.5	Characterization of VTZ-ZnO quantum dots.....	92
4.3.6	Effects of VTS-ZnO on stability of composite EVA films.....	94
4.3.7	Optical properties of silane-capped ZnO:EVA nanocomposites	97
4.4	Conclusion	99
Chapter 5	101

5	Light downshifting silane capped zinc oxide-ethylene vinyl acetate copolymer nanocomposite greenhouse films	101
5.1	Introduction.....	103
5.2	Experimental.....	105
5.2.1	Materials	105
5.2.2	ZnO quantum dot synthesis	106
5.2.3	Physical properties	106
5.2.4	Laminated greenhouse film production	107
5.2.5	Optical properties of laminated film and effect on algae growth	108
5.3	Results and discussion	110
5.3.1	Photoluminescence of nanocomposites	110
5.3.2	Physical properties	112
5.3.3	Optical properties of laminated film and effect on algae growth	116
5.4	Conclusion	120
Chapter 6	122
6	Conclusions and Recommendations	122
6.1	Conclusions.....	123
6.2	Recommendations.....	124
References	126
Appendices	143
Curriculum Vitae	161

List of Tables

Table 1: Parameters to be inputted into DOE for ZnO batch synthesis.....	32
Table 2: Recipes for batch synthesis DOE. Each solution is separately made, and then combined to start the trial.	32
Table 3: ZnO synthesis parameters to be inputted into DOE for growth in a PFR.	35
Table 4: Recipes for PFR synthesis DOE. Each solution is separately made, and then combined to start the trial.	36
Table 5: Reaction parameters tested to determine their effect on the QY of ZnO synthesized in a PFR.....	37
Table 6: Capping agents to be tested for their effect on QY of PFR synthesized ZnO quantum dots.....	38
Table 7: Summary of maximum absorption values from each trial and the corresponding estimated particle size.	40
Table 8: Summary of reaction rates for each trial to be inputted into Minitab as responses for the batch synthesis DOE.	41
Table 9: Summary of maximum absorption values from each trial and the corresponding estimated particle size.	45
Table 10: Summary of QYs obtained for different reaction parameters tested in the ZnO PFR.	48
Table 11: Maximum calculated UV absorption for capped ZnO quantum dots and estimated particle radius.....	49
Table 12: EDX elemental compositions for the two different sized synthetic batches.	69
Table 13: Change in sodium:zinc ratio after centrifugation and washing cycles.	73

Table 14: Photoluminescent properties and size estimates of silane-capped ZnO quantum dots.....	83
Table 15: Tensile properties on silane-capped nanocomposites.....	92
Table 16: Effect of VTS-capped ZnO quantum dots on the tensile properteis of weathered ZnO:EVA composite films.	95
Table 17: Contact angles measured for different QD loadings in EVA nanocomposite film.	113
Table 18: Normalized thermicity values for different loadings of QDs with EVA nanocomposite films.	115

List of Figures

Figure 1: Relationship between band gap, emission and quantum dot size. As quantum dots increase in size, their band gap decreases, and their emission becomes redshifted to longer wavelengths.....	3
Figure 2: Synthesis overview for nanoparticles depicted above with the red and blue squares representing two different ionic species that are combined to form a crystal. The steps are: solvation – dissolving the precursor reagents into ions so they may interact with each other; nucleation – at a certain critical local concentration, the first seeds of crystals form; growth – the remaining ionic species in the reaction arrange themselves on the existing crystal nuclei, growing ordered structure; and Ostwald ripening – the small crystals have high surface energies and minimize this by losing atoms which diffuse to larger crystals, see larger structures form at expense of smaller crystals. Lastly the larger crystals can also aggregate together.	6
Figure 3: Zinc oxide quantum dot showing surface hydroxyls and structure of siloxane capping shell.	11
Figure 4: UV driven Norrish reaction inducing deacetylation of EVA chain. Modified from [93].....	14
Figure 5: Three different contact angle situations: A) hydrophilic where the water spreads into thin film and has contact angle $< 90^\circ$; B) neutral with contact angle of 90° ; and C) hydrophobic with contact angle $> 90^\circ$ where the water beads.....	19
Figure 6: Simple overview of photosynthesis. Sunlight is absorbed by chlorophyll pigments in leaves and used to drive the conversion of carbon dioxide and water to sugars and oxygen.	21
Figure 7: The two chlorophyll pigments primarily absorb light from blue and red wavelengths in the visible light spectrum. Plants have also evolved additional pigments, such as carotenoids, that can capture more photons and transfer that energy to photosynthesis....	22

Figure 8: Schematic representation of PFR. The Zn(OAc)₂·2H₂O and NaOH solutions are loaded into separate syringes and a syringe pump pushes them together to mix in a T-union and then to flow through the reactor tubing..... 34

Figure 9: Pareto chart for the batch DOE (top) indicating which factors are statistically significant and the factorial response chart (bottom). The Pareto chart shows which responses are significant from the experiments ran, as they are the ones whose response is above the cutoff ($\alpha > 0.05$)..... 42

Figure 10: Natural logarithm Arrhenius plot for growth of ZnO QDs in ethanol during batch synthesis. The slope of the trendline will be used to approximate the activation energy for the system. 44

Figure 11: Pareto chart for PFR DOE (top) indicating which factors are statistically significant and factorial response chart (bottom). The Pareto chart shows which responses are significant from the experiments ran, as they are the ones whose response is above the cutoff ($\alpha > 0.05$)..... 46

Figure 12: ¹HMR spectra of (A) precursor reagent zinc acetate dihydrate where the circled peak is assigned to the precursor acetate's hydrogens; (B) unpurified ZnO from the small batch, where the circled peak is assigned to the side product sodium acetate's hydrogens; and (C) unpurified ZnO from the large batch reaction, where the circled peak is assigned to the side product sodium acetate's hydrogens. 60

Figure 13: Photoluminescent emissions of UV excited quantum dots. The two spectra with their maxima centered at 500 nm are the silane-capped ZnO batches (small- and large-scale synthesis), while the third peak centered at 550 nm is the uncapped ZnO quantum dots. 61

Figure 14: XPS survey scan for ZnO quantum dots (top) and VTS-capped ZnO quantum dots. Both show expected Zn and O peaks; however, the capped QDs also contain peaks representing the silane shell atoms (Si and C)..... 63

Figure 15: XPS high resolution Zn 2P_{3/2} scan for ZnO quantum dots (top) and VTS-capped ZnO quantum dots (bottom). A small shift in the peak position is observed with the addition of the silane shell from 1021.32 eV to 1022.12 eV. 64

Figure 16: XPS high resolution Zn LMM scan of ZnO quantum dots (top) and VTS-capped ZnO quantum dots (bottom).....	65
Figure 17: XPS high resolution O 1s scan for ZnO quantum dots (top) and VTS-capped ZnO quantum dots (bottom). Small shift in binding energy observed. Uncapped QDs contained hydroxide peak corresponding to the surface hydroxyls moieties.....	66
Figure 18: EDX spectra of ZnO batches with small-scale synthesis shown in the top spectrum and the large-scale synthesis shown in the bottom spectrum.	68
Figure 19: XRD spectra of the (top) small- and (bottom) large-scale VTS-ZnO synthesis batches. The peaks that correspond to the 100, 002 and 101 facets of ZnO are indicated with arrows.....	70
Figure 20: XRD spectrum of uncapped ZnO quantum dots. 100, 002, and 101 peaks are evident. This spectrum closely matches the one presented in JCPDS 36-1451.....	72
Figure 21: Model of siloxane shell on ZnO nanoparticles. The hydroxides and linked to the methoxide groups on the siloxane via a base-catalyzed condensation reaction. A siloxane shell is formed linking when the siloxanes also link to each other, yielding a structure with the ZnO at its core and the R side chains being presented to the outside environment.....	80
Figure 22: Structures of the siloxanes used in this study. They are vinyltrimethoxysilane (A), 3-aminopropyltriethoxysilane (B), phenyltrimethoxysilane (C), 3-mercaptopropyltrimethoxysilane (D), and triethoxysilane (E).	81
Figure 23: FTIR spectra of the five differently capped QD samples. From the top to bottom they are: VTS (A), TEOS (B), phenyl (C), mercapto (D), and amino (E) silane capped quantum dots.....	85
Figure 24: DMA analysis of storage modulus vs. time for (a) 1% (wt/wt) nanocomposites and (b) 2.5% (wt/wt) nanocomposites, c/d) DMA analysis of loss modulus vs. time for (c) 1% (wt/wt) nanocomposites and (D) 2.5% (wt/wt) nanocomposites.....	88
Figure 25: DMA analysis of tan δ vs. time for (a) 1% (wt/wt) nanocomposites and (b) 2.5% (wt/wt) nanocomposites.....	90

Figure 26: HR-TEM image of vinyl-capped ZnO nanoparticles. The cores of the quantum dots were calculated to be 3.6 nm in diameter.	93
Figure 27: TGA analysis of vinyl capped ZnO. The final mass at 700oC is 86.39% of the sample remaining. ZnO and silane shells are stable at this temperature, so the lost mass comes from the alkyl side chains. From this, one can calculate the mass of the ZnO core in the quantum dots.	94
Figure 28: TGA breakdown of EVA nanocomposites. It is observed that the polymer becomes more thermally stable with the inclusion of larger concentrations of nanoparticles.	96
Figure 29: Visible light transmission of each of the 1% (w/w) nanocomposite films. All of them display excellent transmittance.	97
Figure 30: Confocal image of 1% (w/w) vinyl nanocomposite sample. Micrometer sized aggregates are clearly visible and can act as local stress concentrators.	99
Figure 31: Emission spectrum of UV bulbs used in growth experiments.	108
Figure 32: Growth test setup for VTS-ZnO composite films. The lights were at one end of the growth chamber, with the tested films set vertically just in front of the samples. The distance between the light and the algae cultures was 1.5 meters, so that the PAR measured at that location was $15 \mu\text{mol}\cdot\text{s}^{-1}\cdot\text{m}^{-2}$. The algae tubes were place within cardboard boxes to minimize exposure to any reflected light within the chamber.	109
Figure 33: Normalized photoluminescent spectra of capped and uncapped ZnO QDs excited at their maximum wavelength (top). The capped quantum dots, indicated in blue, have a diameter of 3.2 nm and a maximum emission at 480 nm; and the uncapped, shown in green, have an estimated diameter of 3.6 nm and a maximum emission at 550 nm. Excitation and emission ranges for VTS-ZnO quantum dots (bottom). They have a large excitation and emission range, which has to ability to shift a wide range of UV wavelengths into visible light.	111

Figure 34: Drop test results for different (wt/wt) percentage nanocomposite films. The films tested were (A) 2.5% ZnO, (B) 5% ZnO, (C) 10% ZnO, (D) 2.5% VTS-ZnO, (E) 5% VTS-ZnO, (F) 10% VTS-ZnO, and (G) EVA reference film..... 112

Figure 35: Change in contact angles from increasing loading of QDs within EVA nanocomposite films. 114

Figure 36: Change in thermicity in composite EVA films depending on QD loading. Both capped and uncapped decrease with loading, but silane-capped QDs show much greater thermicity. 116

Figure 37: UV-VIS transmission of VTS-ZnO:EVA nanocomposite coated transparent films. All weight percent composites show excellent transmission above 500 nm, but the higher loaded samples have decreased transmission in lower wavelengths. All sample films show complete UV absorption below 300 nm, likely a property of the base polymer that was coated with the composite. 117

Figure 38: Light changes measured from the different coatings used. The 2.5% VTS-ZnO composite samples shows improvement in PAR detected compared to the EVA reference. This is due to UV absorption and downshifting into visible light. 118

Figure 39: Growth curve for *C.reinhardtii* (left) based on OD750 and corresponding chlorophyll accumulation (right) in the same cultures. Both clearly indicate that the cultures grown behind the 2.5% composite film experiences a faster growth rate than the reference EVA film..... 120

List of Appendices

Appendix A: Transmittance vs wavelength graphs obtained for batch DOE trials from Chapter 2 showing change in UV-VIS spectrum over time during the ZnO synthesis reaction. Each chart is labelled accordingly to what trial they represent.	143
Appendix B: Cubed radius vs time graphs obtained for batch DOE trials from Chapter 2. Each chart is labelled accordingly to what trial they represent.	147
Appendix C: Photoluminescence spectra for PFR synthesized ZnO quantum dots from Chapter 2.	151
Appendix D: UV-VIS transmission spectra for differently capped ZnO quantum dots synthesized in PFR.	153
Appendix E: Photoluminescence spectra for differently capped ZnO quantum dots synthesized in a PFR.	157

List of Equations

Equation 1: LSW model.....	28 and 41
Equation 2: Effective mass model.....	33 and 84
Equation 3: Indirect quantum yield determination.....	37
Equation 4: Arrhenius equation.....	43
Equation 5: Natural logarithm of Arrhenius equation.....	44

List of Abbreviations

ATR-FTIR	Attenuated total reflectance Fourier-transform infrared spectroscopy
DOE	Design of Experiment
FTIR	Fourier-transform infrared spectroscopy
EBA	Ethylene butyl acrylate copolymer
EDX	Energy-dispersive X-ray spectroscopy
EtOH	Ethanol
EVA	Ethylene vinyl acetate copolymer
ICP	Inductively coupled plasma
IPA	Isopropyl alcohol
LDPE	Low density polyethylene
LDS	Light downshifting
LHC	Light harvesting complex
LSW	Lifshitz-Slyozov-Wagner
MeOH	Methanol
NaOH	Sodium hydroxide
PAR	Photosynthetically active radiation
PFR	Plug flow reactor
PFTE	Teflon
PV	Photovoltaic

PVA	Polyvinyl alcohol
PVP	Polyvinylpyrrolidone
QD	Quantum dot
QY	Quantum yield
TEM	Transmission electron microscope
UV	Ultraviolet
UV-VIS	Ultraviolet visible range
VTMS	Vinyltrimethoxysiloxane
VTS-ZnO	Vinyltrimethoxysiloxane-capped zinc oxide
ZnO	Zinc oxide
Zn(OAc) ₂ •2H ₂ O	Zinc acetate dihydrate
XPS	X-ray photoelectron spectroscopy
XRD	X-ray diffraction

Chapter 1

Chapter 1: Introduction

(Motivation, literature review and objective)

1.1 Motivation

The Earth's population is rapidly rising, while the amount of arable land for food production is decreasing steadily [1]. At the same time, climate change has the potential to fundamentally alter the stability of growing seasons for agriculture [2]. Together these can lead to a decrease in the productivity of agriculture operating in traditional outdoors fields. One way to mitigate this issue is through increased usage of greenhouses for food production. Greenhouses address these issues by being resistant to soil erosion and loss, protecting crops from extreme weather events, and extending growing seasons in cooler climates [3]. Greenhouses are self-contained ecosystems that can be optimized to create favorable microclimates accelerating plant growth [4]. The performance of greenhouses can be optimized through construction and agricultural practices, but a novel method to increase their productivity is through nanotechnology, specifically using quantum dots.

1.2 Literature review

1.2.1 Quantum dots

Quantum dots (QDs) are small inorganic crystals, that have one dimension in a range that is less than 100 nm, that can act as semiconductors [5]. When a semiconductor crystal gets small enough, below the compound's Bohr radius, they experience quantum confinement and their valence and conduction energy levels become quantified. This allows for discrete energy levels (Fermi levels). Quantum dots are generally comprised of Group II-VI or III-V combinations of elements with the most studied containing cadmium, mercury, indium, and selenide [6], however these elements are well known for their cytotoxicity. One property of quantum dots of interest to greenhouse applications is their ability to be photoluminescent – i.e the ability to absorb a photon and emit a photon at a lower energy wavelength. As well, due to the quantum confinement effect, the band gap of these nanoparticles is inversely related to their size.

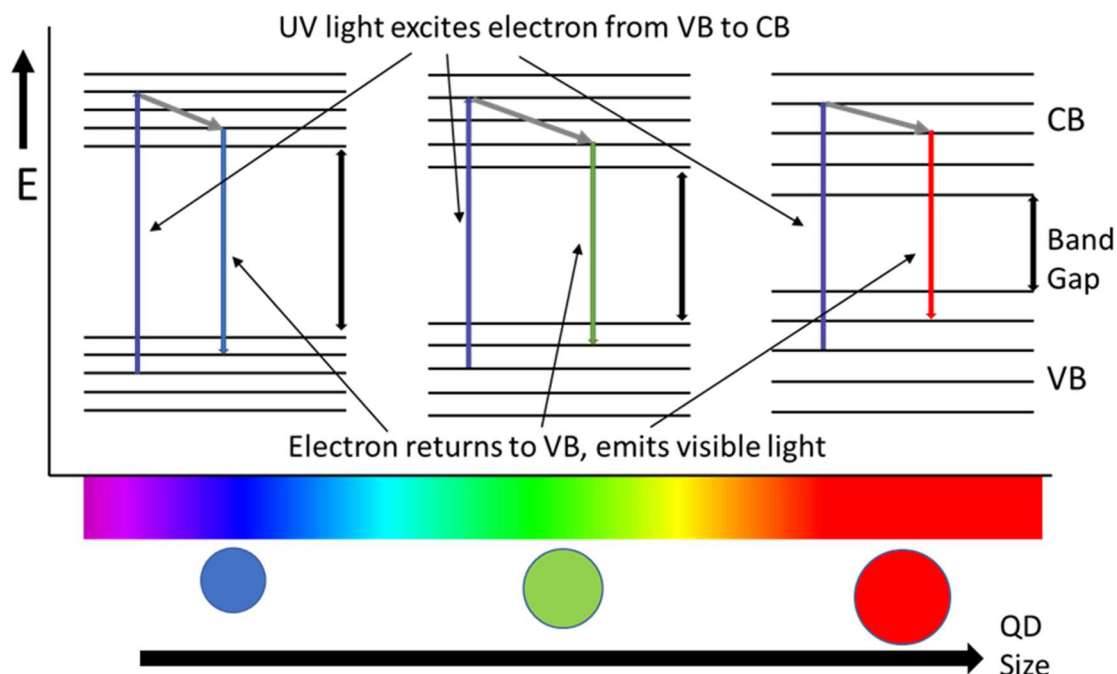


Figure 1: Relationship between band gap, emission and quantum dot size. As quantum dots increase in size, their band gap decreases, and their emission becomes redshifted to longer wavelengths.

1.2.2 Zinc oxide quantum dot overview

Zinc oxide (ZnO) is a UV absorbing material that has many properties that make it ideal for use as a photoluminescent QD. Zinc oxide (ZnO) has a large band gap (3.37 eV), which makes it natively transparent in the visible range [7]. It has a large exciton binding energy of 60 meV, enabling ZnO to undergo excitonic transitions at room temperature, and a radiation hardness to keep it photostable under long excitation periods [8]. It is a n-type semiconductor with a high electrical conductivity which makes it an excellent candidate for photovoltaic applications [9]. When excited with UV radiation, ZnO has an intense and tunable photoluminescence [10]. ZnO is considered a green, or environmentally friendly material because it is biocompatible, biodegradable and has a low toxicity [11]. These properties make it a very attractive candidate for use at the commodity scale. Furthermore, ZnO is a relatively inexpensive nanomaterial to synthesize, not requiring coordinating solvents, high temperatures, or inert conditions

[12]. Due to these properties, ZnO has wide range of potential uses including photovoltaic cells [13], gas sensors [14], light-emitting diodes [15], antibacterial surfaces [16], use as a cross-linker in rubber [17], as a UV absorber in sunscreens [18], and medical imaging [19].

ZnO has a wide band gap of 3.37 eV, which allows it to absorb radiation with wavelengths above 370 nm [20]. However, while bulk ZnO absorbs UV radiation, it does not natively emit in the visible range, rather, it emits in lower energy wavelengths of the UV spectrum (385 nm) [21]. This UV emission originates from the radiative recombination of a hole in the valence band and a photoexcited electron in the conduction band. For ZnO crystals to emit in the visible range, the crystals must be within the Bohr radius of 2.87 nm [22]. When a ZnO crystal is below its Bohr radius, which is the most probable distance from the nucleus to electrons in the valence band, its energy levels experience an effect called quantum confinement, where emission levels are related to the crystal's size. In this case, small ZnO crystals absorb in the UV range and emit with a large Stokes shift in the visible range in a manner tunable with size [23]. However, it must be noted that the quantum yield of ZnO quantum dots – the amount of energy emitted compared to absorbed – decreases with increasing crystal size [24].

1.2.3 Zinc oxide photoluminescence

Nanoparticle ZnO has two primary emissions under UV irradiation and excitement. The first is a relatively weak and narrow UV emission centered around 380 nm (3.25 eV), with a narrow Stokes shift from absorption. A much stronger and broader emission band is situated in the green portion of the visible spectrum between 500-520 nm (2.35-2.5 eV) [25]. The exact mechanism of the green luminescence is not fully understood, but the involvement of crystal and/or lattice defects is proposed to be the source [26]. This is commonly attributed to oxygen vacancies and defects on the surface of the crystal, where the recombination of a photoexcited electron from a surface defect with a deep trap located in a singly charged oxygen vacancy causes green luminescence [25]. The surface defects (usually singly charged oxygen states) trap photo-generated holes, which can then return to the bulk phase via a tunneling process and recombine with oxygen vacancies [11]. The importance of the oxygen vacancies is further substantiated when ZnO is

synthesized under oxygen-deficit conditions, which is found to increase the quantum yield of the nanoparticles [27].

Other types of emission at different wavelengths have also been proposed. For instance, Hodlur et al (2014)[28] reviewed four possibilities: 1) a sharp UV band gap emission, where photoexcited electrons directly transition from the conduction band to the valence band; 2) slightly broader but close to band gap (violet) emission. In this case photoexcited electrons are captured by interstitial Zn defects that are positioned close to the conduction band, which leads to radiative transition to the valence band [29]; 3) a broad blue emission, attributed to discrete energy levels created in the band gap close to the conduction band by extrinsic impurity [7]; and 4) the aforementioned broad (green, yellow, red) emission due to recombination of electrons from the conduction band. Unoxidized interstitial zinc has also been proposed as the source of blue light emission [30]; however, surface defects remain the primarily proposed site of visible light emission. ZnO quantum dots' visible emission. These deep levels are created by oxygen vacancies and defects that originate on the surface of the crystals [25]. This mechanism is further substantiated by the fact that changes to the surface – such as thermal annealing, capping, water degradation – would remove the surface defects leading to an observed decrease in visible light emission. For example, removal of electron scavengers (such as oxygen or different oxides) from the vicinity of the surface defects can completely quench visible emission [25].

One of the main determinants of emission wavelength is the particle size, which can be controlled during the synthesis process by adjusting the reaction time and the ratio of reactants [31]. As particles get smaller, their surface area-to-volume ratio increases and as a result emission in the visible part of the spectrum dominates. The distance between the defects and oxygen vacancies increases with increased particle size, decreasing the likelihood of a visible light emitting recombination [32]. Because of this, their UV emission increases at the expense of the visible light emission, but it should be noted that the overall light emission (UV plus visible) decreases with increasing particle size [26]. Due to the quantum confinement effect, the particle size below the Bohr radius (2.87 nm in ZnO) also determines the band gap, and hence the emission wavelength. In particles

smaller than the Bohr radius, the visible emission is shifted towards the blue part of the spectrum [33]. In contrast, larger particles are generally redshifted, allowing for a mechanism of emission control; however, overall quantum yield decreases with the redshift [21]. Finally, a broad blue emission can also be observed with ZnO particles are capped with oxygen-containing ligands, but the exact mechanism of this behavior is still unknown [34] and appears to originate from a different source than the green emission [29].

1.2.4 Synthesis of ZnO quantum dots

Zinc oxide, like all nanoparticles, can be synthesized in either a top-down or bottom-up manner. When the QDs are produced by breaking down a larger bulk material, this is a top-down approach. This approach was used by Azam et al (2009) when producing ZnO nanoparticles by mechanochemically grinding zinc acetate and tartaric acid and then thermally decomposing the material to yield QDs [35]. The bottom-up approach involves combining smaller precursors which precipitate to give quantum dots. This type of synthesis was first described in 1950 by Lamar and Dinergar [36] and has three steps to it: nucleation, growth, and Ostwald ripening.

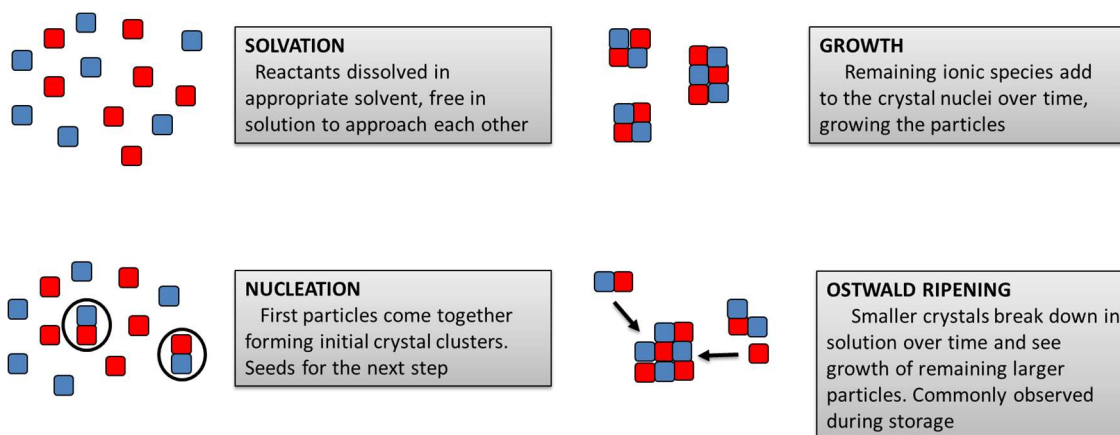
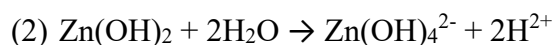
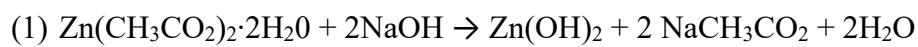


Figure 2: Synthesis overview for nanoparticles depicted above with the red and blue squares representing two different ionic species that are combined to form a crystal.

The steps are: solvation – dissolving the precursor reagents into ions so they may interact with each other; nucleation – at a certain critical local concentration, the first seeds of crystals form; growth – the remaining ionic species in the reaction

arrange themselves on the existing crystal nuclei, growing ordered structure; and Ostwald ripening – the small crystals have high surface energies and minimize this by losing atoms which diffuse to larger crystals, see larger structures form at expense of smaller crystals. Lastly the larger crystals can also aggregate together.

Zinc oxide dots are commonly synthesized via a controlled precipitation reaction involving reducing a zinc salt with a reducing agent in a sol-gel reaction [37]. Sol-gel processes are relatively inexpensive, require mild conditions, and allow for the addition of organic ligands, surfactants, or stabilizers. The mechanism of zinc oxide nucleation in a base catalyzed sol-gel was proposed by Rani et al (2008) [38]:



In the first step of this type of synthesis, zinc acetate dihydrate is hydrolyzed to zinc hydroxide in a basic medium. In the second step the zinc hydroxide is reduced to a zincate ion with the negatively charge ionic species being stabilized by the basic environment. In the third step, which is the nucleation stage for the synthesis, the zincate ions undergo a condensation reaction forming ZnO. The final reaction is an equilibrium reaction, so minimizing the presence of water in the system is critical to drive yield. The process of nucleation only occurs at local critical concentrations, below that, growth occurs. As those two processes occur simultaneously, in order to achieve a narrow size distribution of particles, either the nucleation time must be minimal with all nuclei forming at the same time, or the growth must be slowed. Performing the reactions at a higher base content or slowing the growth with cooler temperatures can help favor nucleation [39]. These conditions can help lead to the formation of smaller QDs with a narrow size distribution. Cations from the chosen base, especially at low pHs, can also form a passivating layer on the surface of the nanoparticles and further limit their growth. The ratio between the base and zinc salt is a commonly used to control the particle size [21]. The ratio of base to zinc salt influences the size of the QDs, which also influences

their emission color as they redshift with decreasing OH^- levels [23]. This also directly impacts their luminescence as the quantum yield is highest when the particles remain small [40]. The visible luminescence is proposed to be a surface effect, so increasing the size decreases the surface area to volume ratio. As well, increased growth leads to more time for complete crystal structures to form, limiting the quantity of surface defects such as oxygen vacancies, which are the visible emission source [41]. Another method of size control is slowing the rates of growth and ripening. This can be accomplished through solvent choice. Solvents that stabilize the products – such as polar solvents stabilized polar ZnO particles – and solvents that affect the solute mobility of the precursors will both limit growth and ripening [42].

Batch reactions, like the described ZnO sol-gel, are excellent for studying the behavior of the reaction system but do have some flaws. Their reaction conditions and precursor concentrations are not uniform as a function of time, making it more difficult to control the growth [43]. They suffer from a lack of precise control over mixing, nucleation and growth processes. During a precipitation reaction, nucleation, growth, ripening and agglomeration can occur simultaneously [44]. This leads to variable products in terms of the final particle size, distribution, crystal structure and properties. More efficient mixing and rapid mass/heat transfer would help optimize the synthesis. This can potentially be achieved by using a continuous microreactor system. These operate as plug flow reactors, so no change in reactant species, concentration, stoichiometric ratio at any one time point [43]. Microreactor systems generally consist of two or more pumps feeding reagent solutions together into a chaotic mixing region, and then the solution is pushed through a narrow tube under laminar flow conditions. The flow, reagent concentrations, temperature, and residence time can all be optimized to produce QDs with desired properties [45]. Microflow reactors also provide for optimal mixing and uniformity of temperature, mass and residence time. Each step of the reaction, such as nucleation, can be controlled allowing for much tighter control of the final product [46]. Microreactors also have the potential to produce quality nanomaterial at an industrial scale, which would be extremely difficult using batch processes [47]. Running hundreds of microreactors in parallel would be one approach to scale the process to commercial levels [48].

1.2.5 Capping of zinc oxide quantum dots

Nanoparticles have a strong tendency to aggregate, which can change their optical properties and thus presents a problem for transparency. This is due to their high surface area-to-volume ratio and high surface energy which drives aggregation and Ostwald ripening in solutions and colloids [49]. Nanoparticles have an extremely high surface area to volume ratio, which leads them to have high surface energies. To minimize this surface energy, nanoparticles will undergo ripening in storage and aggregate into larger structures [49]. This increase in size can redshift the absorption and emission due to the changes in effective crystal size [26]. When the aggregates (or agglomerations) grow above the compound's Bohr radius – above 2.8 nm for ZnO – the particles no longer experience quantum confinement and behave like bulk materials [26]. For ZnO, this means they only will emit in the UV range and their visible emission is completely quenched.

There are several methods that can prevent aggregation. One method to keep ZnO quantum dots dispersed is the use of dispersants such as polyols. For example, Huang et al (2015) kept an ethanoic colloid of ZnO for months stable using PEG as a stabilizer [50]; and Gutal et al (2015) used PVP for a similar stabilizing effect [51]. Residual acetate (or other anions from the zinc salt) can also act as capping agents and help passivate the surface of dots, helping to limit ripening and agglomeration, but that approach has limited feasibility in purified nanomaterial [52]. The use of capping agents/ligands is a method to decrease the surface energy of nanoparticles and decrease their tendency to aggregate [53]. Capping agents are chemical compounds that interact with the surface of nanoparticles to form a layer around the particle core. These stabilize the colloidal stability helping to stop uncontrolled growth and agglomeration [54]. The addition of a capping layer increases the total size of the nanoparticle-capping ligand shell which in turn decreases their surface area to volume ratio, minimizing their surface energy and tendency to aggregate [55]. Besides preventing aggregation, capping can also be used for other purposes. For instance, capping can control particle size by limiting growth of particles after nucleation [37]. Metal oxide quantum dots, such as ZnO, contain varying numbers of hydroxide groups leftover from their synthesis [56]. These polar moieties can link to a range of different ligand functional groups. Ligands containing

thiol, amine, or hydroxyl groups are excellent for capping these types of nanomaterials [57]. A wide variety of different capping agents have been liganded to ZnO, including: dodecylamine [8], oleic acid [49], 3-(trimethoxysilyl)propyl methacrylate [58], (3-(2,3-epoxypropoxy)propyl)trimethoxysilane [23], aminopropyltriethoxysilane [11], polyvinyl alcohol [59], and poly(N-vinylpyrrolidone) [51].

The use of capping agents for ZnO quantum dots is highly desirable both to keep prevent agglomeration with time, but also as a means to protect the dots [60]. The surface of the nanoparticles is predicted to be at the location of the luminescent centers, however it has been shown that water (in solution or atmospheric) can deactivate these centers and lead to loss of emission [61]. It is important to note that the capping agents themselves can affect the emission properties of ZnO quantum dots. For example, capping ZnO with dodecylamine can quench visible emission with no effect on UV emission [8]; while capping with oleic acid shifts the green emission into the blue region of the spectrum [49]. The presence of the capping agent can passivate the surface of the QD, smoothing over the surface defects which are the source of the visible emission [62]. Organic alkylsiloxanes can hydrolyze and link directly with the hydroxyls on ZnO's surface under mild conditions [11]. Many siloxanes are also bi-reactive, with more than one reactive functional group allowing them to form shells around QD centers (see Figure 3) [63], which in turn protects and stabilizes the quantum dots. Siloxanes have also been shown to greatly enhance the quantum yield of ZnO quantum dots [23]. Silica shells can also be used to make ZnO quantum dots water soluble, enabling their use in biological systems for imaging purposes [61]. Capping agents can also be chosen to increase a QD's miscibility within a polymer matrix [56]. This is important as metal oxide quantum dots tend to be polar in nature while most thermoplastic polymers are more hydrophobic. Capping such a quantum dot with a non-polar ligand would greatly improve their miscibility during mixing.



Figure 3: Zinc oxide quantum dot showing surface hydroxyls and structure of siloxane capping shell.

1.2.6 Nanocomposites

Three common approaches for making nanocomposites include: melt processing, solvent casting, and in situ polymerization [64]. Melt processing is the most applicable to industrial scale and is widely used to compound clays into polyolefins. This approach is most scalable to industrial levels, but it is challenging to break up nanoparticle aggregates in this manner. Longer extrusion mixing times help, but too long a mixing time can start to degrade the polymer chains [65]. Using polymers with higher melt viscosities also helps. Mechanical shear stresses introduced during melt mixing or ultra-sonication in solution can help break apart nanoparticle aggregation, overcoming the high binding energy of particles and the van der Waals forces that keep them together [66]. Solvent casting involves dissolving the nanoparticles and polymer in solution and producing nanocomposites by evaporation, spin-coating, laminating, dipping, or spraying [67]. Ultrasonication and high shear mixing in viscous solvents have been employed to disperse nanoparticle aggregates. In situ polymerization eliminates those issues and involves attaching reactive ligands onto the nanoparticles and incorporating them into the polymer during polymerization [5]. This method is less suited for large scale.

Regardless of how they are introduced, small quantities of nanoparticles can have large impacts on the material properties on polymer composites, such as shear modulus, toughness, strength, optical properties, and fluid permeability [68]. These effects are due to interactions between nanoparticles and polymer restricting the motion of polymer chains – such as slippage, reorientation and motion [69]. This can result in a loss of elasticity of the polymer material as a tradeoff. However, minimizing potential nanoparticle aggregation and finding a cost-effective method of dispersion of nanoparticles within a polymer is often an issue with scaled up production and commercialization of nanocomposites [5]. Preventing aggregation becomes inherently more difficult when the nanoparticles have a diameter of less than 50 nm and/or the concentration of the particles increases to above 5 % by weight [70]. The properties of nanoparticles arise from their high surface area to volume ratio, which increases their propensity to aggregate. Van der Waal forces can bind them together into large fractal structures that behave like larger particles, minimizing any positive effect that they might impart [71]. Nanoparticle aggregations decrease the material properties of composite materials, acting as local stress concentrators proportional to their size and they interact with each other via polymer-mediated bridging [72]. The properties of a nanocomposite are affected by the interaction between polymer chains and the dispersion of the nanomaterial with the goal being to increase the enthalpy of mixing so that it overcomes the forces driving nanoparticle agglomeration [70]. The use of coupling agents can facilitate more favorable interactions between particle and polymer. Modifying the surface of the particles is a method to increase the enthalpy of mixing [73]. This can be accomplished with the use of surfactants, capping agents or other modifiers. Capping agents increase the effective size of a particle, decreasing their surface energy and helping to prevent agglomeration [37].

A decrease in crystallinity is also observed with nanocomposite blending [74]. A polymer amorphous region interacts more favorably with nanoparticles compared with the crystalline sections [75]. This subsequent decrease in crystallinity would increase the optical properties, mainly the transparency of a polymer-nanoparticle composite. Transparency is a primary concern for composite materials that will be used for solar applications [76]. Energy from incident light that passes through a nanocomposite film can have two fates: it can be lost by reflection and absorption by the material, or it can be

transmitted through the material [77]. Optical transmittance within a nanocomposite is highly dependent on the nanoparticle dot size and dispersion [78]. Nanoparticles need to be less than 40 nm in size to obtain transparent film and prevent light scattering [64]. Larger particles increase scattering (haze) and can absorb more incident light [77]. Even particles that are smaller in size can agglomerate into aggregates which can interact with the wavelengths of light and decrease the optical transmission of transparent polymers due to light scattering [79]. Particles and agglomerations larger in size can simply absorb light as well. Decreasing the size and aggregation of nanomaterial additives is the main method to optimize light transmittance through a composite. Optical transmittance is maximized when the refractive indices of the polymer and the nanoparticle components are highly similar [64]. This can be accomplished by using nanomaterial with refractive indices close to the polymer matrix, or to the particles with a ligand shell possessing a refractive index close to that of transparent polymers [80].

1.2.7 Greenhouse film overview

The most important factor affecting the growth, development and yield of plants within a greenhouse is visible light transmission [81], specifically photosynthetically active radiation (PAR) which are primarily in the blue and red regions of the visible light spectrum. Sunlight is comprised of three principle types of radiation: ultraviolet (UV) which ranges from 200 to 400 nm wavelength; visible light which ranges from 400 to 700 nm wavelength; and infrared (IR) which ranges from 700 to 3000 nm in wavelength [82]. A good greenhouse cover would have excellent transmission in the visible range, but limited transmission for UV and IR wavelengths. Greenhouses covers, often called cladding, are traditionally constructed with glass, which is a transparent and permanent covering [83]. The downsides of glass are that it is expensive to install and repair, as well as very heavy. Flexible plastics are an attractive alternate due to their low cost, ease of installation and good optical properties. Today, over 80 % of greenhouses worldwide are clad in LDPE, EVA or EBA present as mono or multilayer films between 80 and 220 μm thick [84]. LDPE is the most used polymer in agriculture due to its low cost, transparency and relatively light weight [85]. EVA is another thermoplastic that is used extensively for greenhouse claddings and other solar applications. It accounts for over 80 % of the

polymer used for encapsulating photovoltaic cells [86]. EVA contains moieties of vinyl acetate with stretches of ethylene making it a more polar polymer. This gives it a more amphiphilic nature which makes introducing organic additives more efficient [87] and increases its adhesion to glass. The vinyl acetate side chains help prevent packing with the ethylene sections, decreasing the crystallinity of the polymer matrix, which leads to greater transparency [88]. The presence of the more polar vinyl acetate side chains do carry a significant disadvantage though, it gives EVA poor damp heat and UV stability leading to faster degradation rates [86].

Agricultural films have a lifetime of 6 to 45 months [84] depending on their exposure to UV radiation, mechanical stress, climate factors (humidity, wind, heat, cold, precipitation) and chemical agents [89], with the main driver of film aging and degradation being exposure to UV radiation [4]. LDPE is susceptible to UV breakdown via a chain scission mechanism leading to terminal carbonyl groups increasing its polarity and also being autocatalytic, hastening the degradation [89]. EVA undergoes a two-step degradation: the first being a deacetylation process via a Norrish-type reaction (see Figure 4), and the second being complete chain scission of the main polymer chain [90]. The degradation of EVA occurs primarily in the amorphous regions and its rate is correlated with increasing vinyl acetate content [91]. UV photodegradation leads to polymer brittleness, fading and yellowing, and the production of chromophore products which lead to decreased light transmission [92]. Commercial greenhouse plastics are manufactured containing an assortment of antioxidant compounds to slow this process and lengthen the lifetime of their products [90].

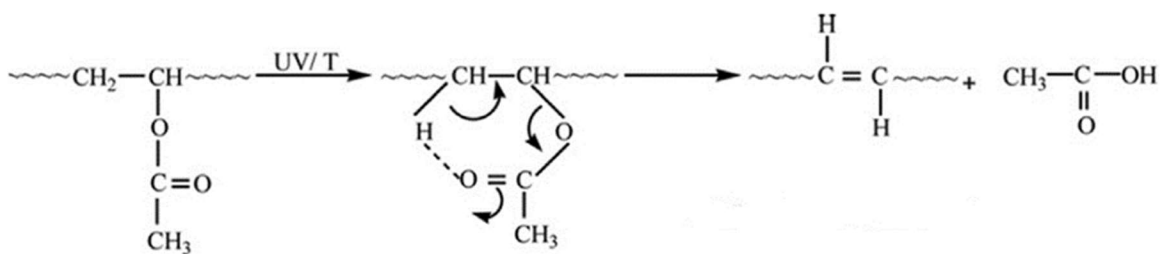


Figure 4: UV driven Norrish reaction inducing deacetylation of EVA chain.

Modified from [93]

1.2.8 Properties of greenhouse films that can be improved with nanotechnology

QD-containing nanocomposites have the potential to enhance greenhouse films in several different manners. Five different film parameters have been identified that could be improved with the inclusion of nanoparticles into greenhouse claddings. These are:

1. Mechanical properties
2. Polymer stability
3. Polymer wettability
4. Thermal properties
5. Light downshifting (LDS)

The following sections will discuss each of these, why they are important, and the manner nanomaterials can improve them. However, the inclusion of nanomaterial should always keep visible light transmission as the most important parameter. This affects the quantity of nanoparticles that can be loaded into a composite [10]. A general rule is that small loadings of nanomaterials increase material properties, but as loadings increase, the nanoparticles tend to aggregate. This leads to a decrease in material properties and a subsequent decrease in visible light transmission [94]. As well, the nanoparticles incorporated into a polymer film need to have a diameter of less than 40 nm and a similar refractive index to the polymer matrix to obtain truly transparent films and prevent light scattering [64].

1.2.8.1 Mechanical properties

The addition of nanoparticles in polymers impacts their mechanical properties – specifically their tensile strength, which is related to tear resistance [95]. Increased tear resistance means less physical damage to greenhouse claddings, extending their functional lifetimes [96]. Nanoparticles accomplish this when they can form favorable interactions with the polymer chains and behave as crosslinking agents [59]. The stronger the interaction with the polymer chain, the greater the increase in strength [87]. Hydrophobic particles interact with hydrophobic polymers (or polymer segments) and hydrophilic particles interact best with more polar polymers (and polymer regions).

Abdel-Galil and Balboul (2015) determined that mixing ZnO into PVA acted as a crosslinking agent; they proposed that the surface hydroxyls on ZnO interacted with the polar polymer chains [97]. This led to an increase in tensile strength in the composite. QDs can also be treated with surfactants or capping agents to aid in dispersion within the polymer matrix [98]. Scaffaro et al (2009) found that treating clay nanoparticles (Cloisite) with an organic modifier, an alkylammonium salt, greatly increased their dispersion when melt-mixed within LDPE and EVA [87]. They found that the tensile strength and tear test results were both increased, with an associated decrease in elasticity, but only if the nanoparticles were well dispersed. Zhou et al (2010) capped cadmium telluride quantum dots with silica and determined that this increased the strength of the material, but only if the nanomaterial was well dispersed [99]. This was found to increase the tensile strength by 46 %, again coupled with a decrease in elasticity. They loaded only 0.2 % by weight nanoparticle and did not observe any agglomeration. Avoiding agglomeration of nanoparticles is critical for a nanocomposite's mechanical properties. Agglomerations of nanoparticles can act as stress concentrators, acting as origin points for cracks and tears [100]. In many of the studies on nanocomposites, it is noted that they have a positive effect on a composite's properties which increases with increasing concentration. But above a certain threshold – dependent on the concentration, mixing conditions, and interactions – nanoparticles begin to agglomerate [71]. This value has varied depending on the study: Esthappan et al (2015) found that nano-ZnO within polypropylene has a net positive effect until a loading of 1.5 percent, then agglomerations appeared and the mechanical properties decreased [94]; Hoang et al (2014) increased the mechanical strength of EVA with the addition of silica, up to 0.5 % weight fraction, but above that the silica had a negative effect [101]; and Rodriguez-Tobias et al (2013) reported that the addition of ZnO nanoparticles to ABS increase its strength to a concentration of 0.5 %, above that it agglomerated and decreases the mechanical properties [100]. The general trend is that the addition of nanomaterial has a positive influence on the material properties of a composite until a critical concentration or lack of dispersion achieved, which then leads to agglomeration and a decrease in material properties.

1.2.8.2 Polymer stability

Exposure to UV, chemicals, moisture, and harsh climate, which is expected to worsen with climate change, can accelerate the degradation of greenhouse polymer films [2]. Under the harshest of climate conditions – including temperatures over 40°C and blowing sand – such as those that can be experienced in hot equatorial greenhouse can adversely affect optical and mechanical properties of agricultural plastics in less than 8 hours [85]. This necessitates the requirement for stabilizing agents for films to be economically practical. Commonly used stabilizing compounds include UV absorbing pigments, hindered amine light stabilizers, and nickel quenchers which primarily target UV radiation as that is the main driver of polymer degradation [102]. The use of these compounds has concerns regarding uniform distribution within the polymer, long-term stability and cost. They are also consumed over time as most are sacrificial in design and a correlation has been reported between the rise in their degradation products and a decrease in mechanical/optical properties [103]. These compounds also migrate through polymer matrices at a rate dependent on their size and diffusion coefficient and can be washed away by environmental moisture [100]. Many of these weaknesses are not present with nanoparticles. Nanomaterials – such as ZnO quantum dots – can be inexpensive [12], extremely photostable [99], and immobile in polymers due to their size [100]. The nanoparticle crosslinking of polymer chains that help increase their mechanical properties also helps increase their thermal stability. The temperature that thermal degradation commences, and each subsequent step increases with the presence of nanomaterial, and it has been shown that the smaller the particle, the greater the effect barring agglomeration [104]. Their inclusion in the composite greater stabilizes the polymer matrix but can destabilize it if the interactions between the particles and polymer is not ideal or agglomeration occurs [105]. Thermal degradation activation energy increases with nanoparticle addition to polymer composites [97]. Nano-TiO₂ performs as a UV absorber better than most organic additives [96], but it does have an opacifying effect. Composites containing nano-ZnO possess effective UV resistance as well, coupled with excellent optical properties. ZnO nanoparticles have been shown to increase the UV resistance in different polymers including EVA [96], polypropylene [106, 107], polyacrylate [105], and PMMA [108]. ZnO has other advantages over other UV

stabilizers such as not migrating in plastics, exhibits broad absorption, chemical and photostability [37].

1.2.8.3 Polymer wettability

One important environmental factor to consider in greenhouse operation is moisture. It is rare that the internal microclimate of a greenhouse exactly matches the temperature and humidity outside. When a solid surface's temperature, such as a greenhouse film, is cooler than the dew point, moisture will condense to form droplets [109]. Condensate on the surface of greenhouse claddings affects light transmission. Fogging is caused when small discrete drops accumulate on the inner surface of a greenhouse cladding. These droplets can cause internal light reflection decreasing a film's transmission [110]. Small drops can form into larger drops which can act as magnifier lenses, focusing light and burning the plants within the greenhouse. The drops can coalesce into larger drops that can drip down onto the plants providing humidity and moisture that is conducive to fungal disease development or crop spoilage [81]. Water can be cleared from greenhouse claddings using active measures such as heaters or blowers, but passive measures are optimal from an energy saving and cost perspective [111]. Passive measures involve changing how water droplets interact with the polymer film. The interaction of a water droplet with a film is characterized by its contact angle, which is defined as the angle formed by a liquid at the three-phase boundary where a liquid, gas and solid interact. Figure 5 depicts the three different types of contact angle situations: hydrophilic, neutral and hydrophobic. Hydrophilic surfaces are often preferred as they spread water droplets into thin films which allows light to pass; while hydrophobic surfaces can also minimize fogging if they are tilted to a minimum sliding angle to allow the droplets to be cleared.

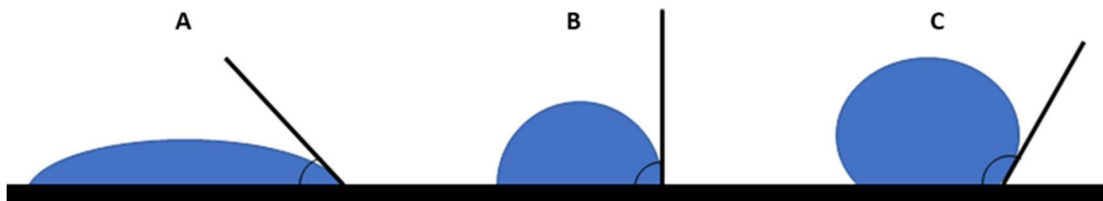


Figure 5: Three different contact angle situations: A) hydrophilic where the water spreads into thin film and has contact angle $< 90^\circ$; B) neutral with contact angle of 90° ; and C) hydrophobic with contact angle $> 90^\circ$ where the water beads.

The wettability of a film surface is controlled by two main factors – surface topology and chemical composition [81]. Engineering the surface of a polymer to present a rougher, nanofibrous appearance drastically alters the wettability of a polymer as water cannot interact properly and forms a film as opposed to droplets [111]. This approach would be difficult to apply to the quantity of polymer films that are present on greenhouses, so altering the chemical composition is more applicable to that scale. This is accomplished by either utilizing a more hydrophilic polymer or the addition of antifogging agents into the polymer matrix. Typical antifogging agents are tensioactive materials, usually nonionic surfactants, which increase the interfacial tension between the solid and vapor, leading to the formation of optically transparent thin water films as opposed to droplets [109]. Antifogging agents are often amphiphilic compounds containing hydroxyl, carboxyl, ester, amino, amide, silane, sulfonic, and dihydrogen phosphate functional groups [111]. One issue with chemical antifogging agents is that they have the ability to migrate within a polymer matrix to the surface where they are slowly washed away and their concentration, and hence effectiveness, decreases with time [109]. This migration rate is affected by the size of the compound, the polymer's crystallinity, the temperature and the water exposure [112]. The best antifogging agents would have poor solubility in water and poor migration through the polymer. Nanoparticles such as TiO_2 , ZnO , SiO_2 and ZrO_2 [96, 109, 113] have been shown to meet these requirements. These are often covered in hydroxyl functional groups that are residual from their synthesis and make the nanoparticles hydrophilic, while their increased bulk decreases their mobility within the polymer [111].

1.2.8.4 Thermal Properties

Another important consideration in the construction and operation of greenhouses is temperature. IR wavelengths, which transfer heat from sunlight, account for 50 % of incident sunlight and can greatly influence the productivity of a greenhouse [4]. While IR is minimally absorbed by plants, it is readily absorbed by installation and construction elements of a typical greenhouse [82]. This issue is especially prevalent in summer months and hotter climates. Too high of a temperature within a greenhouse can lead to damage of a plant cell's membrane lipids, negatively affecting carbon and nitrogen metabolism, and limiting root growth [3]. The cellular machinery involved with photosynthesis is also compromised at increased temperatures [114]. Limiting the rate of photosynthesis directly limits the rate of growth for plants. Mechanical ventilation during the summer can alleviate this, but that has a limited cooling effect and is very energy intensive [82]. Introducing IR blocking additives to control the heat within a greenhouse has been noted to increase the rate of photosynthesis and crop yields within [3]. The opposite issue occurs during cooler months as it would be important to limit the passage of heat through greenhouse films to save on heating costs. IR transmission can be limited by incorporating a reflective outer layer of greenhouse claddings, or introduction of NIR absorbing pigments [115]. While these are extremely effective, blocking over 90 percent of IR transmission, they also have the deleterious effect of lowering PAR transmission. Mineral fillers, such as keolin [116] and modified clays [87] have also been tested and show similar behaviors. SiO₂ has been shown to be an excellent IR blocker, and nanosized particles have limited effects on visible light transmission [96] due to their small size and possessing a refractive index similar to commonly used greenhouse polymers. Silicon is also compatible with many types of polymers and has been demonstrated to be an effective capping agent for QDs in producing thermal blocking composites [117].

1.2.8.5 Light Downshifting (LDS)

The most critical factor in the operation and productivity of greenhouses is the quantity of light within [81]. Sunlight drives photosynthesis, which is the most important biological reaction on the planet. This process uses energy from sunlight to fix atmospheric carbon

dioxide into larger carbon-containing molecules that are the building blocks for living organisms [118]. Figure 6 provides a simple overview of the process. Green plants, algae and cyanobacteria are the primary producers on the vast majority of the planet's ecosystems and generate all the molecular oxygen that is in the atmosphere.

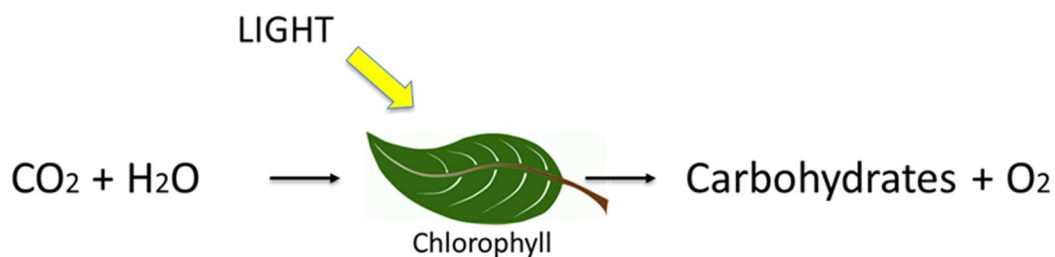


Figure 6: Simple overview of photosynthesis. Sunlight is absorbed by chlorophyll pigments in leaves and used to drive the conversion of carbon dioxide and water to sugars and oxygen.

Photosynthesis is a series of redox reactions that commence when chlorophyll absorbs a photon of light and transfers it through their photosystems to the terminal acceptor, yielding cellular energy equivalents and carbohydrates as products [119]. Not all wavelengths of light are utilized equally, plants use light within the visible region (termed photosynthetically available radiation or PAR) with red and blue photons providing the greatest benefit (see Figure 7).

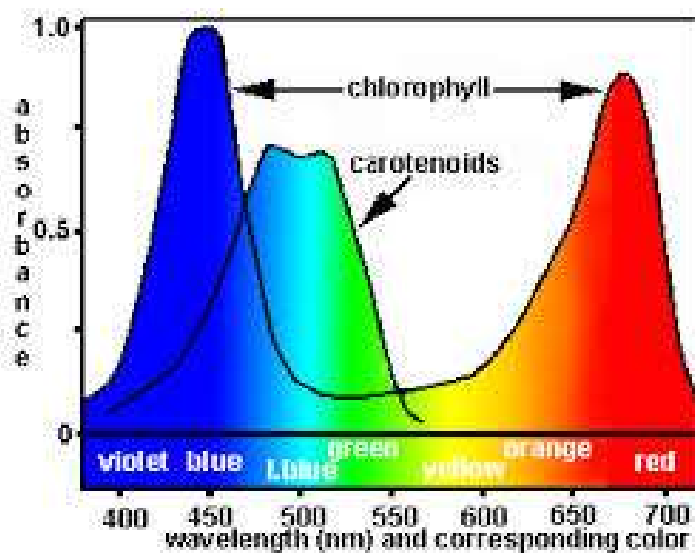


Figure 7: The two chlorophyll pigments primarily absorb light from blue and red wavelengths in the visible light spectrum. Plants have also evolved additional pigments, such as carotenoids, that can capture more photons and transfer that energy to photosynthesis.

The two chlorophyll pigments absorb red and blue primarily, however, plants have evolved a system of other proteins and pigments that help absorb photons and transfer them to the reaction centers. These are the light harvesting complexes (LHCs). These complexes are crucial to get adequate numbers of photons into the photosynthetic reaction centers [120]. LHCs are the most abundant membrane proteins on the planet [121] and they coordinate carotenoids to themselves to aid in collecting light. These systems absorb blue wavelengths most effectively [120].

One way to increase the light available within a greenhouse is through the use of supplemental lighting. LED lighting, specifically in the blue and red regimes, have been shown to increase the dry weight of crop species after specific growing times [122]. The downside to this approach is that LEDs require an additional input of energy and avoiding increased costs is paramount for efficient greenhouse operation. A better way to increase the amount of PAR within a greenhouse is shifting wavelengths that plants do not naturally utilize into ones that they do. Sunlight contains a great deal of energy that is

not specifically utilized for photosynthesis and can be harmful. UV radiation is a form of light that is not utilized to a great degree and can be detrimental to plants. UV radiation, especially with wavelengths below 315 nm, affects plants by directly degrading its DNA as well as damaging its photosystems leading to photoinhibition and photodamage [123]. Blocking most of the UV light that enters a greenhouse would be beneficial to limit this damage. Complete or partial blockage of UV affects the lifecycle of fungal species and interferes with the vision of pest insects [124]. Complete blockage of UV by an agricultural film is not fully desirable either, as UV radiation with wavelengths between 315 to 400 nm is important for secondary metabolite production, which is important for qualities such as taste and color in crops [87]. Some UV light is also required for pollination by bees [115]. Shifting most of the UV radiation to visible light would be a method to increase the productivity and health of a greenhouse.

This can be accomplished using organic dyes that absorb UV light and downshift it into visible light. El-Bashir et al synthesized perylene-doped PMMA films via solvolysis. There were found to increase the quantity of photosynthetic wavelengths during solar exposure [108] and found that soybean growth was enhanced when grown under these films [119]. Their results were extremely promising but may not be ideal for long term usage in agricultural installments. Organic dyes tend to have narrow absorption ranges, broad emissions and are susceptible to degradation from continuous irradiation from excitation sources [125] and like other chemical agents, can migrate through the polymer matrix and be washed away by moisture [109]. QDs are much more stable over time, with the ability to last years under continuous irradiation [59] and remain stable within polymers indefinitely [34]. ZnO quantum dots have been demonstrated numerous times in the literature to be able to absorb UV radiation and downshift it into visible light, with the ability to choose the emission color [37].

As mentioned in section 1.1, QDs can absorb a photon of light and reemit it at a longer, lower energy wavelength. This phenomenon has not been demonstrated to any significant extent in greenhouse films, but it has been tested in the field of photovoltaics (PV). Standard silicon solar panels suffer from low quantum efficiencies in the UV/far blue region due to high front surface recombination rates photo-generated holes. UV photons

also have a shallow absorption depth in silicon due to its refractive index being higher in the UV/blue range [126]. For these reasons, downshifting UV into longer wavelengths has been demonstrated to increase PV efficiency. Rothmund et al (201) showed that incorporating cadmium sulfide QDs into the EVA encapsulant for PV panels lead to an improved relative efficiency of 3.4 % [127]. Other materials have been tested such as Eu^{3+} -containing which absorb strongly in the UV range and emit primarily at 612 nm, which is near the maximum conversion efficiency for crystalline silicon-based solar cells [128]. Tb^{3+} -complexes emit centered around 500 nm and are more appropriate for amorphous silicon-based solar cells [86]. It has been found that the optimal loading on these types of compounds into the solar cell encapsulant is 1 % by weight. Less than that and there is too little light downshifting to be noted; above that and the particles aggregate lowering the polymers transparency. It is expected that similar behavior would be observed in quantum dots used in transparent LDS greenhouse films.

1.3 Objective

Zinc oxide quantum dots can be designed to absorb solar wavelengths that are of less use for greenhouse crops and reemit them into usable wavelengths. Sunlight at ground level is composed of ultraviolet (UV), visible and infrared (IR) wavelengths. These comprise 5%, 40% and 50% of sunlight respectively [82]. It is the objective of this doctoral project to design a nanocomposite greenhouse film that can absorb UV radiation and downshift it into visible light to increase the productivity of a greenhouse. As a plant's growth is directly tied to its rate of photosynthesis, increasing the amount of photosynthetically active radiation (PAR) within a greenhouse will result in higher growth yields. This will be accomplished through a series of logical steps to produce a potential greenhouse nanocomposite:

- i. Identifying what factors contribute to the growth of ZnO QDs to optimize synthesis conditions in order to produce high quality nanoparticles with high quantum yields. This will be accomplished both in batch and continuous manners. Ligands will be identified and tested as capping agents to determine their effects on the photoluminescence.

- ii. Optimizing large scale batch synthesis. This includes confirming that the properties of ZnO QDs are identical when produced at bench and commercial scale. This is a required step to ensure that high quantities of the product can be produced with acceptable characteristics. As well, scaled up purification methods will also be tested.
- iii. Optimizing the capping agent for their inclusion into a transparent polymer matrix. These are designed for use in large-scale constructions (greenhouses) so the material properties, especially strength will be examined. The capping agent family that shows the most improvement in the QY was determined to be alkylsiloxanes. These can have a diverse assortment of functional groups attached, so different siloxanes will be tested as capping agents to determine their effects on the mechanical strength of their nanocomposites. Whichever capping agent shows the most improvement will be further tested on its effects on the material's stability.
- iv. Further physical property testing. Other parameters besides strength and optical affect greenhouse performance. These include wettability and thermicity. These will be examined for the capped quantum dots.
- v. The optical properties will be examined. That includes the transparency of the composites to UV and visible light and their light downshifting behavior. Lastly, a proof-of-concept experiment will be performed. This will determine if the presence of these films and their downshifted light affects the growth of a green photosynthetic organism. A green alga will be used for this test as a model due to its fast growth rate, ability to scale the number of replicates in the experiment and the ability to sample growth rates daily.

Chapter 2

Determining the significant parameters for the growth of zinc oxide quantum dots in batch and continuous reactor systems and optimizing the quantum yield of quantum dots grown in a continuous reactor

Abstract

Zinc oxide quantum dots are a versatile nanomaterial that can be synthesized in batch or continuous processes. The reaction parameters for its growth have been studied extensively in the past for batch reactions, but less so for continuous systems. As well, the effect of different reaction parameters and capping agents on the quantum yield has not been reported. This was investigated in this work using a design of experiment approach to identify which parameters were statistically significant for the two reaction types. The most important factors for growth rate were identified as temperature and total reagent concentration. The effects of changing the parameters for the continuous reactor, and introducing different capping agents, on the ZnO's quantum yield was also tested. The most important parameter for quantum yield was the ratio between the two precursors. The capping agents that gave the highest quantum yields were silanes and polymer capping agents. These results help identify the factors that would be important to design and build a continuous reactor for the large-scale production of highly luminescent ZnO quantum dots.

2.1 Introduction

Zinc oxide (ZnO) is a wide band gap (3.37 eV) semiconductor with a large excitonic energy of (60 meV). These properties allow it to absorb in the UV range, be transparent to visible light, and undergo excitonic processes at ambient conditions [8]. ZnO can be considered a green substance because it is biocompatible, biodegradable, and biosafe with a low toxicity [11]. It absorbs radiation in the UV range, downshifts and natively emits the energy in a lower-energy UV wavelength. However, when the diameter of the particles becomes smaller than its Bohr radius, its energy levels become quantified, making ZnO quantum dots (QDs). These emit visible light when excited with UV irradiation. The UV emission has been ascribed to band-edge recombinations, while the visible emission can be attributed to the recombination of photo-generated holes with singlet electrons found in surface defects, such as oxygen vacancies [129]. The size of the QDs controls their emission properties, with increased size leading to redshifted and decreased emission [23]. ZnO nanoparticles can be used in a wide variety of applications including the rubber industry, UV blocking, textiles, antifouling, photoelectronics, and more [42].

Controlled precipitation in a sol-gel is the most common method for ZnO synthesis. Sol-gel reactions are inexpensive, use relatively mild conditions, and allow for the introduction of organic ligands if desired. This involves using a zinc salt (source of Zn^{2+} ions) and reducing it with a reducing agent (usually hydroxide base) followed by precipitation of the ZnO from solution [37]. The growth of ZnO follows three main steps, which are common to many forms of crystal growth: nucleation, growth, and ripening [130](Forseca et al 2017). The growth of ZnO can be approximated using the Lifshitz-Slyozov-Wagner (LSW) model, where the growth rate is proportional to the cube of the radius, as shown in the following equation:

$$r^3 - r_0^3 = kt$$

Equation 1: LSW model

Where r is the radius of the quantum dot, r_0 is the initial particle size, k is the growth rate, and t is time. In this chapter, different parameters will be studied using a Plackett-Burman design of experiment (DOE). These include reaction temperature, total concentration of precursors (which is an indicator of Zn^{2+} concentration) and the ratio between $Zn^{2+}:OH^-$ present in the reaction. In the batch synthesis, the LSW model will be used to estimate the growth rate. Although the LSW model has been shown to be not entirely accurate in regards to the kinetics of ZnO quantum dot formation [22, 131], it is accurate enough in order to determine the variation in the listed parameters will have on the growth. The effects of those parameters have been described previously. An increase in the reaction temperature leads to an increase in particle growth rate [132]. A higher ratio on OH^- to Zn^{2+} in the reaction leads to smaller, more blueshifted dots [23]. An increase in total concentration of the precursor species leads to increased growth as ZnO growth as its reaction can be considered 3rd order with respect to Zn^{2+} concentration and 0th order with respect to the OH^- ions, as long as they are in excess [133]. However, the combined effects of these parameters and their statistical significances has not been reported, to the best of the authors' knowledge.

Making QDs via the batch process, such as sol-gels, offers a small controllable environment to study their growth and properties, but can be less practical for commercial scale production. Large scale synthesis is still a challenge in the field of nanotechnology and limits its use for high volume commercial products [134]. Batch processes can involve precise control of the sol-gel or rapid injection of precursors into hot flasks, with coordinating ligands, solvents and inert atmospheres [37]. These types of reactions can be limited by slow heat/mass transfers and non-uniform reactor conditions, especially during injection [135]. Batch processes are excellent for studying fundamental properties of nanoparticles, but suffer from difficulties in controlling size, large spread of sizes within a single reaction, and poor reproducibility [48]. These hurdles increase in proportion to the size of the reaction, limiting their ability for reliability and scalability [136]. One solution to this issue is the use of continuous reactor systems, typically microfluidic reactors. Microfluidic devices involve introducing the reactants into a heated, contained tubing and allowing them to react and form their product during their passage. Microfluidics are excellent at making monodisperse, controllable nanoparticles

due to their control over reagent composition, mixing kinetics and temperature, which allows them to have finely tunable properties [137]. They are usually small diameter tubing systems, containing microliters of solvent. Their small size allows for more efficient mass and heat transfer within the reaction [138]. They exist in steady state once the reaction is running [135] and often are based on homogeneous single laminar flow designs [139].

Microfluidic and continuous systems have already been shown to be able to synthesize ZnO [136, 140-142], however quantity of the product is often low due to the narrow tube sizes and small volumes used. In this chapter, we will present a tubular plug flow reactor (PFR) which can synthesize ZnO as a continuous process. A PFR reactor is more optimal for mass production compared to other types of continuous reactor systems – such as continuous stirred tank reactor – because it has a much greater efficiency at the same volume. Given the same residence time, the reaction will proceed to a higher degree of completion. The parameters that influence the particle growth on ZnO during batch and continuous processes will be examined using a design of experiment (DOE) approach to determine which are the most significant for size control during those two types reactions; and whether the same parameters govern batch and continuous processes. Lastly, as many applications for ZnO require their photoluminescent properties, what factors influence their quantum yield (QY) will also be examined. The visible photoluminescence of ZnO can be increased with the formation of new nucleation centers or decreased with increased surface passivation and increased particle size [133]. Quantum dots will be synthesized in the PFR with a variety of different capping agents (ligands) to determine the effect of different ligands on the QY. Capping ligands act as stabilizers, providing colloidal stability to nanoparticles and minimizing uncontrolled growth and agglomeration [54]. They also have been known to stabilize the surface traps of ZnO, enhancing its QY [55]. A variety of different ligands will be tested and their effects on the photoluminescent properties of ZnO will be noted. As we are only interested in the growth as determined by their photonic properties (UV absorption and visible light emission), no purification will be performed at this step. The other constituents of the solutions (solvent, precursors, base and byproducts) do not absorb in the UV range so they will not interfere.

2.2 Experimental

2.2.1 Materials

The synthesis of ZnO QDs is based on the method described by [143]. Modifications to the method include a solvent change from isopropyl alcohol to ethanol (EtOH) and differences in the concentrations and quantities used. Zinc acetate dihydrate ($\text{Zn}(\text{OAc})_2 \cdot 2\text{H}_2\text{O}$) and sodium hydroxide (NaOH) were obtained from Sigma-Aldrich, Canada and used without any purification. Anhydrous ethanol (EtOH) for the reaction was supplied by Commercial Alcohols. Reagent-grade methanol (MeOH) for rinsing was supplied by Caledon Labs. The following chemicals were supplied by Sigma-Aldrich for capping quantum dots and used without any purification: glycerol, oleic acid, tetraethyl orthosilicate (TEOS), vinyltrimethoxysiloxane (VTS), oleylamine, polyvinylpyrrolidone (PVP), citric acid, polyethylene glycol (PEG), ethylene glycol (EG), and dodecanethiol.

2.2.2 Batch synthesis of ZnO growth rate design of experiment

Three parameters were tested to determine their effects on the rate of ZnO nanocrystal growth, i.e. temperature, $\text{Zn}^{2+}:\text{OH}^-$ ratio, and total concentration (in molarity) within the batch reaction. A factorial design of experiment (DOE) was created using the Minitab statistical package creating the following list of trials:

Table 1: Parameters to be inputted into DOE for ZnO batch synthesis.

Trial	Temp (°C)	Ratio (Zn²⁺:OH⁻)	Total Conc. (M)
1	45	0.599	0.0070
2	45	0.292	0.0073
3	45	0.322	0.0143
4	45	0.629	0.0136
5	65	0.599	0.0070
6	65	0.292	0.0073
7	65	0.322	0.0143
8	65	0.629	0.0136
9	55	0.464	0.010
10	55	0.464	0.010

Zn(OAc)₂•2H₂O and NaOH solutions were made separately according to Table 2 and cooled in an ice bath. For each trial, each reagent was dissolved in the specified volume of EtOH and cooled to room temperature. An equal volume of the NaOH solution is added slowly to the other solution while being stirred rapidly, place within a heated water bath, and the growth was measured. All samples were stirred at a constant rate of 350 rpm.

Table 2: Recipes for batch synthesis DOE. Each solution is separately made, and then combined to start the trial.

Trial Number	Zn(OAc) ₂ •2H ₂ O Solutions		NaOH Solutions	
	Mass (g) Zn(OAc) ₂ •2H ₂ O	Volume (ml) EtOH	Mass (g) NaOH	Volume (ml) EtOH
1	0.16	220	0.1	220
2	0.23	150	0.13	150
3	0.23	200	0.07	200
4	0.38	165	0.1	150
5	0.16	220	0.1	220
6	0.23	150	0.13	150
7	0.23	200	0.07	200
8	0.38	165	0.1	150
9	0.28	200	0.11	200
10	0.28	200	0.11	200

At specified time intervals, 1 ml aliquots of the reaction solution were taken for measurement. A Shimadzu UV-3600 spectrophotometer was used to obtain the UV-VIS spectra, which was used to analyze the nanoparticle size. The machine will be blanked with appropriate solvent prior to analysis. The size of the quantum dots was estimated using the effective mass model (Brus equation) [144]. The size can be approximated by

$$E^* \cong E_g^{bulk} + \left(\frac{1}{m_e^* m_0} + \frac{1}{m_h^* m_0} \right) - \frac{1.8e^2}{4\pi\epsilon_0 r} - \frac{0.124e^4}{h^2(4\pi\epsilon_0 r)^2} \left(\frac{1}{m_e^* m_0} + \frac{1}{m_h^* m_0} \right)^{-1}$$

Equation 2: Effective mass model

Where E_g^{bulk} is the bulk band gap, h is Planck's constant, r is the particle radius, m_e^* is the effective mass of electrons, m_h^* is the effective mass of holes, m_0 is the free electron mass, e is the charge on an electron, ϵ_0 is the permittivity of free space, and ϵ is the relative permittivity. Using values of 3.4 eV for bulk band gap, 0.24 for effective mass of electrons, 0.45 for effective mass of holes, and 3.7 for relative permittivity, this equation can be used to estimate the particle sizes from their maximum absorption wavelength

[145]. This size estimate has been shown to be similar to direct measurements of nanoparticles made with a transmission electron microscope (TEM) [130] as well as an atomic force microscope [61]. Furthermore, it would be possible to estimate the activation energy from this experiment using the Arrhenius equation as we would be able to estimate the reaction rate (k) from this experiment.

2.2.3 Plug flow reactor synthesis of ZnO growth rate design of experiment

For the analysis of the factors affecting the synthesis of ZnO under continuous reaction conditions, a PHD ULTRA™ Syringe Pump fitted with two 30 ml syringes, each containing one of the precursor solutions ($\text{Zn}(\text{OAc})_2 \cdot 2\text{H}_2\text{O}$ and NaOH, each dissolved in ethanol). The two syringes were connected to a Swagelok T-fitting which mixes the two components and pushes them into a Microbore PTFE tubing (Cole-Palmer RK-06417-31), as illustrated in Figure 8. The tubing has an ID of 0.032 inches, an OD of 0.056 inches, and a total length of 28.5 m – giving a total volume of 14.79 cm^3 .

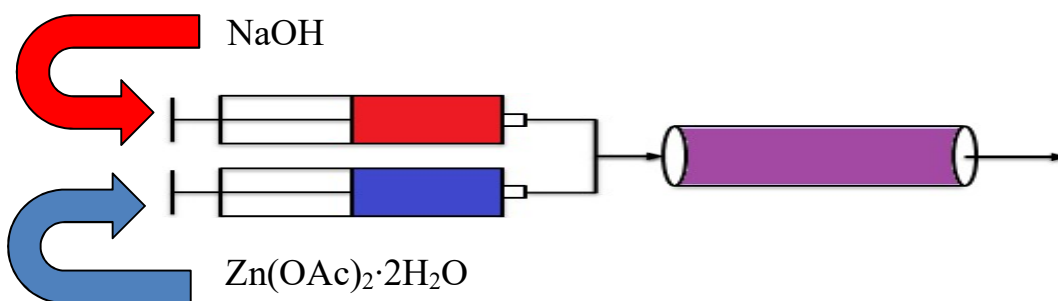


Figure 8: Schematic representation of PFR. The $\text{Zn}(\text{OAc})_2 \cdot 2\text{H}_2\text{O}$ and NaOH solutions are loaded into separate syringes and a syringe pump pushes them together to mix in a T-union and then to flow through the reactor tubing.

The system acts as a plug flow reactor (PFR) operating under laminar conditions, as the flows used will be well under the range required for turbulent mixing. Then temperature of the reactor will be kept at the desired level by immersing the tubing into the reservoir of a Thermo Fisher circulating water bath. The reactor is rinsed with methanol (MeOH) prior to remove any leftover salts or unreacted components prior to each experiment.

The reactions studied in the continuous PFR are shown in Table 3, outlining the factorial DOE that will be used to identify which parameters are most crucial to ZnO growth. Minitab statistical package was used to generate and analyze the DOE. There are four parameters that will be studied: temperature (in °C), precursor ratio of $\text{Zn}^{2+}:\text{OH}^-$, total concentration of the system (in moles per liter), and flowrate through the tubing (in ml/min).

Table 3: ZnO synthesis parameters to be inputted into DOE for growth in a PFR.

Trial	Temp (°C)	Ratio (OH:Zn²⁺)	Total Conc. (M)	Flowrate (ml/min)
1	25	1.50	0.0500	0.5
2	25	1.50	0.0500	1
3	25	1.50	0.100	1
4	25	1.50	0.100	1
5	25	3.05	0.0498	1
6	25	3.05	0.0498	0.5
7	25	3.05	0.0996	0.5
8	25	3.05	0.0996	1
9	45	1.50	0.0500	1
10	45	1.50	0.0500	0.5
11	45	1.50	0.100	0.5
12	45	1.50	0.100	0.5
13	45	3.05	0.0498	0.5
14	45	3.05	0.0498	1
15	45	3.05	0.0996	1
16	45	3.05	0.0996	0.5
17	35	2.00	0.0751	0.75
18	35	2.00	0.0751	0.75

Each of the reagent solutions was prepared separately, as indicated below in Table 4 and then loaded into the syringes. The product was collected at the end for UV-VIS analysis to estimate nanoparticle size. The following table indicates the amounts of reagents

required for each level. They were mixed separately, sonicated in a heated bath, and loaded into 30 ml syringes prior to each trial run. The samples were collected and had their size estimated by their maximum excitation using the effective mass model.

Table 4: Recipes for PFR synthesis DOE. Each solution is separately made, and then combined to start the trial.

Trial	Zn(OAc) ₂ •2H ₂ O Solutions		NaOH Solutions	
	Mass (g) Zn(OAc) ₂ •2H ₂ O	Volume (ml) EtOH	Mass (g) NaOH	Volume (ml) EtOH
1	0.44	50	0.12	50
2	0.44	50	0.12	50
3	0.44	25	0.12	25
4	0.44	25	0.12	25
5	0.27	50	0.15	50
6	0.27	50	0.15	50
7	0.27	25	0.15	25
8	0.27	25	0.15	25
9	0.4	50	0.12	50
10	0.44	50	0.12	50
11	0.44	25	0.12	25
12	0.44	25	0.12	25
13	0.27	50	0.15	50
14	0.27	50	0.15	50
15	0.27	25	0.15	25
16	0.27	25	0.15	25
17	0.55	50	0.2	50
18	0.55	50	0.2	50

2.2.4 Effect of reaction parameters on QY of ZnO synthesized in PFR

In order to determine the effects of different parameters on the quantum yield of the ZnO quantum dots produced in the PFR under the conditions listed below in Table 5. Each

precursor solution was dissolved into ethanol in a 50ml flask, then mixed in the PFR. The photoluminescent emissions were obtained using a PTI Quantamaster 50 spectrofluorometer.

The quantum yield (QY) of the samples were determined via an indirect method using an external reference compound that has a known quantum yield [146]. This involves comparing the response on the ZnO to that of a reference fluorescent dye, in this case Rhodamine B. The following equation was used to approximate the QY.

$$\Phi = \frac{I \eta^2 1 - 10^{-A_R}}{I_R \eta_R^2 1 - 10^{-A}}$$

Equation 3: Indirect QY determination

where Φ is the quantum yield, I is the integrated area under the emission peak, η is the refractive index of the solvent, A is the optical density (absorbance) at the excitation wavelength, and R denotes values to the reference compound. While the QY of the samples is not completely accurate, the estimated values are used for comparing the different synthesis parameters.

Table 5: Reaction parameters tested to determine their effect on the QY of ZnO synthesized in a PFR

Trial	Flow (ml/min)	Ratio (Zn²⁺:OH⁻)	Total Conc. (M)
A1	2	0.292	0.0073
B1	2	0.322	0.0143
C1	2	0.599	0.0070
D1	2	0.629	0.014
A2	1	0.292	0.0073
B2	1	0.322	0.0143
C2	1	0.599	0.0070
D2	1	0.629	0.014

2.2.5 Effect of capping agents on quantum yield of ZnO synthesized in PFR

The PFR synthesis conditions that yields the highest quantum yield will be used as the conditions for studying the effect of capping on the QY. That was sample C2 (Table 5 for synthesis parameters). In addition to the reagents listed in that table, an excess of the selected capping agent is mixed into the Zn²⁺-containing solution. The capping agents and the quantity added are listed below in Table 6. The samples were synthesized, collected and their emissions characterized with a spectrofluorometer. The slit widths could be so that highly luminescent samples did not saturate and obtain decent spectra from QY samples.

Table 6: Capping agents to be tested for their effect on QY of PFR synthesized ZnO quantum dots. All samples were performed with a 2:1 ratio of capping agent to zinc oxide.

Compound	Molecular Weight (g/cm³)	Quantity Added (g)
Glycerol	92.09	0.0645
Oleic acid	282.47	0.198
TEOS	208.33	0.146
VTS	162.23	0.114
Oleylamine	267.46	0.187
PVP	N.A.	0.2**
Citric acid	192.12	0.134
PEG	N.A.*	0.2**
EG	62.07	0.0434
Dodecanethiol	202.40	0.142

*as polymer compounds, they do not have specific molecular weights

**excess quantity of polymer added

2.3 Results and Discussion

2.3.1 Batch synthesis of ZnO growth rate design of experiment

Appendix A contains the graphs showing the change in the UV-VIS transmission spectra of the batch reactions with increasing time after the initial mixing of the reagents. Not all the spectra show high transmission due to the precursors' and products limited solubility in ethanol [130]. From those graphs, the maximum UV absorption can be determined by midpoint of the linear rising portion of the graph, which is where the line's slope is at a local minimum [147]. This absorption maxima can be used in the Brus equation to estimate the size of the particles at this point. Table 7 lists the maximum UV absorption wavelength, the estimated particle sizes at each time point, and their corresponding r^3 values.

Table 7: Summary of maximum absorption values from each trial and the corresponding estimated particle size.

Trial	Time (min)	Max absorb λ (nm)	size (nm)	r^3	Trial	Time (min)	Max absorb λ (nm)	size (nm)	r^3	
1	20	302	1.56	3.83	6	5	321.5	1.89	6.72	
	30	305.5	1.61	4.19		10	324	1.94	7.32	
	40	326	1.99	8.00		20	347	2.79	21.95	
	50	333.5	2.19	10.65		30	353.5	3.31	35.94	
	60	341.5	2.49	15.63		7	5	350	2.99	26.84
2	20	317	1.80	5.83	10		354	3.36	38.07	
	30	327.5	2.03	8.31	20		356	3.61	47.11	
	40	336.5	2.29	12.17	30		357.5	3.84	56.68	
	50	345.5	2.70	19.68	40		359.5	4.24	76.06	
3	10	351.5	3.12	30.31	50	361	4.64	100.1		
	20	354.5	3.42	40.03	8	5	352	3.16	31.63	
	30	355	3.48	42.18		10	354	3.36	38.07	
	40	356.5	3.68	49.97		20	356	3.61	47.11	
	50	357.5	3.84	56.68		30	358.5	4.02	65.12	
4	10	349	2.92	24.89		40	359.5	4.24	76.06	
	20	352	3.16	31.63	50	361	4.64	100.1		
	30	353	3.26	34.59	Mid 1	10	339	2.39	13.82	
	40	354.5	3.42	40.03		20	341	2.47	15.63	
	50	355.5	3.54	44.53		30	350	2.99	27.00	
	60	356	3.61	47.11		40	354.5	3.42	39.30	
	5	5	341	2.47		11.24	50	356	3.61	46.66
10		346	2.73	20.25		Mid 2	10	349.5	2.96	25.83
20		350.5	3.03	27.92			20	352	3.16	31.63
30		353	3.26	34.59	30		353.5	3.31	36.26	
40		356	3.61	46.66	40		355	3.48	42.18	
50		357.5	3.84	56.62	50		358	3.93	60.64	

The growth of ZnO in a sol-gel system can be approximated with the LSW model [131], where plotting the cube of the particle size against the reaction time gives the growth rate for that reaction using the equation:

$$r^3 = rate \times time$$

Equation 1: LSW model

Figure 2 shows the plots of those relationships. The plots of these relationships are contained in Appendix B. From those graphs, the reaction rates for each set of conditions can be determined from their slopes. These are listed below in Table 8 with each trial having the conditions outlined in the materials and methods section.

Table 8: Summary of reaction rates for each trial to be inputted into Minitab as responses for the batch synthesis DOE.

Trial	Reaction Rate	Trial	Reaction Rate
1	0.3006	6	1.2342
2	0.4541	7	1.5094
3	0.6268	8	1.467
4	0.4436	9	1.058
5	0.9573	10	0.8016

The growth rates that were estimated above were inputted into the described Minitab DOE model as the response to identify which factors are most important for the rate of growth of ZnO quantum dots in a basic precipitation reaction. The results are shown in Figure 9.

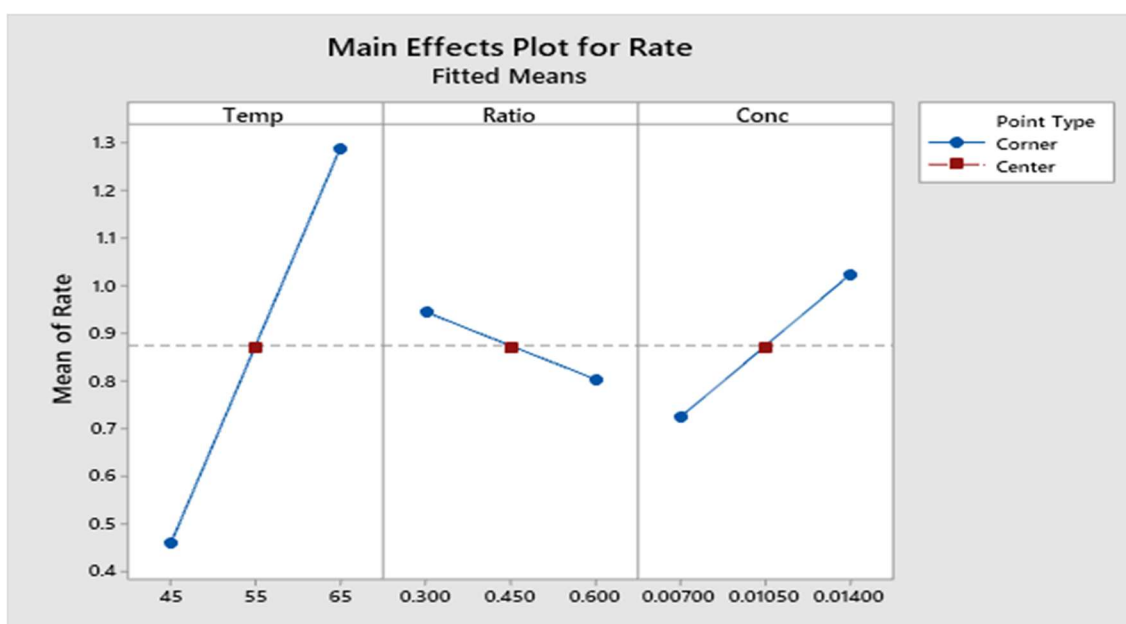
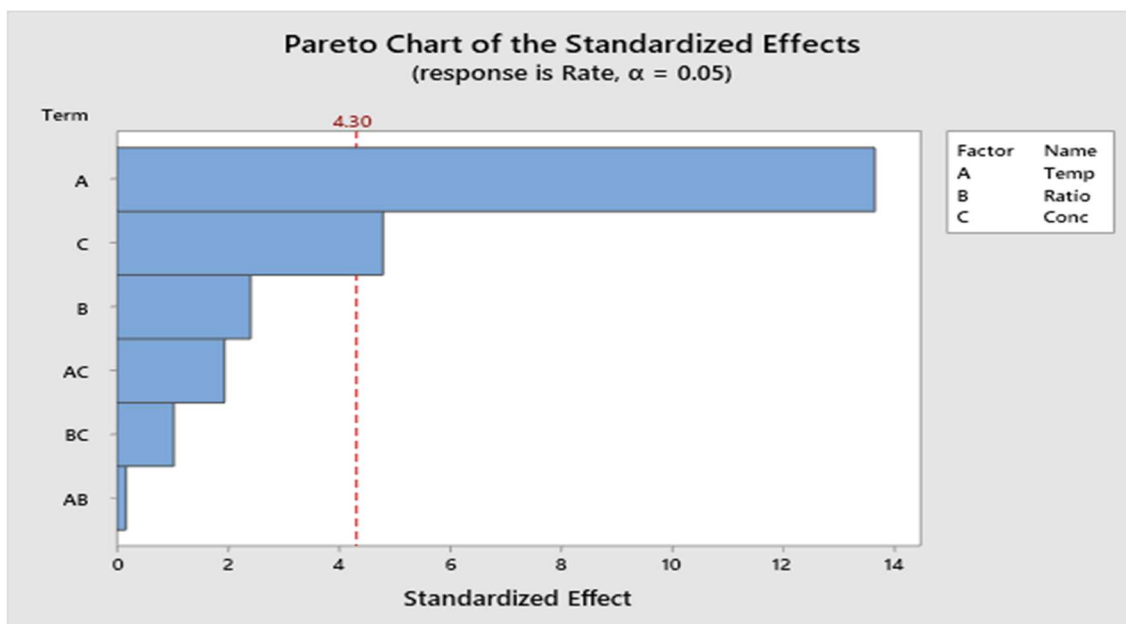


Figure 9: Pareto chart for the batch DOE (top) indicating which factors are statistically significant and the factorial response chart (bottom). The Pareto chart shows which responses are significant from the experiments ran, as they are the ones whose response is above the cutoff ($\alpha > 0.05$)

Figure 9 (top) shows the Pareto chart for the batch DOE. Under the DOE conditions run in this experiment, temperature and total concentration are the statistically significant

parameters for the control of ZnO particle growth. The importance of reaction temperature clearly makes the largest impact on the growth rate, as shown in Figure 9 (bottom). Particle growth is a diffusion limited chemical reaction [148] and higher temperatures increase the rate of those processes. The influence of temperature on the growth of ZnO particles has been identified many times in the literature [41, 129, 144, 149-151]. The second parameter that shows a significant influence on the growth rate is the total concentration of reactants within the system. It has been shown that the concentration of both reagents is not the driving force, rather the concentration of the Zn^{2+} ions [41]. The sol-gel synthesis of ZnO has been proposed to be a 3rd order reaction with respect to the presence of Zn^{2+} and 0th order with respect to the OH^- , as long as the base is in excess [52]. The identity of the cation source (LiOH, KOH, or NaOH) does not matter as much as the concentration of the hydroxide ion [152]. It is the diffusion of Zn^{2+} ions to the growing crystals that influence their rate [56]. The ratio of the zinc ions to hydroxide ions appears to have a more marginal effect on the growth, at least under the ranges examined in this DOE. A larger hydroxide to zinc ratio leads to higher degrees of nucleation within the system [133], but the presence of the base can also form a passivating layer on the nanoparticles [39] limiting the ability for further ions to add to the crystals. These trials were performed in the same solvent with the same stirring speed to remove those parameters from the DOE. Different length straight chain alcohols influence growth in two manners: by stabilizing the final product with long chain, more hydrophobic alcohols [130]; and higher viscosities slowing the diffusion of the zinc ions [153]. Stirring speed plays a minimal role in low viscosity solvents [130] but its effects increase with the solvent's viscosity [151, 154]. Overall temperature has the largest influence on ZnO particle growth in a batch process, while concentration also appears to be a significant factor. It was also possible to calculate the activation energy for the formation of ZnO quantum dots from this experiment as different temperatures were used to calculate the rates. These values were plotted and used to solve for the activation energy from the natural logarithm of the Arrhenius equation (Equation 5).

$$k = Ae^{\frac{-E_a}{RT}}$$

Equation 4: Arrhenius equation

$$\ln k = \ln A - \frac{E_a}{R} \frac{1}{T}$$

Equation 5: Natural logarithm of Arrhenius equation

Where k is the reaction rate (presented in Figure 8), R is the gas constant, T is the temperature in Kelvin, A is the pre-exponential factor and E_a is the activation energy (in J/mol). The values of k , R , and T can be determined from the experiment and be plotted to estimate the activation energy for the synthesis of ZnO quantum dots in this system. From this plot, it can be estimated that the activation energy for the formation of ZnO is 56.9 kJ/mol. This is smaller than what has been previously been reported for ZnO, which was a value of 101.3 kJ/mol [155]. However, that was not for nanosized crystals, more for bulk synthesis where growth and ripening are allowed to proceed at a macroscopic level and would be expected to be slower than a nucleation and minor growth that occurs in quantum dot synthesis.

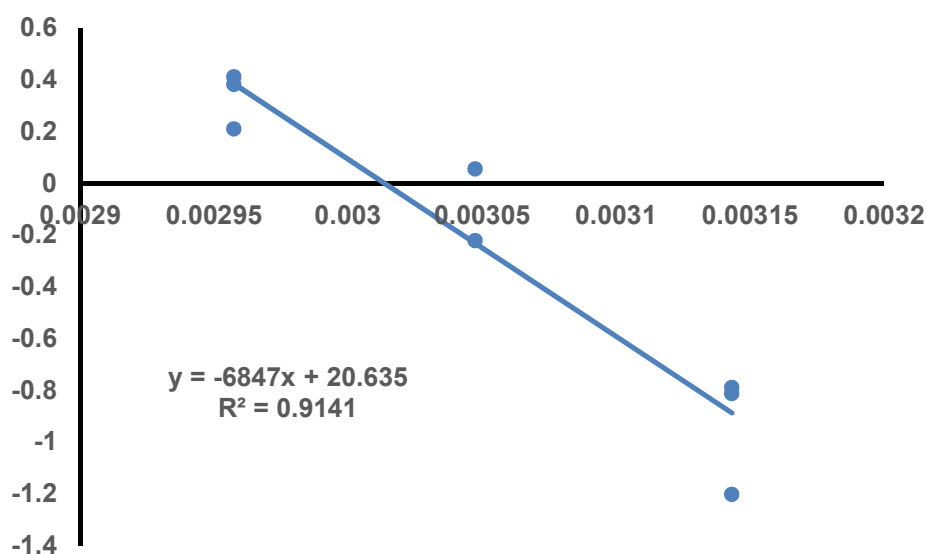


Figure 10: Natural logarithm Arrhenius plot for growth of ZnO QDs in ethanol during batch synthesis. The slope of the trendline will be used to approximate the activation energy for the system.

2.3.2 Plug flow reactor synthesis of ZnO growth rate design of experiment

A similar approach was taken studying the influence of different parameters for a continuous PFR ZnO reactor. The parameters to be studied include those from the batch experiment, but the flow of the reactor through the tubing is another parameter to be included. As the residence time in the reactor is affected by the flow, the LSW approximation cannot be used, so this DOE uses the estimated size of the quantum dot as the response. The estimated sizes of the particles after each PFR run are presented in Table 9. The DOE results from Minitab are shown in Figure 11.

Table 9: Summary of maximum absorption values from each trial and the corresponding estimated particle size.

Trial	Max absorb λ (nm)	size (nm)	Trial	Max absorb λ (nm)	size (nm)
1	354	3.36	10	341	2.47
2	341	2.04	11	310	1.68
3	350	2.99	12	345	2.67
4	340	2.43	13	340	2.35
5	345	2.67	14	330	2.09
6	335	2.24	15	350	2.99
7	340	2.43	16	350	2.99
8	330	2.09	17	325	2.70
9	345	2.57	18	320	2.65

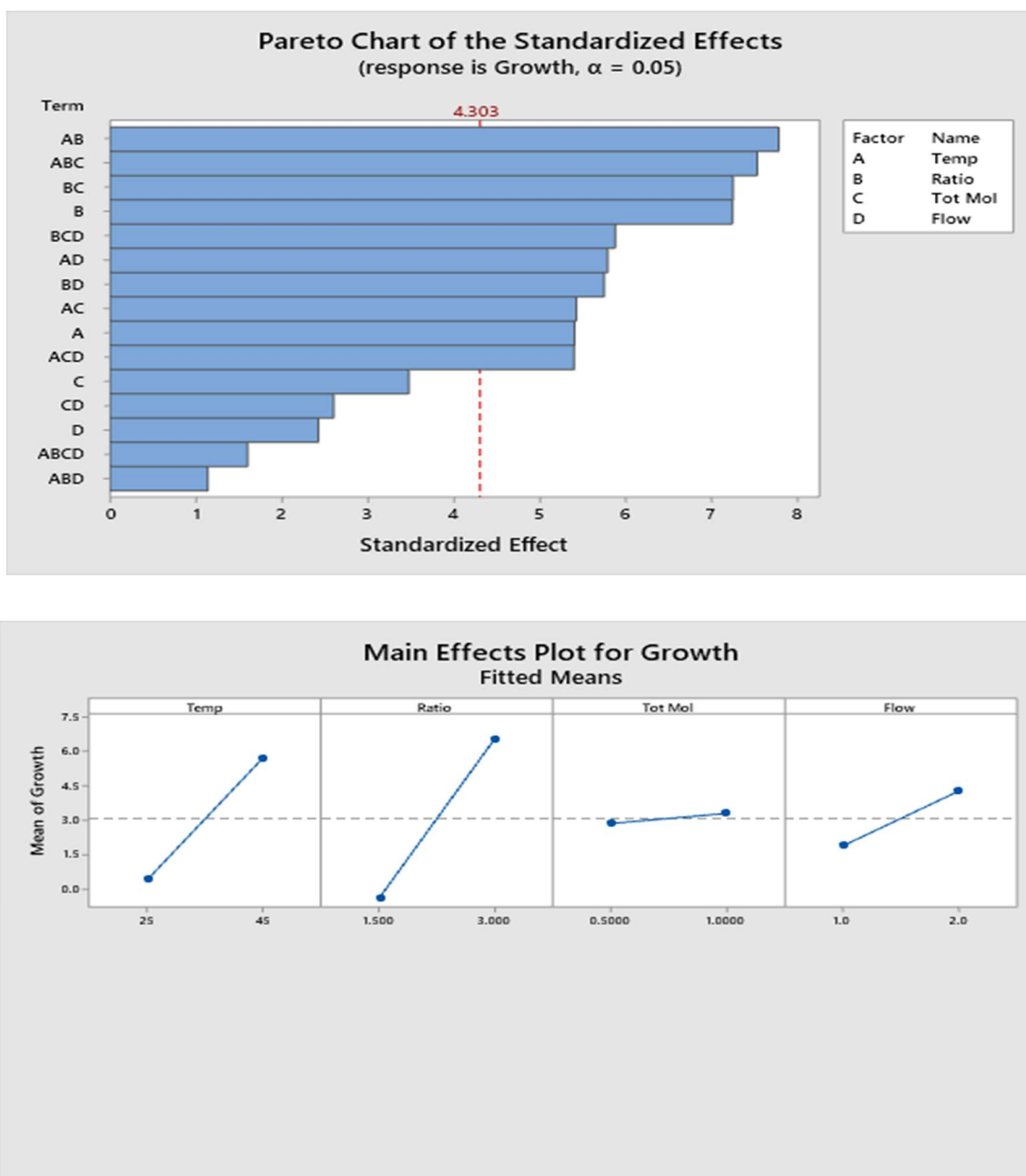


Figure 11: Pareto chart for PFR DOE (top) indicating which factors are statistically significant and factorial response chart (bottom). The Pareto chart shows which responses are significant from the experiments ran, as they are the ones whose response is above the cutoff ($\alpha > 0.05$)

The results of the PFR reactor show that a significantly larger number of factors are statistically significant for this reactor. One interesting point is that temperature is no longer the most dominant factor in the growth rate. It has been reported in microreactors that temperature is a critical factor in ZnO growth in microfluidics [141], but that study used temperatures above the boiling point of the utilized solvent, changing the flow conditions out of single-phase laminar flow [48]. This reactor is much simpler and can be comprised on less heat-resistant materials. This PFR, and all other microfluidic reactor designs, have superior mixing due to minimal bore size of the tubing used, minimizing the effects of heat and mass transfer [137]. The mixing of the reagents in the mixing zone and single laminar flow phase help ensure homogeneity throughout the reaction [135]. This is also apparent in the limited effect that the concentration (total molarity) has in these reactions. Total concentration, more specifically the Zn^{2+} concentration, was an important factor in the batch process, but its influence is much more limited in the PFR due to the more efficient mixing. In this system, the ratio of OH^- to Zn^{2+} plays a more significant role with a higher ratio leading towards greater growth. This could be due to more nucleation in the mixing zone allowing for more growth through the PFR [138]. Lastly, it can be noted that growth is positively correlated with flow. As the flow increases, the laminar mixing also increases, which helps to drive this [135]. It has been shown that flowrate corresponds with the reaction rate in growth of ZnO nanoparticles [156].

2.3.3 Effect of reaction parameters on QY of ZnO synthesized in PFR

The described PFR can generate ZnO quantum dots in a continuous manner, but it is important that those particles have the desired properties for their use. One important factor for quantum dot production is their QY, so the parameters in its synthesis should be characterized. The parameters to be tested are listed in Table 5. Temperature has been shown to have a negative effect on the quantum yields of ZnO synthesized in a microfluidic reactor [141], so its effects were not tested here. The emission spectra and estimated QYs are presented in Appendix C and summarized in Table 10.

Table 10: Summary of QYs obtained for different reaction parameters tested in the ZnO PFR.

Trial	QY (%)	Trial	QY (%)
A1	2	A2	< 1
B1	< 1	B2	< 1
C1	12	C2	13
D1	5	D2	7

It is apparent that the samples with the lower $\text{Zn}^{2+}:\text{OH}^-$ ratios yield much more luminescent nanoparticles. It is well established in batch process that a larger excess of OH^- has been found to increase quantum yield [157, 158] as well as a decrease in the band gap [142] indicating larger, less luminous particles. This could be due to the higher degree of nucleation that occurs within more OH^- rich environments [46]. The increase in nucleation leads to more dots, which have less opportunity to undergo ripening, which can decrease their surface defects, which are proposed sources of the visible emission. Flowrate also seems to impact QY, as the lower flow samples all possessed slightly higher QYs.

2.3.4 Effect of capping agents on quantum yield of ZnO synthesized in PFR

The UV-VIS absorption spectra for the capped quantum dots is shown in Appendix D with UV-VIS transmission chart for uncapped ZnO shown at the top for reference. Most of the spectra have similar shapes, albeit with slight changes. The glycerol, oleic acid and citric acid samples did not possess the same shape, they possessed more rounded curves indicating that the samples were not fully dissolved. This was observed with those samples as they had a visually cloudy look, the rest of the capping agents yielded clear solutions. Table 11 indicates the wavelength of maximum UV absorption on for the nanoparticles, indicated by the local maximum of the slope in the UV region [144]. These wavelengths were used to estimate the size of the quantum dots using the effective mass

model (Brus equation), with the size estimates also presented in Table 11. Two ZnO samples stood out in having the smallest estimated sizes – those capped with ethylene glycol (EG) or those capped with dodecanethiol. As the capping agents can act as an *in situ* size control during growth, those ligands which have the capability to pack the most tightly would limit the nanoparticles' size [159]. EG is a small molecule and dodecanethiol is a relatively inert straight chain, both leading towards larger packing densities on the surfaces of the growing QDs, limiting their growth potential.

Table 11: Maximum calculated UV absorption for capped ZnO quantum dots and estimated particle radius.

Capping Agent	Max UV Absorb (nm)	Max UV Emission (nm)	Estimated Radius (nm)	Quantum Yield (%)
Uncapped	315.5	487	1.8	13
TEOS	313.5	479	1.7	30
VTS	302.5	467	1.6	28
Glycerol	311	464	1.7	< 1
EG	261.5	462	1.2	< 1
PEG	313	480	1.7	27
PVP	315	487	1.8	32
Oleylamine	307.5	464	1.6	8
Oleic acid	303.5	461	1.6	< 1
Citric acid	314.5	466	1.8	< 1
Dodecanethiol	245.5	458	1.1	< 1

The presence of a capping ligand on ZnO nanoparticles makes a significant difference in its QY. The photoluminescent emission spectra for the capped samples are presented in Appendix E. Each of the samples was excited at their maximum UV absorption/excitation wavelength, which are listed in Table 11. The areas under these curves can be summed and those sums can be used to calculate their quantum yields, using the uncapped ZnO emission as a reference. The silane-containing ligands (TEOS and VTS) and those capped with polymers (PEG and PVP) all show substantial increases in QY. As the visible light emission of ZnO has been attributed to oxygen vacancy surface defects [25], these ligands passivate the surfaces stabilize the defect states [159]. The multiple reaction sites available of those ligands would lead towards an interconnected passivating layer, which would help protect the nanoparticle surface. These compounds also act as electron donors when they link with the ZnO QDs, which can cause the valence and conduction bands to widen, thus shrinking the band gap [160]. Silane capping layers are well known to increase the QY of ZnO quantum dots [23]. PEG and PVP have also been reported as good candidates to increase the QY of ZnO [51, 61]. While these increases have been reported previously, those were in batch synthesis systems, not continuous reactor designs. The other tested capping agents were found to have deleterious effects on QY. Glycerol and ethylene glycol have been reported as ZnO capping agents previously [20], although that study focused on the photocatalytic properties of ZnO, not their luminescence. In that case it was found that EG has minimal effect on that property, while glycerol decreased their photocatalysis. In this study, these compounds had negative effects on the QY. The reduction in QY suggests a reduction in the number of, or a smoothing, of the surface defects [159]. As mentioned previously, the EG would pack tightly over the surface of the ZnO nanoparticle due to its small size, which could smooth out the surface defects. A similar behavior is likely occurring with the straight-chain dodecanethiol, which is a known quenching ligand [54], packing tightly which removes the emission centers. The glycerol, citric acid and oleic acid decrease the QY as they are electron withdrawing ligands [161], which decreases the electron density in the surface defects limiting their emission potential. While these can be used for controlling the size and morphology of non-visible light emitting ZnO structures [49,

162], their properties make them undesirable for visible light emitting QDs. Oleylamine was found to have limited effect on the QY, decreasing it slightly. Similar quenching has been reported for long-chain alkyl amines [8], indicating that these types of compounds would not be ideal for bright emitting QDs. For high QY ZnO nanoparticles, it would be best to use silanes or polymer (such as PEG and PVP) capping agents, as they were shown to increase the visible emission. Silane- and polymer-capped QDs would be ideal for keeping them stable long term and using them for composite materials [163] or aqueous environments [50].

2.4 Conclusion

The growth parameters on ZnO quantum dots in batch and continuous systems have been studied and it has been shown that in both types of reactors the most significant factors are reaction temperature and total concentration of the reagents. A continuous PFR has been proposed which has been shown to produce ZnO quantum dots at a relatively large scale (almost 0.2 g/hr or 5 g a day estimated from the flow and concentrations used) if fed with large reservoirs of the reagents. The quantum yield of the PFR nanoparticles is most heavily influenced by the ratio of the two reactants. This type of reactor can allow for the scaleup and mass production of luminous ZnO quantum dots.

Chapter 3

Large scale synthesis and purification of silane-capped ZnO quantum dots

Abstract

A simple batch sol-gel process for the synthesis of large quantities of silane-capped zinc oxide quantum dots has been demonstrated. Large batches of zinc oxide quantum dots have been described previously in the literature, but this process is unique in that *in situ* silane capping was used to control the growth of the nanoparticles. The quantum dots emit visible light in the blue region with a quantum yield > 30 %. This approach yields over 50 grams of nanomaterial in a single batch, with an over 99 % reaction completion yield. The resulting quantum dots are characterized with XPS and PL analysis to confirm successful silane capping. EDX and XRD analysis were performed to confirm the presence of the silane shell and that the large batch is identical to quantum dots produced in small batches. Lastly, the efficiency of centrifugation for large scale purification of quantum dots is demonstrated.

3.1 Introduction

Zinc oxide (ZnO) quantum dots are nanoscale crystals with a small enough Bohr radius to experience quantum confinement [22]. They have a relatively large band gap of 3.37 eV at room temperature and a large exciton binding energy of 60 meV [164]. The large exciton energy makes it one of the brightest emitters among wide band gap semiconductors [27]. ZnO quantum dots can be used as an alternative to organic dyes, a photonic material, chemical sensor [133]; as well as an antimicrobial and antifouling agent [165]. Some advantages of ZnO, compared to other types of quantum dots, is that is a cheap nanomaterial [12]. It also can be produced by nontoxic and less energy intensive manners as opposed to other types of quantum dots [166]. Despite its potential uses, commercial applications of nanosized ZnO are relatively few. Large quantities of nanoparticles are essential for the marketability and commercialization of nano ZnO [167].

Several researchers have published different approaches to solving this problem. Koch et al (2015) made a larger batch in a 280 ml sol-gel, using bubbled air to help drive the reaction [168]. This allowed them to make over 4 g at a time. Gupta and Srivastava (2018) used a sonochemical approach; running a sol-gel in a sonication bath. This allowed them to make 4.4 g of ZnO nanoleaves with a 96% reaction yield after two hours [169]. Azam et al (2009) devised a solvent-free method, utilizing a mechanochemical reaction to form ZnO. This is a more environmentally friendly approach as it does not require the use of solvent systems for synthesis, which would be attractive for a scaled-up process [35]. Ghasaban et al (2017) used a low temperature hydrothermal synthesis that produced 60 g in a solvent-free system [167]. The successful synthesis of ZnO nanoparticles in a 4.5 L CSTR system was demonstrated by Wang et al (2012) [170], who performed an optimization process determining the ideal conditions for ZnO formation. Liu et al (2017) showed that it was possible to synthesize over 20 g of ZnO in a scaled-up ethanoic sol-gel, making quantum dots for LED phosphors [134]. This was done by refluxing the reagents in a heated sol-gel, with an addition of a siloxane capping agent at the end to precipitate the nanoparticles for collection.

The addition of capping ligands helps stabilize the quantum dots [51] and can help prevent their agglomeration [37]. Silane is a commonly used capping agent that also helps protect and stabilize quantum dots [61] as well as alter their electrical and optical properties [54]. Silane shells have been shown to blueshift a quantum dots' excitation and emission wavelengths while significantly improving their quantum yields [23]. One method to introduce capping agents is during the synthesis process so that the quantum dots are capped at a certain size during their growth, preventing secondary growth and ripening [171]. Therefore, *in situ* introduction of a capping agent during a large-scale synthesis could help control the size of the final product.

This experiment will show that it is possible to perform a large-scale synthesis of silane capped ZnO quantum dots (QDs) using a basic ethanoic sol-gel. To the authors' knowledge, this is the first time an *in situ* capping reaction will be performed to limit the growth of the quantum dots and synthesize large quantities concurrently. The reaction yield of a large batch reaction will be compared with a smaller batch. The products will be characterized by their emission, their electronic structure, their composition, and their crystal structure. One major issue with large scale synthesis of quantum dots is the mass purification of quantum dots [172]. The nanomaterial produced for this study will be purified using centrifugation, which the purity of the ZnO tested after subsequent wash and spin cycles to determine the efficiency of the operation.

3.2 Experimental

3.2.1 Materials

Zinc acetate dihydrate ($\text{Zn}(\text{OAc})_2 \cdot 2\text{H}_2\text{O}$), vinyltrimethoxysiloxane (VTS) and sodium hydroxide (NaOH) were obtained from Sigma-Aldrich, Canada and used without any further purification. Isopropyl alcohol (IPA) was supplied by Commercial Alcohols.

3.2.2 ZnO quantum dot synthesis

The synthesis of ZnO QDs used in this experiment was based on the method described by Bang et al. [32], modified to include siloxane capping reactions and the switch from ethanol to IPA as the solvent. Using IPA as the solvent also helps drive the formation of

ZnO quantum dots due to it being less effective at solubilizing the precursors ($\text{Zn}(\text{OAc})_2 \cdot 2\text{H}_2\text{O}$ and NaOH) [153].

For the small batch, zinc acetate dihydrate (0.23 g) was mixed into 30 ml of IPA and sonicated at 65°C for one hour, and then cooled in an ice bath. At this point, 0.25 g of VTS was added to the solution to serve as a capping agent to limit the particles' growth. Sodium hydroxide (0.1 g) was dissolved in 10 ml of IPA, cooled in an ice bath, and added to the zinc acetate solution dropwise. The reaction proceeds for one hour in the ice bath with magnetic stirring, then the unpurified product is collected and dried in a vacuum oven at 60°C for at least 24 hours. A small batch of uncapped ZnO nanoparticles was synthesized in a similar manner, without the inclusion of the VTS capping agent.

The large batch synthesis was performed in the similar manner, with everything scaled up accordingly. 115g of zinc acetate dihydrate was dissolved in 15L of IPA and sonicated at 65°C for one hour, or more, until the solid completely dissolved and the solution was clear. At this point, 125g of VTS was added as the capping agent. The solution was poured into a water-jacketed glass reaction vessel connected to a circulating chiller operating at 2°C. The solution was stirred with a PTFE paddle at 500RPM. 50g of sodium hydroxide was dissolved in 5L of IPA using a heated stir plate and subsequently cooled in an ice bath. The sodium hydroxide solution was added slowly into the reaction vessel, and the synthesis proceeded for 1 hour. The unpurified product is collected and dried in a vacuum overnight.

The samples were dried overnight in a vacuum oven at 75°C to remove the IPA solvent. Samples of the different sized batches were dissolved in minimal methanol and purified via dialysis with methanol (MWCO of 1 KDa, Spectra/Por® 6 Standard RC pre-wetted Dialysis Tubing, diameter 29 mm). This was done three times to ensure the products were clean. The purified products were dried in the vacuum oven and the quantum dots are collected for characterization.

3.2.3 Characterization of quantum dots

The reaction yield of the reaction was determined comparing the ^1H NMR spectra of the starting material and the unpurified product. This was performed on the uncapped dots to simplify the spectra and determine the conversion to ZnO. The ^1H nuclear magnetic resonance spectroscopy (NMR) spectra were recorded using a Varian INOVA 600 spectrometer at 25°C. Methanol- d_4 was used as the solvent and ^1H chemical shifts were referenced to tetramethylsilane (TMS; 0.0 ppm). To determine successful capping of the ZnO with the silane, their photoluminescence was measured using a PTI Quantamaster 50 spectrofluorometer. To confirm the presence of the silane shell and its effect on the electronic properties on the QDs, uncapped and VTS-capped ZnO QDs from the small batch were analyzed by X-ray photoelectron spectroscopy (XPS) using a Kratos AXIS Supra XPS. The survey scan analyses were carried out with an analysis area of 300 x 700 microns and a pass energy of 160 eV. The high-resolution analyses were carried out with an analysis area of 300 x 700 microns and a pass energy of 20 eV. Elemental composition analysis of the small-scale and large-scale batches was performed using energy-dispersive X-ray spectroscopy (EDX). The EDX analysis was run on a 1540XB FIB/SEM. The samples were mounted on double-sided conductive carbon sticky tabs and the analysis was performed with a 30keV beam at approximately 300pA current. The small-scale and large-scale batches were also analyzed using X-ray diffraction (XRD). The XRD spectra were obtained using a Bruker D2 Phaser powder diffractometer using Cu K α radiation (λ for K α is equal to 1.54059 Å) over 2θ 10–80.

3.2.4 Scaled up purification

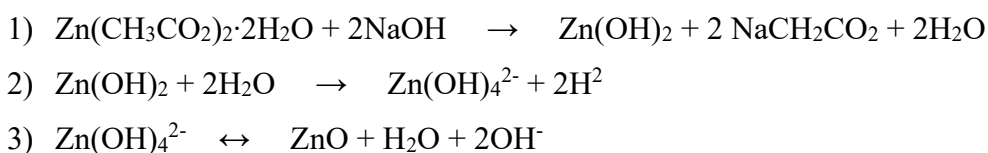
To determine if centrifugation can be used to purify larger quantities of QDs efficiently, samples (~10g) of the unrefined large-scale synthesized VTS-ZnO QDs were transferred to 50ml conical tubes, vortexed in MeOH, and spun in a centrifuge for 60 min at 10000rpm. After each spin, approximately 80 percent of the supernatant was removed. Fresh MeOH was added, the samples were vortexed and spun again. This was repeated as necessary. To determine the quantity of sodium (and hence NaOH) present in each sample, inductively couple plasma (ICP) analysis was performed using a Thermo ICP-OES. After each spin, a weighed quantity of the pelleted material was collected and

dried. These samples were digested in aqua regia, then analyzed in the ICP using NIOSH 7301 as a guide. The ratio of Zn^{2+} to Na^+ will be used to determine the purity of the samples.

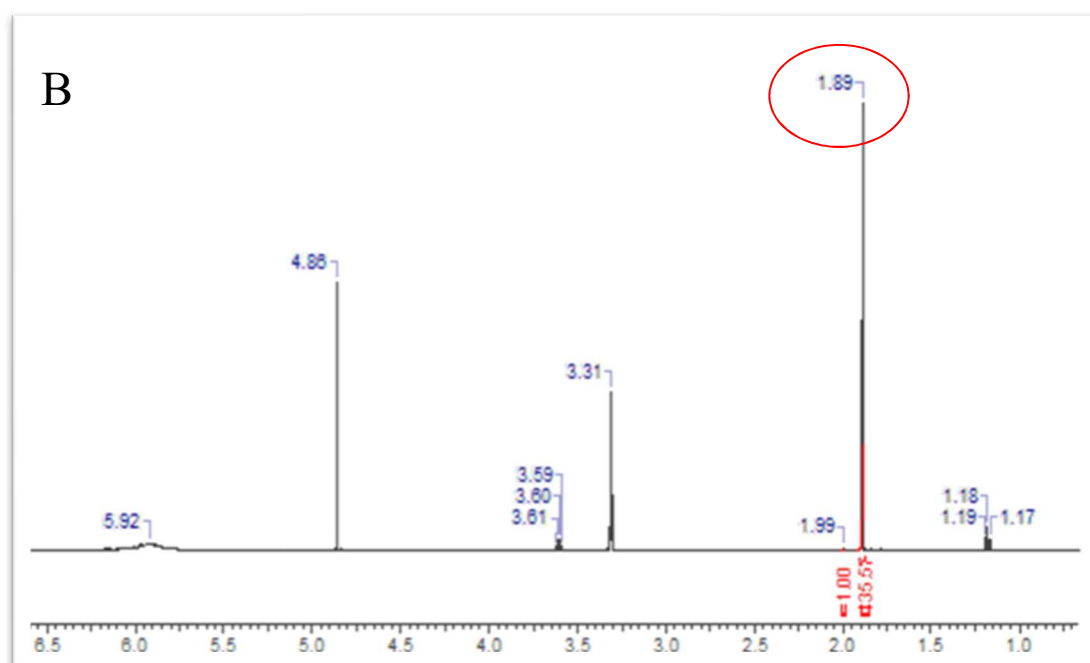
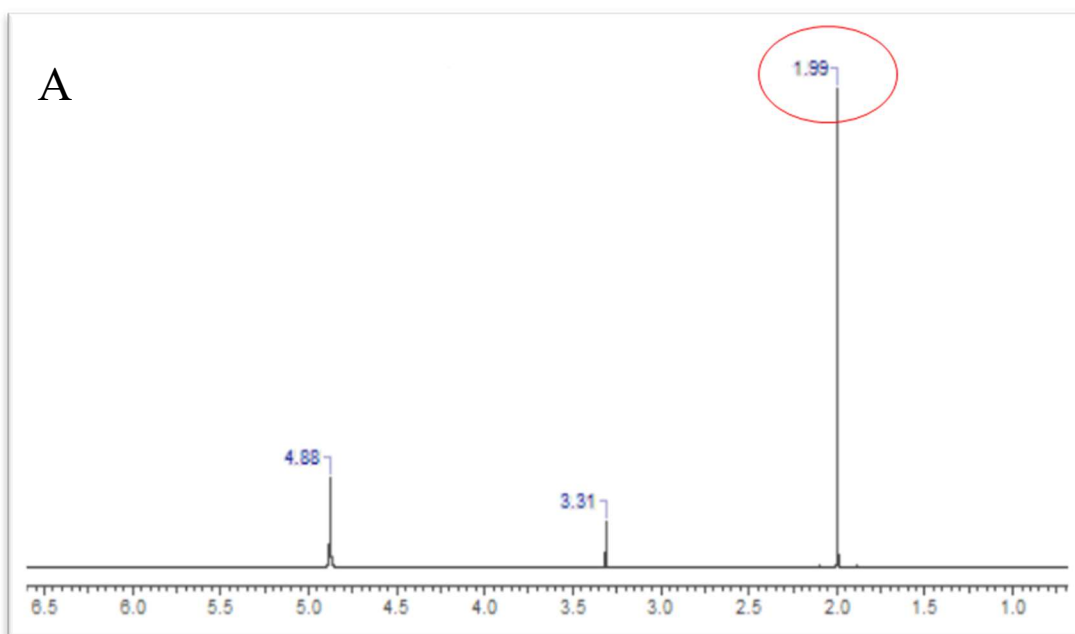
3.3 Results and Discussion

3.3.1 Reaction yield of ZnO synthesis

The formation of uncapped ZnO quantum dots (QDs) in a basic alcoholic environment has been proposed to follow three steps [38, 173]:



The main reactants are zinc acetate dihydrate $\text{Zn}(\text{OAc})_2 \cdot \text{H}_2\text{O}$ and sodium hydroxide (NaOH), with the main products being ZnO QDs, sodium acetate (NaOAc) and water, therefore the change in acetate from zinc to sodium could act as a reference for the conversion of the synthesis. Figure 12a show the ^1H NMR spectra of the precursor $\text{Zn}(\text{OAc})_2$ in methanol. That compound only has one type of hydrogen, those attached to the methyl groups, so no peak splitting would be expected. That peak at 1.99 parts per million (ppm) was assigned to the zinc acetate, with the other smaller peaks representing the solvent. Figure 12b is the NMR spectrum of the crude ZnO product. The peak at 1.99 ppm has almost completely disappeared, indicating an almost complete depletion of $\text{Zn}(\text{OAc})_2$. It is replaced by significant peak at 1.89 ppm (as observed in Figure 11b and 1c), which is assigned to the reaction product, sodium acetate. The other peaks present at 1.18 ppm, 3.60 ppm, and 5.92 ppm could arise from the remaining sodium hydroxide (which was added in excess) and any other side products which could be present and the siloxane. The only hydrogen atoms which would experience a shift in their resonance would be those on the acetate group. According to these results, the sodium acetate precursor is completely consumed, and it can be concluded that the reaction has a conversion of 99%.



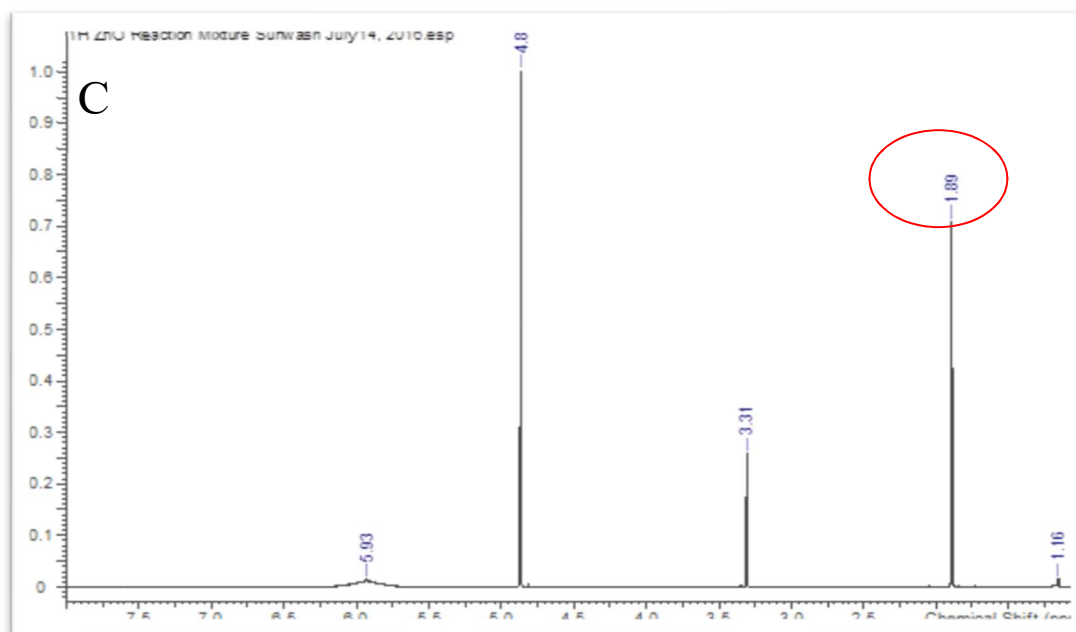


Figure 12: 1HMR spectra of (A) precursor reagent zinc acetate dihydrate where the circled peak is assigned to the precursor acetate's hydrogens; (B) unpurified ZnO from the small batch, where the circled peak is assigned to the side product sodium acetate's hydrogens; and (C) unpurified ZnO from the large batch reaction, where the circled peak is assigned to the side product sodium acetate's hydrogens.

3.3.2 Photoluminescence of ZnO quantum dots

It has been shown that capping ZnO quantum dots with an alkylsiloxane blueshifts their emission spectrum [160]. The vinyltrimethoxysiloxane reacts with leftover hydroxides on the outer surface of the forming quantum dots to limit their growth [171] and help protect them from degradation [160]. Figure 13 shows the normalized PL emission spectrums of the small batch, large batch, and uncapped quantum dots. The capped quantum dots have their emission blue-shifted from the usual green visible emission. The maximum emission of the uncapped samples is at 550nm, while the two capped samples (small batch and large batch) both have maximum emissions centered at 480nm. The excitation wavelengths as well are blue-shifted in the capped quantum dots, with maximum excitation at 310nm, compared to the maximum excitation of 325nm in the uncapped samples. Silane-capped ZnO nanoparticles have been shown to lose their characteristic

green emission and gain blue emission peaks arising from intrinsic defects such as oxygen and zinc interstitials and deep level defects from vacancies [164]. This change in photoluminescence confirms the presence of the silane shell on the capped ZnO. The quantum yield of the dots also was increased from 10 percent for the uncapped ZnO to over 30 percent for the VTS-capped ZnO. These yields were estimated using an external reference methods [146] and the particle sizes were estimated using the effective mass model [145].

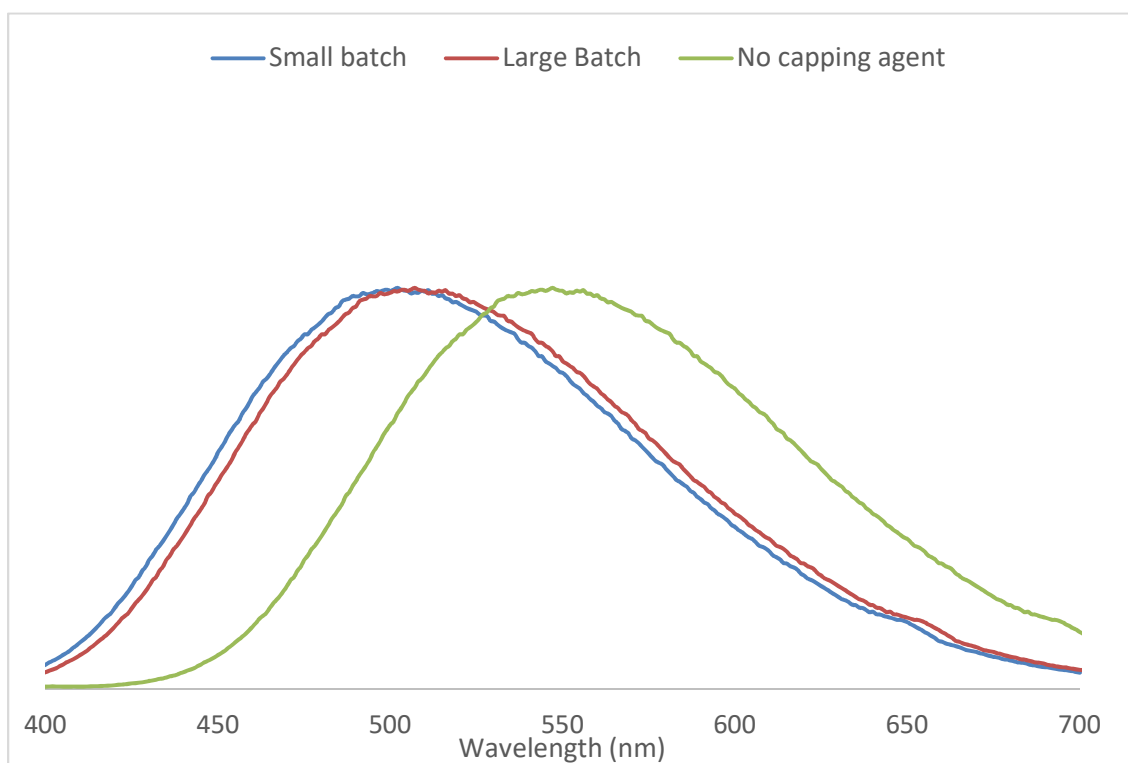


Figure 13: Photoluminescent emissions of UV excited quantum dots. The two spectra with their maxima centered at 500 nm are the silane-capped ZnO batches (small- and large-scale synthesis), while the third peak centered at 550 nm is the uncapped ZnO quantum dots.

3.3.3 XPS analysis of uncapped and silane-capped ZnO quantum dots

Figure 14 shows the survey spectra for the uncapped and VTS-capped ZnO nanoparticles. As expected, the VTS-capped QDs indicates the presence of silicon and carbon from the

alkylsiloxane ligand shell. Sodium is also present in the capped sample, likely leftover adhered to the QDs after the synthesis. High resolution scans for the Zn 2p_{2/3}, Zn LMM (Auger), O 1s, and valence bands are presented in Figures 14, 15, 16, and 17 respectively. The uncapped and silane-capped spectra are similar, with the VTS-capped samples generally showing a slight increase in their binding energies. The Zn 2p_{2/3} scan (Figure 15) shows a slight shift in its binding energy from 1021.32 to 1022.12 eV, which makes it difficult to identify the difference in chemical states for the ZnO samples [174]. This small shift could indicate a slight change in the oxidation state of the Zn ions due to their interactions with the silane shell, [175] but is clear that the zinc atoms in both samples are predominately in the Zn²⁺ oxidation state [176].

The Zn LMM scan also confirms this difference. The Auger parameter determined for the uncapped ZnO samples (Figure 16 top) matches what is expected in the literature for Zn [175] and indicates that the Zn is present in stoichiometric equivalence with oxygen. The Auger parameter for the VTS-ZnO (Figure 16 bottom) shows that the Zn ions are not stoichiometrically balanced with oxygen indicating an increase in oxygen vacancies [174]. The O 1s spectra confirm that with the VTS-ZnO sample (Figure 17 bottom) have a slightly higher binding energy, 531.85eV compared with 530.09eV, compared with the uncapped ZnO sample (Figure 17 top). Figure 17 (top) also contains an O 1s peak corresponding to its surface hydroxides, which are lacking in the capped sample [10, 60].

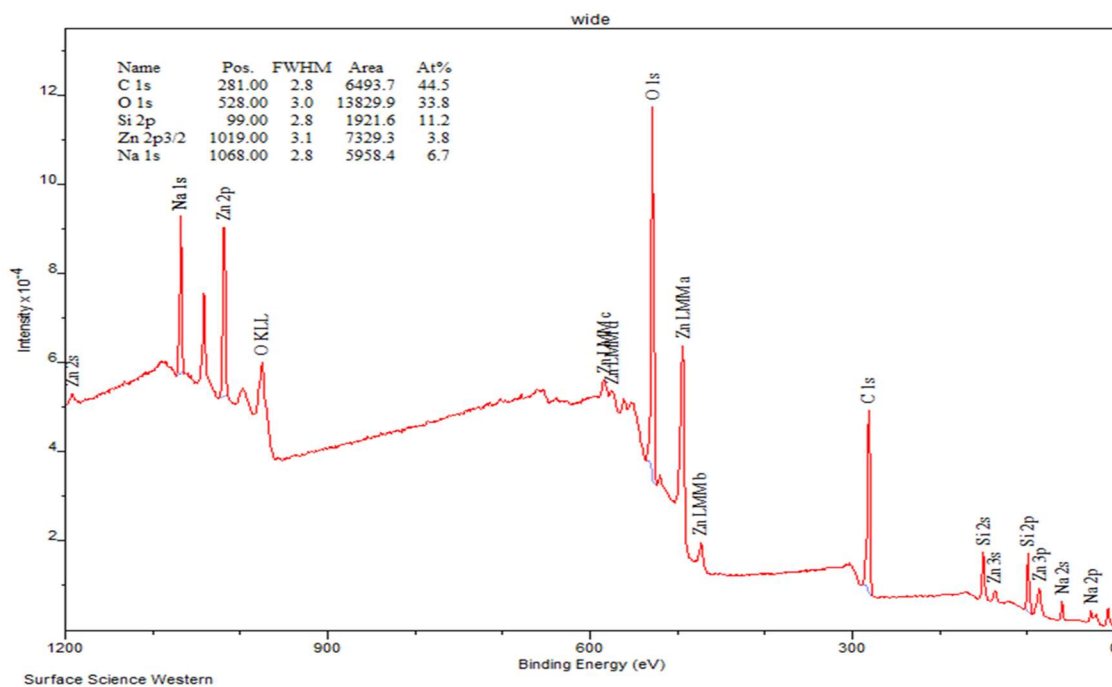
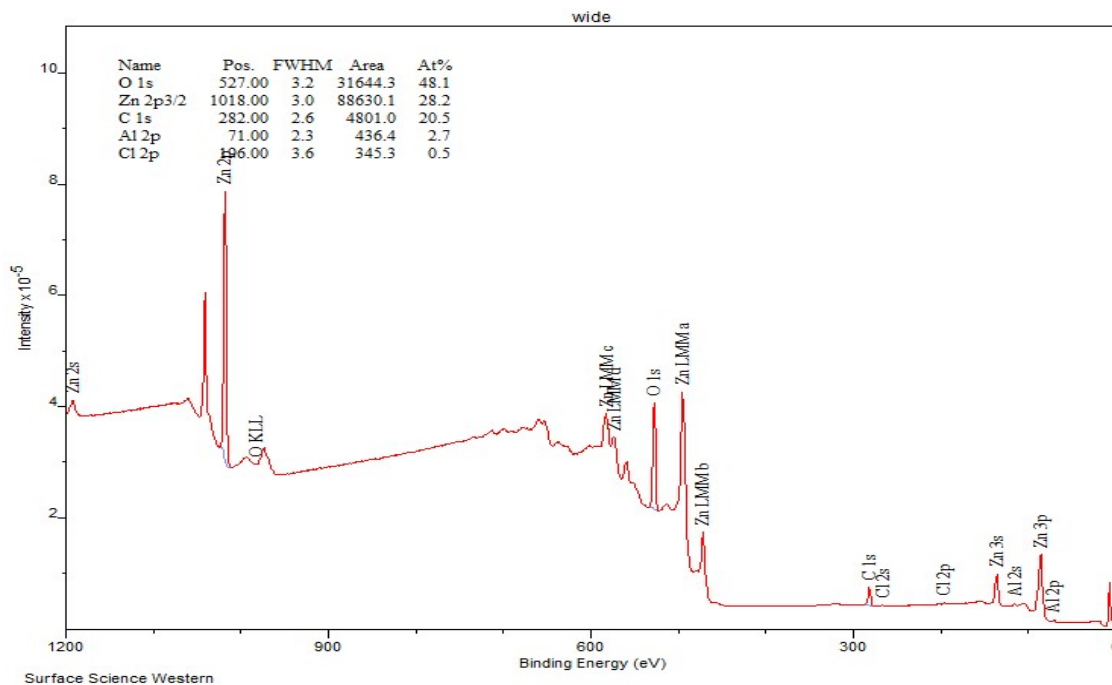


Figure 14: XPS survey scan for ZnO quantum dots (top) and VTS-capped ZnO quantum dots. Both show expected Zn and O peaks; however, the capped QDs also contain peaks representing the silane shell atoms (Si and C).

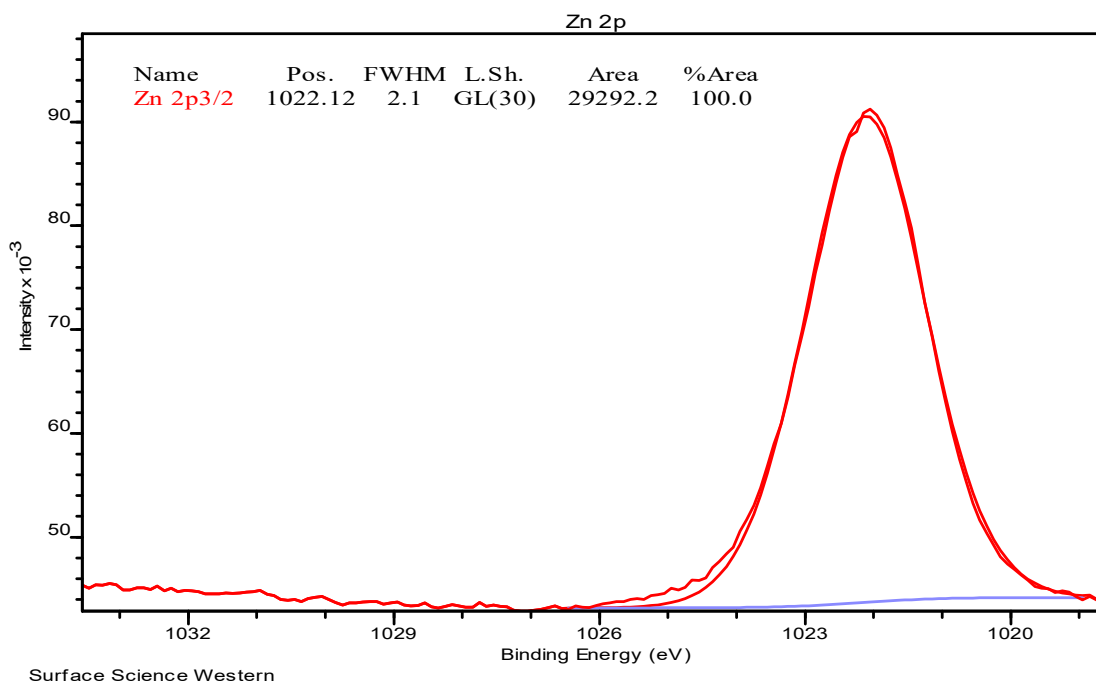
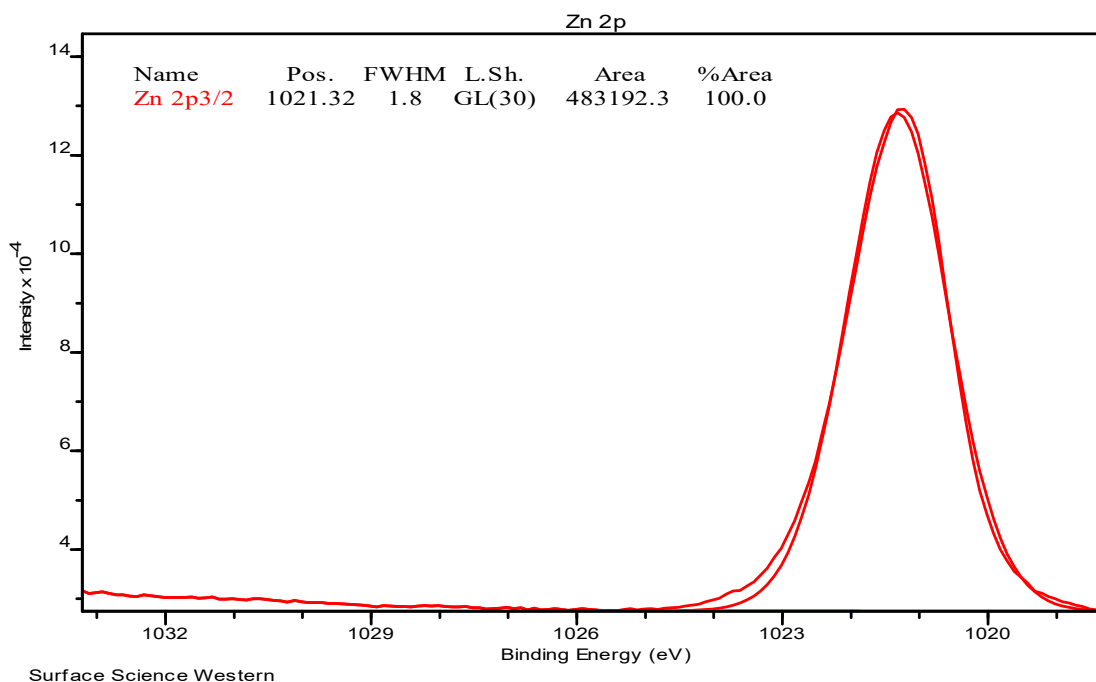


Figure 15: XPS high resolution Zn 2P_{3/2} scan for ZnO quantum dots (top) and VTS-capped ZnO quantum dots (bottom). A small shift in the peak position is observed with the addition of the silane shell from 1021.32 eV to 1022.12 eV.

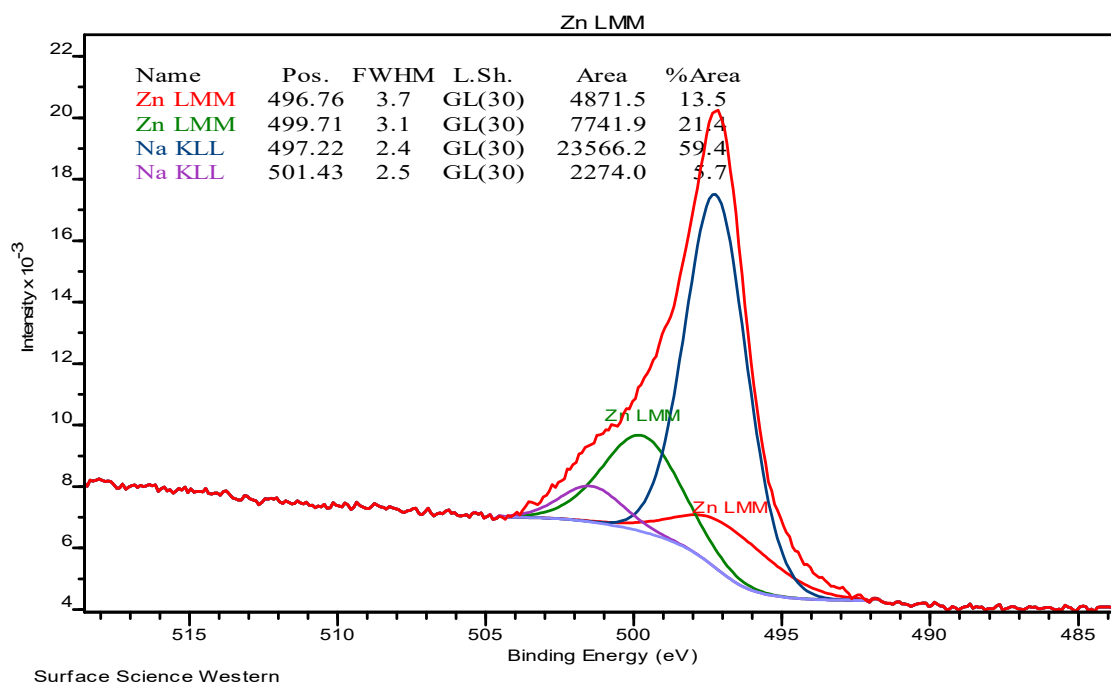
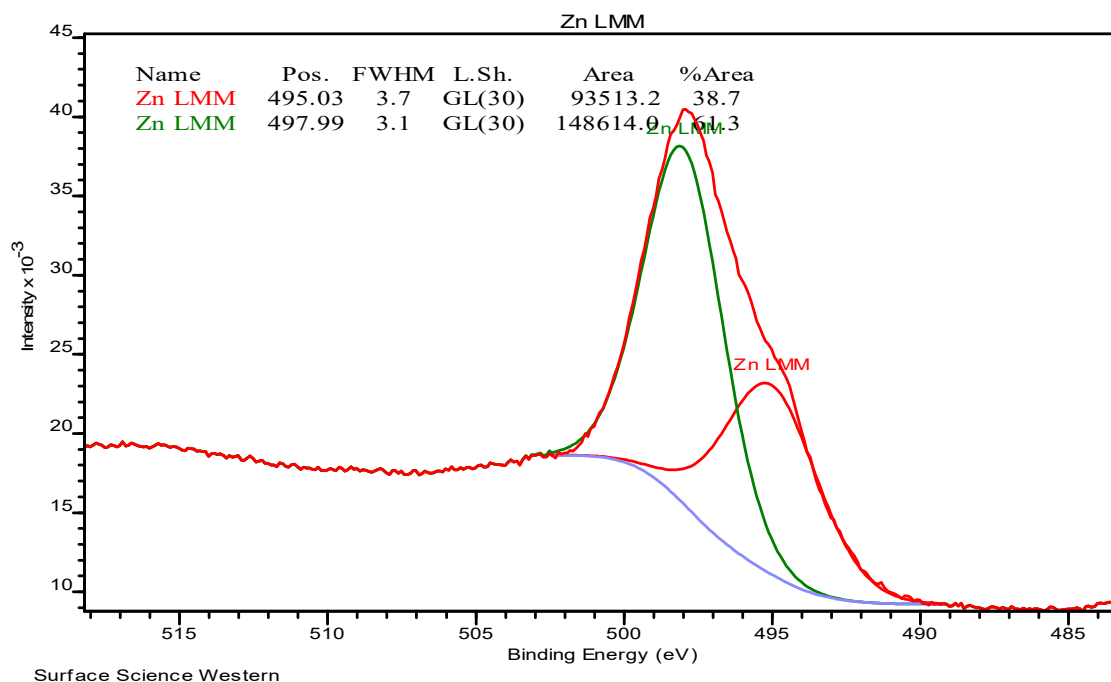


Figure 16: XPS high resolution Zn LMM scan of ZnO quantum dots (top) and VTS-capped ZnO quantum dots (bottom).

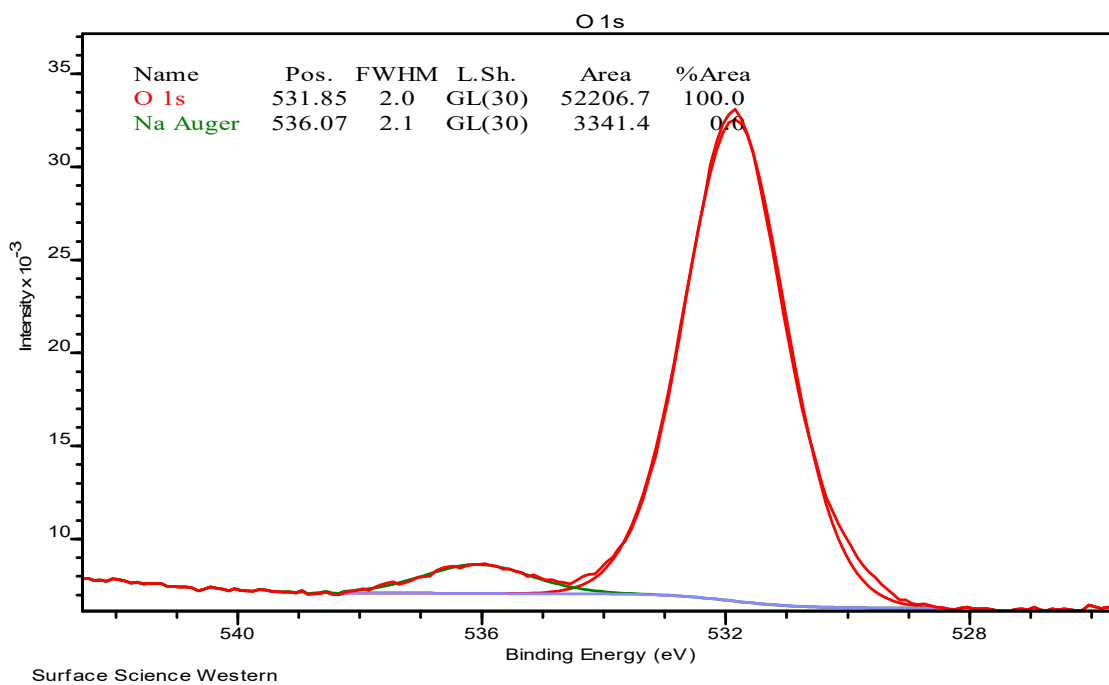
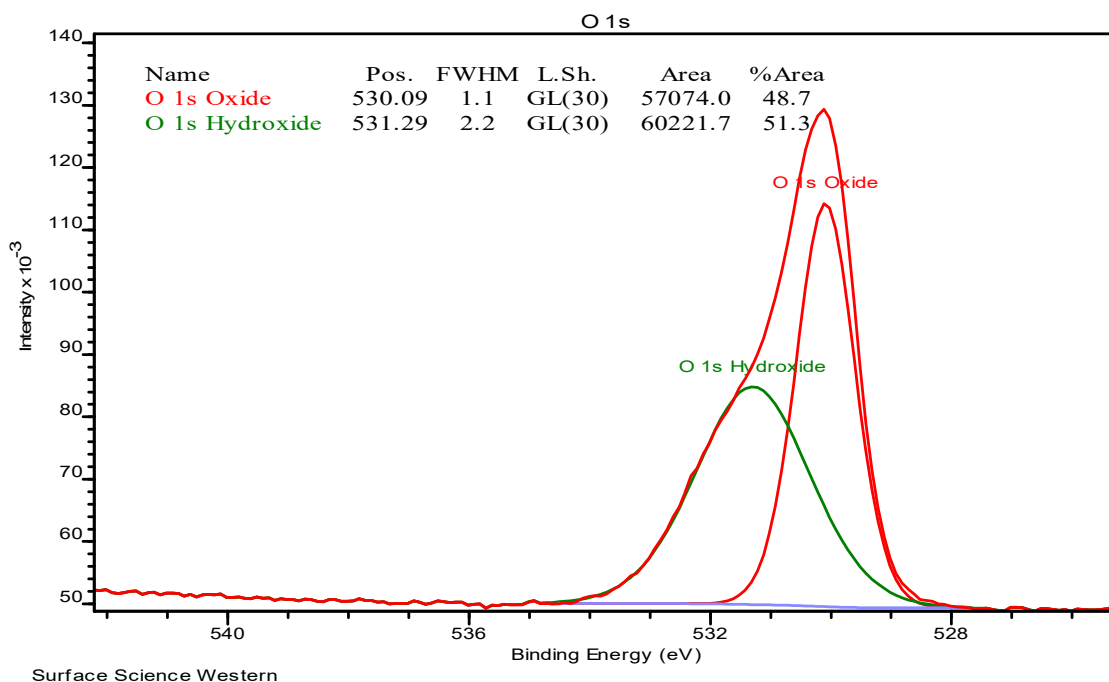


Figure 17: XPS high resolution O 1s scan for ZnO quantum dots (top) and VTS-capped ZnO quantum dots (bottom). Small shift in binding energy observed. Uncapped QDs contained hydroxide peak corresponding to the surface hydroxyls moieties.

3.3.4 EDX analysis of small- and large-scale VTS-ZnO synthesis batches

A further confirmation into the identity of the synthesized silane-capped ZnO nanoparticles was performed using an EDX analysis. Figure 18 depicts the EDX spectra of the small batch and large batch syntheses respectively. The weight percentages of the elements detected are presented in Table 12. It is apparent that the elements present in the samples were the expected ones. Zinc and oxygen are both present in the samples, which clearly arises from the quantum dots. Silicon and carbon were also present, which would be present in the silane shell (although some of the carbon signal could arise from the carbon tab that the samples were residing on). Similar EDX spectra for ZnO quantum dots are reported in the literature [177]; however, those only matched the zinc and oxygen peaks as the authors' samples were uncapped. Lastly, trace amounts of sodium were also present. This sodium originates from the synthesis process, likely from some NaOH which was adsorbed to the nanoparticles and persisted through the dialysis purification step.

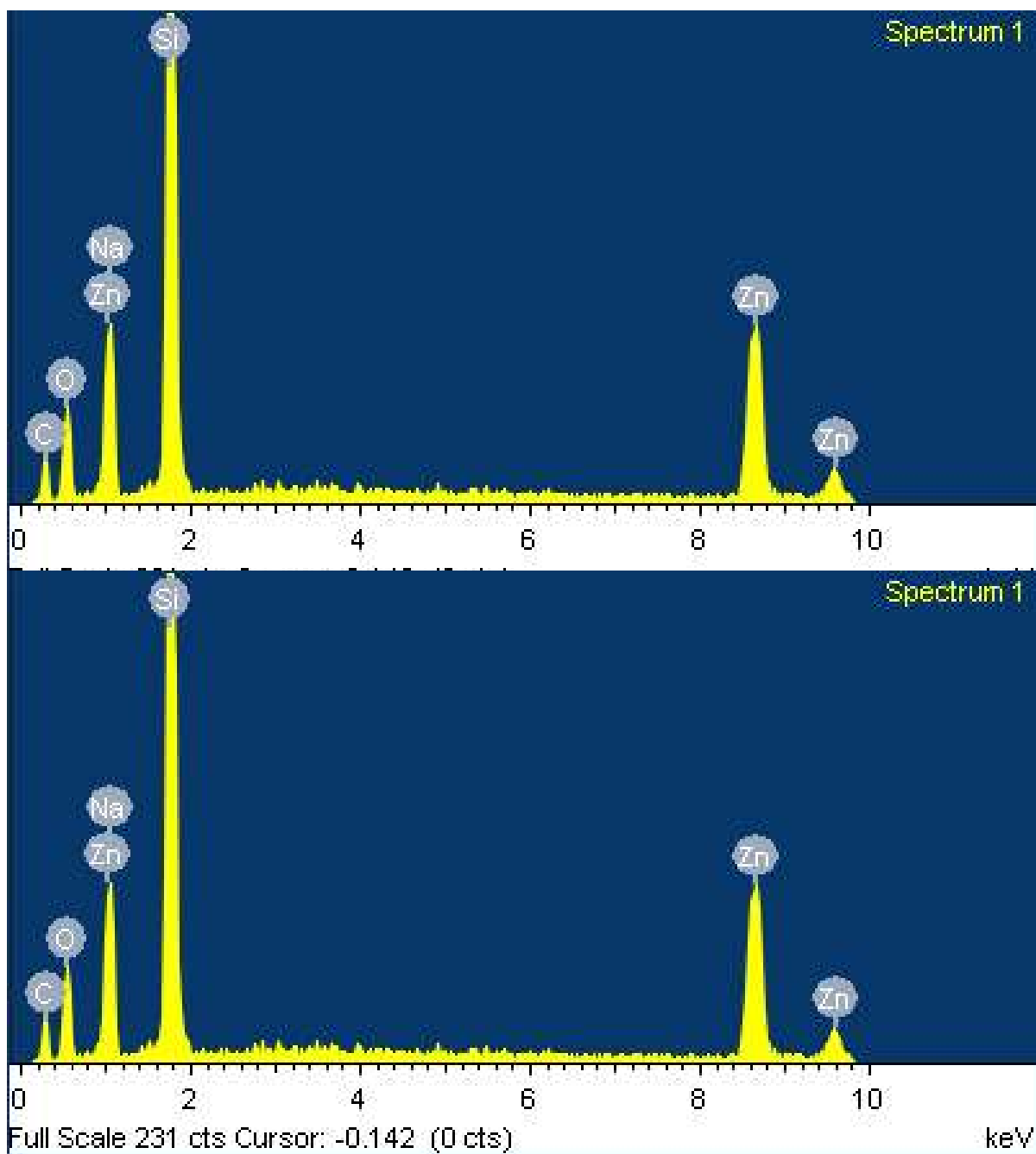


Figure 18: EDX spectra of ZnO batches with small-scale synthesis shown in the top spectrum and the large-scale synthesis shown in the bottom spectrum.

Table 12: EDX elemental compositions for the two different sized synthetic batches.

Small-scale synthesis			Large-scale synthesis		
Element	Weight%	Atomic %	Element	Weight%	Atomic%
C	28.47	44.34	C	27.52	45.05
O	27.33	31.96	O	23.39	28.73
Na	3.75	3.05	Na	2.79	2.38
Si	23.87	15.90	Si	24.94	17.45
Zn	16.58	4.75	Zn	21.37	6.42

3.3.5 XRD analysis of small- and large-scale VTS-ZnO synthesis batches

X-ray diffraction (XRD) was performed on the large and small batches. Their XRD spectra are presented in Figure 19.

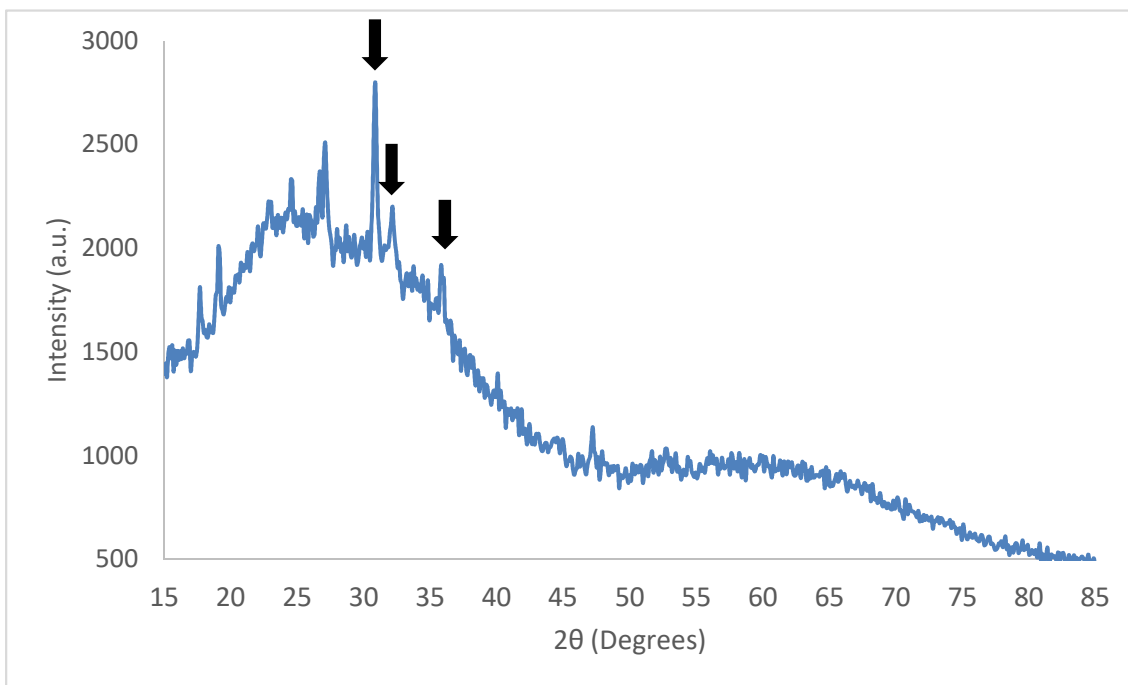
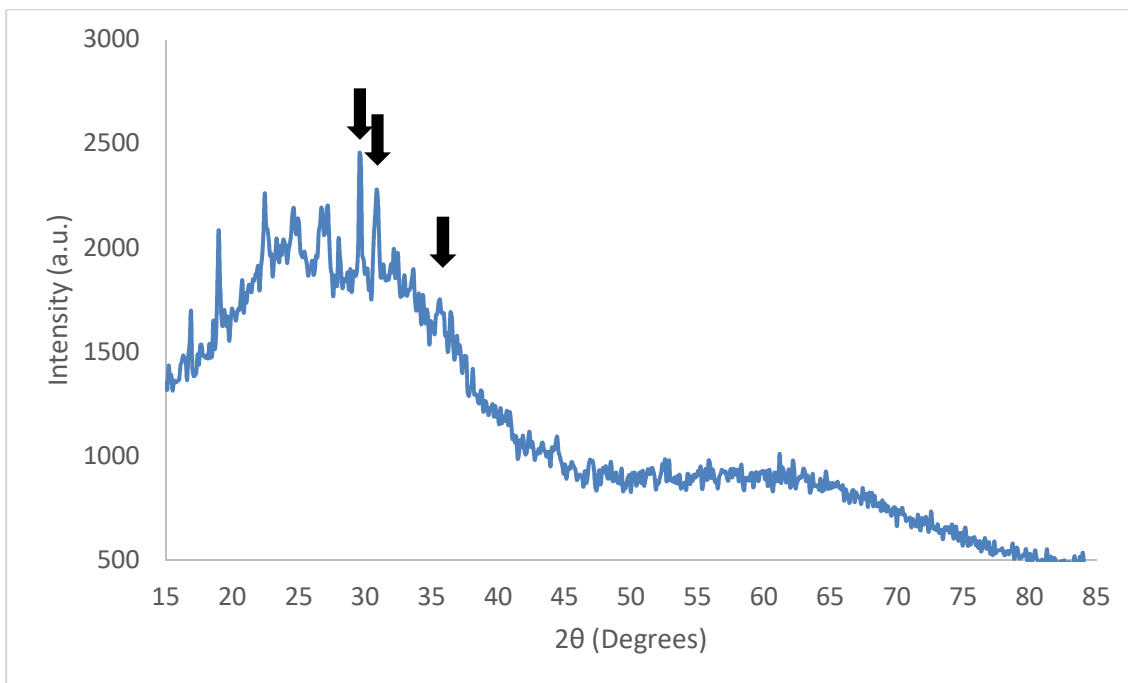


Figure 19: XRD spectra of the (top) small- and (bottom) large-scale VTS-ZnO synthesis batches. The peaks that correspond to the 100, 002 and 101 facets of ZnO are indicated with arrows.

The two samples from both synthesis volumes had extremely similar XRD spectra, confirming that the two products are extremely similar. However, they do not completely match the expected pattern that is depicted in the JCPDS 36-1451. The two spectra have their characteristic 100, 002, and 101 facet peaks shifted slightly. From the quantum dots' emission, it is known that they are < 2 nm in radius and extremely small nanoparticles tend to not yield concise XRD patterns [178, 179]. The synthesis was performed in a lighter alcoholic solvent, IPA, which can contribute to a failed wurtzite structure [56]. It is also possible that silane shell induces strain on the crystal structure, altering the XRD pattern [165, 180]. To test if the growth conditions used allows for the formation of larger quantum dots with the expected XRD pattern, a small batch was produced using identical conditions without any capping agent. This resulted in nanosized ZnO, which was found to be photoluminescent, emitting green visible light. An XRD was performed on this material and it was found that its spectra matched JCPDS 36-1451 perfectly. This result shows that the utilized synthesis method does produce wurtzite zinc oxide crystals. The capping agent, which limits particle growth and Ostwald ripening, causes the XRD spectra to be less distinguishable as shown in Figure 20.

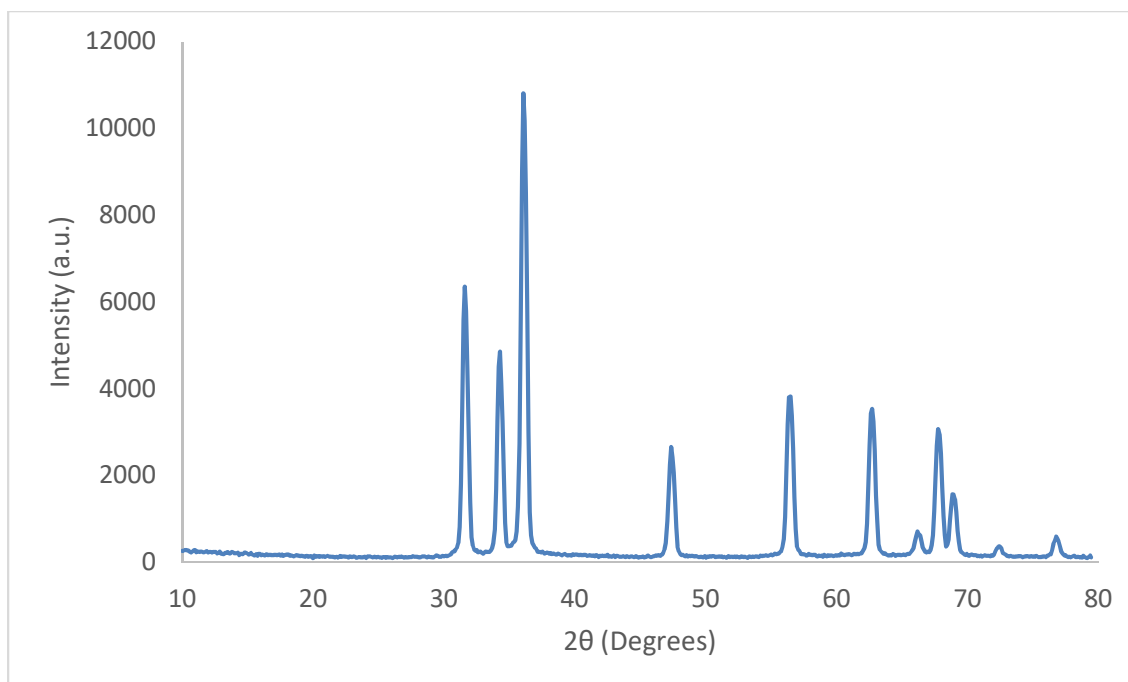


Figure 20: XRD spectrum of uncapped ZnO quantum dots. 100, 002, and 101 peaks are evident. This spectrum closely matches the one presented in JCPDS 36-1451.

3.3.6 Scaled-up purification of VTS-ZnO quantum dots via centrifugation

The purpose of making large batches of ZnO is to help drive this useful nanomaterial to widespread commercial applications [167]. However, producing the quantum dots economically and cheaply is only one of the issues facing this technology. Another is the tendency of the nanocrystals to agglomerate. Due to their extremely high surface area to volume ratio, nanomaterials tend to aggregate together. The added silane shell helps mitigate this issue [23]. Another major issue is the purification of nanomaterials. ZnO quantum dots need to be purified to acceptable levels. As excess NaOH is used in this reaction, removing that strong base is required, as the presence of a strong base could be detrimental to any commercial applications of the QDs [181]. The samples that were characterized in this study so far were purified using dialysis tubing and solvent exchange, which is not a scalable method. Solvent consumption is often a major issue with nanomaterial purification [172], as well as the cost of the dialysis tubing, and the time it takes for each dialysis stage. One method used regularly is centrifugation. As

described in the methods section, large samples (~10 g) of the large batch VTS-ZnO were centrifuged in methanol to remove the polar reagents and side products (NaOAc and NaOH). The vinyl silane capping agent present gives the quantum dots a more hydrophobic nature, allowing them to pellet easier in the spin. The samples were spun, the supernatant removed, washed with methanol, and spun again. This process was repeated until the ZnO was relatively pure. The collected samples were dried and analyzed by ICP for purity; the ratio of sodium to zinc was used to determine the remaining sodium-containing compounds. Table 13 indicates the ratio following the centrifugation cycles.

Table 13: Change in sodium:zinc ratio after centrifugation and washing cycles.

# of Cycles	0	3	5	6
Na ⁺ /Z ²⁺ n Ratio	1.4	0.016	0.012	0.045

It appears that the samples are relatively clean after three centrifuge cycles. It has been previously shown that the majority of precursors and side products are removed after the first purification cycles [150]. There is little change between the third and fifth cycles. However, after six cycles the ratio of Na/Zn starts to rise again, indicating at this point the sodium-containing compounds – either residual NaOH or byproducts – are adsorbed to the nanoparticles [39] and cannot be removed with this type of purification. As well, the amount of ZnO begins decreasing during the spin cycles. It can be beneficial to have residual precursors and side products adsorbed to the QDs they help passivate the surface, stabilizing them, and hindering agglomeration [150]. Therefore, centrifuging the vinyl silane-capped ZnO quantum dots in methanol is an appropriate solution for purifying on the large scale. Five cycles of washing and centrifugation appears to be optimal, with minimal amount of sodium detectable, and no ZnO is lost.

3.4 Conclusion

It has been shown that it is possible to synthesize large quantities of zinc oxide using a large volume sol-gel using a basic alcoholic system. 115 g of zinc acetate dihydrate was used, which underwent a 99% efficient reaction to yield over 50 g of zinc oxide quantum dots. These dots were synthesized with an *in situ* capping reaction so they were capped

with silane shells. The silane shell's presence was confirmed with XPS and blueshifts the QDs' visible emission. It also has been shown that centrifugation is an excellent tool for the purification of large quantities of silane-capped zinc oxide nanoparticles.

Chapter 4

The effect of different siloxane capping agents on the mechanical properties of transparent zinc oxide-ethylene vinyl acetate copolymer nanocomposites

ABSTRACT

In the field of nanotechnology, it is important to determine how capping a nanoparticle with a particular ligand can affect the material properties of the resulting composite. In this study five siloxane agents – 3-aminopropyltriethoxysilane, 3-mercaptopropyltrimethoxysilane, triethoxysilane, vinyltrimethoxysiloxane, and phenyltrimethoxysilane – were used to cap zinc oxide quantum dots and determine their effects on a polymer nanocomposite's material properties. The results showed that the silane vinyltrimethoxysiloxane (VTS) gave to greatest positive change in material properties. Its effect on an ethylene-vinyl acetate nanocomposite was tested in subsequent UV and thermal aging. The addition of the siloxane shell had a positive effect on the stability of the nanocomposite, but only at low concentrations by weight. Above 1 % by weight, it was found that the presence of the quantum dots had detrimental effects of material properties, likely due to nanoparticle aggregates acting as stress concentrators. The VTS ligand was also tested to determine its effect on the thermal stability and UV-accelerated weathering of the nanocomposite.

4.1 Introduction

Polymers are widely used materials in technology and construction due to their excellent mechanical properties, which can be customized by various treatments including chemical doping, heat treatment, and the addition of filler materials [5]. The addition of nanosized particles, also known as fillers, makes the nanocomposite materials attractive due to enhanced material properties (mechanical, thermal, chemical, etc.) gained even at low filler concentrations [94]. One such material is zinc oxide (ZnO) which has a large band gap (3.37 eV), a large exciton binding energy (60 meV), and a radiation hardness to make it ideal as a UV absorbing material [8]. Furthermore, ZnO is transparent to visible light, nontoxic, cheap, and chemically stable in the atmosphere [7]. ZnO readily absorbs UV light and transmits in the UV range [21] in the bulk form. Nanosized crystals of ZnO, below its Bohr radius, undergo quantum confinement, absorb light in the UV range, then downshift it to a lower wavelength and emit it in the visible range [22]. This visible light transmission is tunable with the size of the individual quantum dots [182]. However, it must be noted that the quantum yield of ZnO quantum dots, i.e. the amount of energy emitted compared to that absorbed, decreases with increasing crystal size [24]. The photoluminescence of ZnO can be diminished by agglomeration [132] and surface deactivation via interaction with water [61].

The primary reason that the ZnO is used compared to other nanoparticles is its ability to absorb UV light and downshift it to visible light to increase the quantity of light within a greenhouse. The positive effects of UV downshifting on greenhouse production have been shown with organic dyes [119]; however, organic dyes lack the photostability that quantum dots possess [125]. The capping of the quantum dots with oxygen-containing ligands shifts the emission into the blue region, which is one of the preferred ranges for the efficiency of plants' photosynthesis [183]. The presence of silane capping agents also decreases the nanoparticle core's size, increasing the band gap and subsequently blue-shifting the visible emission [160]. ZnO particles within greenhouse film also give a high UV shielding, helping to mitigate UV damage to polymer films [96].

Due to their extremely small sizes, quantum dots (QDs) possess very high surface to volume ratios, which imparts significant surface energy leading the particles propensity to agglomerate to minimize this energy. Preventing agglomeration becomes inherently more difficult when the nanoparticles have a diameter of less than 50 nm [55], but the use of capping agents as ligands decrease the surface energy and decrease tendency to aggregate [53]. Capping agents create a shell around the quantum dot core, which also protect the QDs from environmental effects that can quench their fluorescence [60]. The capping agents can also promote long term stability [171] and increase the fluorescent yield [184]. A wide variety of different capping agents have been liganded to ZnO, including: dodecylamine [8], oleic acid [49], 3-(trimethoxysilyl)propyl methacrylate [58], (3-(2,3-epoxypropoxy)propyl)trimethoxysilane [23], aminopropyltriethoxysilane [11], polyvinyl alcohol [59], and poly(N-vinylpyrrolidone) [51]. It is important to note that the capping agents themselves can affect the emission properties of the quantum dots. For example, capping ZnO with dodecylamine can quench visible emission with no effect on the UV emission [8]; while capping with oleic acid shifts the green emission into the blue region of the spectrum [49]. Organosiloxanes are attractive capping agents which add stability, hydrophilicity, and are present with many different potential side chains that can be chosen for desired characteristics, and they can also be covalently bonded to the surface of the ZnO nanoparticles under mild conditions [11]. These siloxanes will be examined in this work to form a silane shell around the ZnO quantum dots, which will then be melt-mixed with ethylene-vinyl acetate polymer (EVA) to form nanocomposite optically transparent films. These ZnO-EVA composites can be used for the construction of smart greenhouse film coverings and other solar applications. EVA copolymer is a commonly used optically transparent polymer used in greenhouse and other solar applications [96]. However, as the polymer ages under exposure to UV light, heat, and humidity, it is prone to mechanic degradation over time and requires frequent replacement [185]. The inclusion of metal oxide nanoparticles has been shown to increase the stability of the EVA films [96]. The presence of nanosized ZnO in polymers has been shown to increase the tensile strength of polymers, albeit with a decrease in elasticity [97]. The strengthening has been reported to be enhanced with smaller particles

[104], but it is generally found that low concentrations enhance mechanical properties, while concentrations above 1 % weight tends to show a decrease in strength [186]. The purpose of this work was to examine how the presence of a ZnO filler in ethylene vinyl acetate (EVA) copolymers affects the composite's mechanical properties. These films will be used to produce large polymer sheets, so tensile strength is vital. However, the effects of different capping agents on the material properties of a nanocomposite is a subject that has received little attention in previous studies. Five different alkylsiloxanes – 3-aminopropyltriethoxysilane, 3-mercaptopropyltrimethoxysilane, triethoxysilane, vinyltrimethoxysilane, and phenyltrimethoxysilane – were examined as capping agents, each with a different functional group side chain. The composite composition with the greatest strength was further tested for its thermal stability and its strength after accelerate weathering.

4.2 Experimental

4.2.1 Materials

Zinc acetate dihydrate ($\text{Zn}(\text{OAc})_2 \cdot 2\text{H}_2\text{O}$) and sodium hydroxide (NaOH) were obtained from Sigma-Aldrich, Canada. Anhydrous ethanol (EtOH) for the reaction was supplied by Commercial Alcohols. The alkylsiloxanes used – 3-aminopropyltriethoxysilane, 3-mercaptopropyltrimethoxysilane, triethoxysilane, vinyltrimethoxysilane, and phenyltrimethoxysilane – were also supplied by Sigma-Aldrich. Ethylene vinyl acetate copolymer (EVA) was supplied by DuPont (Elvax 660). All chemicals were used without further purification.

4.2.2 ZnO quantum dot synthesis

The synthesis of ZnO QDs used in this work was based on the method described by Bang et al [32], modified to include siloxane capping reactions. ZnO QDs synthesized in basic alcoholic sol-gels tend to have dangling hydroxide functional groups, which are attractive targets for capping agents [58]. This results in a QD with a ZnO core and a shell of siloxanes as depicted in Figure 21.

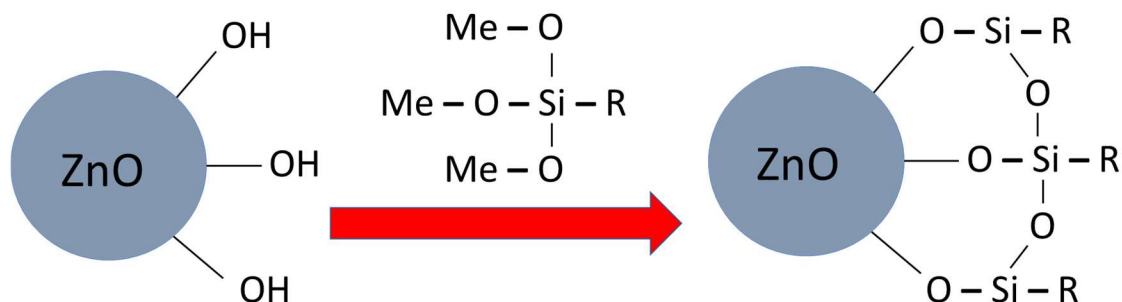


Figure 21: Model of siloxane shell on ZnO nanoparticles. The hydroxides and linked to the methoxide groups on the siloxane via a base-catalyzed condensation reaction. A siloxane shell is formed linking when the siloxanes also link to each other, yielding a structure with the ZnO at its core and the R side chains being presented to the outside environment.

In short, zinc acetate dihydrate (0.46 g) was mixed into 30 ml of anhydrous ethanol and sonicated at 65°C for one hour, and then cooled in an ice bath. One milliliter of alkylsiloxane capping agent was added at this point. Sodium hydroxide (0.2 g) was dissolved in 10 ml of anhydrous ethanol, cooled in an ice bath, and then added to the zinc acetate solution dropwise. The reaction proceeds for one hour in the ice bath with magnetic stirring, then the product was collected and dried in a vacuum oven at 60°C for at least 24 hours. The resulting powder was dissolved in minimal methanol and purified via dialysis with methanol (MWCO of 1 KDa, Spectra/Por® 6 Standard RC pre-wetted Dialysis Tubing, diameter 29 mm). The purified product was dried in the vacuum oven and the quantum dots collected for further analysis and testing. Five different samples were synthesized, each with a different capping agent: 3-aminopropyltriethoxysilane, 3-mercaptopropyltrimethoxysilane, triethoxysilane, vinyltrimethoxysiloxane, and phenyltrimethoxysilane (Figure 22). The ZnO quantum dot samples were respectively termed: amino, mercapto, TEOS, VTS, and phenyl.

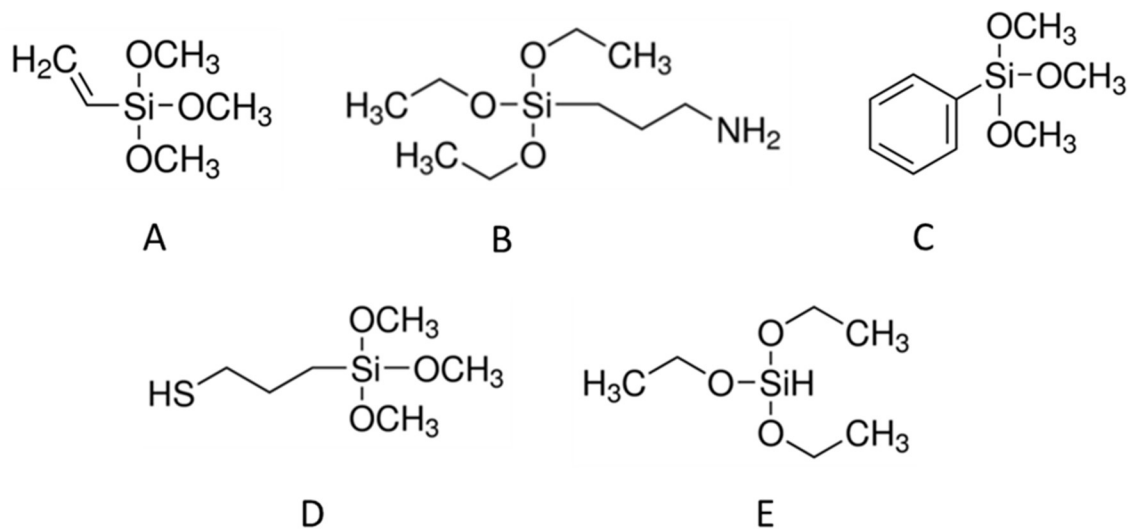


Figure 22: Structures of the siloxanes used in this study. They are vinyltrimethoxysilane (A), 3-aminopropyltriethoxysilane (B), phenyltrimethoxysilane (C), 3-mercaptopropyltrimethoxysilane (D), and triethoxysilane (E).

4.2.3 Characterization of ZnO quantum dots

The confirmation of the alkylsiloxane capping ligands was accomplished using a Nicolet 6700 FTIR spectrometer equipped with a smart iTR diamond horizontal attenuated total reflectance (ATR). Pure, uncapped ZnO nanoparticles were used to background the instrument to emphasize presence of siloxane sidechains. The photoluminescence of the samples was measure using a PTI Quantamaster 50 spectrofluorometer; with their sizes estimated from their maximum excitation using the Brus equation. High-resolution transmission electron microscopy (HR-TEM) was used to confirm the size of the VTS-ZnO QDs estimated using the Brus equation. The HR-TEM image was obtained by dispersing a nanoparticle sample in ethanol and dropping them onto a copper grid. They were then imaged using a Zeiss Libra 200MC TEM and used to confirm the size. The thermal degradation of the VTS-capped nanoparticles was evaluated by thermogravimetric analysis (TGA), which was performed using a Q600 TGA (TA Instruments) from 0°C to 800°C at a heating rate of 20°C/min under an air atmosphere.

4.2.4 Nanocomposite production

The ZnO quantum dots were incorporated into an EVA polymer nanocomposite using a Thermo Scientific HAAKE Mini-Lab II Twin Screw at 140°C, 90 rpm and 10 minutes residence time before extrusion. Two different quantum dots loadings were used for each ligand – 1% weight percent (wt/wt) and a 2.5% weight percent (wt/wt). For the 1% samples, 4.405 g of EVA pellets (Elvax 660, DuPont) were melt mixed with 0.045 g of silane capped ZnO. For the 2.5% samples, 4.3875 g of EVA pellets were melt mixed with 0.1125 g of silane capped ZnO. The extrudate was pressed into circular films for analysis using a Universal Film Maker (ThermoFisher). The dimensions of the pressed films were 2 cm in diameter and 250 μm in thickness. The nanocomposite was also pressed into bars (1 cm x 0.2 cm x 12 cm) for DMA analysis using a hot press and aluminum molds.

4.2.5 Determination of nanocomposite material properties

Characterization of the polymer samples was done in accordance with ASTM D790M-92 using a dynamic mechanical analyzer, DMA Q800 (TA Instruments). The DMA was run in single cantilever mode, a 1 Hz, and a temperature ramp from -50°C to 45°C. From this, the storage modulus, the loss modulus, and the damping factor ($\tan \delta$) was obtained over this temperature range. The tensile properties were measured using a 5943 Universal Testing machine (Instron) equipped with a 500 N load cell. The samples were tested using ASTM D882 as a guide; with the polymer pressed into film samples 250 μm thick and 14 mm wide. For each polymer, a minimum of five (5) independent specimens were tested at a pulling speed of 1 mm/min. Young's modulus was determined by the slope of the linear portion of the stress strain curve, tensile strength was defined as the maximum stress applied prior to failure, and tensile strain was the maximum extension of the material prior to breaking. The composite that showed the greatest increase in mechanical properties was chosen for further characterization.

The stability of the VTS-ZNO nanocomposites were tested under accelerated UV aging conditions. 5 nanocomposite and 5 reference samples were exposed to weathering conditions for a total of 300 hours. The aged samples were tested in accordance to UNE-

EN ISO 4892-2:2006. These were aged in an accelerated weathering chamber with elevated temperature, humidity and exposure to UV light, then their tensile properties were subsequently analyzed. The settings on the weathering chamber were 40°C, 100 % relative humidity, and 25 $\mu\text{mol}\cdot\text{s}^{-1}\cdot\text{m}^{-2}$. The thermal stability of the nanocomposite was evaluated thermogravimetric analysis (TGA), which was performed using a Q600 TGA (TA Instruments) from 20°C to 900°C at a heating rate of 10°C/min under an air atmosphere.

4.2.6 Optical measurements for UV-VIS transmission and dispersion

The dispersion of the quantum dots in the polymer was visualized using a Zeiss LSM 510 multichannel point scanning confocal microscopy. A small piece of the vinyl capped nanocomposite film, 250 μm thickness, was used for imaging. The quantum dots were excited using UV photoactivation, with the visible light emissions observed in the resulting images. To obtain the visible light transmission of the film, a Shimadzu UV-3600 spectrophotometer was used. The 1% (wt/wt) films of each type of capping agent were analyzed in this manner.

4.3 Results and discussion

4.3.1 ZnO quantum dot size estimates

Table 14: Photoluminescent properties and size estimates of silane-capped ZnO quantum dots.

Capping Agent	Max Excitation (nm)	Max Emission (nm)	Radius (nm)
VTS	310	465	1.8
TEOS	312	470	1.8
Phenyl	309	462	1.8
Mercapto	316	477	1.8
Amino	315	475	1.8

The size of the quantum dots was estimated using the Brus equation [148]. The size can be approximated by:

$$E^* \cong E_g^{bulk} + \left(\frac{1}{m_e^* m_0} + \frac{1}{m_h^* m_0} \right) - \frac{1.8e^2}{4\pi\epsilon\epsilon_0 r} - \frac{0.124e^4}{h^2(4\pi\epsilon\epsilon_0 r)^2} \left(\frac{1}{m_e^* m_0} + \frac{1}{m_h^* m_0} \right)^{-1}$$

Equation 2: Effective mass model

where E_g^{bulk} is the bulk band gap, h is Planck's constant, r is the particle radius, m_e^* is the effective mass of electrons, m_h^* is the effective mass of holes, m_0 is the free electron mass, e is the charge on an electron, ϵ_0 is the permittivity of free space, and ϵ is the relative permittivity. Using values of 3.4 eV for the bulk band gap, 0.24 for the effective mass of electrons, 0.45 for effective mass of holes, and 3.7 for relative permittivity, this equation can be used to estimate the particle sizes from the excitation maximum [148]. The excitation and emission maxima are shown in Table 1. From this, we determined that the nanoparticles used in this study were all 1.8 nm in radius and emit in the blue region. Their small size is due to their extremely basic growth conditions [21] and the presence of a capping ligand during synthesis [49].

4.3.2 Confirmation of ligand attachment

The purified quantum dots were analyzed using IR analysis in ATR mode to confirm the successful capping of the quantum dots. The nanoparticles were capped during synthesis which leads to a higher density of capping agent and helps limit the particle growth [171]. The samples were run using uncapped ZnO to blank the instrument to eliminate any peaks from that material. The resulting spectra are shown in Figure 23. It is evident that each of the spectra are different from each other, confirming the presence of different functional groups on each of the samples. Furthermore, characteristic peaks were observed in the samples' IR spectra [187]. The major peak present in each of the samples is a large one centered at 1000 cm^{-1} which is characteristic for the Si-O bond. The spectrum for the VTS sample (A) shows peaks for C=C stretching at 1475 and 1600 cm^{-1} , as well a peak at 3010 to 3100 cm^{-1} for the =CH stretch. The spectrum for the TEOS sample (B) contains no organic bonds and therefore no peaks are readily identifiable. The phenyl sample (C) shows the C=C stretch at 1475 and 1600 cm^{-1} , as well as a C-H stretch from 3000 to 3020 cm^{-1} . The mercapto sample (D) shows C-H peaks throughout,

and it also shows the weak peak at 2560 to 2590 cm^{-1} that is characteristic for S-H stretching. This peak has a weak intensity due to the small dipoles between the C-S and S-H bonds. The amino sample (E) contains the broad N-H stretching peaks at 3300 to 3500 cm^{-1} and a peak at 1500 to 1640 cm^{-1} arising from N-H bending. The unique spectra obtained for each sample, coupled with the presence of characteristic IR peaks, confirms that each different ligand was present in the samples.

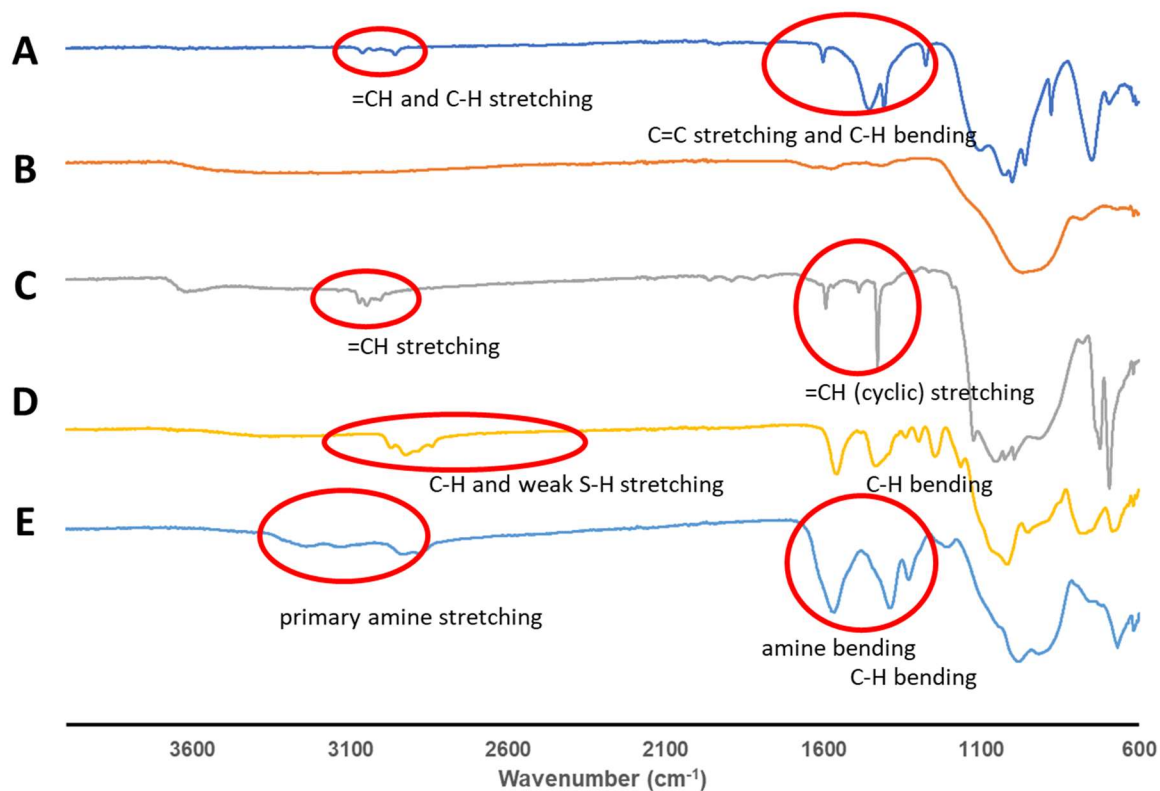


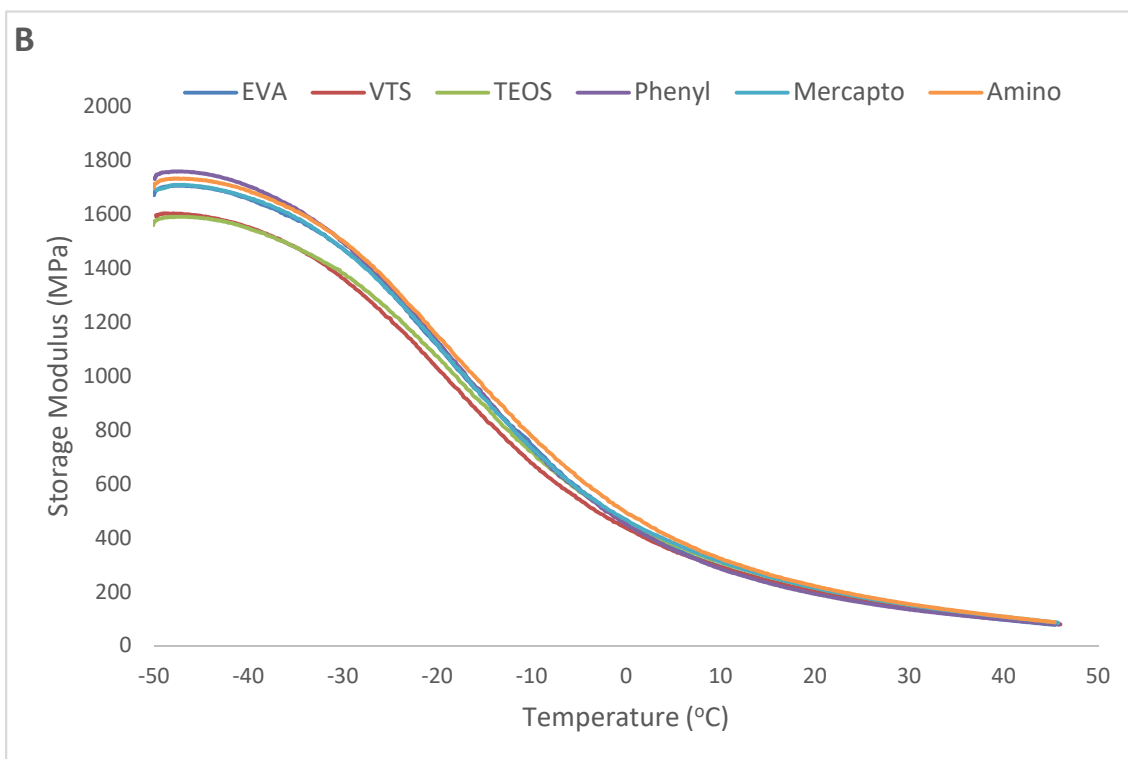
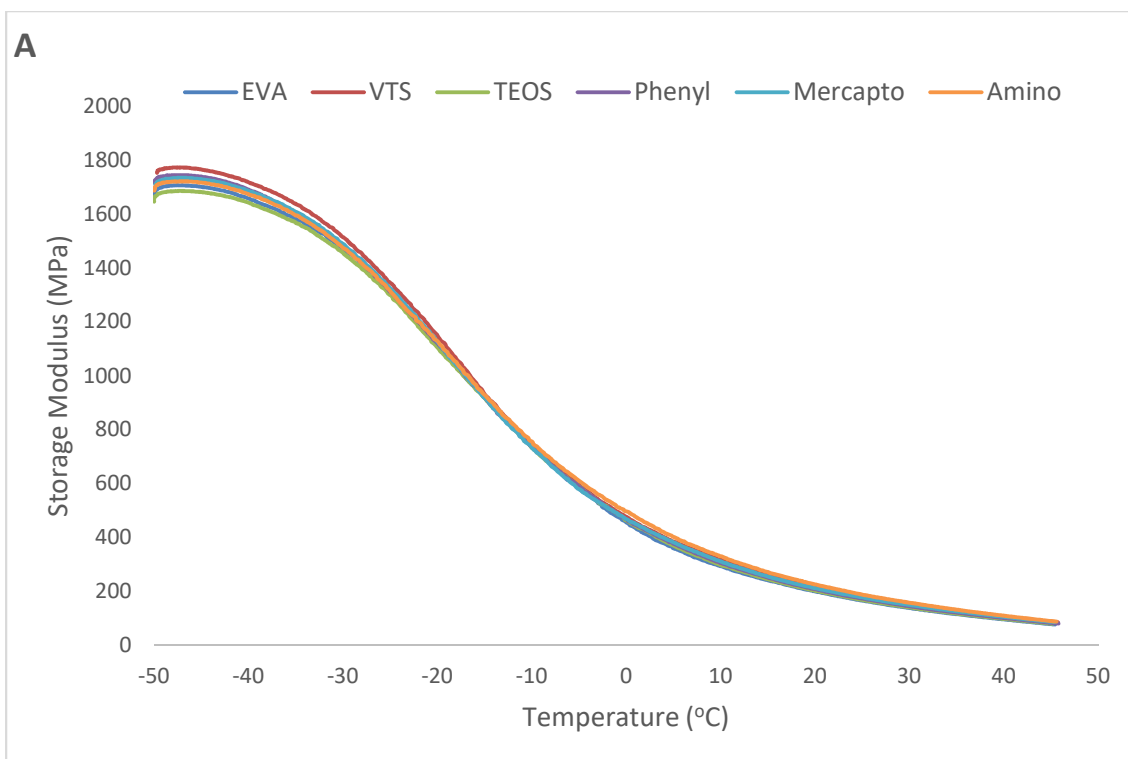
Figure 23: FTIR spectra of the five differently capped QD samples. From the top to bottom they are: VTS (A), TEOS (B), phenyl (C), mercapto (D), and amino (E) silane capped quantum dots.

4.3.3 Dynamic mechanical analysis of nanocomposites

Dynamic mechanical analysis (DMA) measures the stiffness and dampening properties of a material [188]. The relationship between storage modulus and temperature is shown in Figure 24. Storage modulus is an indication of the maximum amount of elastic energy stored in a material during one round of oscillation. This also gives a measure of the

stiffness and load capability. The nanocomposite samples were found to have a lower storage modulus than the reference sample, with the higher weight percentage samples showing a greater depression of their moduli. A lower storage modulus is indicative of greater interaction between a nanoparticle filler and the polymer chains [98]. From the samples loaded with 1% (w/w) filler (Fig 23a), the TEOS sample shows the largest effect at low temperatures (-50°C), with the rest of the additive samples being similar.

However, as the temperature increases, this difference is diminished and at the highest temperature tested (50°C), there are no differences between the samples and the reference polymer. A much greater disparity is present in the higher percentage samples. Again, when the samples are in the cold region, the reference samples had a significantly higher storage modulus than the others. The TEOS sample is once again one of the lower curves, but the vinyl sample is similarly depressed. As the temperature increases, the differences between the moduli do decrease; however, in this case, the reference is also higher than the nanocomposite samples. Even at the higher temperatures tested, the 2.5% vinyl nanocomposite shows a lower modulus than the others. The storage modulus is sensitive to a number of parameters such as molecular weight of polymer chains, cross-linking, and interfacial bonding between filler and polymer [98]. The depression of the storage modulus indicates that nanoparticles are interacting with polymer chains with the TEOS and vinyl samples having the strongest interactions. These results suggest that the VTS and TEOS capped quantum dots would contribute more to the material properties of a composite in cold weather, such as is experienced in northern climates.



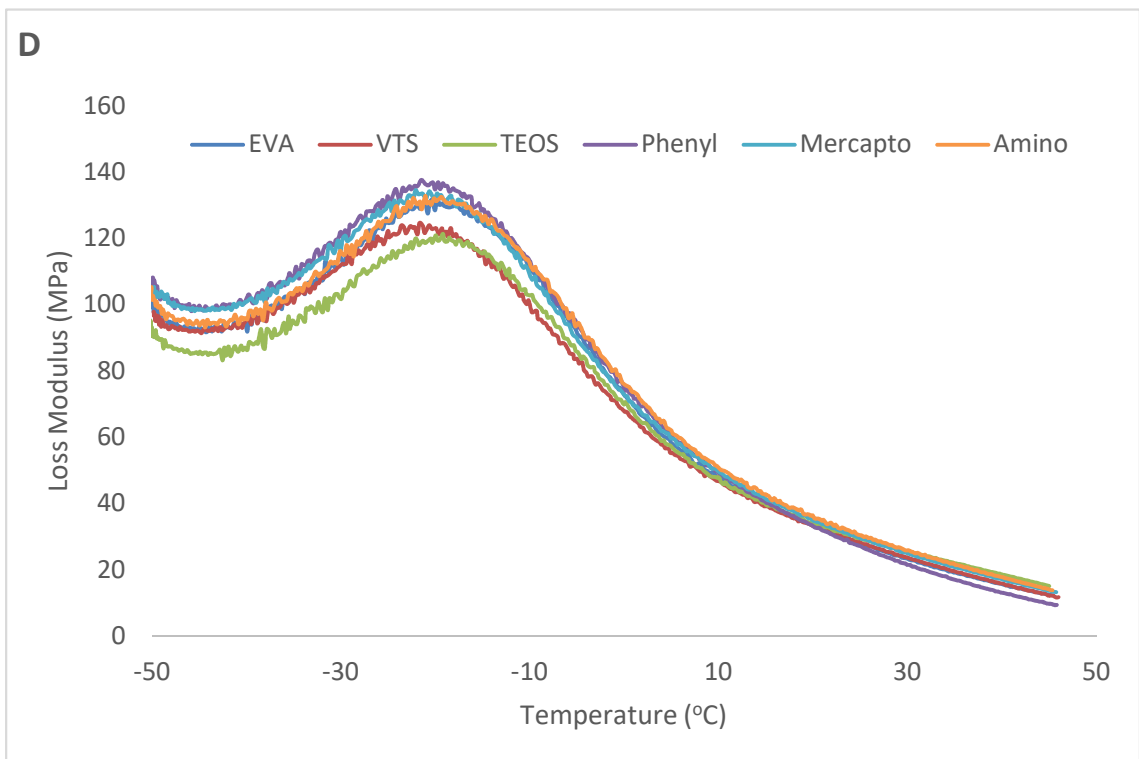
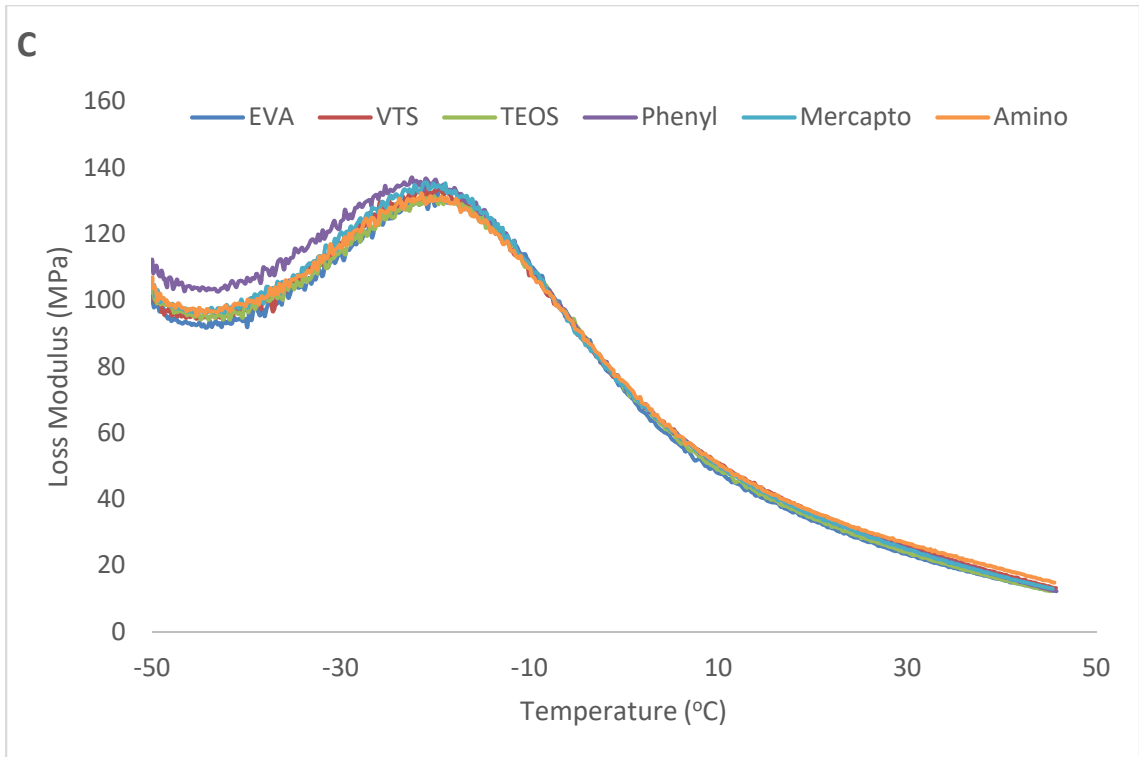


Figure 24: DMA analysis of storage modulus vs. time for (a) 1% (wt/wt) nanocomposites and (b) 2.5% (wt/wt) nanocomposites, c/d) DMA analysis of loss

modulus vs. time for (c) 1% (wt/wt) nanocomposites and (D) 2.5% (wt/wt) nanocomposites.

Figure 24c/d depicts how the loss modulus is affected by the presence of the ZnO QDs. The loss modulus is a measure of how much elastic energy is lost as heat and is sensitive to the motion of the polymer chains [188]. A similar pattern is observed with this modulus as before: the reference polymer sample had the largest loss modulus while the nanocomposites were all lower. This indicates that the polymer chains within the nanocomposites had their individual motion restricted, likely due to interfacial bonding and particle cross-linking. The TEOS sample showed the largest depression of the modulus at both tested concentrations. At 2.5 % weight filler, the vinyl composite also shows a significant decrease compared to the other samples. The decrease in the loss modulus could be due to filler restricting motion of polymer chains [98]. This would suggest that the TEOS and vinyl ligands interact significantly with the polymer chains, in agreement with the behavior observed with the storage modulus.

The ratio between the storage and loss modulus, the damping factor, of the nanocomposites is shown in Figure 25. The damping factor, $\tan \delta$, is related to the degree of molecular mobility of the filler within the polymer matrix [188]. It can also be a further indication of the degree of interfacial bonding between the filler and polymer [189]. As expected, the reference polymer sample showed the lowest damping at low temperatures indicating that the addition of the nanoparticles all decreased the viscoelasticity of the polymer. However, as the temperature increased, the $\tan \delta$ curves are similar; except the phenyl sample, which is higher at both concentrations. A lower damping curve can also be an indication of the interaction between the polymer and the nanoparticles [189], indicating that the phenyl is not decreasing elasticity via interfacial interactions. It is possible that the bulky phenyl group sterically hinders the ability of the polymer chains to slide past each other. The glass transition temperatures of the polymer samples can also be determined from this chart and are shown in Table 2. These changes also indicate that the polymer chain relaxation events are being affected by the presence of the particles [132]. It is observed that the phenyl sample, which had the highest $\tan \delta$, glass transition temperature is most depressed, likely due to the mentioned steric

hindrance limiting the mobility of the polymer chains. The vinyl and TEOS samples, which showed the lowest loss moduli, increased the glass transition temperature.

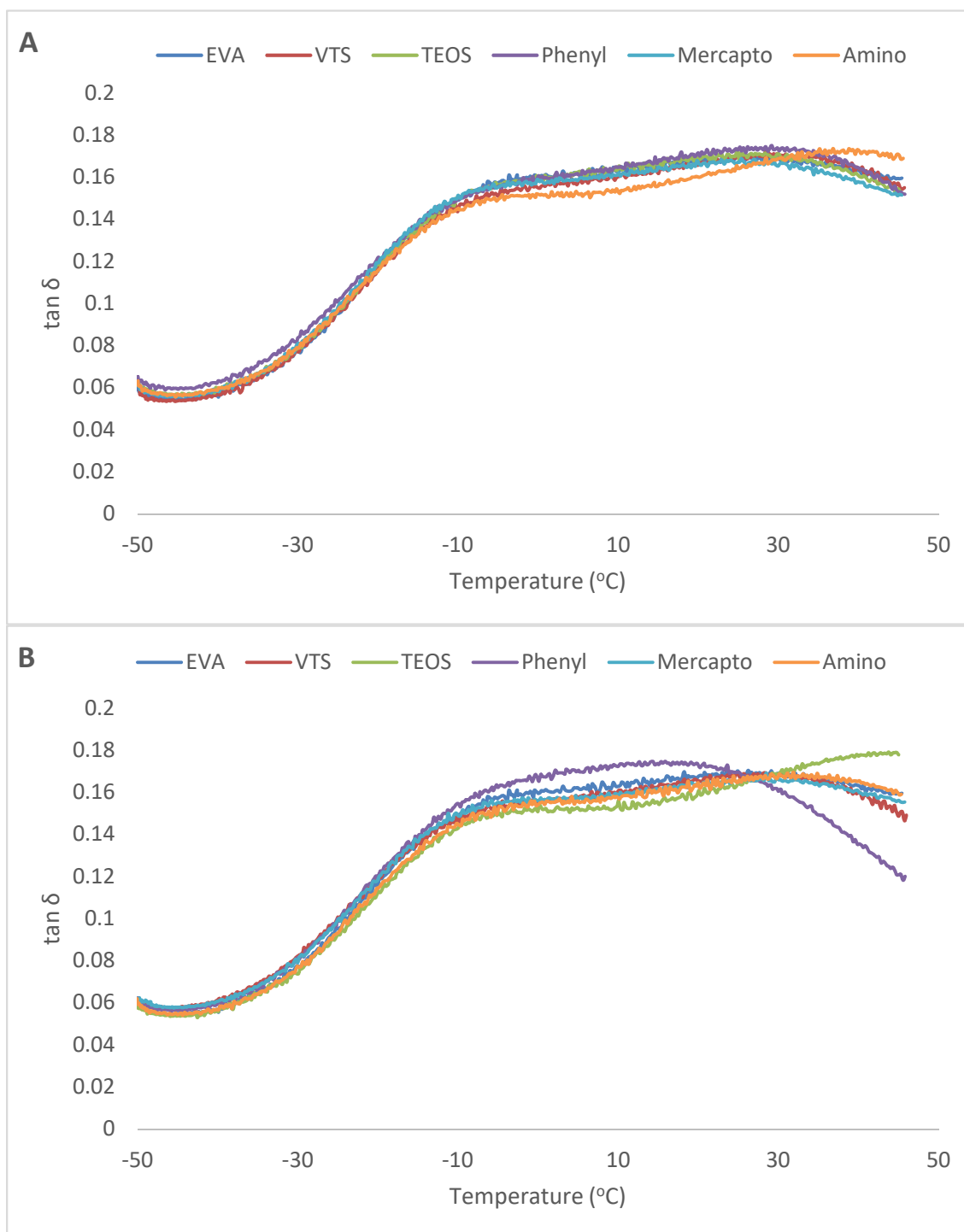


Figure 25: DMA analysis of $\tan \delta$ vs. time for (a) 1% (wt/wt) nanocomposites and (b) 2.5% (wt/wt) nanocomposites.

4.3.4 Tensile testing on nanocomposites

The results of the tensile testing are shown in Table 15. The presence of some of the QDs have a negative effect on the tensile properties, even at the relatively low 1 % loading used. It has been reported that low concentrations of fillers should increase the tensile strength [104] but show decrease in elasticity [72]. The nanoparticles interact with the polymer chains, crosslinking to prevent them coming apart under load; however, the same linking hinders their elastic properties but limiting the local matrix flexibility [97]. The samples that showed a positive effect on tensile strength were the 1 % vinyl, 1 % mercapto, and 1 % TEOS. The vinyl capped nanoparticles showed the greatest increase in tensile strength, approximately 15 % relative to the pure polymer. The dispersion of filler particles within the polymer matrix is influenced by the strength of their interactions to the polymer chains [190, 191] and it has been shown [192] that additives' functional groups that are similar to the polymer structure interact more strongly. The vinyl moiety of the vinyl siloxane ligand interacts favorably with the vinyl portions of the EVA polymer, which was also reported by Lopez et al [190]. The 1 % vinyl sample also possessed the lowest Young's modulus of the 1 % by weight samples, further indicating that it was interacting the polymer chains. The mercapto can be considered to mix well with the polymer chains due to its non-charged, alkyl-like sidechain. The TEOS capped QDs show a small improvement in tensile strength and might act like a crosslinking agent. The amino capped nanoparticles present a hydrophilic exterior to the composite and would create a mismatch with the more hydrophobic EVA used. An EVA polymer with a higher vinyl acetate percentage would likely interact more favorably with that particle. The phenyl capped quantum dots show the lowest tensile strength, likely due to the steric size of the bulky phenyl moieties [191]. One reason that the presence of the QDs is negatively impacting the tensile strength is agglomeration. Smaller particles, like the ZnO quantum dots used in this experiment, tend to agglomerate more and be tougher to dissociated even with melt mixing [189]. The agglomeration of the particles reduces the effective interfacial interactions [94] and can also act as local stress concentrators [100] weakening the nanocomposite. The agglomerations were more significant at the 2.5 % weight loadings, which could explain that the samples showed decreased properties compared with the lower concentration samples. A similar effect was noted [94] showing

that the maximum tensile strength increase in a ZnO-polypropylene composite was found to be at 1.5 % loading, but tensile strength decreased with higher concentrations.

Table 15: Tensile properties on silane-capped nanocomposites.

Sample	Young's Modulus (MPa)	Ultimate Tensile Stress (MPa)	Ultimate Tensile Strain (mm/mm)	*Glass Trans. Temp (°C)
Amino 1%wt	57.5 ± 1.7	6.7 ± 0.5	6.9 ± 0.6	-21.5
Amino 2.5%wt	48.8 ± 1.3	6.5 ± 0.6	6.5 ± 0.7	-21.0
Mercapto 1%wt	51.0 ± 1.5	7.0 ± 0.3	8.7 ± 0.4	-20.9
Mercapto 2.5%wt	53.2 ± 1.7	6.7 ± 0.4	7.6 ± 0.3	-22.1
Phenyl 1%wt	49.9 ± 1.6	6.5 ± 0.3	7.4 ± 0.5	-22.5
Phenyl 2.5%wt	45.8 ± 2.9	6.4 ± 0.4	7.7 ± 0.6	-21.5
TEOS 1%wt	46.1 ± 3.1	7.2 ± 0.4	9.0 ± 0.6	-20.1
TEOS 2.5%wt	52.8 ± 2.7	6.1 ± 0.2	6.4 ± 0.4	-19.2
Vinyl 1%wt	47.5 ± 2.7	8.3 ± 0.4	10.3 ± 0.4	-19.6
Vinyl 2.5%wt	50.2 ± 2.1	6.5 ± 0.2	7.0 ± 0.4	-21.7
Reference (EVA)	58.1 ± 6.8	7.0 ± 0.3	8.6 ± 1.0	-20.5

*glass transition temperature obtained from Figure 24

4.3.5 Characterization of VTZ-ZnO quantum dots

The vinyltrimethoxysiloxane-capped quantum dots were shown to have the greatest positive contribution to the material properties of EVA nanocomposites. These nanoparticles were selected for further characterization. To confirm their size estimate, the VTS capped quantum dots were imaged using HR-TEM and shown in Figure 26. The image shows the capped quantum dots, siloxane shell and ZnO core, were about 5 nm in diameter, so the core should be in the range of the estimated 3.6 nm diameter. The TGA analysis of the VTS QDs is shown in Figure 27. Two observations can be gained from

this graph. First, the sample only loses 13.41 % of its mass during the heating cycle. It has been reported that silane-capped ZnO undergoing such a heating will lose their sidechains but not the silica shell or ZnO core [160]. Therefore, the mass loss is solely due to the vinyl side chain; from this it can be estimated that the QDs are ~50 % ZnO by mass. Secondly, the DTG curve shows an extremely narrow rate of maximum change peak at 215°C indicating that the mass loss at that temperature is rapid [161] at that temperature, which could be a loss of adsorbed water while the siloxane vinyl sidechains degrade steadily from 235 to 600°C [39].

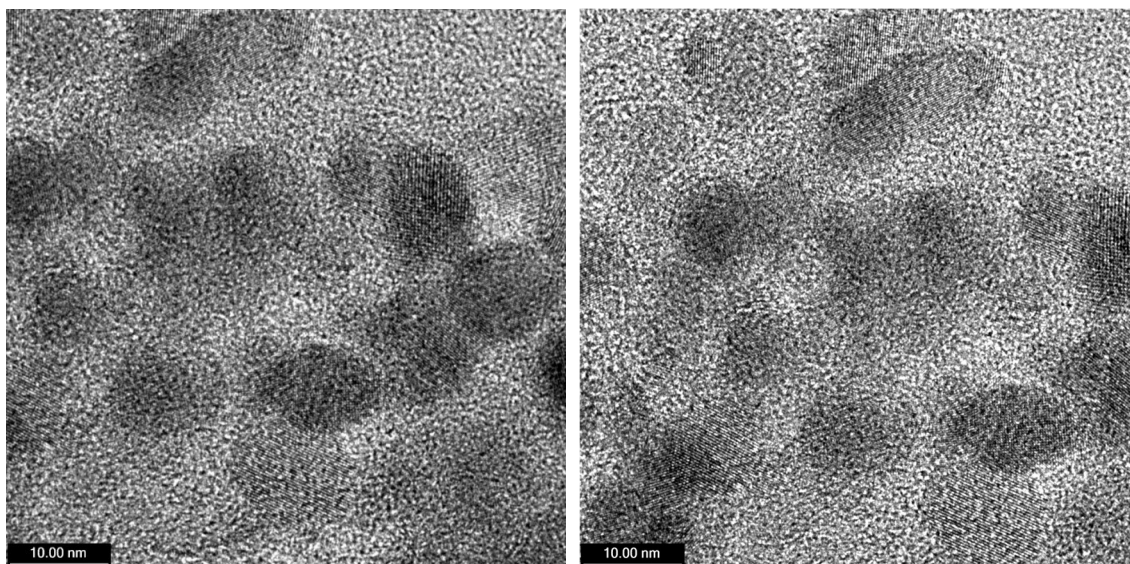


Figure 26: HR-TEM image of vinyl-capped ZnO nanoparticles. The cores of the quantum dots were calculated to be 3.6 nm in diameter.

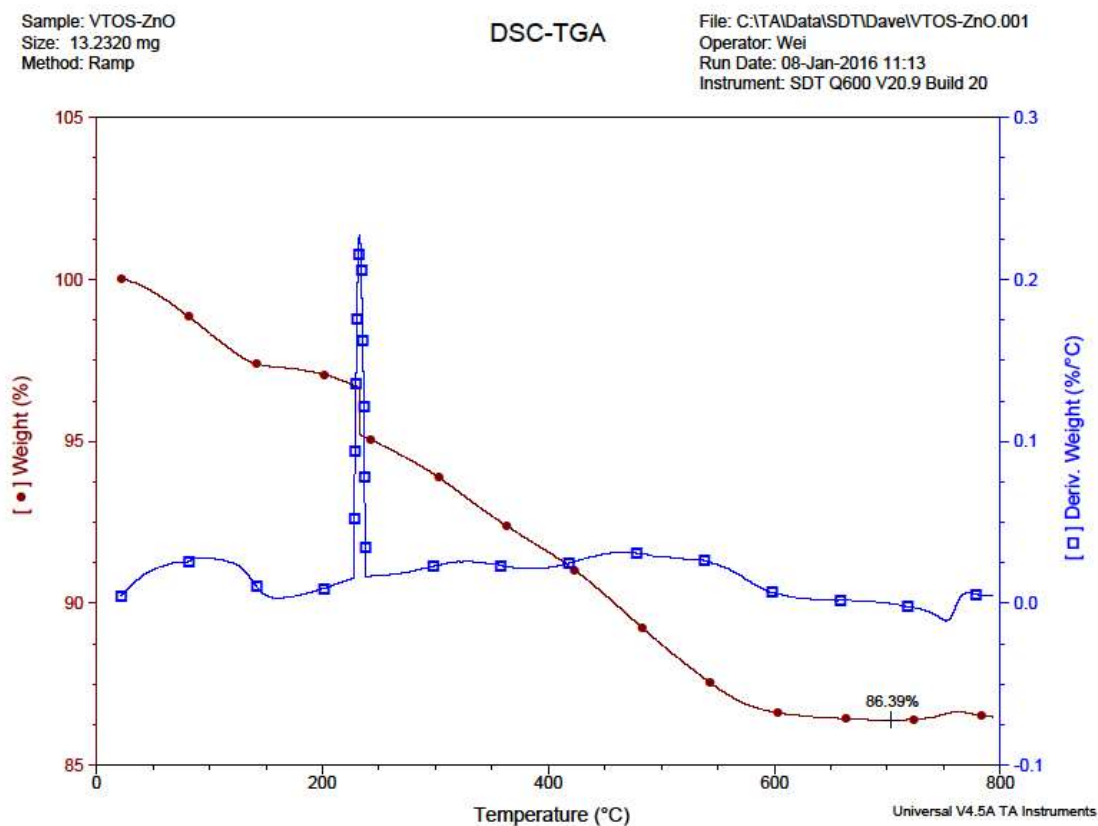


Figure 27: TGA analysis of vinyl capped ZnO. The final mass at 700°C is 86.39% of the sample remaining. ZnO and silane shells are stable at this temperature, so the lost mass comes from the alkyl side chains. From this, one can calculate the mass of the ZnO core in the quantum dots.

4.3.6 Effects of VTS-ZnO on stability of composite EVA films

4.3.6.1 Tensile testing of aged nanocomposites

As the VTS-capped ZnO particles were found to increase the composite strength the most, these were selected for further characterization. The effect of accelerated weathering on the tensile strength was evaluated using an accelerated weathering chamber which subjected the film samples, and reference polymer films, to UV exposure and damp heat. These conditions are well established to degrade EVA and that accelerated weathering has been shown to be comparable to years of environmental exposure [193]. The results of the weathering are listed in Table 16.

Table 16: Effect of VTS-capped ZnO quantum dots on the tensile properties of weathered ZnO:EVA composite films. Five replicates of each sample were aged and analyzed.

Sample	Aging Time (hr)	Young's Modulus (MPa)	Ultimate Tensile Stress (MPa)	Ultimate Tensile Strain (mm/mm)
EVA	0	58.1 ± 6.8	7.0 ± 0.3	8.6 ± 1.0
	150	45.0 ± 7.5	6.2 ± 0.5	8.3 ± 1.2
	300	35.0 ± 5.6	5.9 ± 0.6	6.3 ± 0.9
VTS-ZnO 1% (wt/wt)	0	47.5 ± 2.7	8.3 ± 0.4	10.3 ± 0.4
	150	46.3 ± 3.7	7.8 ± 0.7	8.1 ± 0.8
	300	42.0 ± 4.0	6.4 ± 0.8	7.5 ± 0.8

It was observed that the composites containing the vinyl quantum dots were much more stable than the reference sample. Similar behaviours were also noted in literature as noted by an increase in UV stability due the presence of uncapped ZnO quantum dots in EVA [96], in polymethacrylic acid [119], in polylactic acid [186], and in polypropylene [106]. Over the course of 300 hours in the chamber, the reference samples' average tensile strength was found to decrease almost 16 %, while the tensile strength of the nanocomposite decreased 20 %. However, the composite sample was found to have retain its tensile strength longer even with the aging. After 300 hours, it possessed a similar tensile strength as the EVA reference sample at 150 hours. A corresponding decrease in elasticity was also noted, with the Young's modulus for the reference sample dropping almost 40 %, while the nanocomposite saw only a 12 % decrease in its Young' modulus. This indicates that the quantum dot containing retains superior mechanical properties during the aging process.

4.3.6.2 Thermal stability of VTS-ZnO nanocomposites

The vinyl silane capped quantum dots showed the greatest tensile strength and weathering resistance when compared to other nanocomposites and the EVA-only samples. To further test the effect of these films, different vinyl capped ZnO-EVA composites were tested for their thermal stability using TGA analysis. The thermal

degradation of the EVA generally is a two-step process: first is deacetylation and acetic acid generation from the vinyl acetate moieties of the polymer; the second is a breakdown of the ethylene backbone [194]. Figure 28 shows the effect that different loading of the vinyl capped quantum dots has on the thermal stability of EVA.

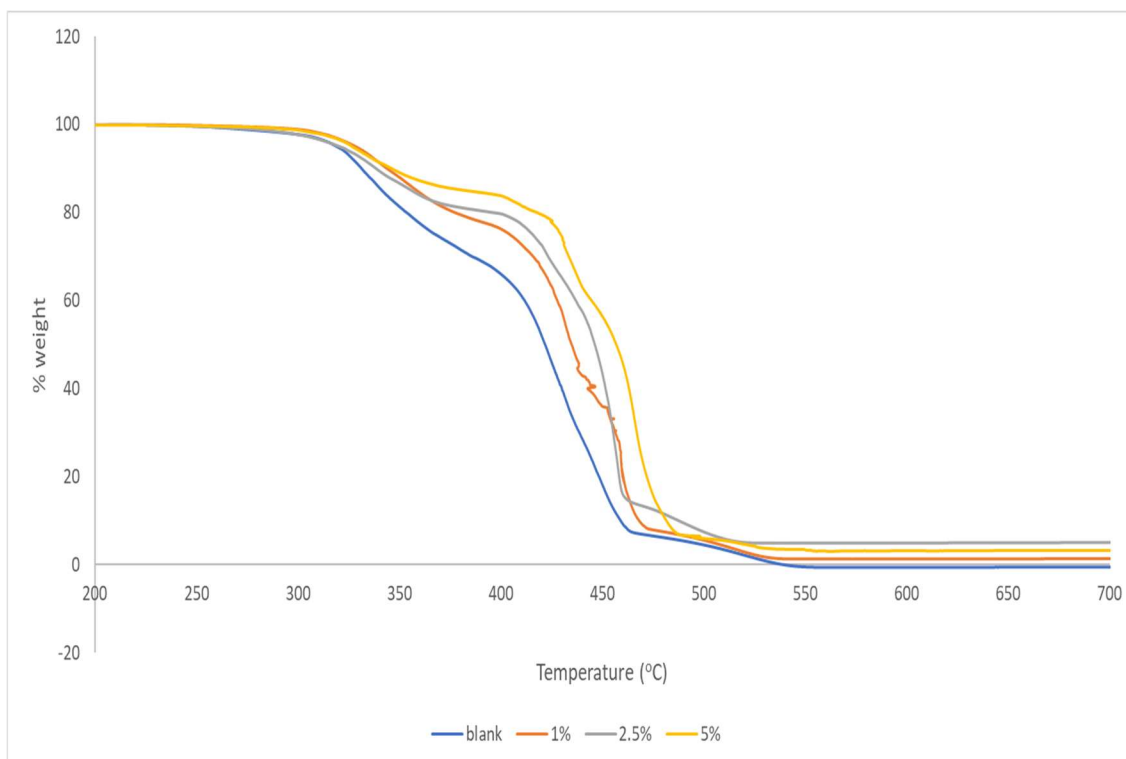


Figure 28: TGA breakdown of EVA nanocomposites. It is observed that the polymer becomes more thermally stable with the inclusion of larger concentrations of nanoparticles.

Figure 28 clearly shows the presence of vinyl ZnO would yield a much more thermally stable film. The same crosslinking behavior which increased the tensile strength contributes to the increased thermal stability. Similar trends were noted using ZnO fillers in different polymers such as polypropylene [94], polylactic acid [186], ABS plastic [100], and polyoxymethylene [104]. With increased concentrations of quantum dots, each step of the polymer degradation occurs at a higher temperature. The interaction between the nanoparticles and the polymer chains minimizes their breakdown.

4.3.7 Optical properties of silane-capped ZnO:EVA nanocomposites

4.3.7.1 Visible light transmission of nanocomposites

The films generated from the nanocomposites by melt extrusion and compressing are intended for use in greenhouse operations, so optical transparency is of interest. The visible light transmission of the 1% films are presented in Figure 29 and indicate that all the films at that loading level are optically transparent over the investigated wavelength range. Higher concentrations of QD loading were shown to be detrimental to the material properties of the composites, so only the 1% loadings would see use in greenhouse applications. It has been observed in the literature that concentrations of nanomaterial above 3% show decreased visible light transmission due to agglomeration [186].

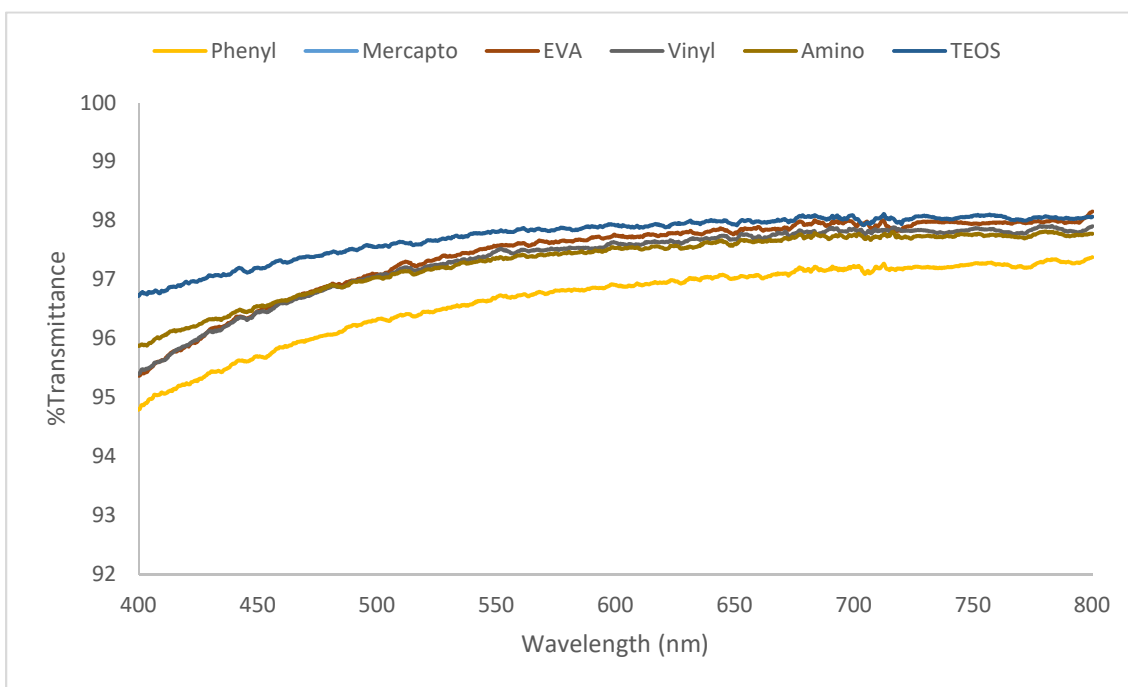


Figure 29: Visible light transmission of each of the 1% (w/w) nanocomposite films. All of them display excellent transmittance.

4.3.7.2 Dispersion of VTS-ZnO with EVA polymer

It was found that generally the presence of the QDs in the films decreased the tensile strength of the nanocomposites, especially at the higher loading concentration. This behavior has been observed with other researchers and has been attributed to the presence of agglomerations that act as stress concentrator points [94, 191, 192]. The presence of the aggregates decreases effective interfacial interactions at the location and limit polymer chain mobility decreasing the local viscoelasticity [72, 195]. The dispersion of the quantum dots within polymer was visualized in the 1% (w/w) vinyl sample using confocal microscopy and as shown in Figure 30. Similar behavior was observed by Demir et al [195] who noted that ZnO nanoparticles have a strong tendency to aggregate at a weight fraction above 1.24%, and subsequently decrease material properties. Numerous aggregates were observed in the polymer, all of which could act as stress concentrators. This poor dispersion via melt mixing has been reported in other quantum dot nanocomposite systems using confocal microscopy [102] and SEM [94] to visualize. More effective dispersion of the quantum dots would likely lead to better mechanical properties of the composite.

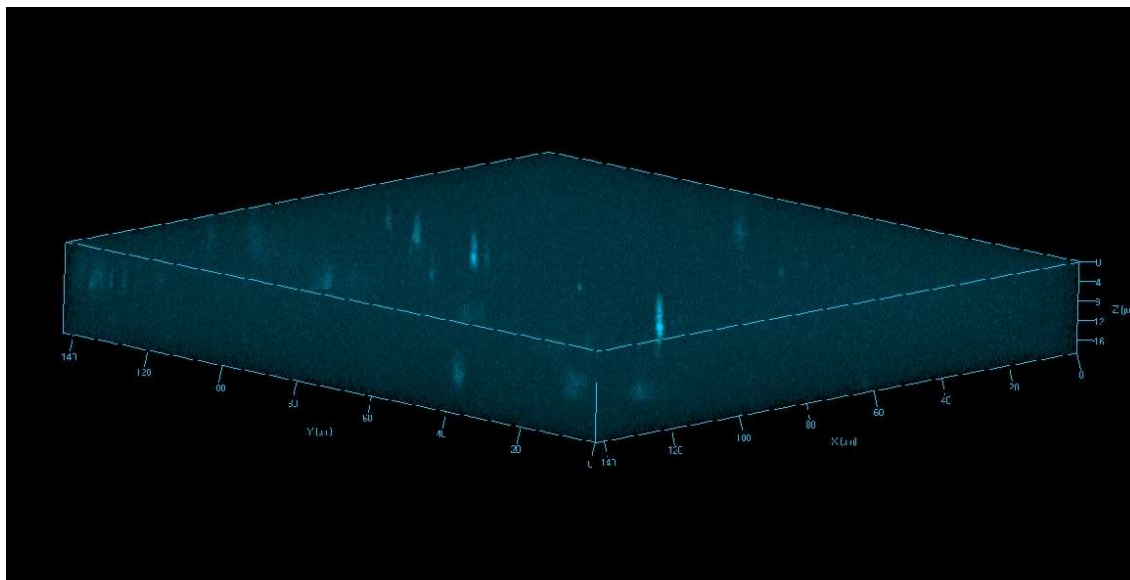


Figure 30: Confocal image of 1% (w/w) vinyl nanocomposite sample. Micrometer sized aggregates are clearly visible and can act as local stress concentrators.

4.4 Conclusion

Five different siloxanes were used to cap ZnO quantum dots for incorporation with an EVA polymer matrix. Overall, it was found that the 1% (w/w) loaded nanocomposites tended to exhibit greater tensile strength. Some of the chosen siloxane ligands showed excellent promise as additives to improve material properties. Vinyltrimethoxysiloxane was found to be the optimal capping agent of those tested, with 3-mercaptopropyltrimethoxysilane and triethoxysilane also showing promise. A 1% loading by weight was found to increase the tensile strength of the nanocomposite by a maximum of 15 % relative to a pure polymer reference. It can be surmised that this increase is due to favourable interactions between the silane side chain and the vinyl groups within the polymer. The strongest polymer-filler interaction between the vinyl quantum dots and the polymer chains is also confirmed from the DMA analysis. Higher loaded samples were found to all have deleterious effects on the mechanical properties, likely due to the nanoparticle aggregates acting as local stress concentrators. The 1% (w/w) vinyl capped nanocomposites were tested for their ability to minimize the effects of degradation in a UV accelerated weathering chamber and in terms of thermal degradation; with both tests

showing a positive influence. The 1% (w/w) vinyl capped quantum dots are the optimal nanoparticles proposed from this study for use in nanocomposite greenhouse films.

Chapter 5

Light downshifting silane capped zinc oxide-ethylene vinyl acetate copolymer nanocomposite greenhouse films

Abstract

Nanotechnology has the potential to introduce new functions to polymer films. This can be applied to greenhouse films to increase their productivity using zinc oxide quantum dots to downshift UV light to visible light to increase the rate of plant growth within, as it is well established that the rate of growth is governed by the rate of photosynthesis, which itself is dependent on the quantity of light. Zinc oxide quantum dots were mixed with ethylene vinyl acetate copolymer to make a transparent composite that absorbs UV wavelengths and emits visible light. The composite films were also found to have insulating properties and an increase in hydrophobicity. The effect on the growth rate of photosynthetic organisms was tested using the model green algae, *Chlamydomonas reinhardtii*. An algal system was used due to the ability to plot the growth rate vs. time based on cell concentration. A full spectrum UV bulb was used as a light source and the light was passed through the experimental nanocomposite films before being used by the algae for growth. It was determined that the growth rate for the algae is increased when grown behind the experimental films, indicating that the downshifted light has a positive effect on the rate of photosynthesis. These ZnO containing composites can be implemented as a next generation greenhouse film to increase their productivity.

5.1 Introduction

The Earth's population is increasing rapidly, while the amount of arable land for food production decreasing [1]. The use of greenhouse production can help mitigate this issue due to their increased agricultural efficiency. Greenhouses, and the inherent protection they offer, are of importance in many regions whose local microclimates would not be favorable to plant growth [3] or soil conditions do not favor crop growth [85].

Greenhouses can be constructed of a wood or metal frame clad in a transparent material such as glass or polymer films. The parameters that are most important to their operation are their optical properties, strength and durability, IR transmission, and antifog properties. In general glass possesses better properties for many of those factors, but that is heavily offset by the greater construction expense of using glass, its increased weight requiring sturdy framings, and its propensity to scratches and abrasions over its lifetime, which can lead to expensive repairs. Transparent polymer claddings are significantly more economical, so much that over 80 % of greenhouses are constructed of polymers such as LDPE, EVA, and EBA [4]. One way to improve the properties of polymer greenhouse claddings is the introduction of nanomaterials within the polymer films to form composites. Nanocomposites have been shown to be able to improve on many of a greenhouse film's important parameters

Nanocomposites have been shown to alter aspects of a polymer film's physical parameters in manners which would improve the properties of a greenhouse film. It has been well established that effective mixing of nanomaterials within a polymer matrix increases properties such as its tensile strength [191] by interactive favorably with polymer chains and acting as cross linking agents preventing the individual chains from sliding past one another. This linking behavior also has the benefit of increasing the stability and durability of the polymers, so they can withstand more stresses – both physical and environmental [89, 119]. The expected increase in UV exposure and increase in global temperatures is expected to have a major impact on building materials and greenhouse films; the use of nanomaterials can help mitigate this issue [2].

Nanoparticles have loaded into hollow nanotubes for controlled pesticide release [196]. Physical properties on greenhouse films, such as its wettability and thermal conductivity

are other parameters that influence greenhouse productivity. To insulate greenhouse films and lower energy costs, researchers have loaded different types of nanomaterial into polymers to decrease their IR transmission [96, 119]. Nanomaterials have also been used to change the hydrophilic/hydrophobic nature of films to minimize water-related issues within greenhouses [109, 111]. Different nanomaterials have been used to influence these properties including compounds such as clays for physical properties, silica for thermal properties, and TiO₂ and zinc oxide (ZnO) for radiometric properties [96, 117, 119].

ZnO is a wide bandgap semiconductor with a bandgap of 3.37 eV which allows it to be transparent to visible light [129]. It also possesses a large exciton binding energy of 60 meV, allowing it to undergo excitonic transitions at room temperature [23]. If ZnO particles are synthesized with their size smaller than their Bohr radius of 2.34 nm, they become quantum dots where the continuous band gap is replaced by discrete energy levels [197]. Under these conditions, ZnO still absorbs in the UV regime, but its emission shifts to visible light [23]. The visible light emission of ZnO is due to the radiative recombination of a photogenerated hole with an electron that belongs to a singly ionized oxygen vacancy on the surface of the QD [28, 62]. The native visible emission is green, centered around a wavelength of 550 nm. However, it is possible to cap the ZnO QDs with siloxanes to create a silane shell that both stabilizes the QD [23], enables better dispersion within a polymer [163], and upshifts the visible emission into blue visible light [171]. The presence of a silane shell also increases the photoluminescent yield of a QD [160, 184].

Introducing silane-capped ZnO QDs within a transparent greenhouse polymer would provide an excellent UV absorber which downshifts the absorbed UV to photosynthetically active radiation (PAR) which could influence the growth of any green photoactive organisms. It has previously been shown by El-Bashir et al [108] that the addition of an organic perylene dye to greenhouse cladding increases the amount of PAR a plant receives. However, organic dyes tend to have narrow absorption, broad emission and are susceptible to degradation from continuous radiation exposure [37]. QDs have a much greater resistance to radiative degradation [125], while silane-capped QDs having been shown to be stable to years [59].

UV light – which accounts for 5% of all incident photons as compared to 40% which is visible [198] – is downshifted into blue light by the VTS-ZnO. Blue light is the maximally absorbed wavelengths by photosystem II (PSII) and chlorophyll *a* [199]. Plants also have extensive networks of light-harvesting carotenoid pigments to further increase their blue light absorption [120]. These blue light-harvesting proteins are among the most abundant membrane proteins in the world [121] whose main purpose is to absorb light and transfer the excitation energy to the photosynthetic reaction center. Light in blue spectral region has also been shown to have other significant physiological benefits to green plants. Blue light is important for a range of processes such as germination and stomatal control [200]. Exposure to blue light also helps plants mitigate UV damage [199].

In this experiment, VTS-ZnO containing nanocomposite films will be tested to whether they increase the growth rate of photosynthetic organisms. It has been shown that increasing lighting using supplementary lighting on agricultural crops directly influences their rate of photosynthesis and growth [115], albeit with an increased energy cost. The VTS-ZnO composite should show similar increase with no extra energy cost, as the additional PAR comes from sunlight. A model algal species, *Chlamydomonas reinhardtii*, will be used to test the film's effects on growth as algae's growth rate can be measured accurately and periodically via spectroscopic measurements, as opposed to plant species which are typically measured at the end of their growth cycle. It is expected that the growth rate of the algae should be directly influenced by the amount of PAR that it receives [201] allowing to observe a direct correlation between light quantity and photosynthetic organism growth. As well, it will be determined if the presence of the QDs also improve other important greenhouse polymer physical parameters such as hydrophobicity and IR blocking.

5.2 Experimental

5.2.1 Materials

Zinc acetate dihydrate ($\text{Zn}(\text{OAc})_2 \cdot 2\text{H}_2\text{O}$), (NaOH), and vinyltrimethoxysiloxane (VTS) were obtained from Sigma-Aldrich, Canada and used without any purification.

Anhydrous ethanol (EtOH) for the reaction was supplied by Commercial Alcohols. Ethylene vinyl acetate copolymer (EVA) was supplied by DuPont (Elvax 3185).

5.2.2 ZnO quantum dot synthesis

The synthesis of ZnO QDs used in this experiment (VTS-ZnO) was based on the method described by Bang et al. (2006) [32], modified to include siloxane capping reactions. In short, zinc acetate dihydrate (0.46g) was mixed into 30 ml of anhydrous ethanol and sonicated at 65°C for one hour, and then cooled in an ice bath. One milliliter of the capping agent, VTS, was added at this point. Sodium hydroxide (0.2 g) was dissolved in 10 ml of anhydrous ethanol, cooled in an ice bath, and added to the zinc acetate solution dropwise. The reaction proceeds for one hour in the ice bath with magnetic stirring, then the product was collected and dried in a vacuum oven at 60°C for at least 24 hours. The resulting powder was dissolved in minimal methanol and purified via dialysis with methanol (MWCO of 1 KDa, Spectra/Por® 6 Standard RC pre-wetted Dialysis Tubing, diameter 29 mm). The purified product was dried in the vacuum oven and the quantum dots are collected. The uncapped ZnO quantum dots were synthesized in a similar fashion, just with no addition of VTS. The photoluminescence of the QDs were measured using a PTI Quantmaster 50 spectrofluorometer. The size of the nanoparticles were estimated from their maximum excitation using the Brus equation [148].

5.2.3 Physical properties

Small batches of nanocomposite were made using a Thermo Scientific HAAKE Mini-Lab II Twin Screw at 140°C, 90 rpm and 10 minute residence time. The extrudate was pressed into circular films for analysis using a Universal Film Maker (ThermoFisher) and a Carver press. The dimensions of the pressed films were 2 cm in diameter and 25 µm in thickness. EVA only films were made as well to use as a reference. Films were produced for uncapped ZnO and capped VTMS-ZnO composites at 2.5, 5 and 10 percent by weight (%wt/wt). The hydrophobicity of the nanocomposites was tested using a Henniker Plasma PGx Portable Contact Angle meter. The pressed films were analyzed with a Nicolet 6700 FTID spectrophotometer equipped with a smart iTR diamond horizontal attenuated total reflectance (ATR). The transmission of IR radiation through a polymer

film can be measured by its thermicity [117]. The thermicity was calculated from the FTIR spectra as a ratio of the area under the transmittance curve from 700 to 1400 cm^{-1} . The thermicity of the pure EVA is taken to be 100 % and the nanocomposites are fractions compared to the reference EVA.

5.2.4 Laminated greenhouse film production

Coating transparent polyester films with VTS-ZnO nanocomposites was required to produce large enough films for the growth studies. An EVA solution of approximately 1000 centipoise was made by dissolving 5 g of Elvax 660 in 30 ml of boiling toluene. The samples with VTS-ZnO nanoparticles were made in the same manner, only weighed portions of the nanopowder was added along with the polymer beads into the toluene. The solutions were mixed for 6 hours using a stir bar to ensure complete dissolution. The films were produced using a ChemInstruments HLC-101 Hot Melt Laboratory Drawdown Coater. For the samples, the PFTE side dams were set 22 cm apart, which determines the width of the final laminated film; and the thickness was set to 0.1 cm. The reservoir and coating rod heaters were set to 130°C to ensure the solution stayed liquid. A transparent PET polyester substrate film was loaded onto the machine and drawn through the heated coating head at a steady pace to form a transparent, uniform coating of the EVA (or VTS-ZnO:EVA) onto the film. The coated films were cut from the machine and left to dry, coated side up, overnight yielding transparent polyester film with a transparent EVA coating. Films were prepared with coatings containing 2.5, 5, and 10 percent weight (%wt/wt) quantum dots.

The light transmission of the nanocomposite coated films was tested using an Agilent Cary 60 UV-VIS spectrophotometer. Small portions of the composite films were cut and inserted into the viewing cell with the nanocomposite coating facing the incident light source. The UV-VIS transmission through the films was measured in scan mode over a range from 250 to 800 nm.

The lighting used for the growth experiments was provided by four ZooMed Reptisun 5.0 UVB T5 HO bulbs in a fluorescent fixture. The spectrum of the lights was measured using an Ocean Optics STS-UV and is shown in Figure 31.

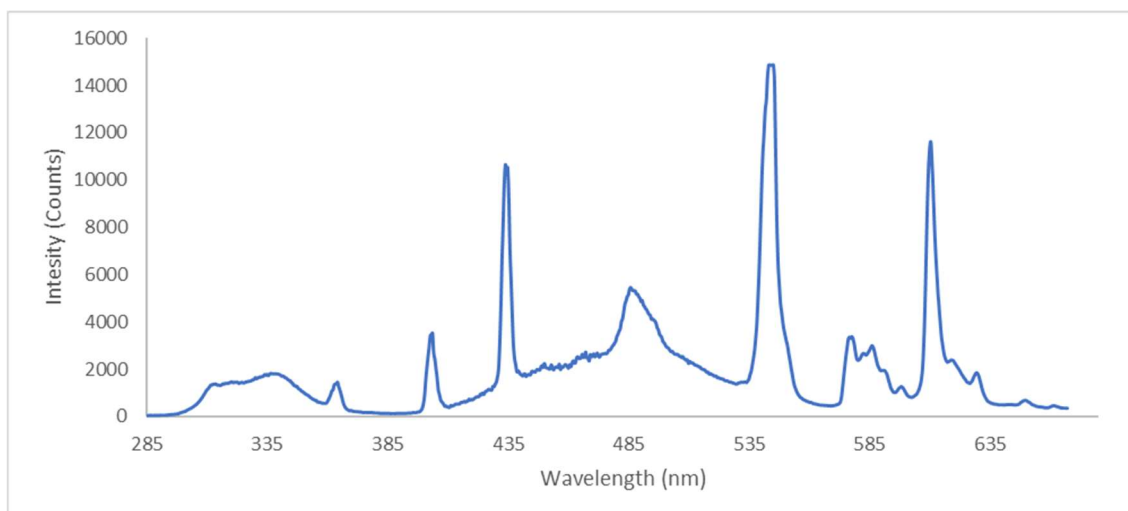


Figure 31: Emission spectrum of UV bulbs used in growth experiments.

To quantify the change in light when passing through the coated films, a Li-Cor LI-189 handheld meter was used to measure the change in photosynthetic active radiation (PAR) which has a range of 400 to 700 nm. The change in UV radiation was measured using a LightScout UV meter, which measures the range of 250 to 400 nm. The coated films were stretched flat in a wooden frame and placed at three different distances from the light source with the nanocomposite coating on the incident side. Measurements were taken at 30, 60, and 90 cm and the results were averaged showing the transmission and change in UV on the light passing through the coated films.

5.2.5 Optical properties of laminated film and effect on algae growth

Algae cultures were used to test the films for their effect on the growth rate of photosynthetic organisms. The testing apparatus was situated within a temperature- and humidity-controlled growth chamber and the setup is depicted in Figure 2. The temperature was 25°C and 60 % relative humidity.

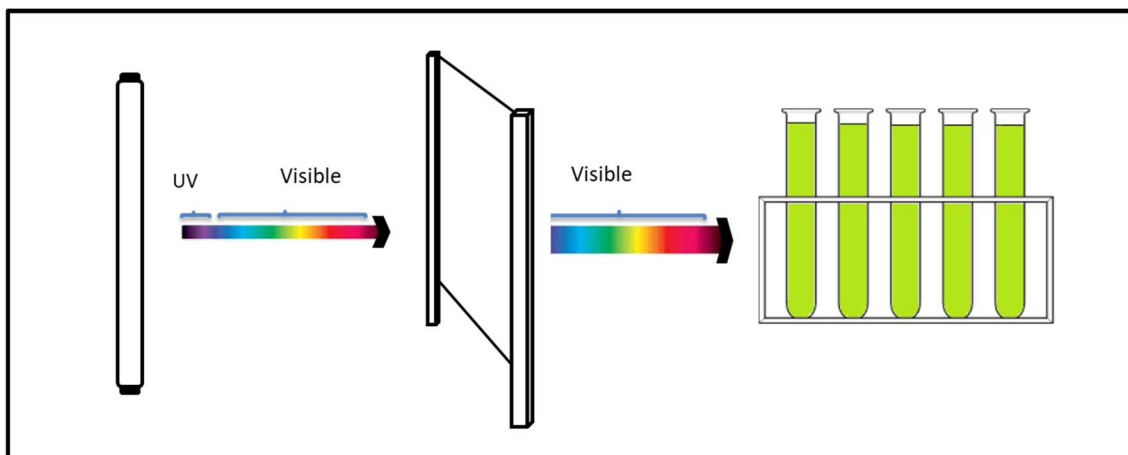


Figure 32: Growth test setup for VTS-ZnO composite films. The lights were at one end of the growth chamber, with the tested films set vertically just in front of the samples. The distance between the light and the algae cultures was 1.5 meters, so that the PAR measured at that location was $15 \mu\text{mol}\cdot\text{s}^{-1}\cdot\text{m}^{-2}$. The algae tubes were place within cardboard boxes to minimize exposure to any reflected light within the chamber.

Chlamydomonas reinhardtii strain cc-1690 was grown axenically in Bold's Basal Medium (BBM) in 250 ml glass growth tubes at a constant temperature of 25°C. The cultures were aerated continuously with ambient air filtered through sterile cotton batting. A continuous irradiance of $15 \mu\text{mol}\cdot\text{s}^{-1}\cdot\text{m}^{-2}$ of PAR lighting, which was measured with a Li-Cor LI-189 radiometer and supplied via the aforementioned lighting setup. Cell growth was estimated by determining the absorbance of the culture at 750 nm using an Agilent CARY 60 UV-VIS spectrophotometer. The chlorophyll concentration was determined by extracting the pigment from the cell culture with acetone. Briefly, an aliquot of the culture was removed from the growth tube every 24 hours and centrifuged at 16,000g for 3 minutes to pellet the algal cells. The supernatant was discarded, and the pellet resuspended in an acetone:water solvent (90:10 v/v) to extract the chlorophyll. The suspension was centrifuged at 16,000 g for 3 minutes to remove insoluble particles and the absorbance was measured at 647 and 644 nm. The concentrations of chlorophyll a and chlorophyll b were calculated as described by Jeffrey and Humphrey [202]. Due to the relative quick growth time and small space allotted for each culture tube, a total of 18

samples (n=18) was growth for each film tested. An EVA-coated film was used as a reference. A 2.5% (wt/wt) and a 10% (wt/wt) film were tested for their effectiveness. The specific growth rate was determined from these values accordingly. The results were plotted using GraphPad Prism and statistical significance was determined using its two-way ANOVA analysis.

5.3 Results and discussion

5.3.1 Photoluminescence of nanocomposites

The composite films used in this study contained VTS-ZnO QDs. One important aspect of the siloxane capped nanoparticles compared to uncapped is their emission peak. The normalized photoluminescence spectra of the uncapped and silane-capped QDs are shown in Figure 33 (top), both excited at their maximum wavelength. The VTS-ZnO QDs max emission is at 470 nm with the bulk of the emission peak centered in the blue region. In contrast, the uncapped ZnO QDs have their maximum emission in the green region, which would be less desirable for photosynthetic purposes and leads to decreased growth rates [203]. Capping with silane shells also has the added benefit of increasing the quantum yield (QY) of the nanoparticles, which is the efficiency of radiative emission for each UV photon absorbed. In this study, it was found that the capped QDs have a QY of 30 %, compared with 10 % for the uncapped. These yields were estimated using an external reference method [146]. Similar effects of silane capping were reported by Shi et al (2011) [23] when they used a different siloxane capping agent for stability studies. The QDs used in this study were also found to have a wide excitation and emission ranges. Figure 32 (bottom) shows that the QDs can be excited in the UV range from 270 to 325 nm, with their maximum excitation at 305 nm. This wide absorption would enable them to collect almost the entire UV range, increasing the quantity of downshifted PAR they provide. Their emission is a wide and Gaussian shaped curve that stretches from 405 to 585 nm, with its maximum at 480 nm. This wide emission would have the advantage to provide additional light at the absorption maximum of not only the chlorophyll pigments, but other light harvesting pigments which further shuttle photons into the photosystems [121].

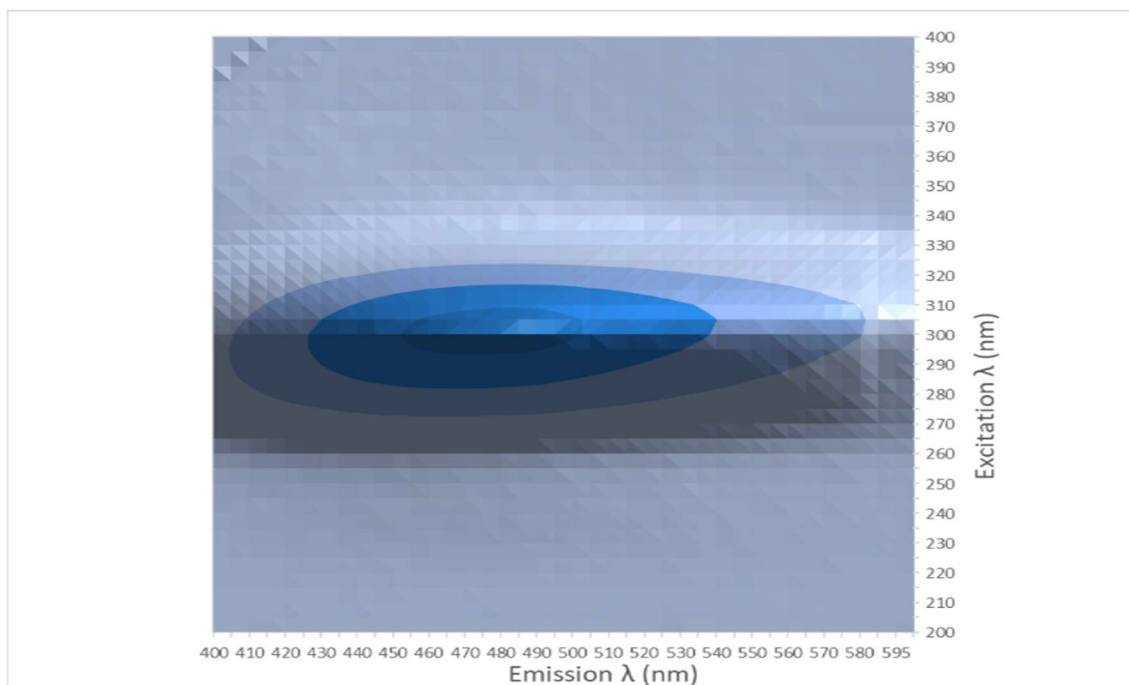
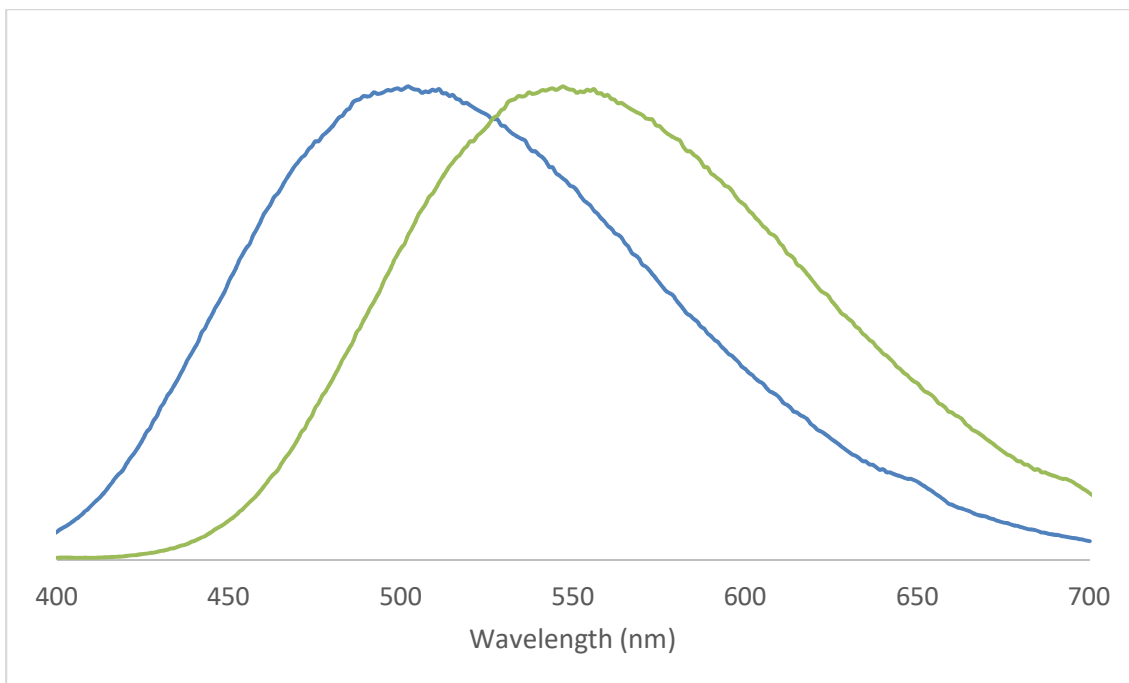


Figure 33: Normalized photoluminescent spectra of capped and uncapped ZnO QDs excited at their maximum wavelength (top). The capped quantum dots, indicated in blue, have a diameter of 3.2 nm and a maximum emission at 480 nm; and the uncapped, shown in green, have an estimated diameter of 3.6 nm and a maximum emission at 550 nm. Excitation and emission ranges for VTS-ZnO quantum dots

(bottom). They have a large excitation and emission range, which has to ability to shift a wide range of UV wavelengths into visible light.

5.3.2 Physical properties

5.3.2.1 Changes in nanocomposite wettability

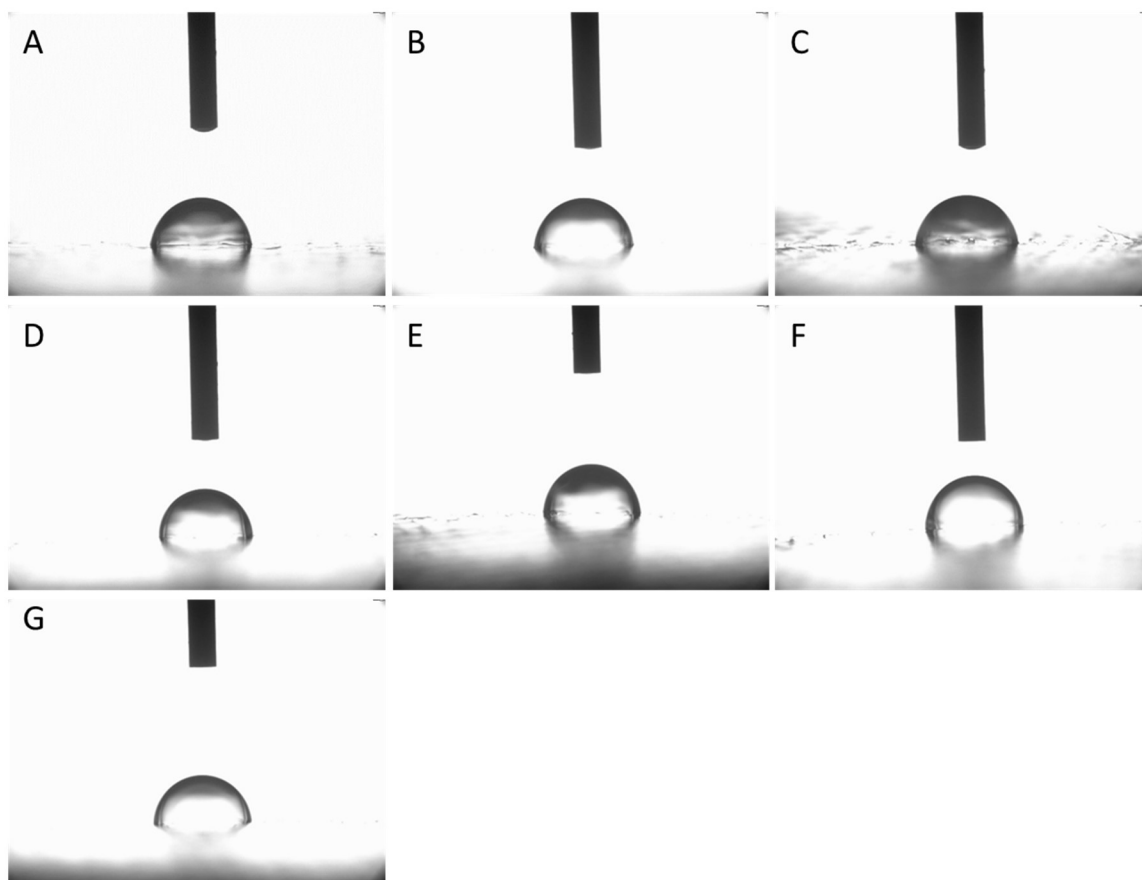


Figure 34: Drop test results for different (wt/wt) percentage nanocomposite films. The films tested were (A) 2.5% ZnO, (B) 5% ZnO, (C) 10% ZnO, (D) 2.5% VTS-ZnO, (E) 5% VTS-ZnO, (F) 10% VTS-ZnO, and (G) EVA reference film.

Table 17: Contact angles measured for different QD loadings in EVA nanocomposite film.

QD wt/wt%	ZnO:EVA			VTMS-ZnO:EVA		
	Sample 1	Sample 2	Sample 3	Sample 1	Sample 2	Sample 3
0	88.5	88.3	88.9	88.5	88.3	88.9
2.5	90.6	90.3	90.3	92.7	94.1	93.5
5	92.1	92.7	93.2	97.3	96.5	96.5
10	94.2	94.2	94.2	101.1	101.3	101.1

The hydrophobicity of the films was tested using contact angle measurements (Figure 34). It was found that the contact angle increased with increased loading of QDs in the composite, indicating a corresponding increase in hydrophobicity. The presence of silane nanoparticles has been reported to make polymers more hydrophobic [95], and it was observed in this study that the presence of VTS-ZnO lead to higher contact angles compared with the uncapped ZnO QDs, as indicated in Figure 35.

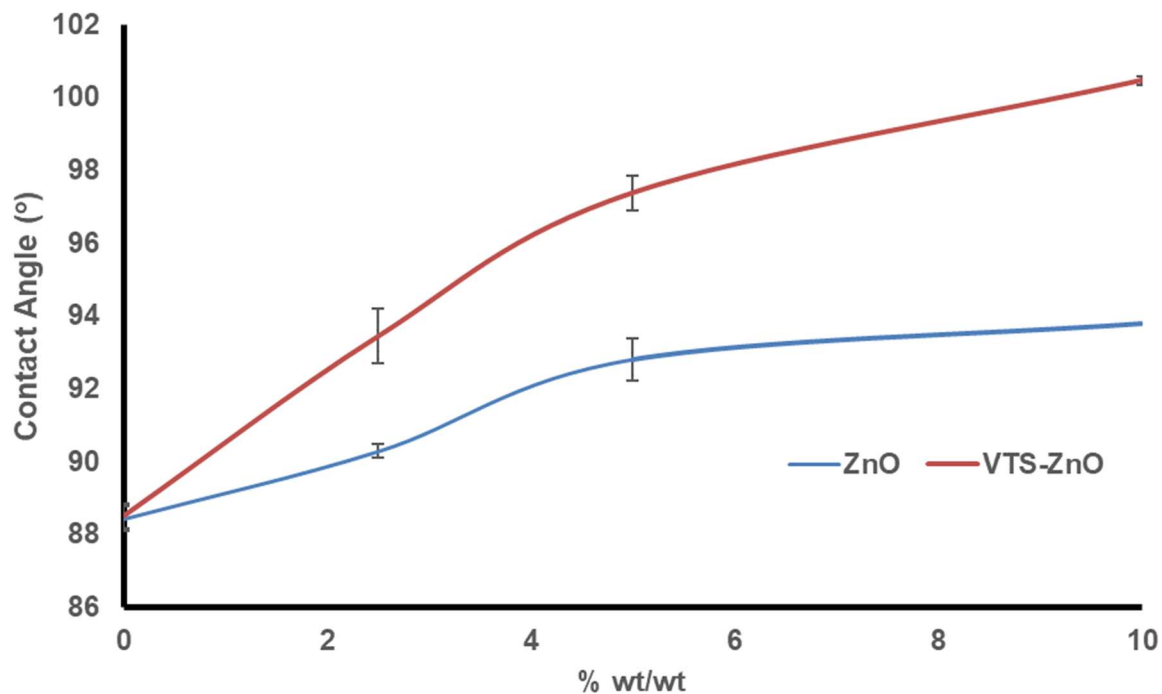


Figure 35: Change in contact angles from increasing loading of QDs within EVA nanocomposite films.

It was found that increasing the concentration (%wt/wt) of the QDs within the polymer showed an increase in the contact angle, with the maximum tested showing a 13 percent increase at 10 % loading for the VTS-ZnO within the EVA polymer. A similar trend was reported by Ibrahim et al (2017) [113] when they reported a 14 percent increase in contact angle due to a 10 % (wt/wt) loading of SiO₂ nanoparticles within polystyrene.

The lower loadings tested, down to 2.5 %, did not show as impressive of an increase but they still made the material slightly more hydrophobic. Antifogging agents used in polymers are typically comprised of tensioactive materials, such as nonionic surfactants, that alter the interaction between the solid surface and water vapor [109]. In use, these compounds migrate to the surface of the polymer where they are lost over time. Their loss rate is controlled by their solubility their solubility and diffusion coefficients within the polymer. Larger particles, such as the nanomaterials used in this migrate much slower and thus keep their effects longer during the polymer's lifetime and would be expected to

improve the wettability properties at a consistent rate for the lifetime of the composite films.

5.3.2.2 Changes in nanocomposite thermicity

Over half of sunlight's photons are in the IR range and controlling the transmission of these through their claddings is critical for greenhouse operation [115]. This pertains to summer months to limit the amount of heat entering a greenhouse to avoid heat stressing the crops within; as well as in the winter months to limit heat escape and minimize heating costs [3]. The transmission of IR through a film is measured by its thermicity, where the lower the thermicity, the lower the transmission. Controlling thermicity in a nanocomposite film can enhance a greenhouse's productivity [117]. Different nanoparticles can be added to a film to achieve this effect. Clay particles work well but have a negative effect on the visible light transmission [115]. Silica nanoparticles have been shown to decrease a film's thermicity and have better visible light transmission due to their refractive indices being similar to those of commonly used transparent polymers [96]. The nanoparticles used in this study have a silane shell which should match their refractive index to the EVA they are embedded and gives them better thermal insulating properties than similarly sized uncapped ZnO QDs as listed in Table 18 and depicted in Figure 36.

Table 18: Normalized thermicity values for different loadings of QDs with EVA nanocomposite films.

QD %(wt/wt)	ZnO	VTS-ZnO
0	100 ± 0.1	100 ± 8
2.5	70 ± 2	49 ± 2
5	55 ± 2	22 ± 2
10	19 ± 1	4 ± 1

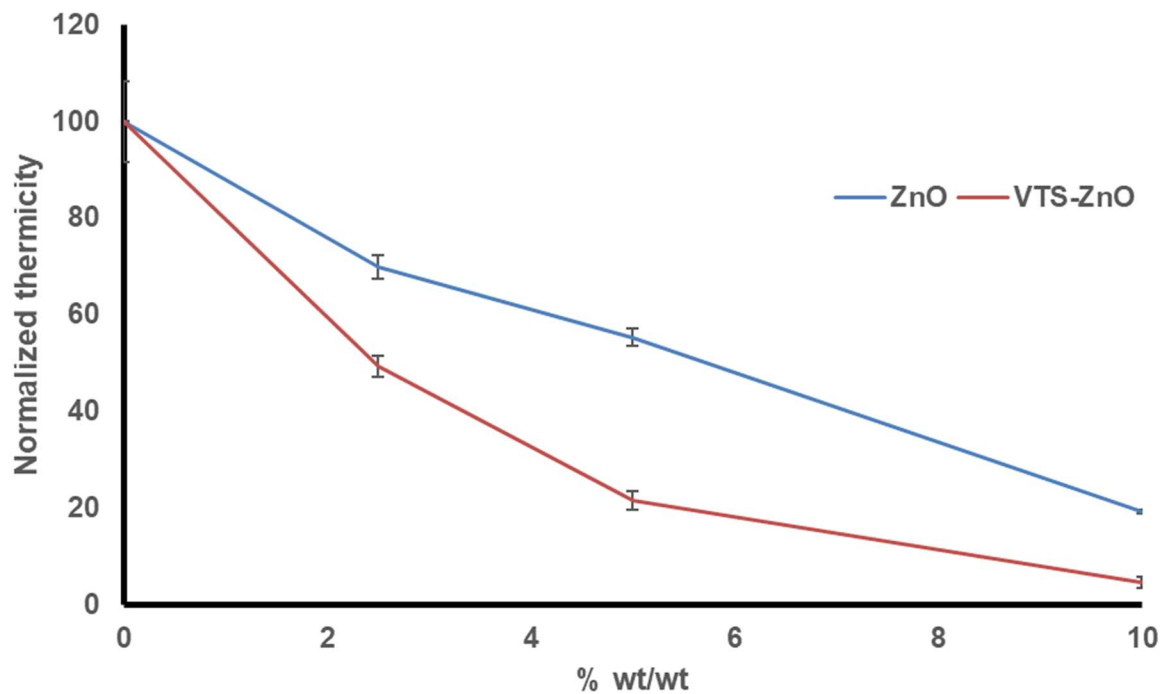


Figure 36: Change in thermicity in composite EVA films depending on QD loading. Both capped and uncapped decrease with loading, but silane-capped QDs show much greater thermicity.

5.3.3 Optical properties of laminated film and effect on algae growth

The composites used for the growth studies were coated as described onto clear polyester to generate a two-layer material. Four different films were coated: one with only EVA and the others at 2.5, 5 and 10 weight percent (%wt/wt) VTS-ZnO. The samples' UV-VIS transmission from 200 to 800 nm were measured and the results are illustrated in Figure 37. The QD nanocomposite was positioned on the incident side of the light source for this experiment.

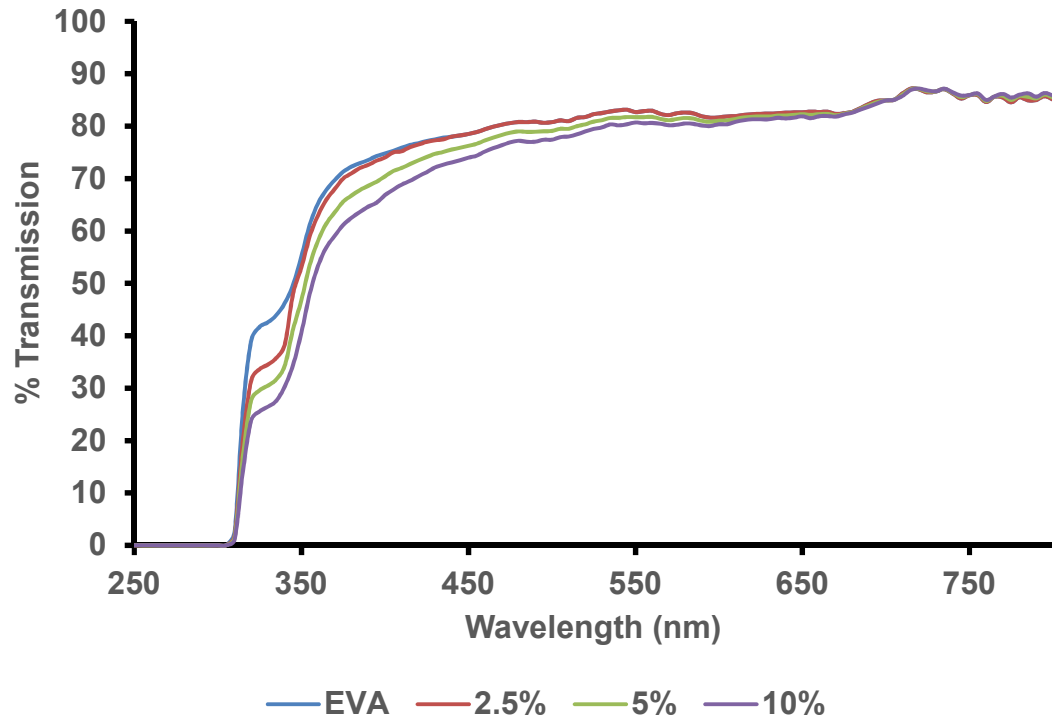


Figure 37: UV-VIS transmission of VTS-ZnO:EVA nanocomposite coated transparent films. All weight percent composites show excellent transmission above 500 nm, but the higher loaded samples have decreased transmission in lower wavelengths. All sample films show complete UV absorption below 300 nm, likely a property of the base polymer that was coated with the composite.

From Figure 37, it is obvious that the samples show excellent transmission in the NIR and red regions of the spectrum. However, the transmission begins to decrease in the green-blue region (below 550 nm) for the nanocomposite-coated films for all the nanocomposite samples, especially the ones with higher weight percentages of QDs. This behavior is noted in the literature with visible light transmission generally decreasing in nanocomposites with loadings about 1% wt/wt [204]. The 2.5% wt/wt coating matches the transmission of the EVA only sample complete within the visible region (> 400nm), so that loading was chosen to proceed with. It is expected that if this were not a coating, but a nanocomposite film, a decrease in physical properties would be expected [191], but as these are nanocomposite coating, light transmission is the most important parameter. In fact, light transmission is the most important parameter for greenhouse films, as that

directly influences the rate of photosynthesis within [205]. As expected, the UV transmission drops rapidly with increased loading of the nanoparticles as the VTS-ZnO absorbs it. This is advantageous to greenhouse construction as large quantities of UV light can damage a plant's PSII leading to photoinhibition and photodamage [123]. UV light can also directly damage organic bonds within the plants [115]. Not all the UV light is absorbed, some does pass through the films which is important because some UV is required for pollination and signaling within crops [96]. UV light is also important for the generation of secondary metabolites within plants, which govern crucial factors within crops such as color, taste, and nutritional content [123].

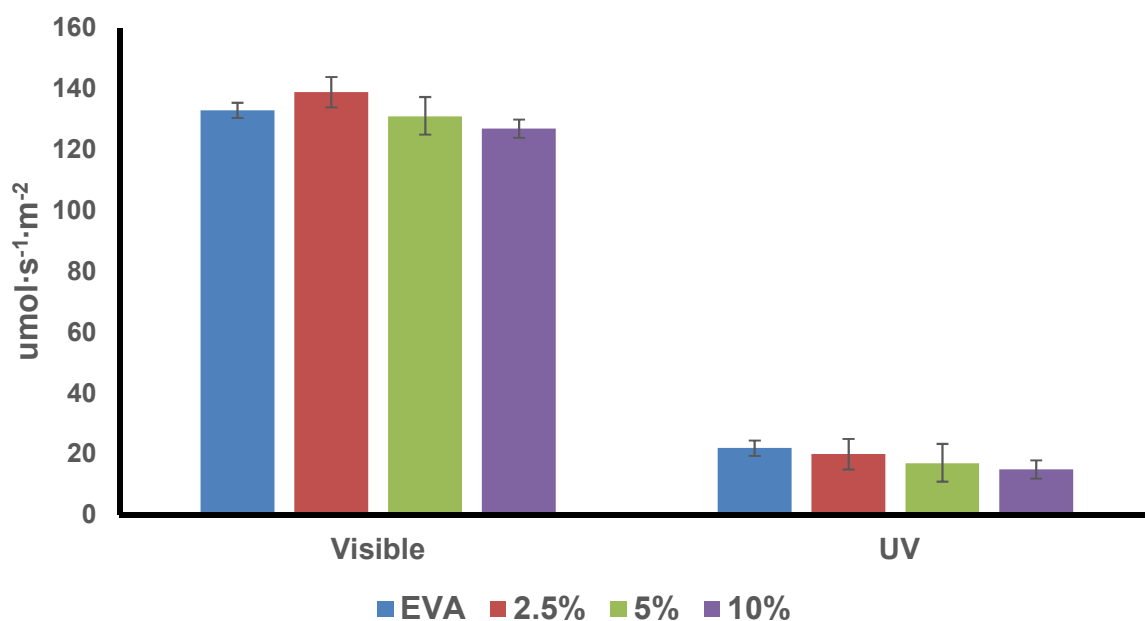
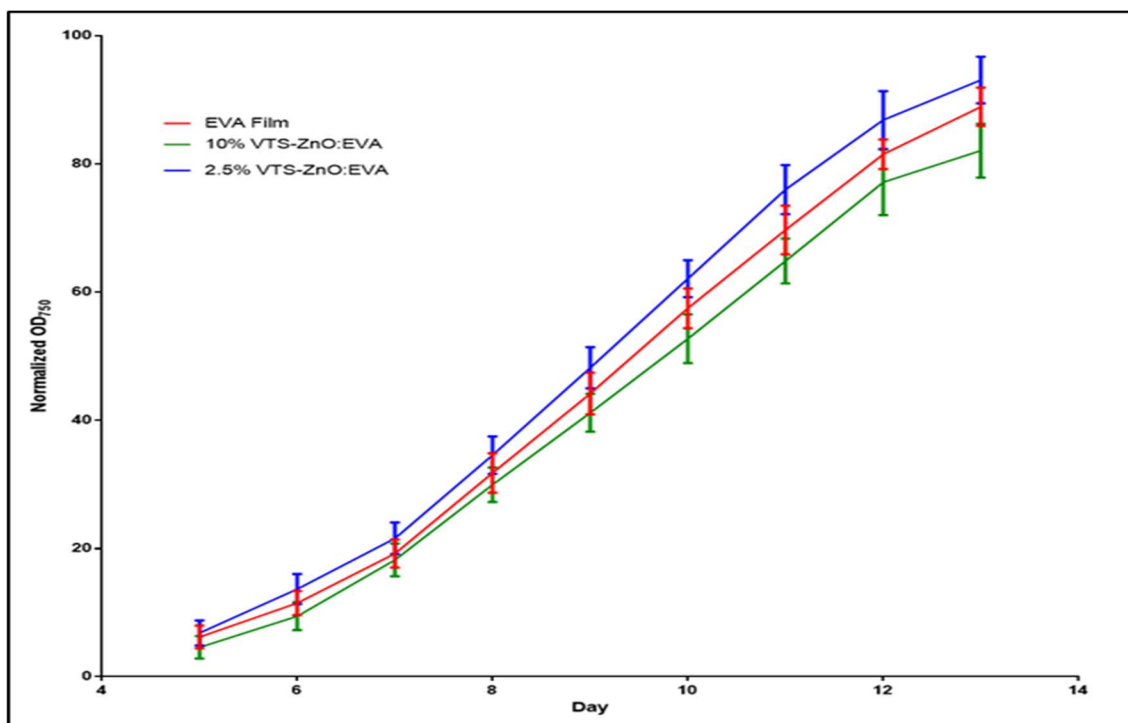


Figure 38: Light changes measured from the different coatings used. The 2.5% VTS-ZnO composite samples shows improvement in PAR detected compared to the EVA reference. This is due to UV absorption and downshifting into visible light.

A PAR light meter and a UV light meter were used to quantify the changes in light transmission from a full spectrum UV bulb passing through the nanocomposite coated films. These results are shown in Figure 38. The UV photons which are absorbed by the composite's QDs is downshifted to lower energy blue light, which can be used for the algae in this experiment to increase its growth rate [201]. The 2.5% wt/wt coated film

shows a larger amount of detected PAR than the EVA reference film. This is due to the visible light transmission in addition to the downshifted blue light. The other two nanocomposite coated samples, 5 % and 10 % (wt/wt), show a greater degree of UV loss, but less detected PAR than the reference EVA coated film. Therefore, it would be expected that the 2.5 % sample would show an increase in photosynthesis leading to an increased rate of algal growth in this experiment. The algal growth rates and chlorophyll accumulation rates of the EVA coating, the 2.5 % VTS-ZnO coating and the 10 % VTS-ZnO coating are presented in Figure 39.



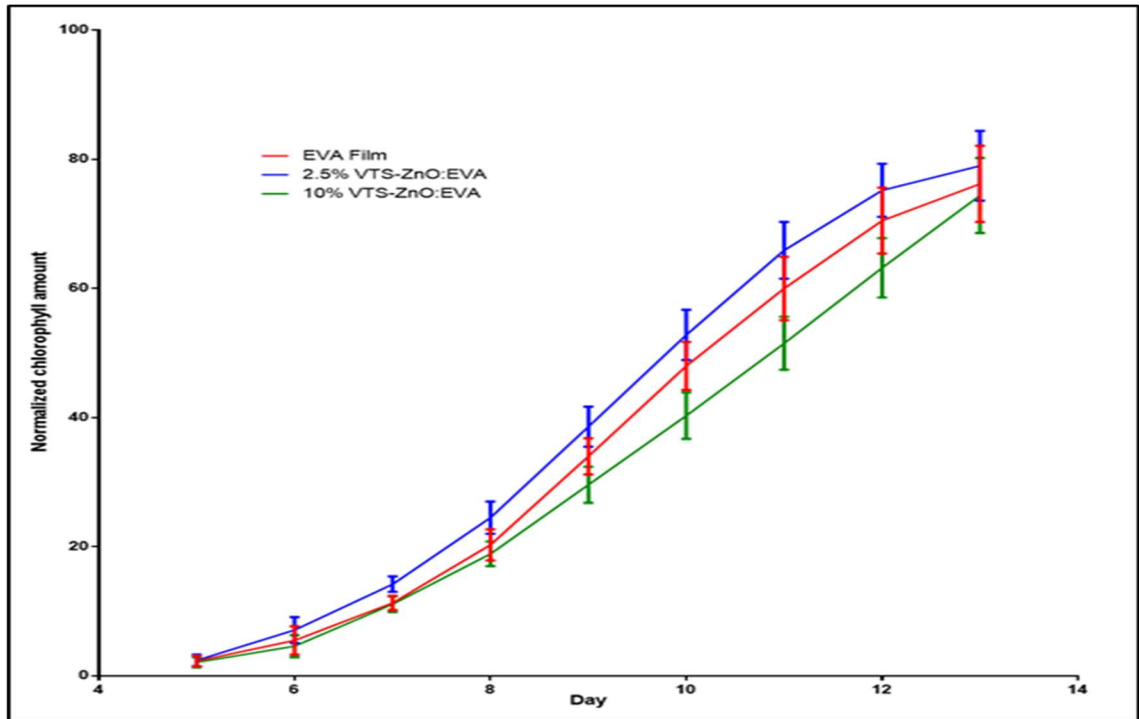


Figure 39: Growth curve for *C.reinhardtii* (left) based on OD750 and corresponding chlorophyll accumulation (right) in the same cultures. Both clearly indicate that the cultures grown behind the 2.5% composite film experiences a faster growth rate than the reference EVA film.

There is a statistically significant increase in the algal growth rate for the sample that was behind the 2.5 % (wt/wt) nanocomposite film as shown in Figure 39. This correlates to the increase in PAR depicted in Figure 37. As lighting levels are directly correlated with the growth rate for *C.reinhardtii* [206], the increased growth rate is definitely expected. For comparison purposes, the growth rate of the 10 percent film was also measured and found to be depressed, which would be expected due to the decrease in PAE noted in Figure 38. From the linear portion of the growth curves, it can be estimated that the 2.5 % (wt/wt) composite film gives the algae a 4.7% increased growth rate in this experiment.

5.4 Conclusion

Silane-capped ZnO quantum dots were used to produce next functional greenhouse films. It was found that these films have an increased hydrophobicity, decreased IR transmission and excellent UV-VIS light transmission. The light downshifting property

of the VTS-ZnO quantum dots shows an increased amount of PAR and were shown to increase the growth rate of a photosynthetic green algae. These films can be used as a next generation greenhouse cladding for improved properties and production of agricultural crops.

Chapter 6

Conclusions and Recommendations

6.1 Conclusions

The objective of this project was to produce a transparent nanocomposite film that could be used to increase the productivity of greenhouses. That was successfully accomplished at a laboratory scale. Vinyltrimethoxysiloxane-capped zinc oxide quantum dots were incorporated into ethylene vinyl acetate copolymer to yield a transparent film that was shown to increase the growth rate of a model photosynthetic organism. To the author's knowledge, this was the first work that confirmed that siloxane capping agents bind to the surface hydroxyls on ZnO nanoparticles, which was observed in the XPS spectra. The addition of the VTS-ZnO into EVA also showed additional benefits. The films produced were found to have an increased hydrophobicity and thermicity – two film parameters that would be beneficial to greenhouse construction. The quantum dots also increased the tensile strength of the film material, as well as its stability to thermal and UV-induced degradation. Therefore, it can be concluded that this composite material is a promising new technology for future greenhouse constructions.

Another issue that was addressed was in this study was the synthesis of zinc oxide. The parameters for its growth were examined and determined to be similar for both batch reactions and continuous tubular reactions. The effects on different synthesis conditions was also tested to optimize the quantum yield of ZnO nanoparticles produced in a tubular reaction. The effects of various capping agents were also tested, determining that siloxanes and polymer capping agents are to be used is high visible light emission is required. These two tests both showed that vinyltrimethoxysiloxane would be the best capping agent in terms of positive contributions to physical properties and to photoluminescence.

Lastly it must be remembered that this project was designing films for use in greenhouses. Greenhouses are enormous constructs, required hundreds of square meters of film for cladding. Zinc oxide has been identified as a cheap nanomaterial and does not require any extreme conditions to produce it. This study presented two manners which could produce these quantum dots on a commodity scale. The first was is the continuous plug flow reactor. This reactor has the potential to produce 5 grams of quantum dots a day, which can be scaled up by reactors running in parallel. A large quantity of ZnO

nanoparticles was also synthesized using a batch reaction yielding over 50 grams of luminescent particles indistinguishable to what a bench scale reaction would yield. Either of these methods could successfully produce large quantities of ZnO if required.

In summary, this project determined: the significant factors in the growth of ZnO; designed and tested a continuous reactor system for its production; determined which capping agent would be optimal for quantum yield and for mechanical properties; shown that thermicity and hydrophobicity were improved with incorporation of VTS-ZnO into greenhouse films; and proved that the light downshifting effect of the films increases the growth rate of green algae, which is a model photosynthetic organism. These results are a promising foundation for furthering this technology to a larger scale and potentially commercialization.

6.2 Recommendations

- 1) It was shown in Chapter 2 that the quantum yield is heavily influenced by using siloxane and polymer capping agents. Further studies on those including differing concentrations, and reaction conditions should be studied. One thing that absolutely needs to be tested is changing the spacetime of the reaction in the PFR. This can be accomplished by changing the flowrates and column dimensions.
- 2) The PFR tested in Chapter 2 showed promise for continuous production of nano-zinc oxide. However, due to the small volume syringes used, only 20 ml of solution was produced at a time. Larger reservoirs and a more continuous pumping system should be tested for high volume product. An HPLC, LC, or other type of peristaltic pump would meet this requirement.
- 3) VTS-capped zinc oxide quantum dots were found to be the best for the requirements tested, including quantum yield and material properties. As these present a vinyl group to the environment, experimenting with linker agents could be of interest, especially biological ones. These could be linked with proteins and/or enzymes for creating robust markers for ELISA and other sensitive diagnostics.
- 4) The quantum dots stabilized with the PEG and PVP both showed excellent quantum yields, these could be introduced into polymer systems to study the

effects on dispersion. As PEG and PVP are extremely bulky, this should minimize the aggregation issues observed with nanoparticles.

- 5) The algae growth was enhanced through the use of the nanocomposite films and the LDS capabilities. That is an excellent proof-of-concept for this technology. It would be advisable to move onto a plant system next, such as growing *Arabidopsis thaliana*. That is the model plant which has a short growing time and small stature. This would allow for growing under controlled conditions within a growth chamber to ensure absolutely no interfering effects. As well, its small size would allow for many replicates to get a large number for statistical analysis. Larger plants in greenhouse would be subject to variation in their growth conditions.
- 6) The VTS-ZnO:EVA nanocomposite was shown to increase the rate of growth in algae. This was under the assumption that the increased visible light increased the rate of photosynthesis. The photosynthesis rate could be directly measured to confirm this hypothesis.
- 7) Increased amounts of visible light were observed when passing a UV-containing source through the films. This technology also has potential in the field of solar energy production. This film could be applied to photovoltaic cells to increase their efficiency. That would make an interesting study and new application for this robust and economical composite.

References

1. Fischer, R.A. and D.J. Connor, *Issues for cropping and agricultural science in the next 20 years*. Field Crops Research, 2018. **222**: p. 121-142.
2. Andrady, A.L., et al., *Consequences of stratospheric ozone depletion and climate change on the use of materials*. Photochem Photobiol Sci, 2015. **14**(1): p. 170-84.
3. Alsadon, A., et al., *The effects of plastic greenhouse covering on cucumber (*Cucumis sativus L.*) growth*. Ecological Engineering, 2016. **87**: p. 305-312.
4. Balocco, C., et al., *Experimental transmittance of polyethylene films in the solar and infrared wavelengths*. Solar Energy, 2018. **165**: p. 199-205.
5. Balazs, A., T. Emrick, and T. Russel, *Nanoparticle polymer composites: where two small worlds meet*. Science, 2006. **314**(5802): p. 1107-1110.
6. Mansur, H.S., *Quantum dots and nanocomposites*. Wiley Interdiscip Rev Nanomed Nanobiotechnol, 2010. **2**(2): p. 113-29.
7. Zhang, Y., et al., *Highly transparent bulk PMMA/ZnO nanocomposites with bright visible luminescence and efficient UV-shielding capability*. Journal of Materials Chemistry, 2012. **22**(24).
8. Norberg, N.a.G., DR, *Influence of surface modification on the luminescence of colloidal ZnO nanocrystals*. Journal of Physical Chemistry B, 2005. **109**(44): p. 20810-20816.
9. Sahal, M., et al., *Structural, electrical and optical properties of ZnO thin films deposited by sol-gel method*. Microelectronics Journal, 2008. **39**(12): p. 1425-1428.
10. Demir, M., Koynov, K, Akbey, U, Bubeck, C, Park, I, Lieberwirth, I & Wenger, G, *Optical properties of composites of PMMA and surface-modified zincite nanoparticles*. Macromolecules, 2007. **40**(4): p. 1089-1100.
11. Costenaro, D., et al., *Preparation of luminescent ZnO nanoparticles modified with aminopropyltriethoxy silane for optoelectronic applications*. New Journal of Chemistry, 2013. **37**(7): p. 2103-2109.
12. Teng, X.M., et al., *Photoluminescence of ZnO thin films on Si substrate with and without ITO buffer layer*. Journal of Physics D: Applied Physics, 2006. **39**(3): p. 471-476.

13. Mawyin, J., et al., *Hybrid Heterojunction Nanorods for Nanoscale Controlled Morphology in Bulk Heterojunction Solar Cells*. The Journal of Physical Chemistry C, 2011. **115**(21): p. 10881-10888.
14. Kim, J. and K. Yong, *Mechanism Study of ZnO Nanorod-Bundle Sensors for H₂S Gas Sensing*. The Journal of Physical Chemistry C, 2011. **115**(15): p. 7218-7224.
15. Bakin, A., et al., *ZnMgO-ZnO quantum wells embedded in ZnO nanopillars: Towards realisation of nano-LEDs*. physica status solidi (c), 2007. **4**(1): p. 158-161.
16. Singh, N. and A. Turner, *Leaching of copper and zinc from spent antifouling paint particles*. Environ Pollut, 2009. **157**(2): p. 371-6.
17. Das, A., et al., *Preparation of zinc oxide free, transparent rubber nanocomposites using a layered double hydroxide filler*. Journal of Materials Chemistry, 2011. **21**(20).
18. Mueen, R., et al., *Na-doped ZnO UV filters with reduced photocatalytic activity for sunscreen applications*. Journal of Materials Science, 2019. **55**(7): p. 2772-2786.
19. Cho, E.C., et al., *Inorganic nanoparticle-based contrast agents for molecular imaging*. Trends Mol Med, 2010. **16**(12): p. 561-73.
20. Akhil, K., et al., *Effect of various capping agents on photocatalytic, antibacterial and antibiofilm activities of ZnO nanoparticles*. J Photochem Photobiol B, 2016. **160**: p. 32-42.
21. Tang, X., et al., *Synthesis of ZnO Nanoparticles with Tunable Emission Colors and Their Cell Labeling Applications*. Chemistry of Materials, 2010. **22**(11): p. 3383-3388.
22. Caetano, B.L., et al., *In Situ and Simultaneous UV-vis/SAXS and UV-vis/XAFS Time-Resolved Monitoring of ZnO Quantum Dots Formation and Growth*. The Journal of Physical Chemistry C, 2011. **115**(11): p. 4404-4412.
23. Shi, H.Q., et al., *Synthesis of silane surface modified ZnO quantum dots with ultrastable, strong and tunable luminescence*. Chem Commun (Camb), 2011. **47**(43): p. 11921-3.
24. van Dijken, A., Makkinje, J., and Meijerink, A., *The influence of particle size on the luminescence quantum efficiency of nanocrystalline ZnO particles*. Journal of Luminescence, 2001. **92**(4): p. 323-328.
25. van Dijken, A., Meulenkamp, E.A., Vanmaekelbergh, D., and Meijering, A., *The luminescence of nanocrystalline ZnO particles: The mechanism of the ultraviolet and visible emissions*. Journal of Luminescence, 2000. **87**(9): p. 454-456.

26. Bera, D., et al., *Photoluminescence of ZnO quantum dots produced by a sol-gel process*. Optical Materials, 2008. **30**(8): p. 1233-1239.
27. Asok, A., M.N. Gandhi, and A.R. Kulkarni, *Enhanced visible photoluminescence in ZnO quantum dots by promotion of oxygen vacancy formation*. Nanoscale, 2012. **4**(16): p. 4943-6.
28. Hodlur, R.M., M.K. Rabinal, and I. Mohamed Ikram, *Influence of dipole moment of capping molecules on the optoelectronic properties of ZnO nanoparticles*. Journal of Luminescence, 2014. **149**: p. 317-324.
29. Zeng, H., et al., *Blue Luminescence of ZnO Nanoparticles Based on Non-Equilibrium Processes: Defect Origins and Emission Controls*. Advanced Functional Materials, 2010. **20**(4): p. 561-572.
30. Rehman, N.-u., et al., *Control of optical properties of ZnO nanostructures grown by a novel two-step synthesis approach*. Chemical Physics Letters, 2014. **609**: p. 26-32.
31. Abdullah, M., Lenggoro, IW, Okuyama, K & Shi, FG, *In situ synthesis of polymer nanocomposite electrolytes emitting a high luminescence with a tunable wavelength*. Journal of Physical Chemistry B, 2003. **107**(9): p. 1957-1961.
32. Bang, J., H. Yang, and P.H. Holloway, *Enhanced and stable green emission of ZnO nanoparticles by surface segregation of Mg*. Nanotechnology, 2006. **17**(4): p. 973-8.
33. Ghosh, M. and A.K. Raychaudhuri, *Shape transition in ZnO nanostructures and its effect on blue-green photoluminescence*. Nanotechnology, 2008. **19**(44): p. 445704.
34. Zhao, L.-H. and S.-Q. Sun, *Synthesis of water-soluble ZnO nanocrystals with strong blue emission via a polyol hydrolysis route*. CrystEngComm, 2011. **13**(6): p. 1864-1869.
35. Azam, A., Ahmed, F, Arshi, N, Chaman, M, and Naqvi, A.H., *Low temperature synthesis of ZnO nanoparticles using mechanochemical route: A green chemistry approach*. International Journal of Theoretical & Applied Sciences, 2009. **1**(2): p. 12-14.
36. Janotti, A. and C.G. Van de Walle, *Fundamentals of zinc oxide as a semiconductor*. Reports on Progress in Physics, 2009. **72**(12).
37. Kolodziejczak-Radzimska, A. and T. Jesionowski, *Zinc Oxide-From Synthesis to Application: A Review*. Materials (Basel), 2014. **7**(4): p. 2833-2881.

38. Rani, S., et al., *Synthesis of nanocrystalline ZnO powder via sol–gel route for dye-sensitized solar cells*. Solar Energy Materials and Solar Cells, 2008. **92**(12): p. 1639-1645.
39. Arslan, O., L. Belkoura, and S. Mathur, *Swift synthesis, functionalization and phase-transfer studies of ultrastable, visible light emitting oleate@ZnO quantum dots*. Journal of Materials Chemistry C, 2015. **3**(45): p. 11965-11973.
40. Raoufi, D., *Synthesis and photoluminescence characterization of ZnO nanoparticles*. Journal of Luminescence, 2013. **134**: p. 213-219.
41. Ghaemi, B., et al., *Process-dependent photocatalytic performance of quantum sized ZnO nanoparticles*. Materials Research Express, 2018. **5**(11).
42. Ludi, B. and M. Niederberger, *Zinc oxide nanoparticles: chemical mechanisms and classical and non-classical crystallization*. Dalton Trans, 2013. **42**(35): p. 12554-68.
43. Parashar, V.K. and M. Gijs, *Dimensional tailoring of hydrothermally grown zinc oxide nanostructures in a continuous flow micro reactor*. Chem Commun (Camb), 2018. **54**(93): p. 13064-13067.
44. Zhao, C.-X., et al., *Nanoparticle synthesis in microreactors*. Chemical Engineering Science, 2011. **66**(7): p. 1463-1479.
45. Wang, H., et al., *Highly Luminescent CdSe/ZnS Nanocrystals Synthesized Using a Single-Molecular ZnS Source in a Microfluidic Reactor*. Advanced Functional Materials, 2005. **15**(4): p. 603-608.
46. Yen, B.K.H., et al., *A Microfabricated Gas-Liquid Segmented Flow Reactor for High-Temperature Synthesis: The Case of CdSe Quantum Dots*. Angewandte Chemie, 2005. **117**(34): p. 5583-5587.
47. Nightingale, A.M. and J.C. Demello, *Segmented flow reactors for nanocrystal synthesis*. Adv Mater, 2013. **25**(13): p. 1813-21.
48. Marre, S., et al., *High-Pressure/High-Temperature Microreactors for Nanostructure Synthesis*. Journal of the Association for Laboratory Automation, 2009. **14**(6): p. 367-373.
49. Fu, Y.S., Du, X.W., Kulinich, S.A., Qiu, J.S., Qin, W.J., Li, R., Sun, J. and Liu, J., *Stable aqueous dispersion of ZnO quantum dots with strong blue emission via simple solution route*. Journal of the American Chemical Society, 2007. **129**(51): p. 16029-16033.
50. Huang, W., et al., *The synthesis of ultrasmall ZnO@PEG nanoparticles and its fluorescence properties*. Journal of Sol-Gel Science and Technology, 2015. **74**(3): p. 718-725.

51. Gutul, T., et al., *Preparation of poly(N-vinylpyrrolidone)-stabilized ZnO colloid nanoparticles*. Beilstein J Nanotechnol, 2014. **5**: p. 402-6.
52. Segets, D., Maraczak, R, Shafer, S, Paula, C, Gnichwitz, JF, Hirsch, A & Peukert, W, *Experimental and theoretical studies on the colloidal stability of nanoparticles - a general interpretation based on stability maps*. ACS NANO, 2011. **5**(6): p. 4658-4669.
53. Mary Jacob, N. and T. Thomas, *Digestive ripening and green synthesis of ultra-small ($r < 2\text{nm}$) stable ZnO quantum dots*. Ceramics International, 2014. **40**(9): p. 13945-13952.
54. Green, M., *The nature of quantum dot capping ligands*. Journal of Materials Chemistry, 2010. **20**(28).
55. Rajabi, H.R. and M. Farsi, *Study of capping agent effect on the structural, optical and photocatalytic properties of zinc sulfide quantum dots*. Materials Science in Semiconductor Processing, 2016. **48**: p. 14-22.
56. Van Ngo, G., et al., *Synthesis of ZnO nanoparticles with tunable size and surface hydroxylation*. Journal of Nanoparticle Research, 2012. **15**(1).
57. Zimmermann, L.M., P.V. Baldissera, and I.H. Bechtold, *Stability of ZnO quantum dots tuned by controlled addition of ethylene glycol during their growth*. Materials Research Express, 2016. **3**(7).
58. Hung, C.-H. and W.-T. Whang, *Effect of surface stabilization of nanoparticles on luminescent characteristics in ZnO/poly(hydroxyethyl methacrylate) nanohybrid films*. Journal of Materials Chemistry, 2005. **15**(2).
59. Gong, X., et al., *Characterization of poly(vinyl alcohol) (PVA)/ZnO nanocomposites prepared by a one-pot method*. Composites Part B: Engineering, 2014. **60**: p. 144-149.
60. Wu, Y.L., et al., *Surface modification of ZnO nanocrystals*. Applied Surface Science, 2007. **253**(12): p. 5473-5479.
61. Moussodia, R.-O., L. Balan, and R. Schneider, *Synthesis and characterization of water-soluble ZnO quantum dots prepared through PEG-siloxane coating*. New Journal of Chemistry, 2008. **32**(8).
62. Dhingra, M., et al., *Polyaniline mediated enhancement in band gap emission of Zinc Oxide*. Composites Part B: Engineering, 2013. **45**(1): p. 1515-1520.
63. Wu, J.M. and L.Y. Tsay, *ZnO quantum dots-decorated ZnO nanowires for the enhancement of antibacterial and photocatalytic performances*. Nanotechnology, 2015. **26**(39): p. 395704.

64. Althues, H., J. Henle, and S. Kaskel, *Functional inorganic nanofillers for transparent polymers*. Chem Soc Rev, 2007. **36**(9): p. 1454-65.
65. Paul, D.R. and L.M. Robeson, *Polymer nanotechnology: Nanocomposites*. Polymer, 2008. **49**(15): p. 3187-3204.
66. Chen, X., J. Gug, and M.J. Sobkowicz, *Role of polymer/filler interactions in the linear viscoelasticity of poly(butylene succinate)/fumed silica nanocomposite*. Composites Science and Technology, 2014. **95**: p. 8-15.
67. Bousmina, M., *Study of intercalation and exfoliation processes in polymer nanocomposites*. Macromolecules, 2006. **39**(12): p. 4259-4263.
68. Jancar, J., et al., *Current issues in research on structure–property relationships in polymer nanocomposites*. Polymer, 2010. **51**(15): p. 3321-3343.
69. Zhang, Z., J.-L. Yang, and K. Friedrich, *Creep resistant polymeric nanocomposites*. Polymer, 2004. **45**(10): p. 3481-3485.
70. Mackay, M., Tuteja, A, Duxbury, PM, Hawker, CJ, Van Horn, B, Guan, ZB, Chen, GH & Krishnan, RS, *General strategies for nanoparticle dispersion*. Science, 2006. **311**(5768): p. 1740-1743.
71. To, D., et al., *Deagglomeration of nanoparticle aggregates via rapid expansion of supercritical or high-pressure suspensions*. AIChE Journal, 2009. **55**(11): p. 2807-2826.
72. Yang, J., et al., *Keys to enhancing mechanical properties of silica nanoparticle composites hydrogels: The role of network structure and interfacial interactions*. Composites Science and Technology, 2014. **95**: p. 1-7.
73. Kumar, S.K. and R. Krishnamoorti, *Nanocomposites: structure, phase behavior, and properties*. Annu Rev Chem Biomol Eng, 2010. **1**: p. 37-58.
74. Jordan, J., et al., *Experimental trends in polymer nanocomposites—a review*. Materials Science and Engineering: A, 2005. **393**(1-2): p. 1-11.
75. Gelfer, M., Burger, C, Chu, B, Hsiao, BS, Drozdov, AD, Si, M, Rafailovich, M, Sauer, BB & Gilman, JRW, *Relationships between structure and rheology in model nanocomposites of ethylene-vinyl-based copolymers and organoclays*. Macromolecules, 2005. **38**(9): p. 3765-3775.
76. Liu, W.-S., et al., *Improving the optoelectronic properties of gallium ZnO transparent conductive thin films through titanium doping*. Journal of Alloys and Compounds, 2014. **616**: p. 268-274.

77. Ashiri, R., *Development and investigation of novel nanoparticle embedded solutions with enhanced optical transparency*. Journal of Materials Research, 2014. **29**(24): p. 2949-2956.
78. Tachikawa, S., et al., *Optical Properties of ZnO Nanoparticles Capped with Polymers*. Materials (Basel), 2011. **4**(6): p. 1132-1143.
79. Xiong, H.-M., *Photoluminescent ZnO nanoparticles modified by polymers*. Journal of Materials Chemistry, 2010. **20**(21).
80. Li, Y., Yang, Y, Sun, CQ & Fu, SY, *Significant enhancements in the fluorescence and phosphorescence of ZnO quantum dots/SiO₂ nanocomposites by calcination*. Journal of Physical Chemistry C, 2008. **112**(44): p. 17397-17401.
81. Cemek, B. and Y. Demir, *Testing of the condensation characteristics and light transmissions of different plastic film covering materials*. Polymer Testing, 2005. **24**(3): p. 284-289.
82. Xie, X., et al., *Feasibility study of a new solar greenhouse covering material*. Journal of Quantitative Spectroscopy and Radiative Transfer, 2019. **224**: p. 37-43.
83. Picuno, P., *Innovative Material and Improved Technical Design for a Sustainable Exploitation of Agricultural Plastic Film*. Polymer-Plastics Technology and Engineering, 2014. **53**(10): p. 1000-1011.
84. Espí, E., et al., *The effect of different variables on the accelerated and natural weathering of agricultural films*. Polymer Degradation and Stability, 2007. **92**(12): p. 2150-2154.
85. Djakhane, K., et al., *The effect of sand wind, temperature and exposure time on tri-layer polyethylene film used as greenhouse roof*. Plastics, Rubber and Composites, 2016. **45**(8): p. 346-351.
86. Jiang, S., et al., *Encapsulation of PV Modules Using Ethylene Vinyl Acetate Copolymer as the Encapsulant*. Macromolecular Reaction Engineering, 2015. **9**(5): p. 522-529.
87. Scaffaro, R., L. Botta, and F.P. La Mantia, *Preparation and Characterization of Polyolefin-Based Nanocomposite Blown Films for Agricultural Applications*. Macromolecular Materials and Engineering, 2009. **294**(6-7): p. 445-454.
88. Abrusci, C., et al., *Photodegradation and biodegradation by bacteria of mulching films based on ethylene-vinyl acetate copolymer: Effect of pro-oxidant additives*. Journal of Applied Polymer Science, 2012. **126**(5): p. 1664-1675.
89. Dehbi, A., A.-H.I. Mourad, and A. Bouaza, *Degradation assessment of LDPE multilayer films used as a greenhouse cover: Natural and artificial aging impacts*. Journal of Applied Polymer Science, 2012. **124**(4): p. 2702-2716.

90. Badiee, A., Ashcroft, IA & Wildman, RD, *The thermo-mechanical degradation of ethylene vinyl acetate used as a solar panel adhesive and encapsulant*. International Journal of Adhesion & Adhesives, 2016. **68**: p. 212-218.
91. Liu, Z., et al., *Effect of crystal form and particle size of titanium dioxide on the photodegradation behaviour of ethylene-vinyl acetate copolymer/low density polyethylene composite*. Polymer Degradation and Stability, 2011. **96**(1): p. 43-50.
92. Ayutthaya, S.I.N. and J. Wootthikanokkhan, *Investigation of the photodegradation behaviors of an ethylene/vinyl acetate copolymer solar cell encapsulant and effects of antioxidants on the photostability of the material*. Journal of Applied Polymer Science, 2008. **107**(6): p. 3853-3863.
93. Oliveira, M.C.C.d., et al., *The causes and effects of degradation of encapsulant ethylene vinyl acetate copolymer (EVA) in crystalline silicon photovoltaic modules: A review*. Renewable and Sustainable Energy Reviews, 2018. **81**: p. 2299-2317.
94. Esthappan, S.K., A.B. Nair, and R. Joseph, *Effect of crystallite size of zinc oxide on the mechanical, thermal and flow properties of polypropylene/zinc oxide nanocomposites*. Composites Part B: Engineering, 2015. **69**: p. 145-153.
95. Maji, P.K. and A.K. Bhowmick, *Structure-property correlation of polyurethane nanocomposites: Influence of loading and nature of nanosilica and microstructure of hyperbranched polyol*. Journal of Applied Polymer Science, 2013. **127**(6): p. 4492-4504.
96. Espejo, C., et al., *Nanocomposite films with enhanced radiometric properties for greenhouse covering applications*. Journal of Plastic Film & Sheeting, 2012. **28**(4): p. 336-350.
97. Abdel-Galil, A., Ali, H.E. and Balboul, M.R., *Nano-ZnO doping induced changes in structure, mechanical and optical properties of PVA films*. Arab Journal of Nuclear Sciences and Applications, 2015. **48**(2): p. 77-89.
98. Biswal, M., et al., *Effect of functionalized nanosilica on the mechanical, dynamic-mechanical, and morphological performance of polycarbonate/nanosilica nanocomposites*. Polymer Engineering & Science, 2013. **53**(6): p. 1287-1296.
99. Zhou, L., C. Gao, and W. Xu, *Simultaneous photoluminescence import and mechanical enhancement of polymer films using silica-hybridized quantum dots*. Journal of Materials Chemistry, 2010. **20**(27).
100. Rodríguez-Tobías, H., et al., *Effect of Zinc Oxide Nanoparticles Concentration on the Mechanical Properties and UV Protection of In Situ Synthesized ABS Based Nanocomposites*. Macromolecular Symposia, 2013. **325-326**(1): p. 147-155.

101. Hoang, T., et al., *Tensile, rheological properties, thermal stability, and morphology of ethylene vinyl acetate copolymer/silica nanocomposites using EVA-g-maleic anhydride*. Journal of Composite Materials, 2013. **48**(4): p. 505-511.
102. Mumin, M.A., W.Z. Xu, and P.A. Charpentier, *Quantum dots/silica/polymer nanocomposite films with high visible light transmission and UV shielding properties*. Nanotechnology, 2015. **26**(31): p. 315702.
103. Oreski, G., G.M. Wallner, and R.W. Lang, *Ageing characterization of commercial ethylene copolymer greenhouse films by analytical and mechanical methods*. Biosystems Engineering, 2009. **103**(4): p. 489-496.
104. Wacharawichanant, S., et al., *Effect of particle sizes of zinc oxide on mechanical, thermal and morphological properties of polyoxymethylene/zinc oxide nanocomposites*. Polymer Testing, 2008. **27**(8): p. 971-976.
105. Liufu, S., H. Xiao, and Y. Li, *Investigation of PEG adsorption on the surface of zinc oxide nanoparticles*. Powder Technology, 2004. **145**(1): p. 20-24.
106. Zhao, H. and R.K.Y. Li, *A study on the photo-degradation of zinc oxide (ZnO) filled polypropylene nanocomposites*. Polymer, 2006. **47**(9): p. 3207-3217.
107. Ammala, A., Hill, AJ, Meakin, P, Pas, SJ & Turney, TW, *Degradation studies of polyolefins incorporating transparent nanoparticulate zinc oxide UV stabilizers*. Journal of Nanoparticle Research, 2002. **4**: p. 1667-174.
108. El-Bashir, S.M., et al., *Spectral Properties of PMMA Films Doped by Perylene Dye-stuffs for Photoselective Greenhouse Cladding Applications*. Polymers (Basel), 2019. **11**(3).
109. Rosen-Kligvasser, J., et al., *A novel methodology for controlled migration of antifog from thin polyolefin films*. Polymer Engineering & Science, 2014. **54**(9): p. 2023-2028.
110. Geoola, F., et al., *Quality evaluation of anti-drop properties of greenhouse cladding materials*. Polymer Testing, 2004. **23**(7): p. 755-761.
111. Duran, I.R. and G. Laroche, *Water drop-surface interactions as the basis for the design of anti-fogging surfaces: Theory, practice, and applications trends*. Adv Colloid Interface Sci, 2019. **263**: p. 68-94.
112. Irusta, L., et al., *Migration of antifog additives in agricultural films of low-density polyethylene and ethylene-vinyl acetate copolymers*. Journal of Applied Polymer Science, 2009. **111**(5): p. 2299-2307.
113. Ibrahim, S., et al., *Synthesis of super-hydrophobic polymer nanocomposites as a smart self-cleaning coating films*. Polymer Composites, 2017. **38**: p. E147-E156.

114. Slattery, R.A. and D.R. Ort, *Carbon assimilation in crops at high temperatures*. Plant Cell Environ, 2019. **42**(10): p. 2750-2758.
115. Lamnatou, C. and D. Chemisana, *Solar radiation manipulations and their role in greenhouse claddings: Fresnel lenses, NIR- and UV-blocking materials*. Renewable and Sustainable Energy Reviews, 2013. **18**: p. 271-287.
116. Espí, E., et al., *New Ultrathermic Films for Greenhouse Covers*. Journal of Plastic Film & Sheeting, 2016. **22**(1): p. 59-68.
117. Mumin, M.A., et al., *Multifunctional mesoporous silica nanoparticles in poly(ethylene-co-vinyl acetate) for transparent heat retention films*. Journal of Polymer Science Part B: Polymer Physics, 2015. **53**(12): p. 851-859.
118. Hall, D.O.R., K.K., *Photosynthesis Sixth Edition*. 1999, Cambridge, UK: Cambridge University Press.
119. El-Bashir, S.M., et al., *Red photoluminescent PMMA nanohybrid films for modifying the spectral distribution of solar radiation inside greenhouses*. Renewable Energy, 2016. **85**: p. 928-938.
120. Croce, R. and H. van Amerongen, *Natural strategies for photosynthetic light harvesting*. Nat Chem Biol, 2014. **10**(7): p. 492-501.
121. Drop, B., et al., *Light-harvesting complex II (LHCII) and its supramolecular organization in Chlamydomonas reinhardtii*. Biochim Biophys Acta, 2014. **1837**(1): p. 63-72.
122. Massa, G., Kim, HH, Wheeler, RM & Mitchell, CA, *Plant productivity in response to LED lighting*. Hortscience, 2008. **43**(7): p. 1951-1956.
123. Takahashi, S., et al., *The solar action spectrum of photosystem II damage*. Plant Physiol, 2010. **153**(3): p. 988-93.
124. Kittas, C., et al., *Effect of two UV-absorbing greenhouse-covering films on growth and yield of an eggplant soilless crop*. Scientia Horticulturae, 2006. **110**(1): p. 30-37.
125. Zhang, Y. and A. Clapp, *Overview of stabilizing ligands for biocompatible quantum dot nanocrystals*. Sensors (Basel), 2011. **11**(12): p. 11036-55.
126. Thomas, C.P., A.B. Wedding, and S.O. Martin, *Theoretical enhancement of solar cell efficiency by the application of an ideal 'down-shifting' thin film*. Solar Energy Materials and Solar Cells, 2012. **98**: p. 455-464.
127. Rothmund, R., et al., *External quantum efficiency analysis of Si solar cells with II-VI nanocrystal luminescent down-shifting layers*. Energy Procedia, 2011. **10**: p. 83-87.

128. Sheng, X., et al., *Enhanced ultraviolet responses in thin-film InGaP solar cells by down-shifting*. *Phys Chem Chem Phys*, 2013. **15**(47): p. 20434-7.
129. Kumar, S. and P.D. Sahare, *Observation of band gap and surface defects of ZnO nanoparticles synthesized via hydrothermal route at different reaction temperature*. *Optics Communications*, 2012. **285**(24): p. 5210-5216.
130. Fonseca, A.S., et al., *Parametric analysis of the growth of colloidal ZnO nanoparticles synthesized in alcoholic medium*. *Journal of Nanoparticle Research*, 2017. **19**(2).
131. Viswanatha, R., et al., *Growth mechanism of nanocrystals in solution: ZnO, a case study*. *Phys Rev Lett*, 2007. **98**(25): p. 255501.
132. Chen, Z., et al., *A sol-gel method for preparing ZnO quantum dots with strong blue emission*. *Journal of Luminescence*, 2011. **131**(10): p. 2072-2077.
133. Sikora, B., et al., *The growth kinetics of colloidal ZnO nanoparticles in alcohols*. *Journal of Sol-Gel Science and Technology*, 2011. **61**(1): p. 197-205.
134. Liu, K.-K., et al., *Large-scale synthesis of ZnO nanoparticles and their application as phosphors in light-emitting devices*. *Optical Materials Express*, 2017. **7**(7).
135. Sounart, T.L., et al., *Spatially-resolved analysis of nanoparticle nucleation and growth in a microfluidic reactor*. *Lab Chip*, 2007. **7**(7): p. 908-15.
136. Jung, J.-Y., et al., *High throughput process for the continuous preparation of quantum dots using fluid dynamically controlled reactor*. *Journal of Alloys and Compounds*, 2019. **784**: p. 816-821.
137. Nightingale, A.M. and J.C. de Mello, *Controlled synthesis of III-V quantum dots in microfluidic reactors*. *Chemphyschem*, 2009. **10**(15): p. 2612-4.
138. Kwon, B.H., et al., *Continuous in situ synthesis of ZnSe/ZnS core/shell quantum dots in a microfluidic reaction system and its application for light-emitting diodes*. *Small*, 2012. **8**(21): p. 3257-62.
139. Yang, R.D., et al., *Photoluminescence and micro-Raman scattering in ZnO nanoparticles: The influence of acetate adsorption*. *Chemical Physics Letters*, 2005. **411**(1-3): p. 150-154.
140. Kang, H.W., et al., *Continuous synthesis of zinc oxide nanoparticles in a microfluidic system for photovoltaic application*. *Nanoscale*, 2014. **6**(5): p. 2840-6.
141. Schejn, A., et al., *Size-controlled synthesis of ZnO quantum dots in microreactors*. *Nanotechnology*, 2014. **25**(14): p. 145606.

142. Yang, W., et al., *The effect of concentration precursor reagents on the excitation spectra of the ZnO quantum dots in the solution*. Materials Letters, 2015. **141**: p. 330-332.
143. Hale, P., Maddox, LM, Shapter, JG, Voelcker, NH, Ford, MJ, & Walclawik, ER, *Growth kinetics and modeling of ZnO nanoparticles*. Journal of Chemical Education, 2005. **82**(5): p. 775-778.
144. Hu, Z., G. Oskam, and P.C. Searson, *Influence of solvent on the growth of ZnO nanoparticles*. Journal of Colloid and Interface Science, 2003. **263**(2): p. 454-460.
145. Pesika, N., Stebe, KJ & Searson, PC, *Relationship between absorbance spectra and particle size distributions for quantum-sized nanocrystals*. Journal of Physical Chemistry B, 2003. **107**(38): p. 10412-10425.
146. Grabolle, M., Spieles, M, Lesnyak, V, Gaponik, N, Eychmuller, A & Resch-Genger, U, *Determination of the fluorescent quantum yield of quantum dots: suitable procedures and achievable uncertainties*. Analytical Chemistry, 2009. **81**(5): p. 6285-6294.
147. Hu, Z., et al., *Influence of the reactant concentrations on the synthesis of ZnO nanoparticles*. J Colloid Interface Sci, 2005. **288**(1): p. 313-6.
148. Wong, E.M., Bonevich, J.E. and Searson, P.C., *Growth kinetics of nanocrystalline ZnO particles from colloidal suspensions*. Journal of Physical Chemistry B, 1998. **102**(40): p. 7770-7775.
149. Zhang, S.C. and X.G. Li, *Preparation of ZnO particles by precipitation transformation method and its inherent formation mechanisms*. Colloids and Surfaces A: Physicochemical and Engineering Aspects, 2003. **226**(1-3): p. 35-44.
150. Marczak, R., et al., *Optimum between purification and colloidal stability of ZnO nanoparticles*. Advanced Powder Technology, 2010. **21**(1): p. 41-49.
151. Yavarinia, N., et al., *Effects of temperature, stirring velocity and reactant concentration on the size and the optical properties of ZnO nanoparticles*. Journal of Luminescence, 2013. **135**: p. 170-177.
152. Anžlovar, A., et al., *Impact of Inorganic Hydroxides on ZnO Nanoparticle Formation and Morphology*. Crystal Growth & Design, 2014. **14**(9): p. 4262-4269.
153. Liu, X., et al., *Controllable synthesis and change of emission color from green to orange of ZnO quantum dots using different solvents*. New Journal of Chemistry, 2015. **39**(4): p. 2881-2888.

154. Alveroglu, E., N. Yavarinia, and Y. Yilmaz, *Kinetics of ZnO nanoparticle formation via fluorescence measurements*. Journal of Luminescence, 2013. **143**: p. 741-745.
155. Kuan, C.-Y., et al., *Growth behavior, microstructure characterization and field-emission property of 6-fold hierarchical Zn/ZnO structures prepared by direct annealing*. Crystal Growth & Design, 2009. **9**(2): p. 813-819.
156. Choi, C.-H., Y.-W. Su, and C.-h. Chang, *Effects of fluid flow on the growth and assembly of ZnO nanocrystals in a continuous flow microreactor*. CrystEngComm, 2013. **15**(17).
157. Dejene, F., et al., *Optical properties of ZnO nanoparticles synthesized by varying the sodium hydroxide to zinc acetate molar ratios using a Sol-Gel process*. Open Physics, 2011. **9**(5).
158. Yang, Q., et al., *Physicochemical insights of irradiation-enhanced hydroxyl radical generation from ZnO nanoparticles*. Toxicol Res (Camb), 2016. **5**(2): p. 482-491.
159. Chang, J. and E.R. Waclawik, *Experimental and theoretical investigation of ligand effects on the synthesis of ZnO nanoparticles*. Journal of Nanoparticle Research, 2012. **14**(8).
160. Muşat, V., et al., *Size-dependent photoluminescence of zinc oxide quantum dots through organosilane functionalization*. RSC Adv., 2014. **4**(108): p. 63128-63136.
161. Musal, V., Budrugaec, P & Gheorghies, C, *Effect of reagents mixing on the thermal behavior of sol-gel precursors for silica-based nanocomposite thin films*. Journal of Thermal Analysis and Calorimetry, 2008. **94**(2): p. 373-377.
162. Zobel, M., et al., *The evolution of crystalline ordering for ligand-ornamented zinc oxide nanoparticles*. CrystEngComm, 2016. **18**(12): p. 2163-2172.
163. Maji, P., R.B. Choudhary, and M. Majhi, *Structural, electrical and optical properties of silane-modified ZnO reinforced PMMA matrix and its catalytic activities*. Journal of Non-Crystalline Solids, 2017. **456**: p. 40-48.
164. Babu, K.S., A.R. Reddy, and K.V. Reddy, *Controlling the size and optical properties of ZnO nanoparticles by capping with SiO₂*. Materials Research Bulletin, 2014. **49**: p. 537-543.
165. Snedeker, L.P., et al., *Organic phase conversion of bulk (wurtzite) ZnO to nanophase (wurtzite and zinc blende) ZnO*. Solid State Sciences, 2005. **7**(12): p. 1500-1505.

166. Hwang, R., et al., *Current approaches for safer design of engineered nanomaterials*. *Ecotoxicol Environ Saf*, 2018. **166**: p. 294-300.
167. Ghasaban, S., M. Atai, and M. Imani, *Simple mass production of zinc oxide nanostructures via low-temperature hydrothermal synthesis*. *Materials Research Express*, 2017. **4**(3).
168. Koch, S., et al., *Air bubble promoted large scale synthesis of luminescent ZnO nanoparticles*. *Journal of Materials Chemistry C*, 2015. **3**(48): p. 12430-12435.
169. Gupta, A. and R. Srivastava, *Zinc oxide nanoleaves: A scalable disperser-assisted sonochemical approach for synthesis and an antibacterial application*. *Ultrason Sonochem*, 2018. **41**: p. 47-58.
170. Wang, Y.-m., J.-h. Li, and R.-y. Hong, *Large scale synthesis of ZnO nanoparticles via homogeneous precipitation*. *Journal of Central South University*, 2012. **19**(4): p. 863-868.
171. Moghaddam, E., et al., *Photoluminescence investigation of ZnO quantum dots surface modified with silane coupling agent as a capping agent*. *Journal of Luminescence*, 2015. **168**: p. 158-162.
172. Kim, D., et al., *Continuous flow purification of nanocrystal quantum dots*. *Nanoscale*, 2014. **6**(23): p. 14467-72.
173. Kumar, V., et al., *Influence of ultrasonication times on the tunable colour emission of ZnO nanophosphors for lighting applications*. *Ultrason Sonochem*, 2014. **21**(4): p. 1549-56.
174. Bera, S., et al., *Analysis on Binding Energy and Auger Parameter for Estimating Size and Stoichiometry of ZnO Nanorods*. *International Journal of Spectroscopy*, 2012. **2012**: p. 1-4.
175. Haranath, D., et al., *Investigation of confinement effects in ZnO quantum dots*. *Nanotechnology*, 2009. **20**(42): p. 425701.
176. Winiarski, J., et al., *XPS and FT-IR Characterization of Selected Synthetic Corrosion Products of Zinc Expected in Neutral Environment Containing Chloride Ions*. *Journal of Spectroscopy*, 2018. **2018**: p. 1-14.
177. Fakhari, S., M. Jamzad, and H. Kabiri Fard, *Green synthesis of zinc oxide nanoparticles: a comparison*. *Green Chemistry Letters and Reviews*, 2019. **12**(1): p. 19-24.
178. Lin, K.-F., et al., *Band gap variation of size-controlled ZnO quantum dots synthesized by sol-gel method*. *Chemical Physics Letters*, 2005. **409**(4-6): p. 208-211.

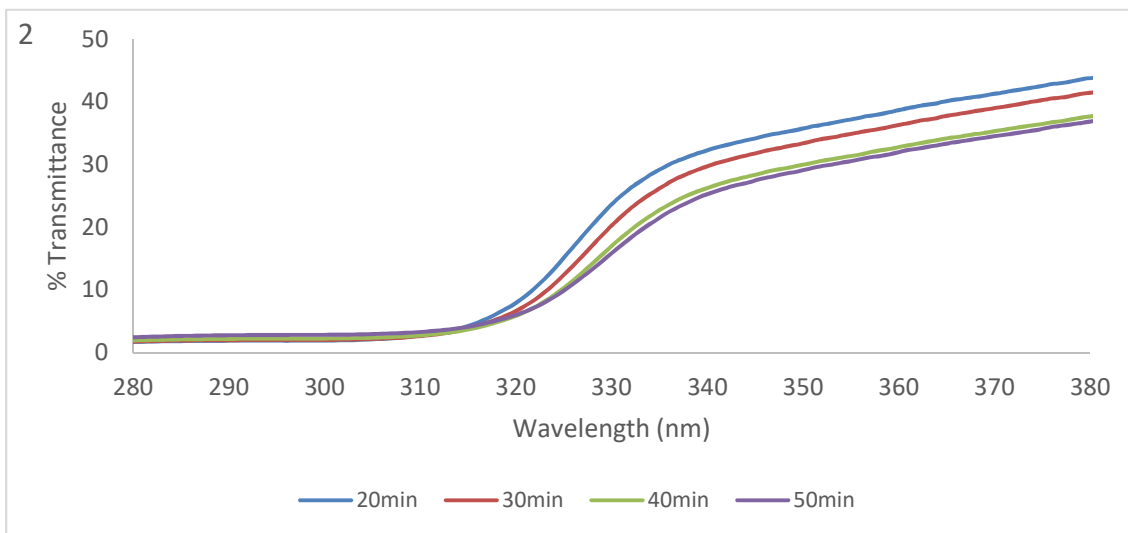
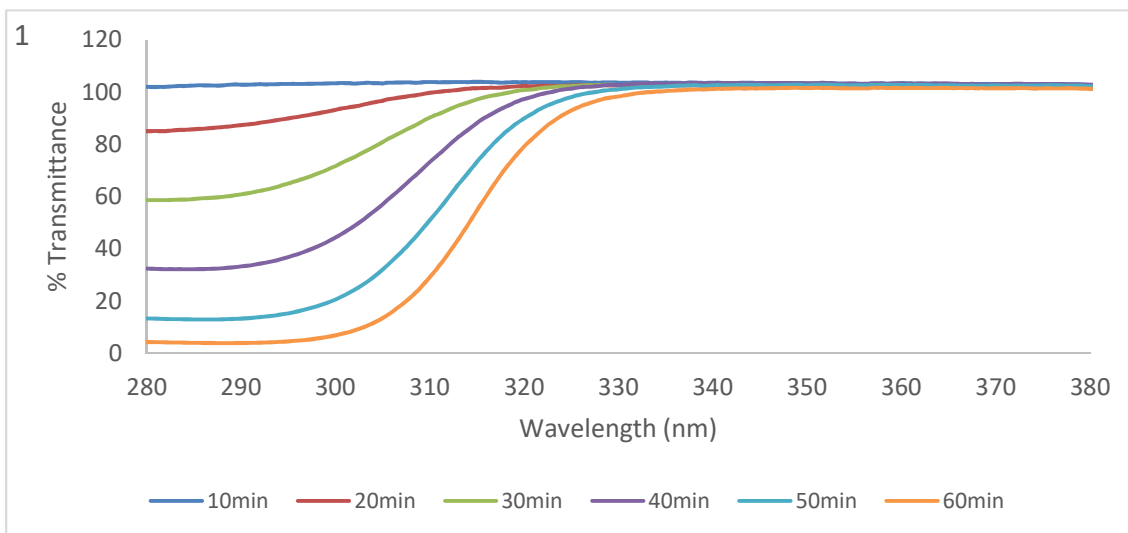
179. Niederdraenk, F., et al., *Ensemble modeling of very small ZnO nanoparticles*. Phys Chem Chem Phys, 2011. **13**(2): p. 498-505.
180. Limaye, M.V., et al., *Epitaxially grown zinc-blende structured Mn doped ZnO nanoshell on ZnS nanoparticles*. Materials Research Bulletin, 2009. **44**(2): p. 339-344.
181. Baah, C.B., Ji, *Polypropylene degradation in NaOH environments*. Materials and Design, 2002. **23**: p. 341-343.
182. Xu, X., et al., *Identification of visible emission from ZnO quantum dots: Excitation-dependence and size-dependence*. Journal of Applied Physics, 2012. **111**(8).
183. Wondraczek, L., et al., *Shifting the Sun: Solar Spectral Conversion and Extrinsic Sensitization in Natural and Artificial Photosynthesis*. Adv Sci (Weinh), 2015. **2**(12): p. 1500218.
184. Matsuyama, K., et al., *Transparent polymeric hybrid film of ZnO nanoparticle quantum dots and PMMA with high luminescence and tunable emission color*. J Colloid Interface Sci, 2012. **367**(1): p. 171-7.
185. Vox, G. and E. Schettini, *Effects of agrochemicals, ultra violet stabilisers and solar radiation on the radiometric properties of greenhouse films*. Journal of Agricultural Engineering, 2013. **44**(2).
186. Murariu, M., et al., *Current progress in the production of PLA-ZnO nanocomposites: Beneficial effects of chain extender addition on key properties*. Journal of Applied Polymer Science, 2015. **132**(48): p. 1-10.
187. Long, D.A., *Infrared and Raman characteristic group frequencies. Tables and charts George Socrates John Wiley and Sons, Ltd, Chichester, Third Edition, 2001. Price £135*. Journal of Raman Spectroscopy, 2004. **35**(10): p. 905-905.
188. Mandal, S. and S. Alam, *Dynamic mechanical analysis and morphological studies of glass/bamboo fiber reinforced unsaturated polyester resin-based hybrid composites*. Journal of Applied Polymer Science, 2012. **125**(S1): p. E382-E387.
189. Tian, M., L. Cheng, and L. Zhang, *Interface and mechanical properties of peroxide cured silicate nanofiber/rubber composites*. Journal of Applied Polymer Science, 2008. **110**(1): p. 262-269.
190. Lopez, J.F., L.D. Perez, and B.L. Lopez, *Effect of silica modification on the chemical interactions in NBR-based composites*. Journal of Applied Polymer Science, 2011. **122**(3): p. 2130-2138.
191. Cruz, S.M. and J.C. Viana, *Structure-Properties Relationships in Thermoplastic Polyurethane Elastomer Nanocomposites: Interactions between Polymer Phases*

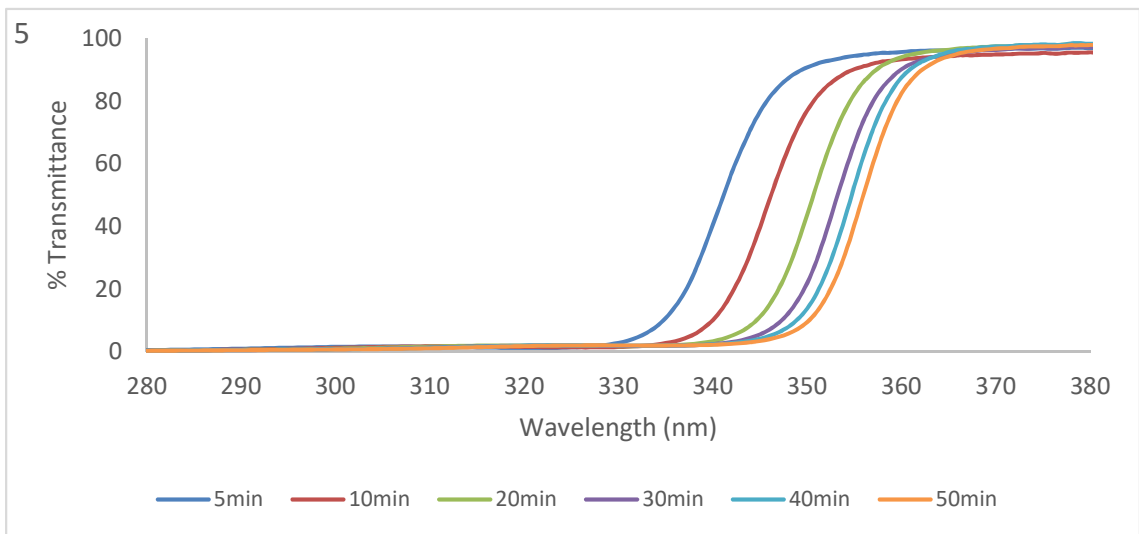
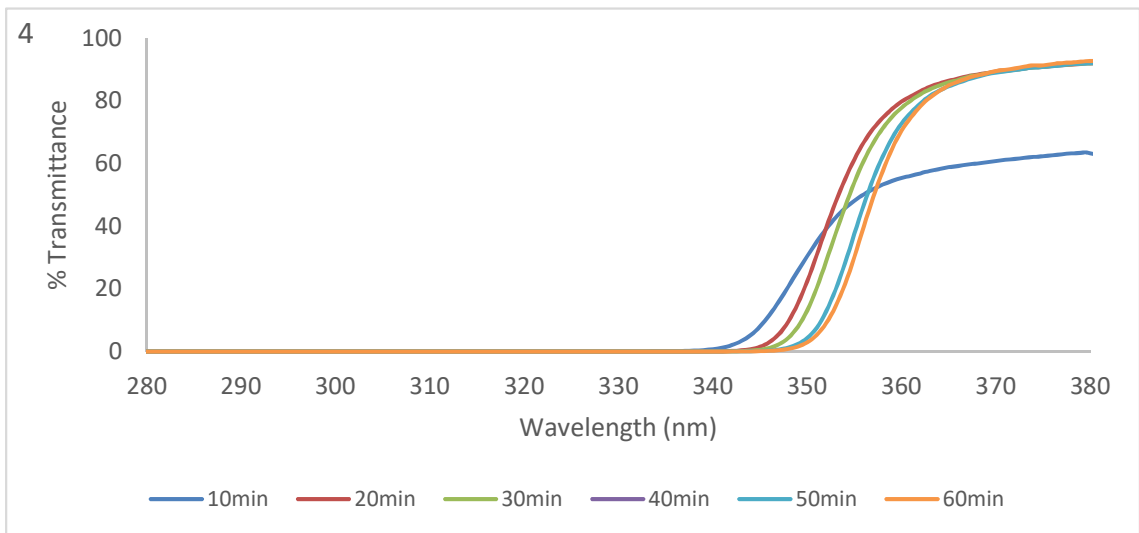
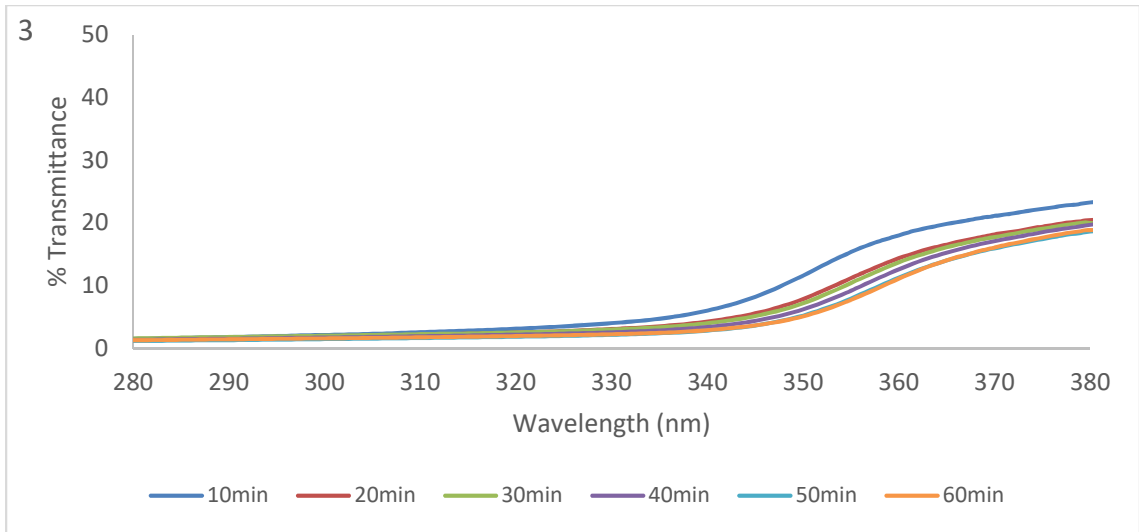
- and Nanofillers*. Macromolecular Materials and Engineering, 2015. **300**(11): p. 1153-1162.
192. Ma, C.-C.M., Y.-J. Chen, and H.-C. Kuan, *Polystyrene nanocomposite materials: Preparation, morphology, and mechanical, electrical, and thermal properties*. Journal of Applied Polymer Science, 2005. **98**(5): p. 2266-2273.
 193. Gagliardi, M., P. Lenarda, and M. Paggi, *A reaction-diffusion formulation to simulate EVA polymer degradation in environmental and accelerated ageing conditions*. Solar Energy Materials and Solar Cells, 2017. **164**: p. 93-106.
 194. Badiee, A., I.A. Ashcroft, and R.D. Wildman, *The thermo-mechanical degradation of ethylene vinyl acetate used as a solar panel adhesive and encapsulant*. International Journal of Adhesion and Adhesives, 2016. **68**: p. 212-218.
 195. Demir, M.M., et al., *Optical Properties of Composites of PMMA and Surface-Modified Zincite Nanoparticles*. Macromolecules, 2007. **40**(4): p. 1089-1100.
 196. Seven, S.A., et al., *Insecticide-releasing LLDPE films as greenhouse cover materials*. Materials Today Communications, 2019. **19**: p. 170-176.
 197. He, R.T., T., *Room Temperature Synthesis of ZnO Quantum Dots by Polyol Methods*, in *State-of-the-Art Quantum Dot Systems Fabrications*, A. Al-Ahmadid, Editor. 2012, Intech.
 198. Li, Y.-N., et al., *Effect of annealing atmospheres on photo-luminescence property of ZnO nano-thin films*. Materials Research Bulletin, 2012. **47**(11): p. 3508-3512.
 199. Hoffmann, A.M., G. Noga, and M. Hunsche, *High blue light improves acclimation and photosynthetic recovery of pepper plants exposed to UV stress*. Environmental and Experimental Botany, 2015. **109**: p. 254-263.
 200. Morrow, R., *LED Lighting in Horticulture*. Hortscience, 2008. **43**(7): p. 1947-1950.
 201. Singh, S.P. and P. Singh, *Effect of temperature and light on the growth of algae species: A review*. Renewable and Sustainable Energy Reviews, 2015. **50**: p. 431-444.
 202. Jeffrey, S.W. and G.F. Humphrey, *New spectrophotometric equations for determining chlorophylls a, b, c1 and c2 in higher plants, algae and natural phytoplankton*. Biochemie und Physiologie der Pflanzen, 1975. **167**(2): p. 191-194.
 203. Park, Y. and E.S. Runkle, *Spectral effects of light-emitting diodes on plant growth, visual color quality, and photosynthetic photon efficacy: White versus blue plus red radiation*. PLoS One, 2018. **13**(8): p. e0202386.

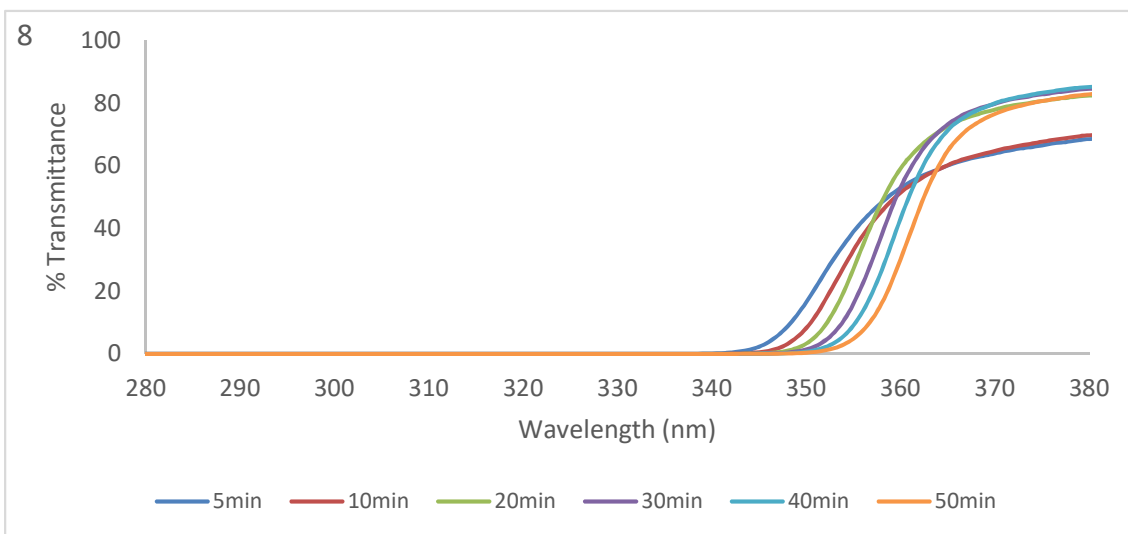
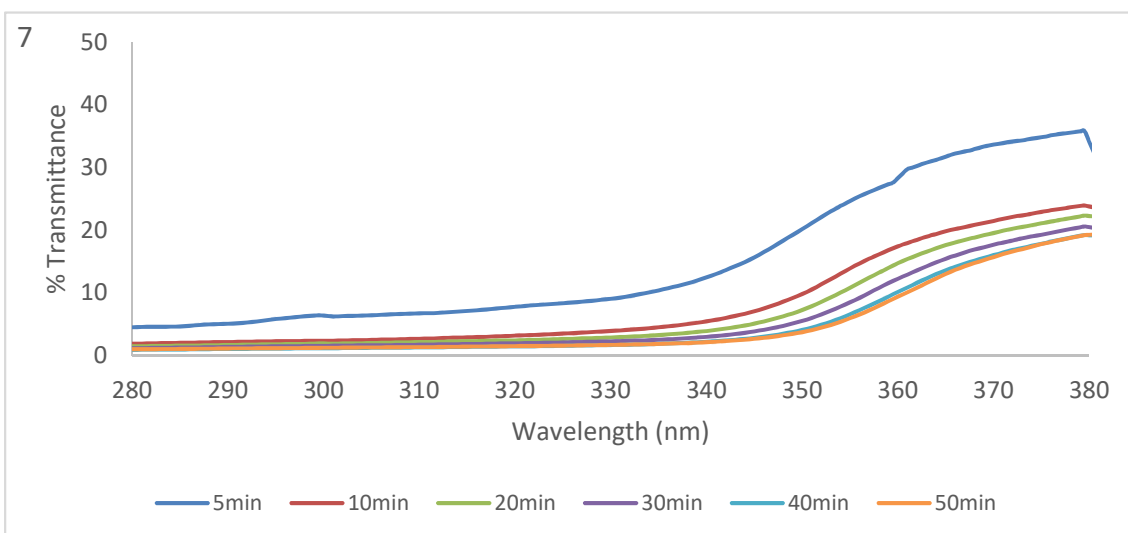
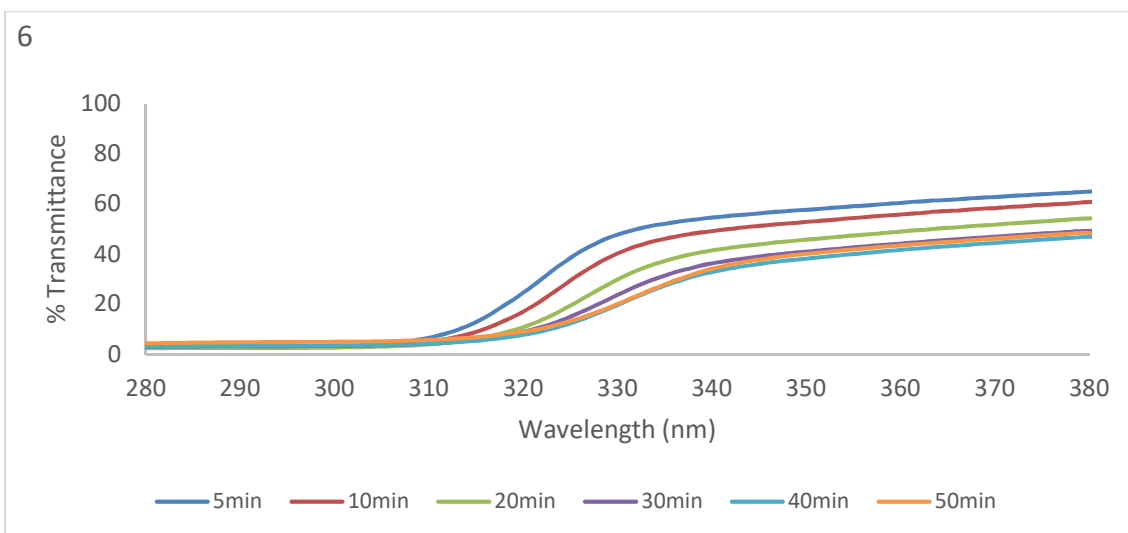
204. Yang, Y., et al., *Novel ultraviolet-opaque, visible-transparent and light-emitting ZnO-QD/silicone composites with tunable luminescence colors*. Polymer, 2010. **51**(12): p. 2755-2762.
205. Emekli, N.Y., K. Büyüktaş, and A. Başçetinçelik, *Changes of the light transmittance of the LDPE films during the service life for greenhouse application*. Journal of Building Engineering, 2016. **6**: p. 126-132.
206. Sharma, P.K., et al., *Luminescence studies and formation mechanism of symmetrically dispersed ZnO quantum dots embedded in SiO₂ matrix*. Journal of Luminescence, 2009. **129**(6): p. 605-610.

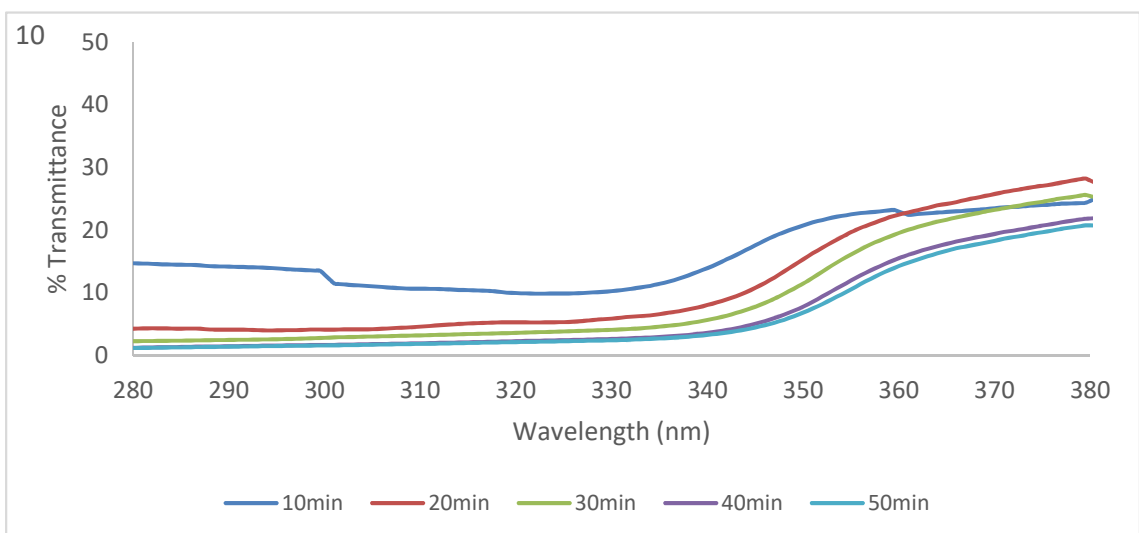
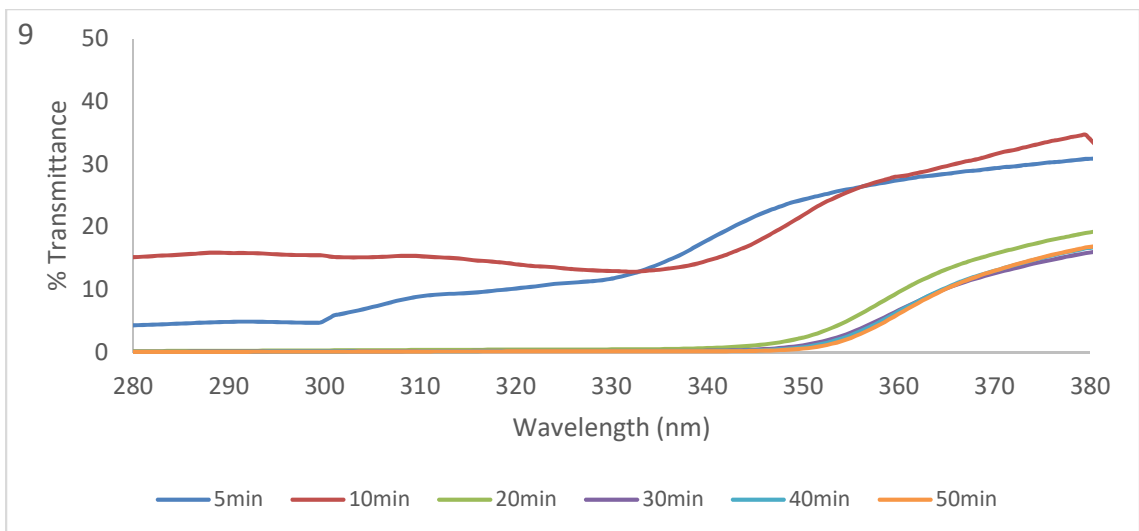
Appendices

Appendix A: Transmittance vs wavelength graphs obtained for batch DOE trials from Chapter 2 showing change in UV-VIS spectrum over time during the ZnO synthesis reaction. Each chart is labelled accordingly to what trial they represent.

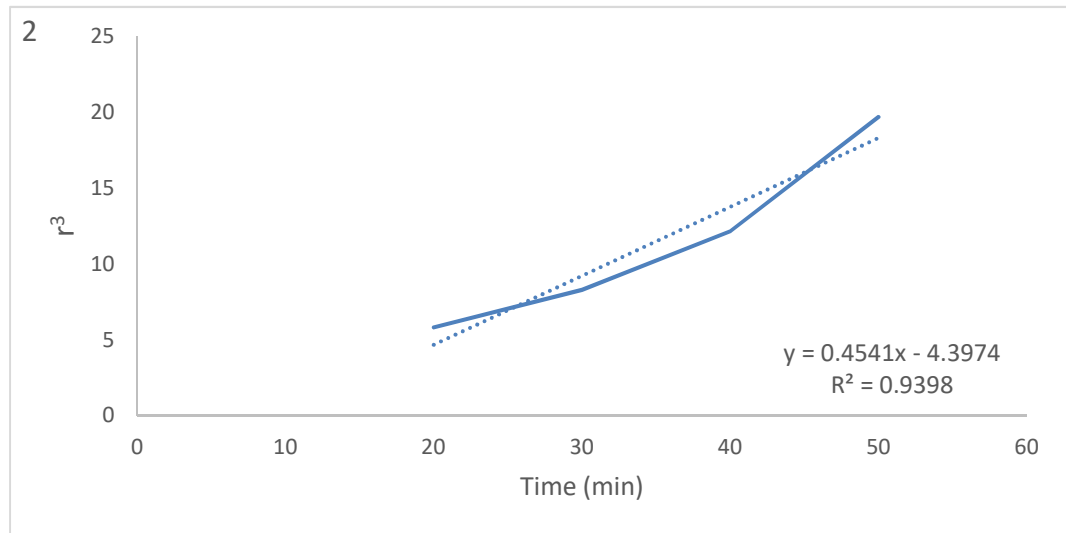
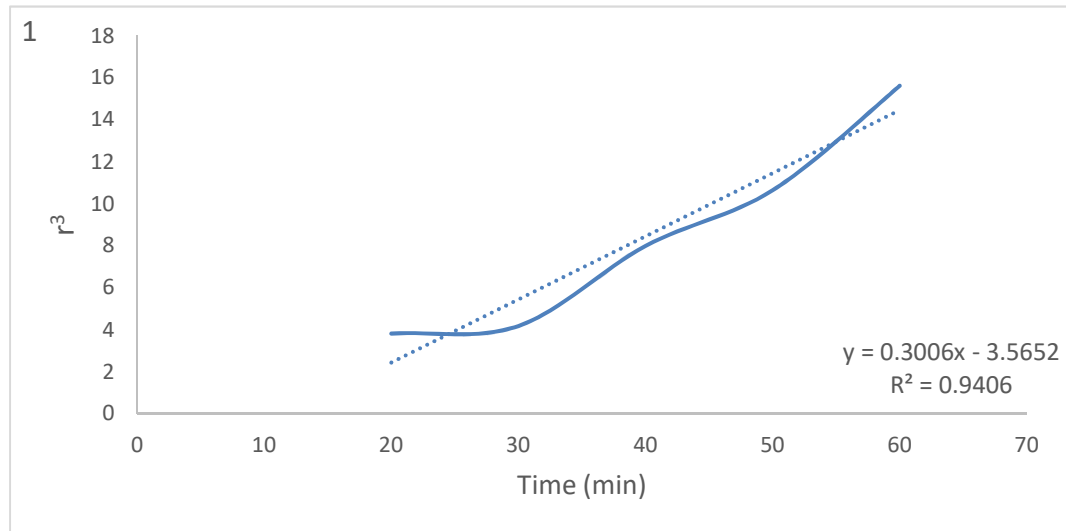


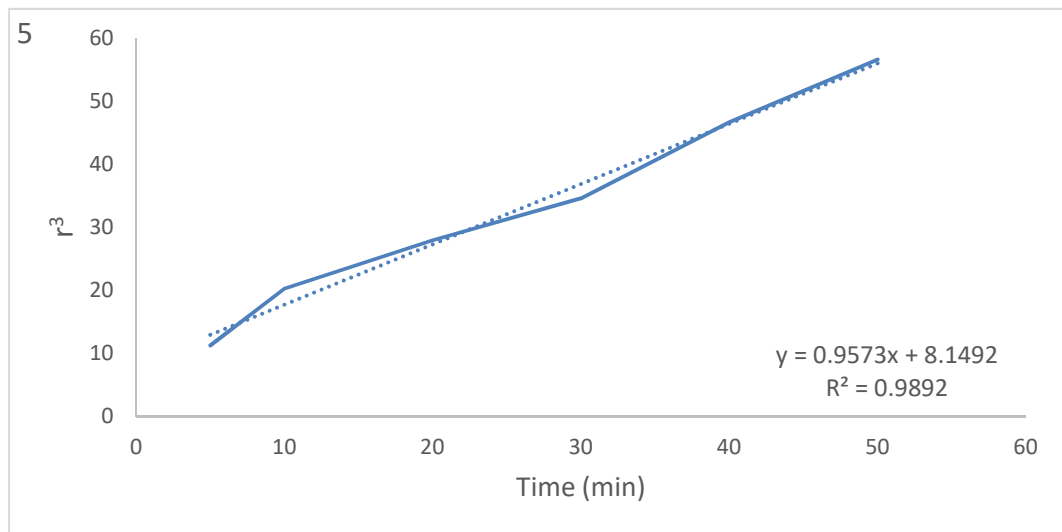
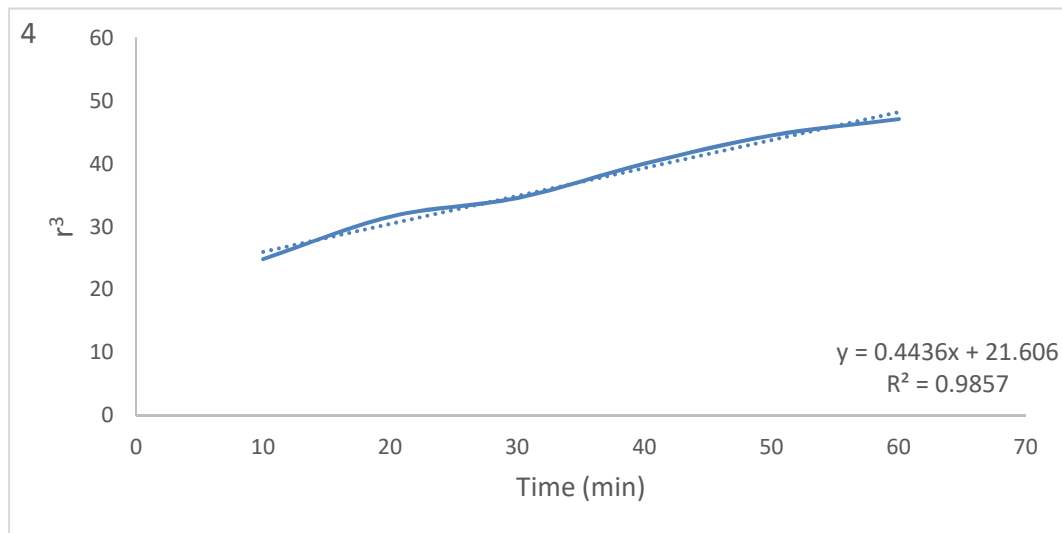
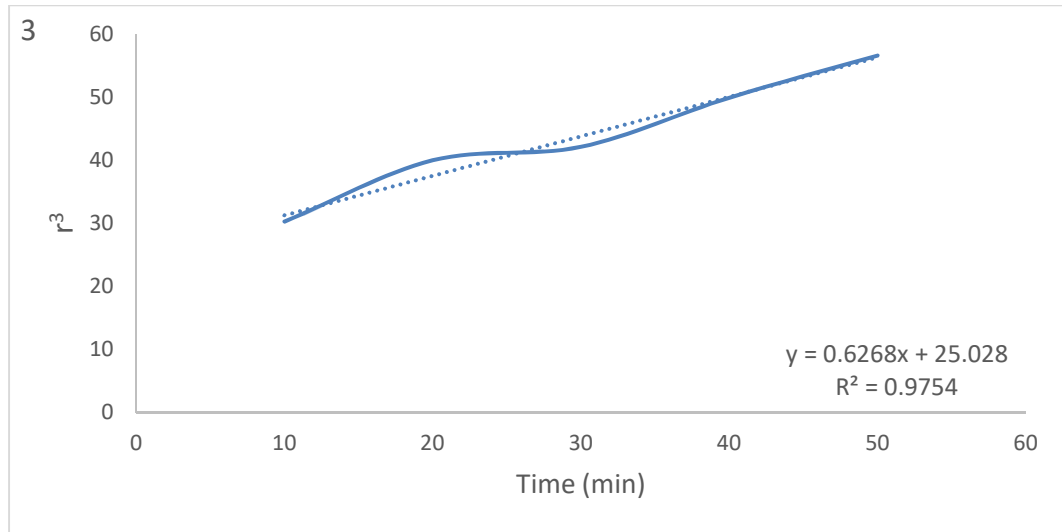


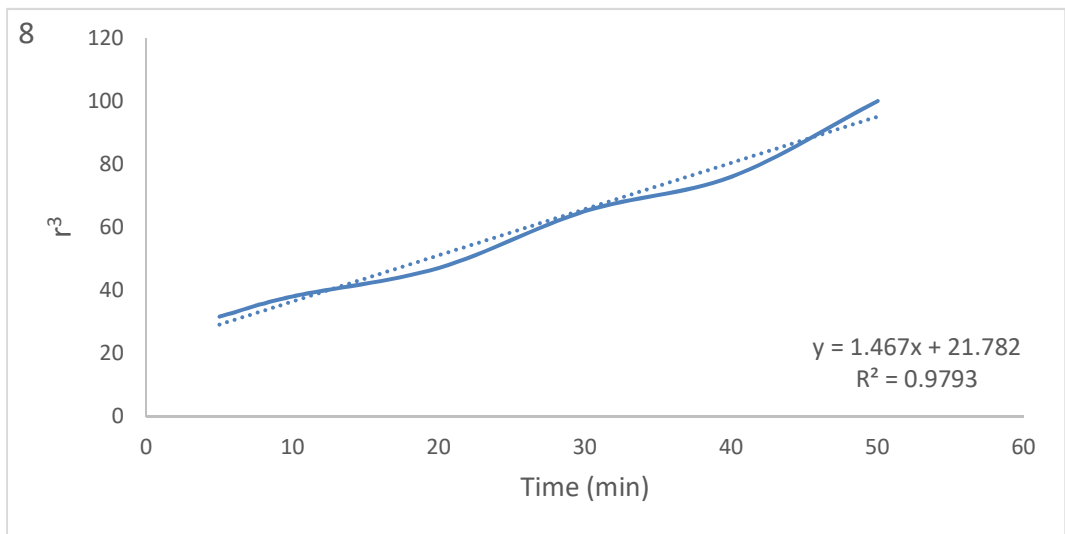
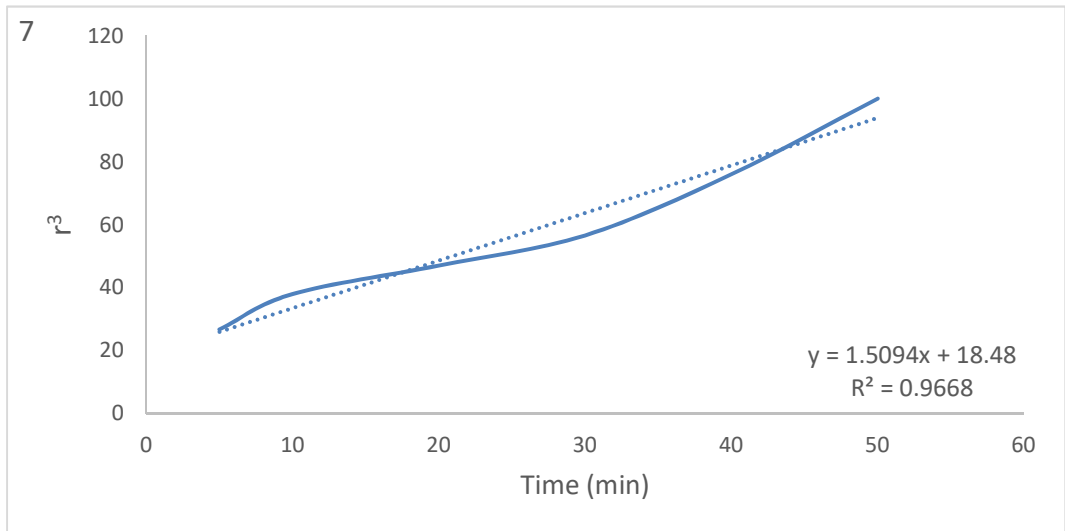
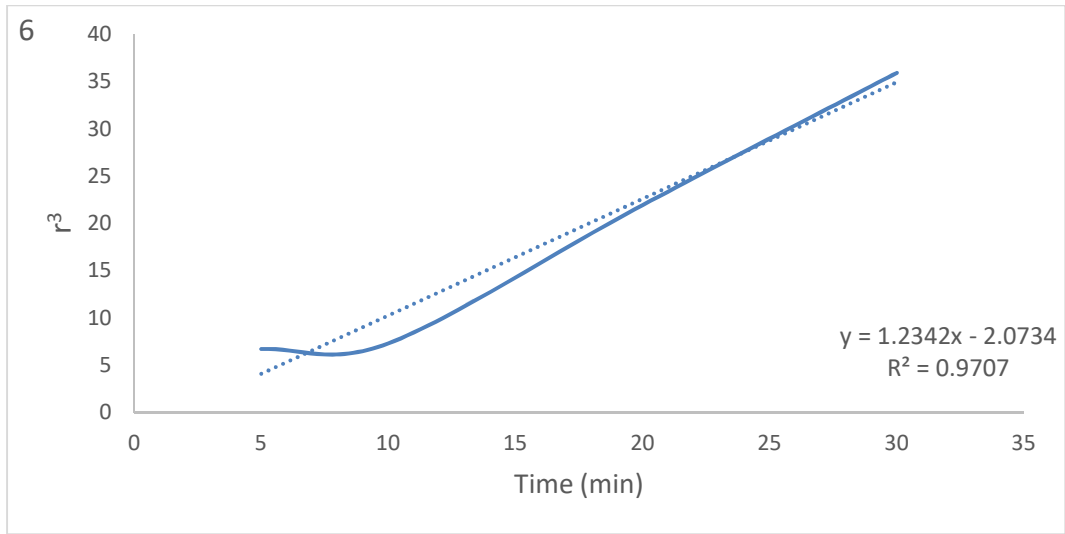


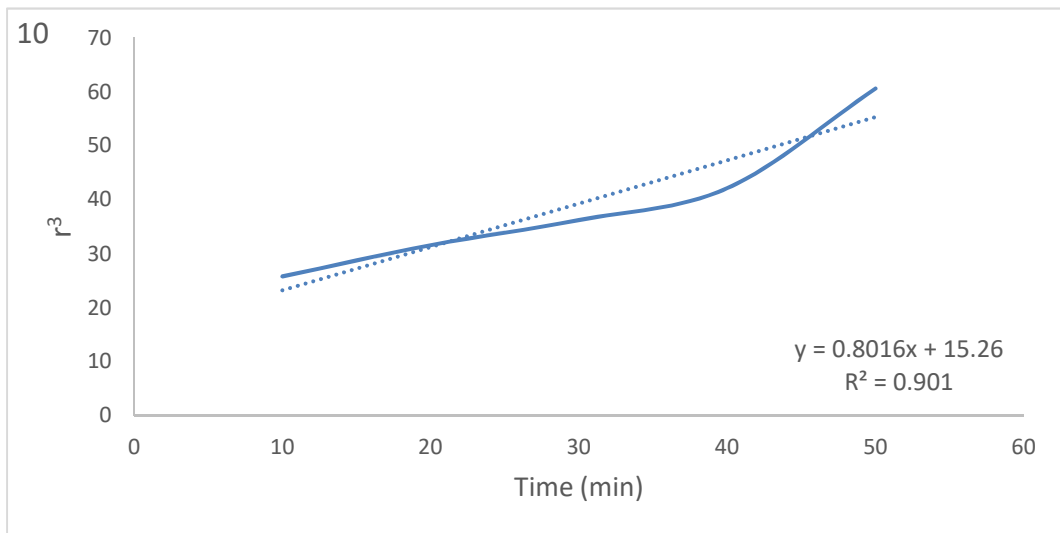
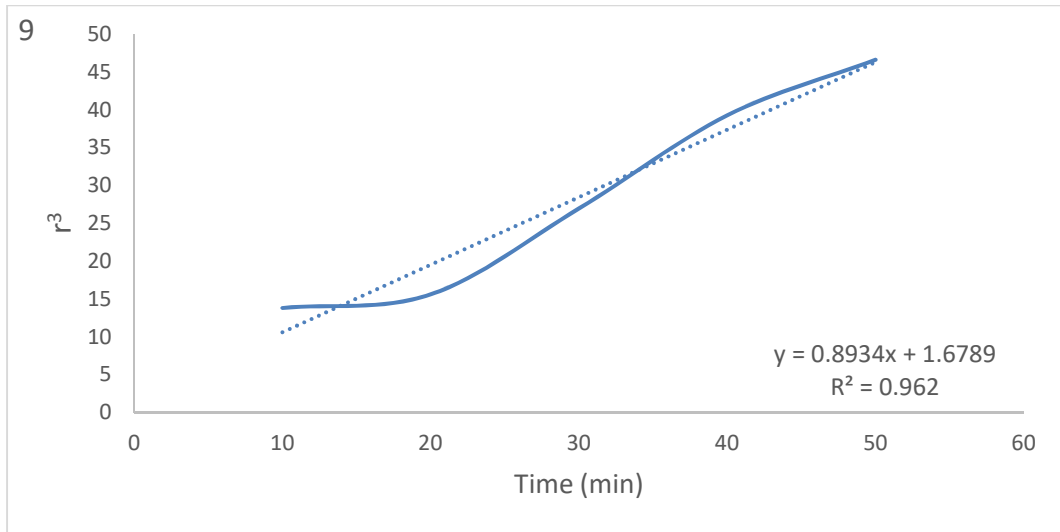


Appendix B: Cubed radius vs time graphs obtained for batch DOE trials from Chapter 2. Each chart is labelled accordingly to what trial they represent.

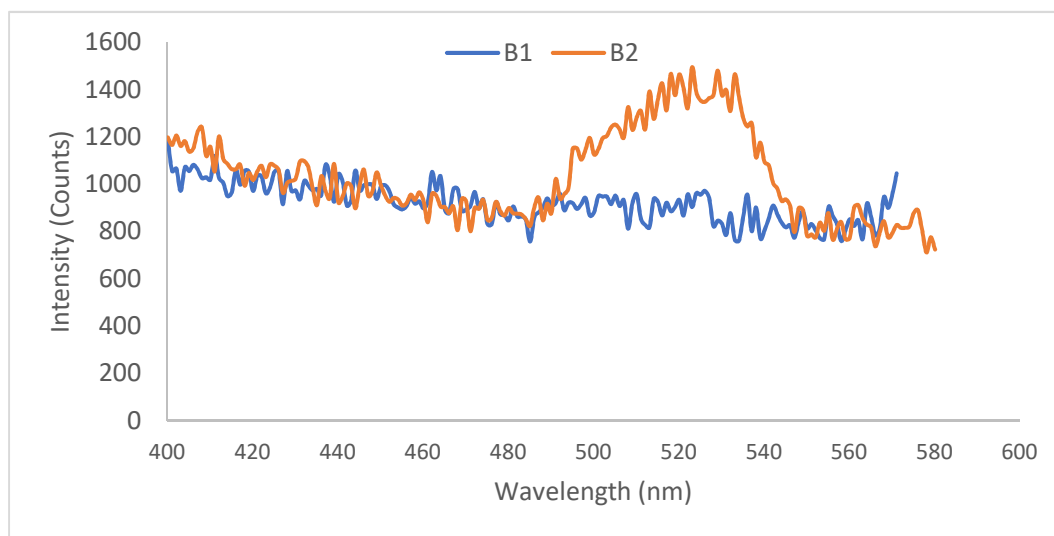
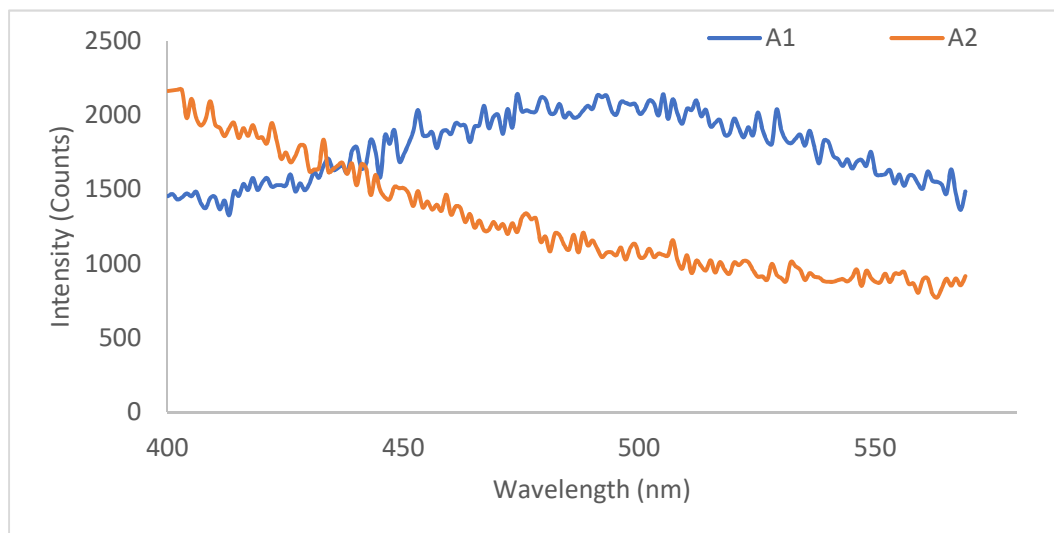


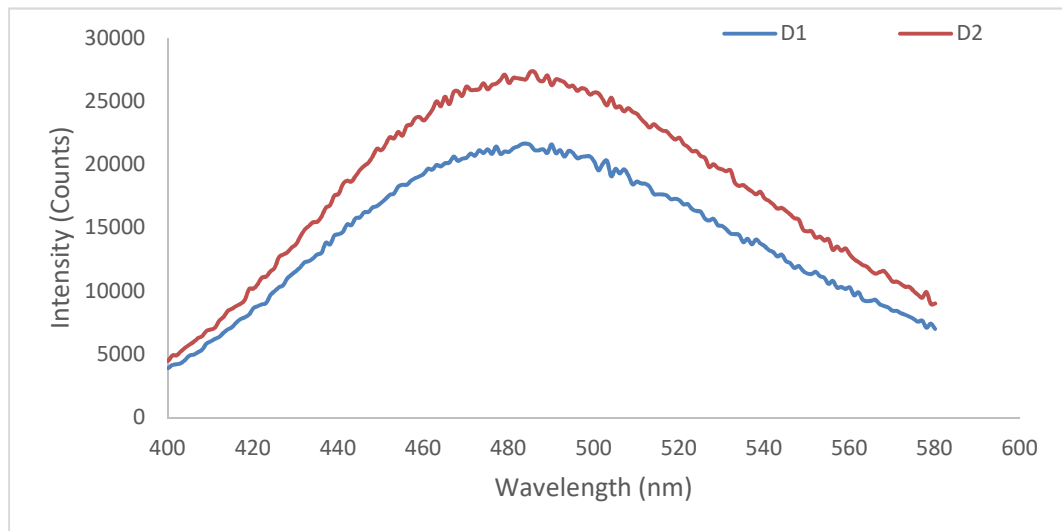
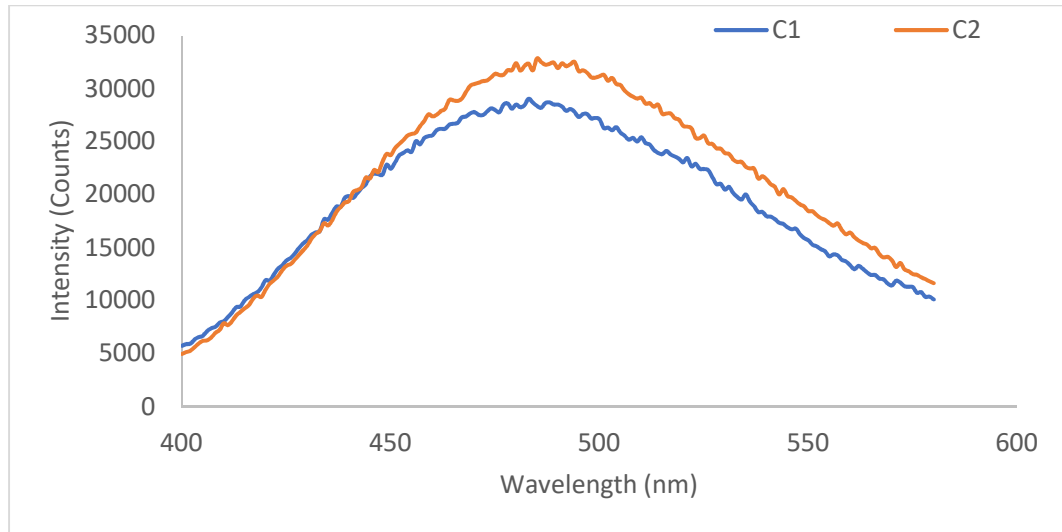




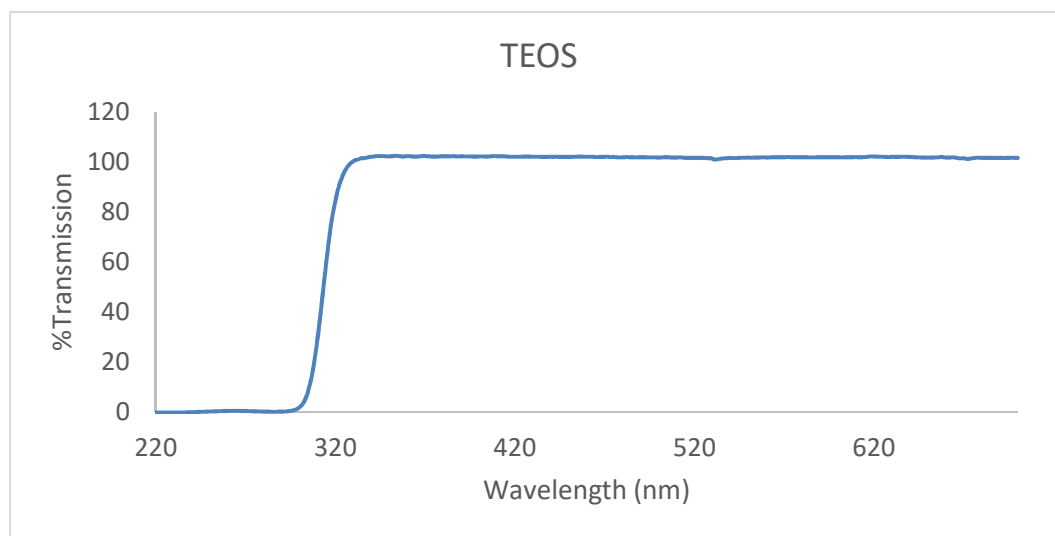
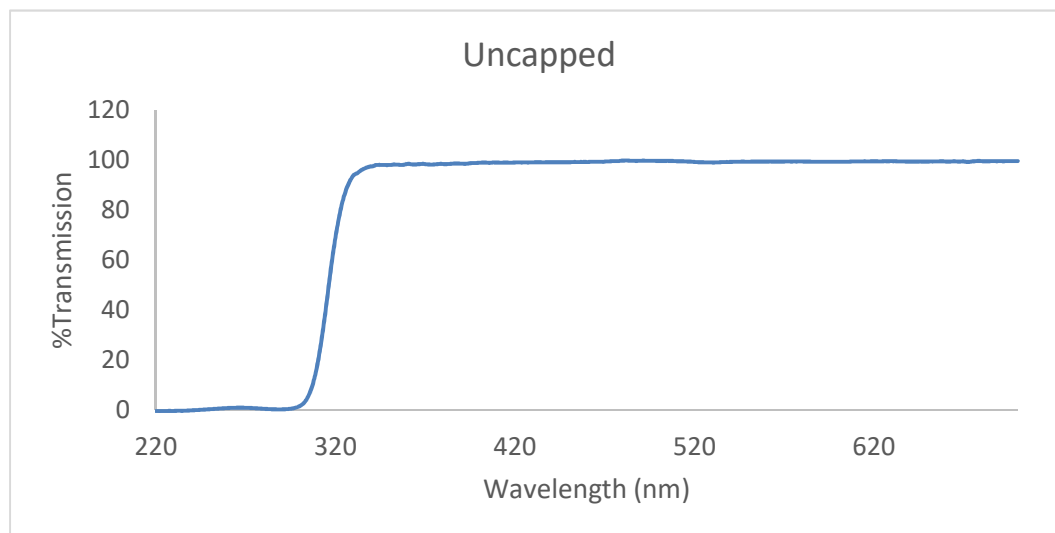


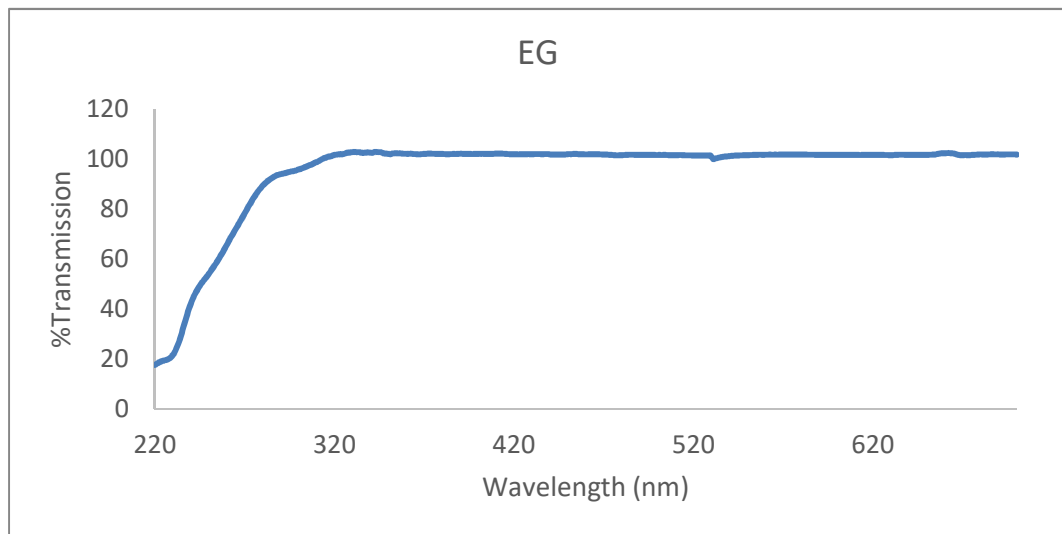
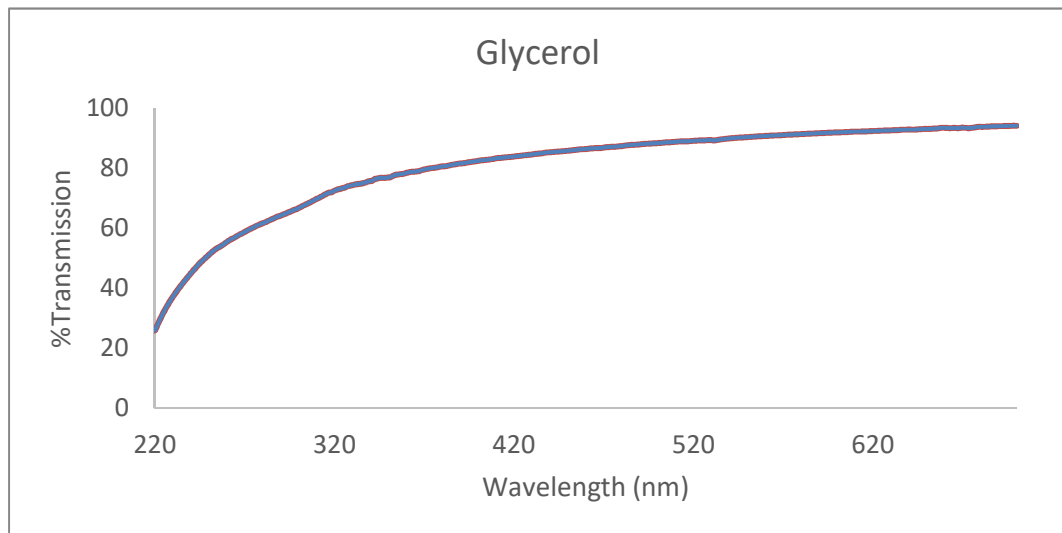
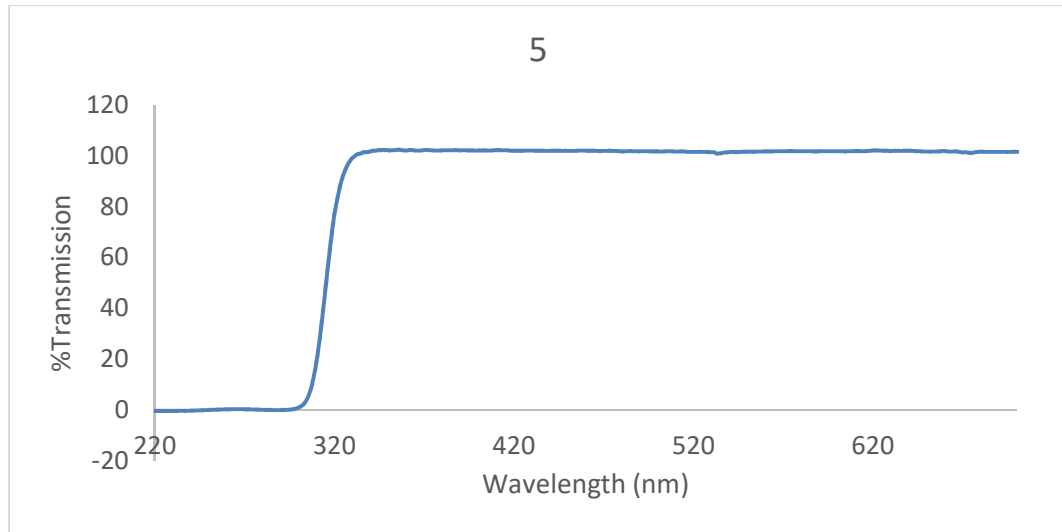
**Appendix C: Photoluminescence spectra for PFR synthesized ZnO quantum dots
from Chapter 2.**

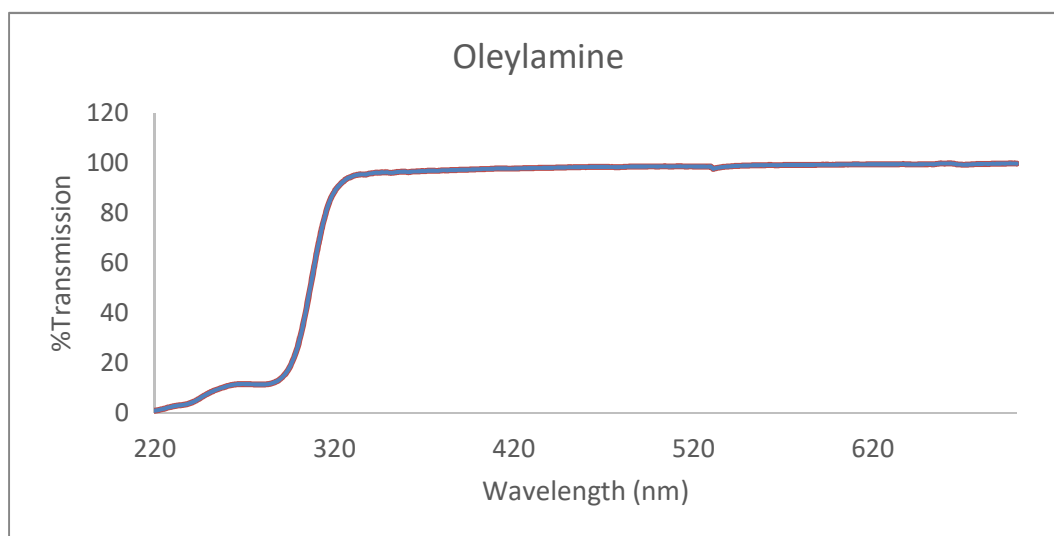
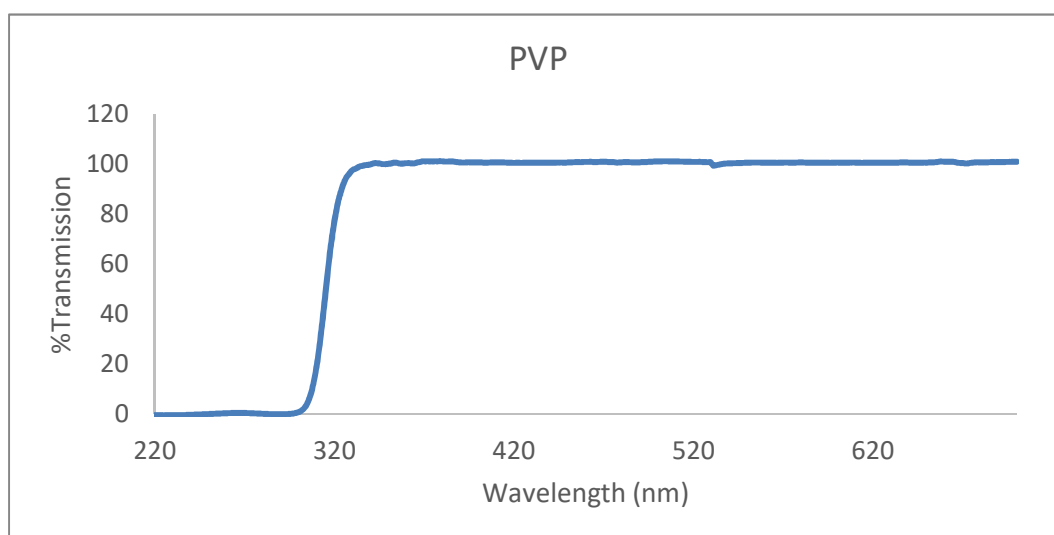
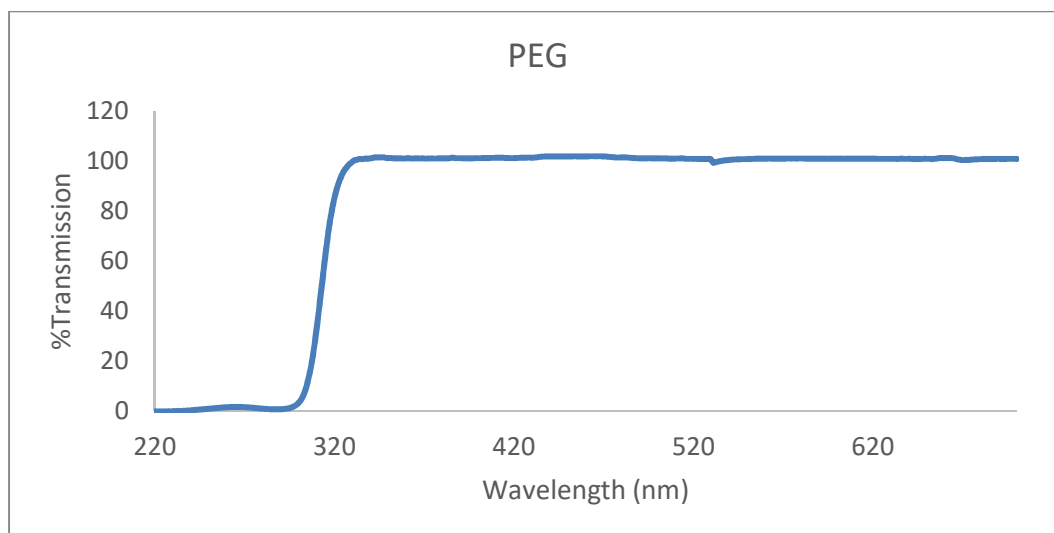


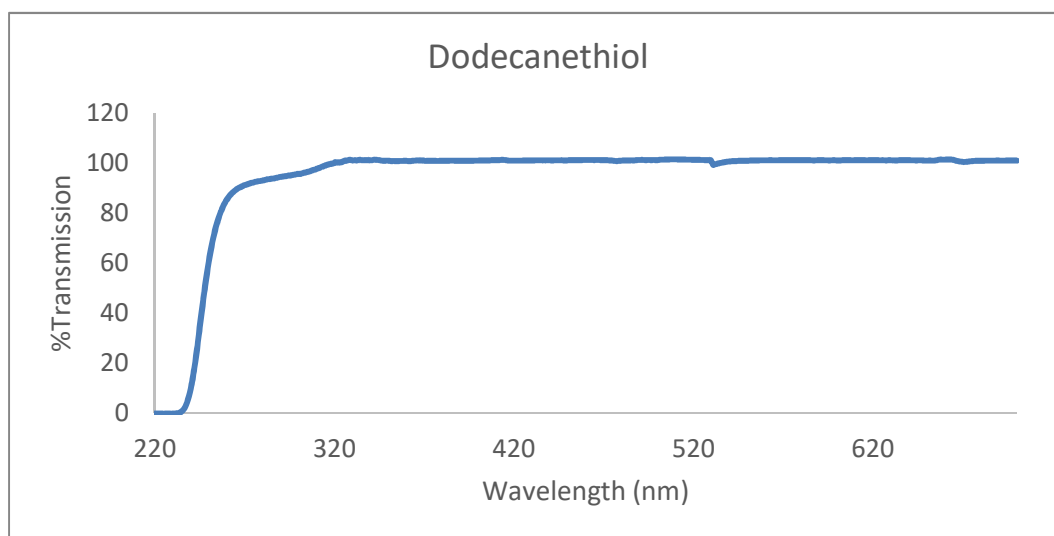
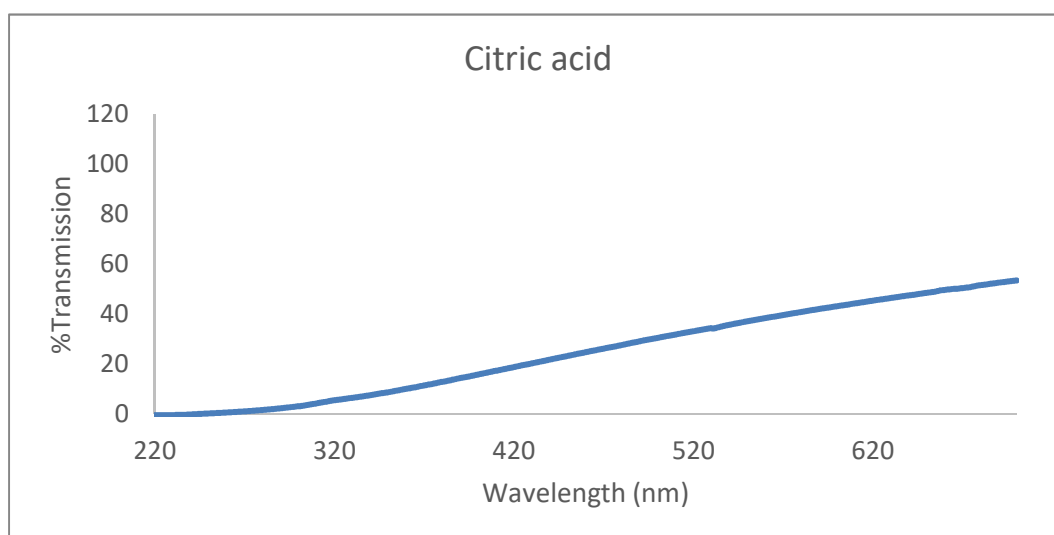
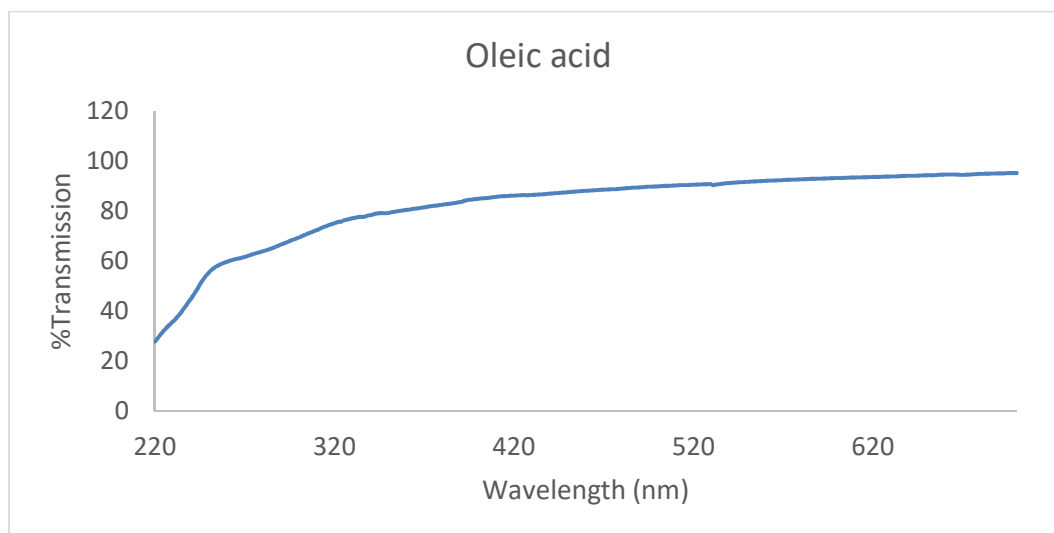


Appendix D: UV-VIS transmission spectra for differently capped ZnO quantum dots synthesized in PFR.

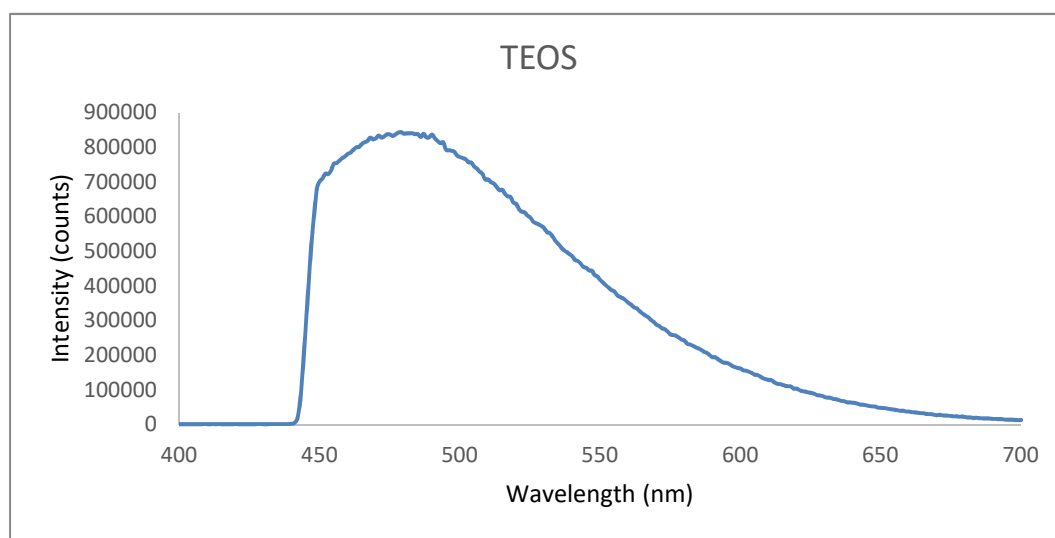
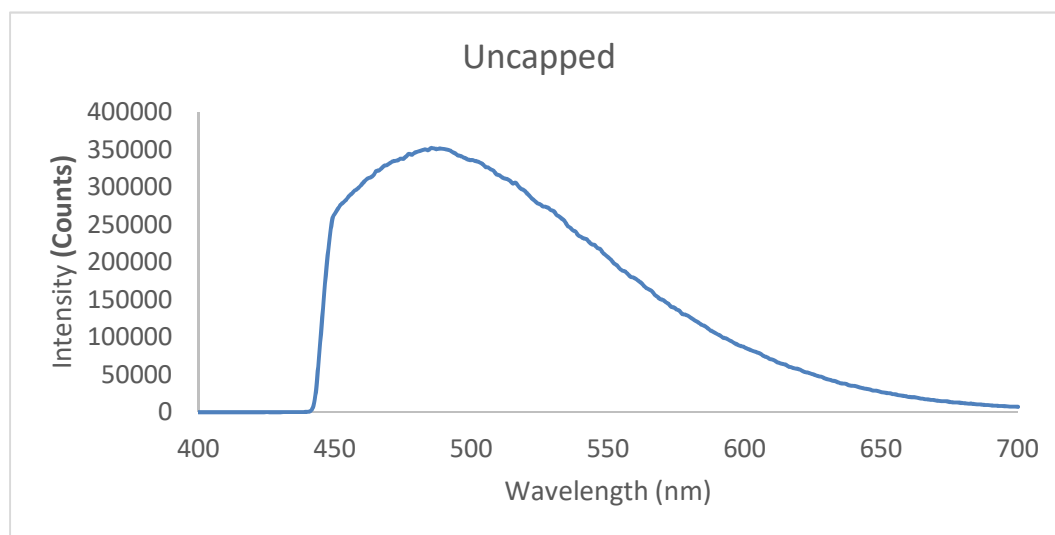


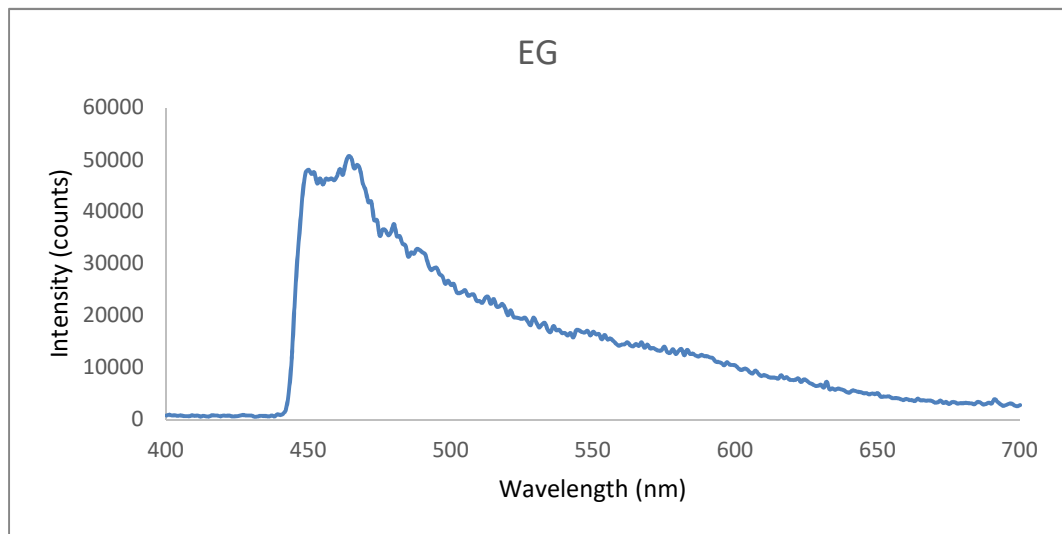
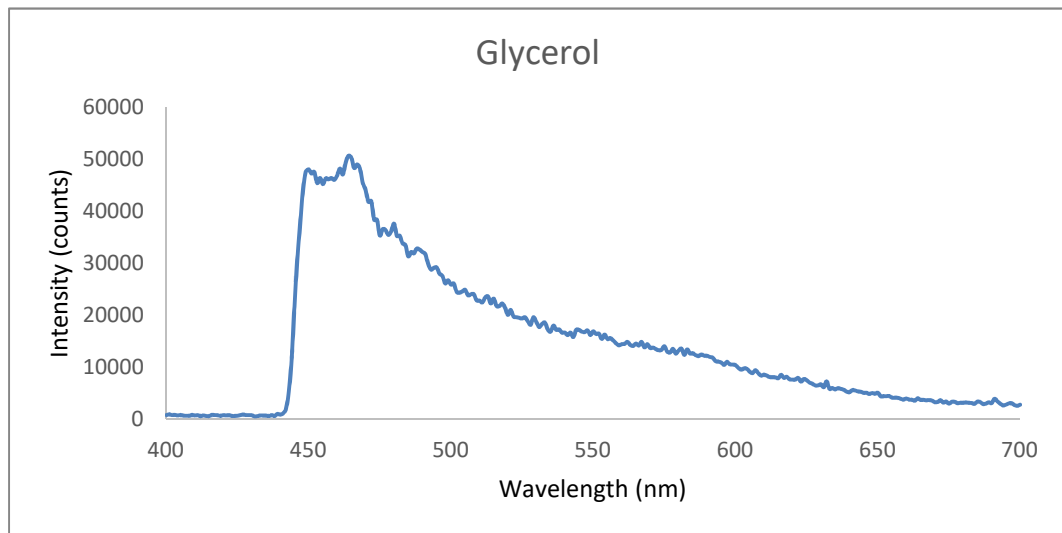
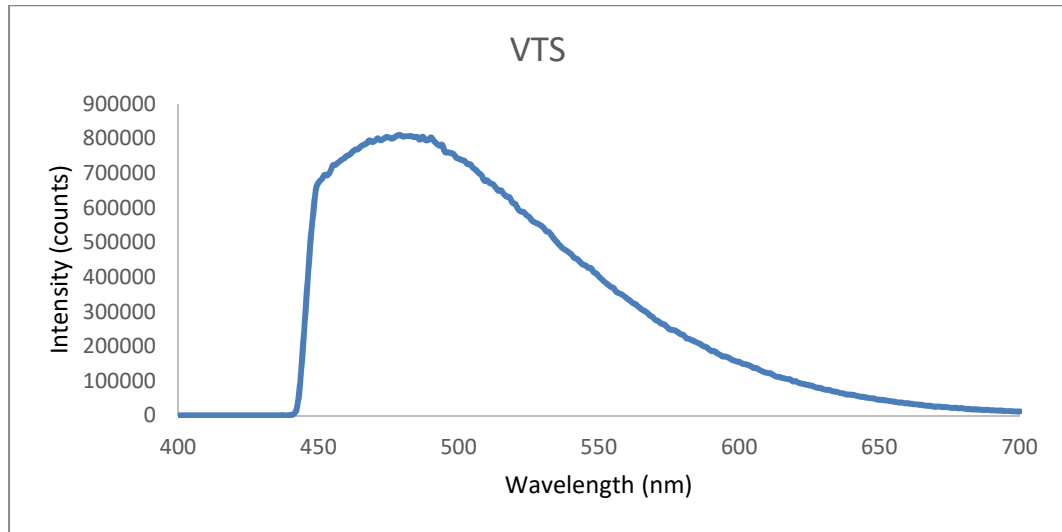


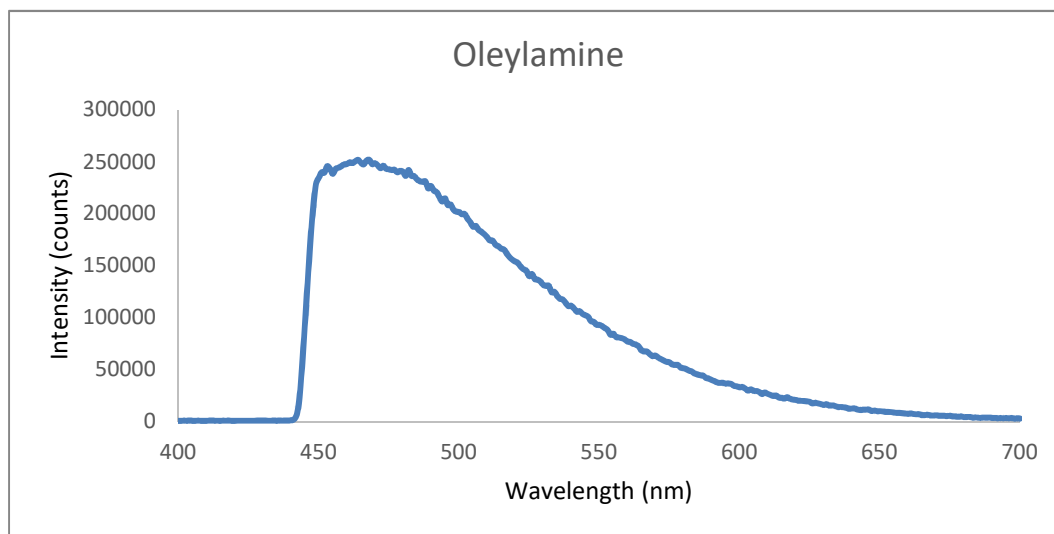
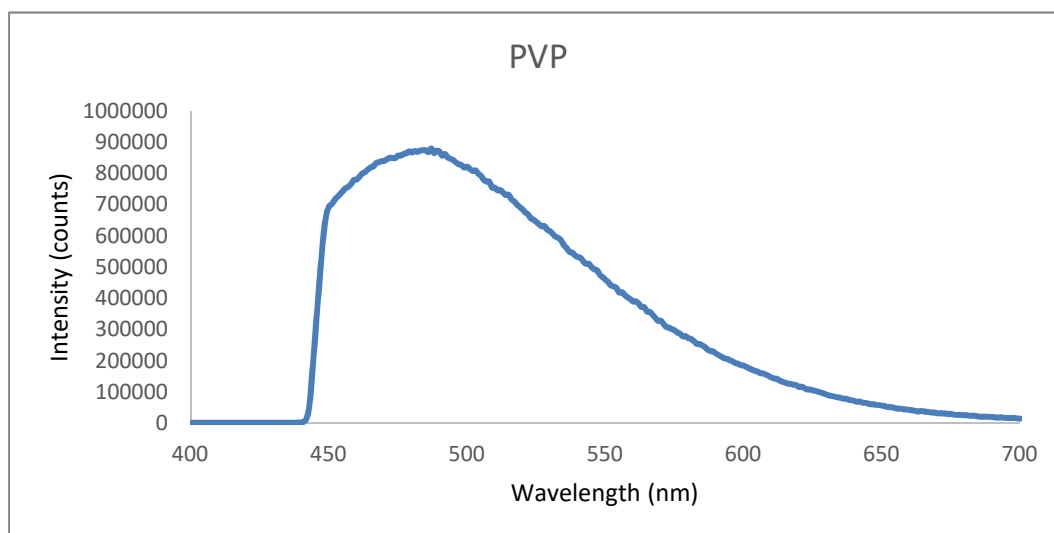
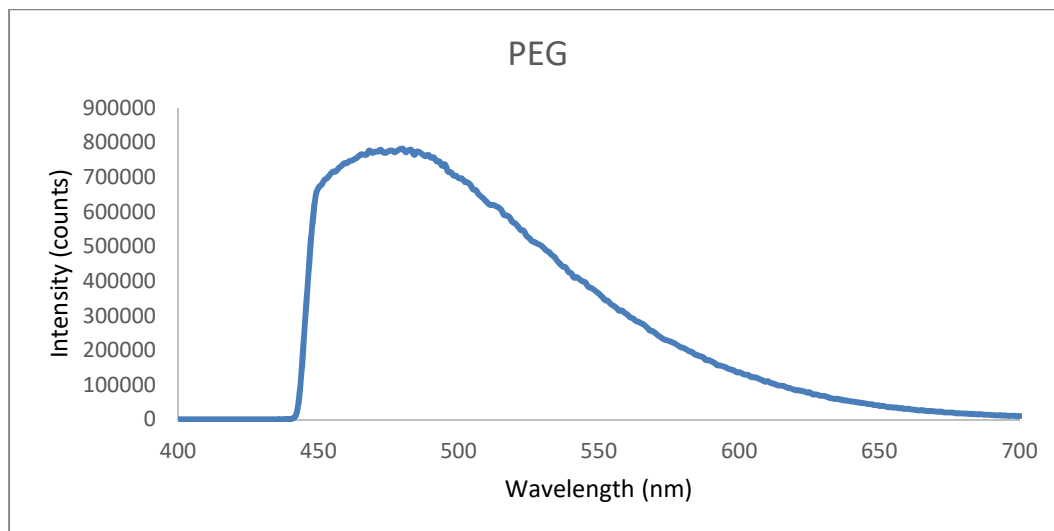


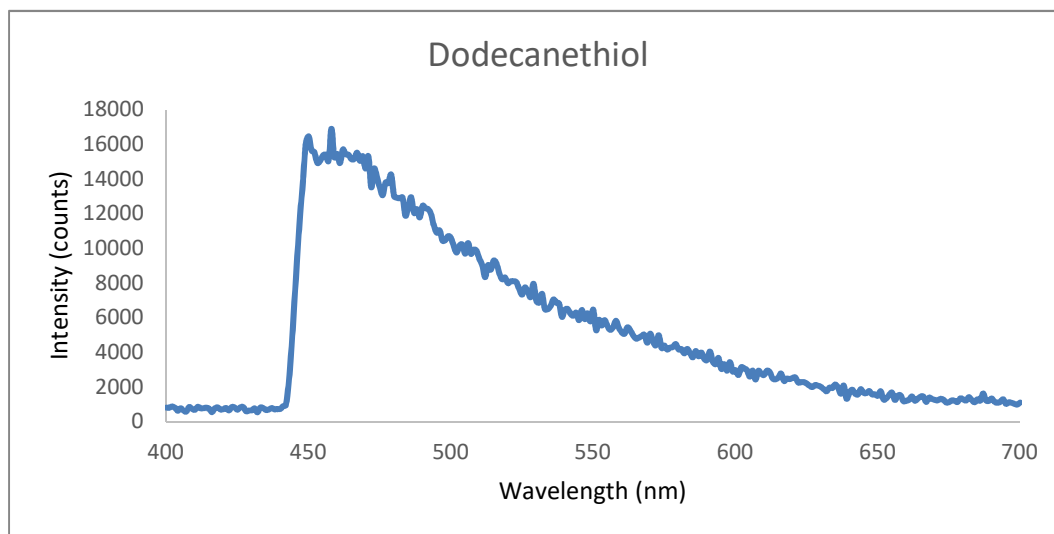
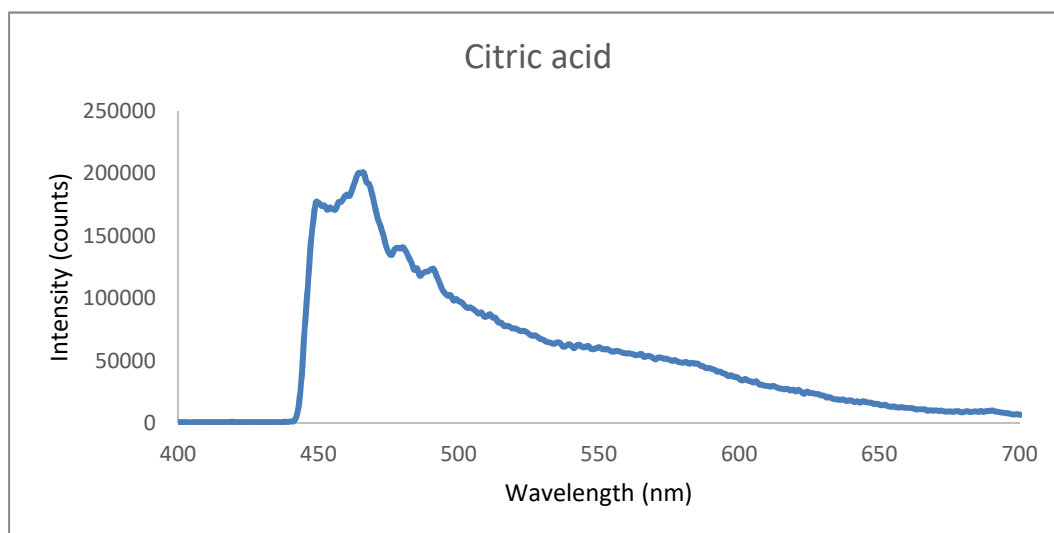
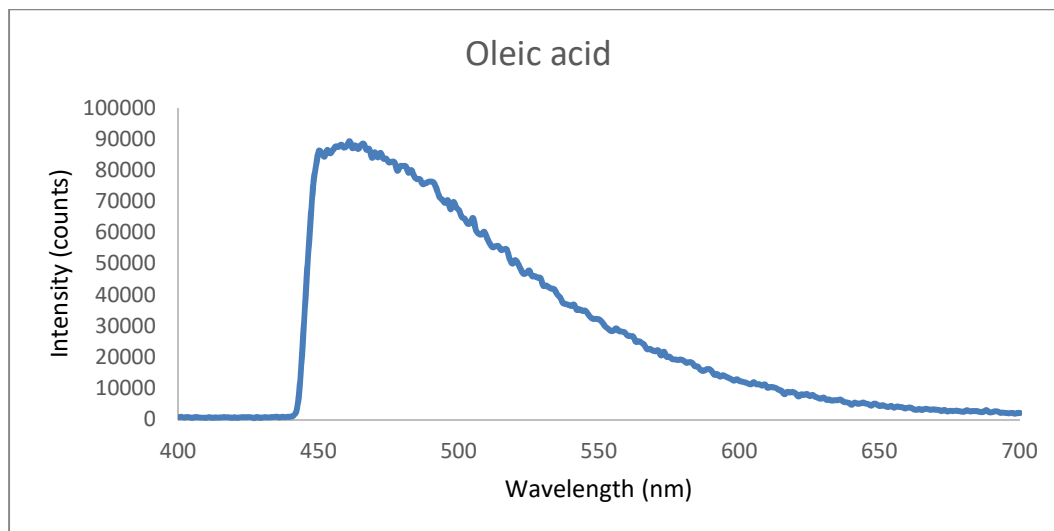


Appendix E: Photoluminescence spectra for differently capped ZnO quantum dots synthesized in a PFR.









Curriculum Vitae

Name: David Hiscott

Post-secondary Education and Degrees: The University of Western Ontario
London, Ontario, Canada
Sept. 2014 – April 2020 PhD
Chemical and Biochemical Engineering

Carleton University
Ottawa, Ontario, Canada
2001-2006 HBSc
Biochemistry

Honours and Awards: Province of Ontario Graduate Scholarship
1993-1994, 1994-1995

Social Science and Humanities Research Council (SSHRC)
Doctoral Fellowship
1995-1999

Related Work Experience Teaching Assistant
The University of Western Ontario
Sept. 2014 – Dec. 2018

Graduate Research Assistant
The University of Western Ontario
Sept. 2014 – Dec. 2019

Analytical Chemist
CASSEN Testing Laboratories
Toronto, Ontario, Canada
Feb. 2007 – Aug. 2014

Honors & Awards Greenfield Global Challenge 2018
\$15,000

Ross and Jean Clark Scholarship 2017
\$3000

Publications:

Hossain, MZ, Jhavar, AK, Chowdhury, MBI, Xu, WZ, Hiscott, DV & Charpentier, PA. (2016). Using subcritical water for decarboxylation of oleic acid into fuel range hydrocarbons. *Energy & Fuels* 31(4), 4013-40232

Conferences:

Converging on Nanomanufacturing, NanoCanada 1st National Conference, Montreal, Quebec (2017). Poster

100th Canadian Chemistry Conference and Exhibition, Canadian Society for Chemistry, Toronto, Ontario (2017). Poster

69th Canadian Chemical Engineering Conference, Canadian Society for Chemical Engineering, Halifax, Nova Scotia (2019). Presentation

Other Activities:

Graduate Engineering Society VP Internal (2016-2018)

Graduate Management Consulting Agency Director of Events (2016)

SOGS Councilor for Engineering Science (2016-2017)

City of London Environmental and Ecological Planning Advisory Committee (2014-2017)

Chemical and Biochemical Engineering Graduate Seminar Committee (2015-2016)

Associate Member of Ontario Hygiene Association (2012-2014)